Experimental and Numerical Assessment of a Tidal Turbine Control Strategy

---

Magnus Johnston Harrold

Idcore
Industrial Doctoral Centre
for Offshore Renewable Energy

A thesis submitted in partial fulfilment of the requirements for the award of an Engineering Doctorate

University of Strathclyde

2016

IDCORE

This thesis is submitted in partial fulfilment of the requirements for the award of an Engineering Doctorate, jointly awarded by the University of Edinburgh, the University of Exeter and the University of Strathclyde. The work presented has been conducted under the industrial supervision of Tidal Energy Ltd. as a project within the Industrial Doctoral Centre for Offshore Renewable Energy (IDCORE).

Declaration

I declare that this thesis was composed by myself and that the material presented, except where clearly indicated, is my own work. I declare that that the work has not been submitted for consideration as part of any other degree or professional qualification. Furthermore, the conference papers in Appendix A are also my own work.

Signed:

Abstract

Interest has increased on the usage of renewable energy in order to reduce the current global dependence on fossil fuels, a finite source of power that is also contributing to climate change. For many coastal countries, this has led to a number of research developments in tidal stream energy extraction, whereby flowing water is harnessed in a manner similar to the way in which wind turbines generate power from moving air. Unlike wind energy, however, the tides are predictable and thus tidal turbines could provide a reliable contribution of renewable energy to meet national energy demands.

In 2015, Tidal Energy Ltd. (TEL) installed a grid connected tidal turbine off the Pembrokeshire coast in Wales, U.K., making it one of the first full-scale tidal stream energy demonstration projects underway worldwide. The device has many parallels to a typical wind turbine, featuring three blades on a horizontal-axis rotor that drive an induction generator. However, its power regulation control strategy is unlike the standard methods used in the wind industry. The turbine was designed to limit both power and thrust in high tidal flows through the controlled overspeed of the rotor. This can be achieved with minimal controller complexity, plus there are a number of perceived cost and reliability benefits for the turbine system as a whole by adopting this control philosophy.

The control system is assessed in this thesis by firstly developing a numerical model of the turbine. Simulation results from the model were found to agree favourably with those obtained independently from a commercially available tidal turbine design code, predicting that the control strategy yields desirable power and thrust characteristics in all flow conditions. Further verification of the control strategy was subsequently achieved by experimentally testing a 1:30 scale model turbine in a laboratory flume tank. Using only the measurement of rotor speed as an input to the control system, the model turbine successfully tracked the maximum power condition in a time varying flow, before overspeeding to limit power and thrust in the highest flows.

Prior to the testing of the full-scale turbine, the flow sensors to be installed alongside the device were tested in both harbour and laboratory environments in order to better understand their capabilities. The results of which provided supplementary evidence to form conclusions on the performance of the full-scale device, including the ability to identify suspected yaw errors and track unsteady upstream flows. Once the turbine was installed at sea, its initial power performance was assessed in accordance to industry guidelines, while a methodology was developed to infer the operational rotor forces from strain gauges placed in the blades. The full-scale turbine demonstrated the expected power and thrust limiting behaviour from overspeeding the rotor, but a control system upgrade is required for the device to fully realise its potential.

Thus the research in this thesis contributes to current understanding of numerical modelling, scale model testing, environmental characterisation, and full-scale testing for the purposes of tidal stream energy generation.

Acknowledgements

I gratefully acknowledge the funding from the Energy Technologies Institute (ETI) and the RCUK Energy Programme for the Industrial Doctoral Centre for Offshore Renewable Energy (Grant number EP/J500847/1) that made the research presented here possible.

I wish to thank Tidal Energy Ltd. for not only giving me an interesting and rewarding research problem, but for the confidence and support they have shown me throughout my doctorate. First and foremost I would like to thank Pete Bromley for the day-to-day guidance he provided during my research, and for constantly pushing me to seek improvement in my work. Secondly, I thank Chris Williams for showing an unwavering belief in me as well as making much of the work in this thesis possible, and for being a consistent source of optimism. I would also like to thank Mérin Broudic for his commitment, resourcefulness and reliable assistance during the experimental sections of this thesis. Lastly, to all of the other members of Tidal Energy Ltd., I thank you for the positive environment created in the workplace. It has been a pleasure to be a part of such a dedicated, innovative and successful team.

For his sound advice throughout this research project, I thank my primary academic supervisor, David Clelland. I also thank David for ensuring that my focus did not deviate from the completion of this thesis, and for his voice of support that enabled me to attend a number of excellent and invaluable conferences over the last three years.

I thank the staff at Strathclyde University and the Kelvin Hydrodynamics laboratory for their assistance throughout the test campaign held there, as well as their preparatory work involved in manufacturing test equipment. On a similar level, I thank the staff and students at Cardiff University for their support during the scale model tests, including the access to the flume tank and the loan of test equipment.

Lastly, I thank my family for their undiminishing love and support in all of my endeavours. Thanks to my Mum for instilling her determination and self-belief in me, to my Dad for sharing his wisdom and level-headedness, to Ingrid for her selfless care and role model influence, and to Rebecca for the longstanding companionship and the joy she brings to all of us. A special thanks also to my Granny and Grandad, Margaret and Tom, for the significant role they played in the privileged upbringing that we Grandchildren enjoyed.

Table of Contents

List of Figures

List of Tables

1. Introduction

1.1 Global Energy Perspective and Climate Change

Global energy consumption more than doubled in a 40 year period between 1973 and 2013 [1], with this increasing trend only expected to continue in the 21st century. Approximately 80% of this energy consumption figure was met by fossil fuels, namely coal, oil and natural gas. It has been estimated that coal reserves should last for just over 100 years, while the other two fossil fuels just over 50 years [2]. It is clear, then, that other sources of energy will be required to meet the demands of a growing population, with improvements in energy efficiency only capable of prolonging the inevitable conclusion of fossil fuels.

This challenge is further complicated by the inescapable truth that fossil fuels are contributing to climate change, as a consequence of the production of carbon dioxide (CO_2) from their conversion to useable energy. As shown in Figure 1.1, atmospheric CO_2 concentrations have increased by 40% since the industrial revolution [3], and in the same period global average surface temperatures and sea levels have risen. This has resulted in an unprecedented number of droughts and floods, as well as changes to the ecosystem. It is clear, then, that these consequences of climate change are adversely affecting the health of human societies [4].

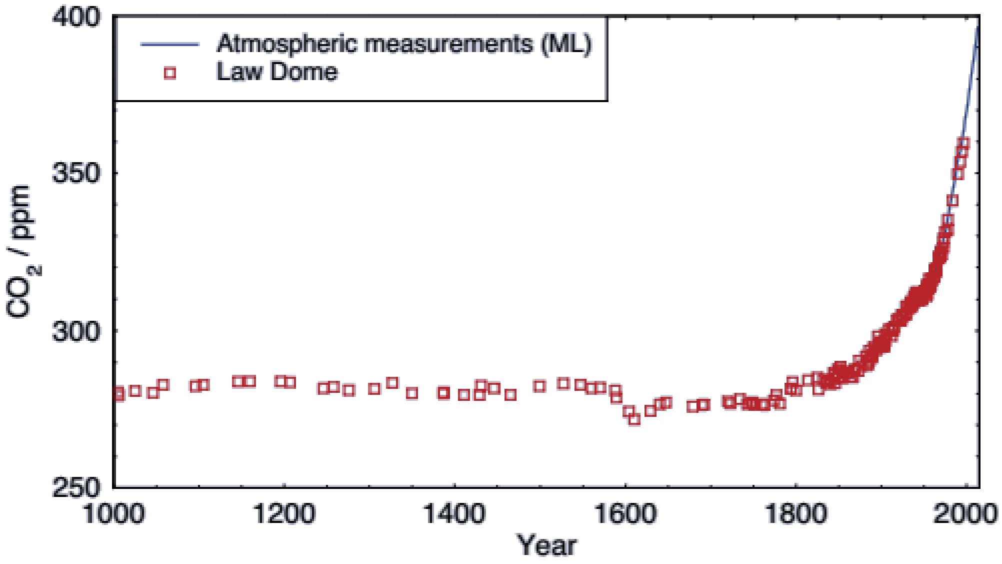

Figure 1.1: *Atmospheric concentration of CO_2 derived from ice cores in Antarctica (red) and obtained from recent measurement technology (blue) [3]*

To address the climate change problem, the Kyoto Protocol was adopted in 2005 to commit member states of the United Nations into taking preventative measures against climate change through the reduction of greenhouse gas emissions. The U.K., for example, is committed to ensuring that its carbon emissions are 80% lower in 2050 than levels in 1990 [5].

Nuclear power is a low carbon energy source that is often touted as an alternative to fossil fuel generation, and currently accounts for an estimated 2.5% of global energy consumption [6]. However, since the beginning of the 21st century, global electricity generation from nuclear power has remained almost constant [7]. This is arguably a consequence of public acceptance issues surrounding nuclear power, especially after the tragic events at Chernobyl and Fukushima. Opinion polls tend to suggest that public support for nuclear power is among the lowest of all forms of energy generation [8], [9], although this varies depending on a number of factors, including knowledge on climate change, knowledge on nuclear power, and proximity to nuclear power stations [10]. In addition to public challenges, contrasting opinions [11], [12] on the cost of nuclear power has affected the global adoption of the technology. Despite this, some governmental [13] and intergovernmental [14] studies estimate that nuclear power can be cost competitive with fossil fuel generation (Figure 1.2), but recognise that analyses of this type are sensitive to the high capital cost of nuclear technology.

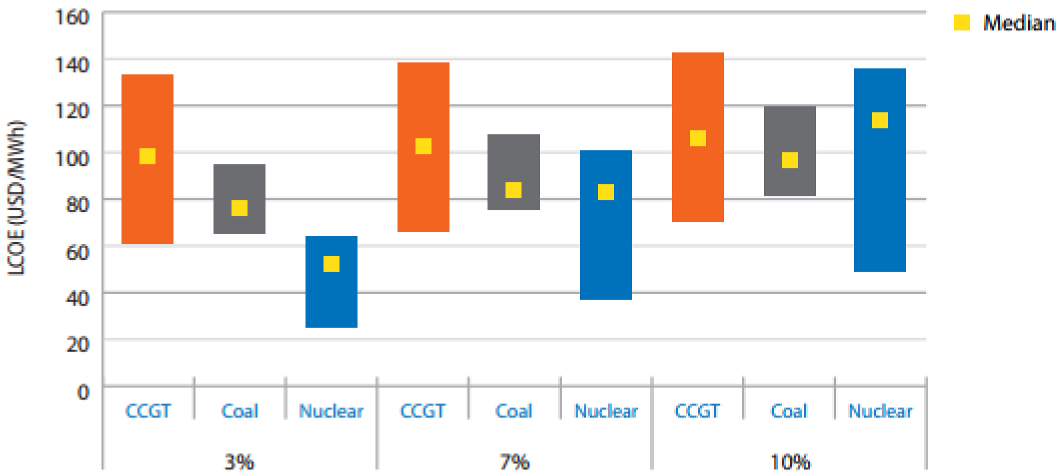

Figure 1.2: *The levelised cost of electricity (LCOE) for combined-cycle gas turbine (CCGT), coal and nuclear technology, compared at a discount rate between 3% – 10% [13]*

1.2 Renewable Energy

As a result of the identified challenges of conventional power generation and international obligations to address climate change, there is an increasing global interest in renewable energy. This has led to a number of countries creating renewable energy policy targets. For members of the European Union (EU), national targets have been set to raise the proportion of energy consumption that comes from renewable sources to 20% across the EU by 2020 [15], with the U.K. set a 15% target.

Hydropower systems have provided a reliable source of renewable energy for several decades, contributing an estimated 3.9% of global share of energy consumption in 2014 [6]. This proven technology has been used to develop some of the most economical schemes (large flow and head) in a number of countries, but there are still significant resources available worldwide, particularly in Asia and South America [16]. It has been estimated that just 20% of the technical hydropower potential has been developed globally [17]. The main challenges to new developments include unresolved environmental and social concerns, and the considerable capital investment required to build a new hydropower station, meaning that the payback period can be long.

The growth rate of hydropower has been steady over the last few years with recently commissioned projects in China, Brazil and Turkey [6]. However, in the same period greater amounts of generation capacity have been added from other renewable sources, namely solar PV and wind energy technologies. The increasing prevalence of these renewable energy sources is a result of technological improvements that have led to cost reductions [18], although the price of wind projects has fluctuated in recent years as a result of unstable commodity costs, e.g. steel [19]. Despite this, onshore wind is now regarded as cost-competitive with fossil fuel power generation, and there are an increasing number of solar PV projects that can also make this claim [20] (Figure 1.3).

While these renewable energy technologies are becoming increasingly appealing from a cost perspective, solar and wind require large areas of land to generate power on a utility scale when compared with conventional energy sources. This often results in opposition from local stakeholders that can lead to projects failing to achieve consent. As many as 57% of onshore wind farm applications in the U.K. were rejected in 2014, compared with 21% in 2008 [21]. This is despite public support for onshore wind remaining high at 65% - 70% during this time [22].

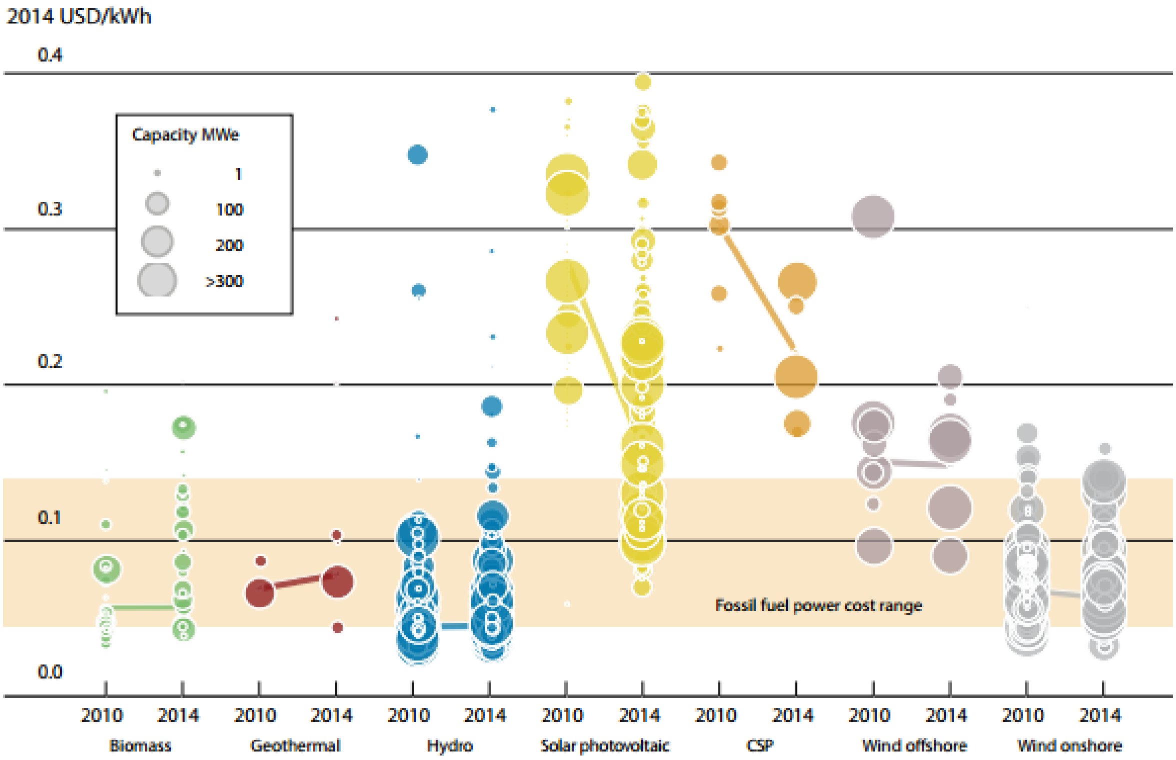

Figure 1.3: *The levelised cost of electricity for various renewable energy technologies. The area of the circle is proportional to the project capacity [20]*

Offshore wind resolves some of these stakeholder challenges and benefits from a better energy resource, thus allowing turbines to operate at higher capacity factors, i.e. the average power produced relative to the turbine capacity. However, the capital costs of offshore wind are approximately twice that of onshore projects due to the costs associated with marine operations, turbine foundations, and the additional design requirements for the offshore environment, to list a few [19]. Combine this with the higher operations and maintenance costs that arise from performing these tasks at sea, offshore wind is more expensive than onshore wind and is currently not competitive with fossil fuel power generation (Figure 1.3), although the price has been predicted to come down [23].

Combining the discussed renewables with bioenergy, geothermal energy and renewable waste, it has been estimated that the renewable energy provides a 19.2% share of global energy consumption [6]. Meanwhile, statistics released by the EU suggest that it is on course to meet the 20% target by the end of the decade, with the figure rising from 8.5% to 16% in a period of ten years to 2014 [24]. Therefore, renewables are clearly making a contribution to addressing climate change and reducing the global dependence on fossil fuels, but new advancements and techniques will be required to maintain this momentum and overcome the challenges, e.g. intermittency and energy storage.

1.3 Tidal Energy

In addition to the aforementioned types of renewable energy, there is interest in developing a number of other clean power sources that currently do not make sizeable contributions to energy statistics, one of which is tidal energy. The tides result from the rotation of the earth and the gravitational forces exerted on it from the moon and sun, causing periodic changes in sea level. The magnitude of these variations is mostly dependent on earth-moon-sun alignment and geographic location, with some parts of the world experiencing two low and high tides per day, while others just one. In areas where the tidal range (the difference between low and high water) is significant, there is potential to harness the energy from this movement of water. Furthermore, since both the magnitude and timing of the tides can be predicted to a high level of accuracy, so too can the quantity and availability of this energy resource. This is in contrast to most other forms of renewable energy.

While historically this resource was used to turn waterwheels for milling grain, there are now a few noteworthy MW scale tidal barrages [25], [26]. These are essentially dam structures that span across estuaries with an appreciable tidal range. The flow of water into the estuary is controlled by sluice gates placed in the barrage walls, which passes through turbines to generate electricity on both the ebb (water flowing out of the estuary) and flood (water flowing into the estuary) tides. The theoretical amount of energy, E, that can be produced from a barrage is proportional to both the area of the entrapped basin, A_{basin}, and the tidal range, h, squared, implying that small differences in the latter significantly influence the potential energy yield:

$$E = \frac{1}{2} \cdot A_{basin} \cdot \rho \cdot g \cdot h^2 \tag{1.1}$$

Where ρ and g are the density of water and acceleration due to gravity respectively.

The 750 m long La Rance barrage in Brittany, France, became the world's first commercial tidal power station after it opened in 1966 [27]. It is capable of generating 240 MW from its 22 km^2 basin and 8 m average tidal range. La Rance remained the largest tidal power plant by generation capacity for over four decades. This is perhaps a reflection of the level of interest in tidal barrage technology. Not only are there just a few locations in the world where the required site specific conditions could make tidal barrages a viable source of energy, but the capital cost associated with building this type of technology has resulted in some proposed projects failing to progress. For example, it has been suggested that a Severn barrage could provide up to 5% of the UK's current electricity generation, but a feasibility study by the government could not see a strategic case for public investment [28]. In addition to this, there is considerable uncertainty on the environmental impacts of tidal barrages due to a lack of adoption of the technology [25], with the La Rance project reporting on some negative and beneficial effects [29].

Tidal energy is not, however, restricted to the vertical motion of water. In some circumstances this tidal motion also creates a strong horizontal flow of water, referred to as tidal current or stream. This is particularly pronounced around headlands and islands due to the influence that bathymetry has on moving water, with the tidal currents generally travelling in two dominant flow directions, corresponding to the ebb and flood conditions. The expression for the amount of power, P, in flowing water is given by:

$$P = \frac{1}{2} \cdot \rho \cdot A \cdot v^3 \tag{1.2}$$

Where A is the area of the extraction plane perpendicular to the flowing water travelling at velocity, v. It is clear, then, that v is the critical term in assessing the power available from a tidal stream. The potential power from tidal stream globally is greater than it is from tidal range [30].

The tidal stream power relationship (Equation 1.2) is identical to that for wind energy, and consequently it should come as no surprise that the majority of the built tidal stream energy converters have much in common with wind turbines, with horizontal-axis turbines being the most prevalent. A tidal turbine, however, can be much smaller than its wind counterpart for the same power output, a result of the significant difference in density between air and water (approximately 800 times greater). This is despite wind generally travelling faster than tidal currents. It has been suggested that a horizontal-axis tidal turbine could have a rotor radius approximately one third of an equivalently power rated wind turbine, based on typical tidal current and wind speeds [31]. However, the tidal turbine would be subject to greater structural loading and must have stronger rotor blades to withstand these forces.

Unlike onshore wind turbines, another key consideration for the design of a tidal turbine is its seabed fixing. Some turbines have been mounted off structures pile driven into the seabed [32], while others sit there under their own weight on gravity based foundations [33]. Additionally, floating and semi-submerged [34] support structures with mooring systems have been tested. The choice of seabed fixing is usually dictated by several factors, including seabed composition, water depth, environmental and navigational constraints, cost, and ease of access for turbine maintenance.

Interest in the development of tidal stream technology has grown since the end of the 20th century, commencing with the testing of a 10 kW turbine in Loch Linnhe, Scotland, in 1994 [32]. This led to the development and testing of the first commercial scale turbine, an 11 m diameter, 300 kW device installed off the Devon coast in England in 2003 [35]. In the same year the European Marine Energy Centre (EMEC) was established, a dedicated test centre for wave and tidal devices located in Orkney, Scotland. Since the tidal stream site at EMEC opened in 2006, it has hosted more devices than any other location in the world [36], including MW scale turbines, e.g. [37]. Elsewhere, notable tidal turbine installations have been achieved in Canada [38], France [39], Northern Ireland [32], the U.S.A. [40], and the Netherlands [41].

As would be expected, these countries all benefit from considerable tidal stream resources from which tidal turbines could make a sizeable contribution towards regional and, in some cases, national energy demands. The U.K., for example, has the best tidal stream resource in Europe. The Crown Estate estimated that 95 TWh of energy could theoretically be produced per year from tidal stream devices around the U.K., with considerable resource areas found around the Scottish islands, the Welsh coastline, and in the English Channel [42]. The Carbon Trust also estimated the U.K. tidal stream resource, but considered practical constraints that would reduce the amount of energy that could be produced at a site, including shipping, fishing and designated areas [43]. Based on 30 sites around the U.K. (Figure 1.4), the practical resource was estimated to be 21 TWh per year, with 33% of this coming from the Pentland Firth and 28% from the Channel Islands. This 21 TWh would equate to 7% of the U.K.'s estimated annual electricity consumption [44].

If tidal turbines are to provide this level of energy generation, it has been recognised that there are a number of environmental, financial and technical challenges that need to be overcome [30], [43], [45]. As of 2016, it is expected that tidal turbines will soon be deployed in small numbers in the U.K. [46] and elsewhere in Europe [47], forming the first array, or tidal farm, projects. These projects will aim to provide evidence that tidal stream energy can make an appreciable contribution to local demands in a cost-effective, reliable and environmentally friendly manner.

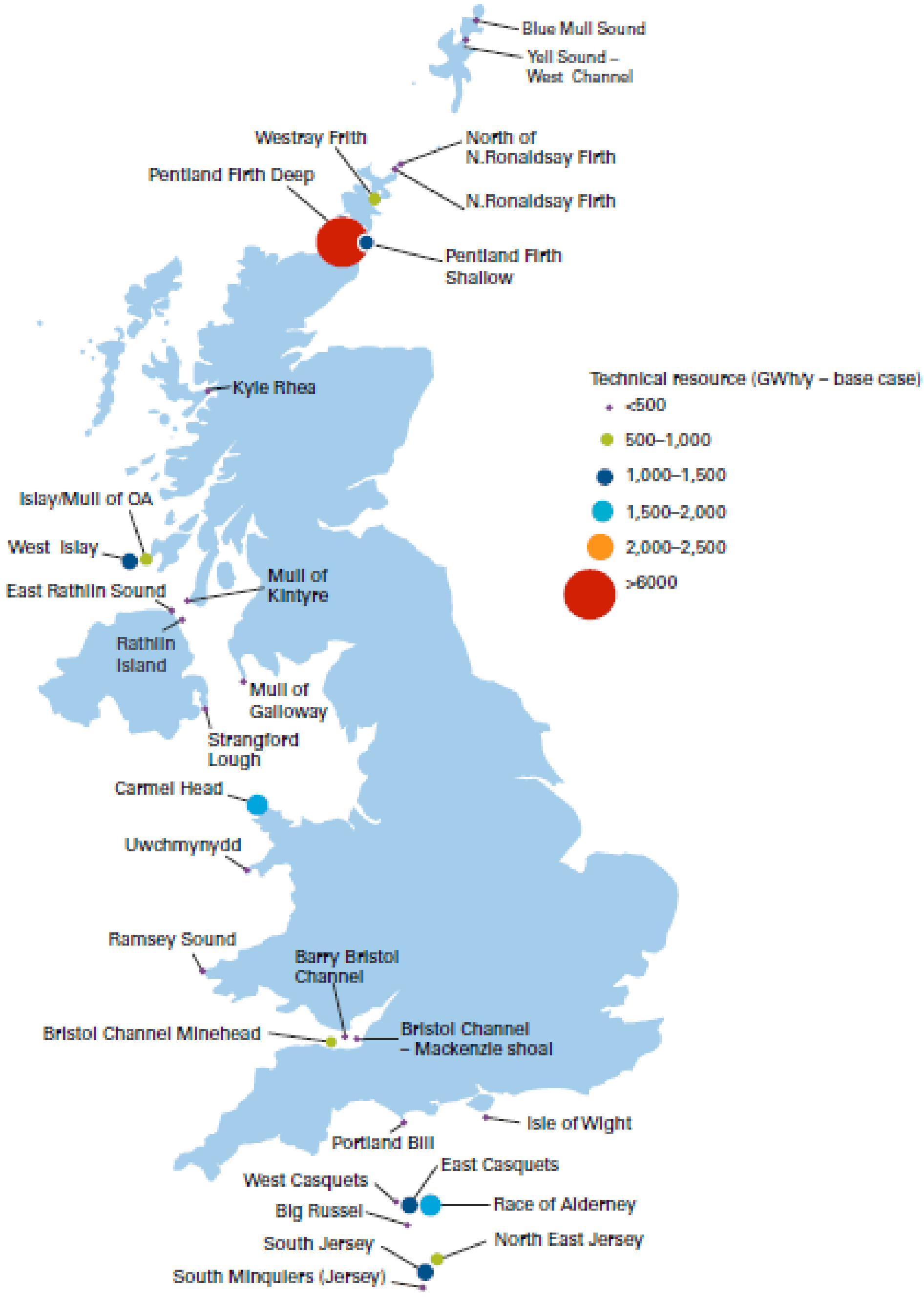

Figure 1.4: *The resource available from key tidal stream sites around the U.K. [43]*

1.4 Tidal Energy Ltd. (TEL)

Tidal Energy Ltd. (TEL) is a U.K. based tidal stream technology developer that has built and tested a 400 kW grid connected turbine, referred to as DeltaStream^{TM}. The device, pictured in Figure 1.5, is a 3-bladed horizontal axis turbine with a 12 m diameter rotor. Other key features include a hydraulic yaw system, a triangular gravity frame, and rock penetrating feet for seabed stability.

The turbine utilises a control strategy to regulate both power and structural loading by overspeeding the rotor. This concept of operation differs from conventional horizontal-axis turbine control methods, but has recently received some research interest (see Chapter 2). TEL adopted this control strategy because it allows the turbine to maintain a fixed-pitch rotor, thus ensuring that the cost and complexity of a pitching rotor is not added to the turbine system. Furthermore, it prevents the rotor from unpredictable and dynamic stall effects, i.e. the standard operational region for power regulation of fixed-pitch turbines. The overspeed control strategy is a key area of focus in this thesis.

Figure 1.5: *TEL's 400 kW, 12 m diameter rotor turbine, DeltaStream*^{TM}

In 2015 the turbine was installed at Ramsey Sound, a tidal race located between Ramsey Island and the Pembrokeshire coastline in southwest Wales (Figure 1.6). At the time of writing, test activities are ongoing at Ramsey Sound and TEL intends to continue advancing its technology at the site until commencing the deployment of DeltaStream^{TM} units in number. TEL has an agreement for lease with the Crown Estate for a 10 MW array project at the nearby location of St. Davids Head.

The turbine system is equipped with an extensive array of environmental and operational sensors, with the aim of understanding the effects of the Ramsey Sound environment on the turbine and vice versa. Of particular interest to this thesis are the two acoustic sensors that were installed at the site with the turbine, providing a number of measurements to better understand device performance, including profiles of the upstream and vertical flow velocity, as well as flow direction and wave properties.

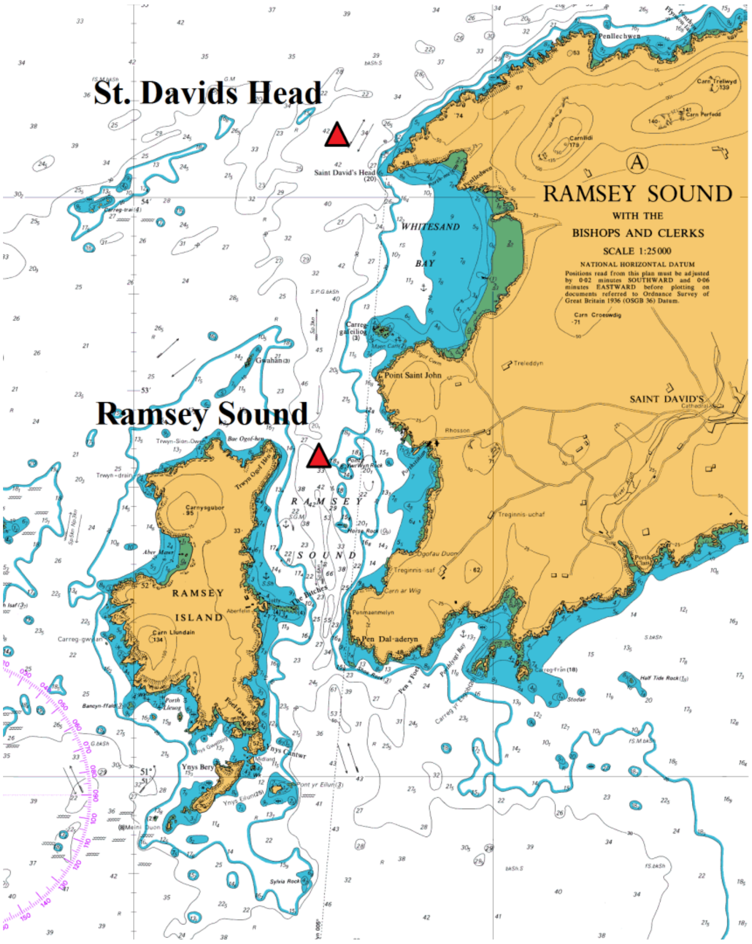

Figure 1.6: *DeltaStream^{TM} test site, Ramsey Sound, and the proposed St. Davids Head array site*

1.5 Research Objectives and Thesis Structure

The primary aim of this thesis is to assess the performance of a tidal stream turbine which utilises an overspeed based control strategy, through the usage of a combination of experimental and numerical methods. The following objectives were defined to address this aim:

- ***Objective 1:*** *Develop and validate a numerical model of a tidal turbine*

  This tool will allow the control system to be assessed numerically before a physical test, and will also lead to the creation of a development environment in which modifications to the turbine or its concept of operation can be quickly evaluated, provided that a validation of the model is achieved.

- ***Objective 2:*** *Test the control strategy on a scale model tidal turbine*

  These tests will provide experimental data to validate the numerical model predictions of tidal turbine performance (objective 1). The tests will also act as the first physical demonstration of the turbine control strategy, allowing its dynamics to be studied at low risk to provide confidence ahead of future and larger trials.

- ***Objective 3:*** *Evaluate the capabilities of flow sensors to be used in the tidal environment*

  Determining the strengths and limitations of the flow instrumentation will lead to increased certainty on characterising the tidal environment in which the full-scale turbine is tested (objective 4). Hence, conclusions on the operational performance of the turbine can be made in the knowledge that its surrounding environment is understood with confidence.

- ***Objective 4:*** *Assess the performance of a full-scale tidal turbine*

  Only full-scale testing at sea can capture the real world phenomena in which a tidal turbine operates. Therefore, this is the ultimate assessment of the turbine and its control strategy. The findings from these tests also feedback into each of the previous objectives, identifying the merits of each.

This thesis reviews the state of the art of tidal energy research in Chapter 2, focusing specifically on numerical modelling, environmental characterisation methods, physical testing, and tidal turbine control strategies. Thereafter, the thesis addresses each of the previously defined objectives in Chapters 3 – 6. These are summarised below:

Chapter 3 details the development of a mathematical model capable of simulating a turbine in dynamic conditions representative of the tidal stream environment. The model is validated against a commercially available code.

Chapter 4 describes the testing of a 1:30 scale turbine in a laboratory flume. The turbine was configured to adhere to the logic of an overspeed based control system in time-varying flows. Experimental results are compared with predictions of device performance made using the numerical model developed in Chapter 3.

Chapter 5 reports on two separate test campaigns of the flow instrumentation. The first of which characterised a harbour environment with an appreciable tidal flow, while the second addressed instrument uncertainty by testing the instruments in well understood laboratory conditions.

Chapter 6 assesses both the power performance and rotor loading of the full-scale DeltaStream^{TM} turbine from its initial operational trials at Ramsey Sound, in accordance with best practices from the industry. Results are derived relative to flow measurements obtained from the sensors tested in Chapter 5, and are compared with numerical predictions made in Chapter 3.

Chapter 7 discusses how the work in this thesis has contributed to the current level of knowledge on numerical modelling, physical testing at both scale and full-scale, and environmental characterisation for the purposes of tidal stream energy.

Chapter 8 concludes the main findings from this thesis.

2. Literature Review

2.1 Numerical Modelling of Tidal Turbines

Numerical models are used throughout the design and development of a tidal turbine. Much of the research in this area has led to the development of models that originate from existing wind turbine codes [48], particularly for horizontal-axis turbines. The most notable of which are based on blade element momentum (BEM) theory [49], which models the rotor aerodynamics, or hydrodynamics for the case of a tidal turbine, and has been used widely in tidal turbine research [50], [51], [52], [53]. This is a hybrid of both blade element theory and momentum theory. The former splits the turbine rotor blades into separate elements in the radial direction and along the blade length, each of which perform as individual 2-dimensional aerofoils without any interaction with the other segments. The aerodynamic forces on each aerofoil are calculated from its lift and drag characteristics and the current environmental conditions, allowing the net rotor loads to be determined via a summation of the elemental forces. Momentum theory, in contrast to this, treats the rotor as an idealised actuator disc which extracts energy in the rotor plane, causing a loss of momentum in the flow. The corresponding pressure drop decreases the rotor flow velocities in the axial and radial directions, with the relative decrease referred to as an induction factor. The resulting inflow in the rotor plane is required to calculate the forces in blade element theory. Both theories result in separate expressions for elemental rotor thrust and torque. Through the choice of appropriate initialisation values, these equations are usually solved through an iteration process to determine the induction factors, and hence the rotor loads.

The basic form of BEM theory fails to capture a number of dynamic effects, and as a result several modifications have been developed to the standard code in order to account for these complexities. This usually includes corrections for the effects that vortices created in the turbine wake have on the rotor inflow [49], [54]. These vortices are produced at the rotor hub and tip, resulting in an efficiency decrease as a consequence of reduced lift, torque and power being developed [51].

Standard BEM codes will also evaluate the elemental forces on the blades in a constant flow velocity, leading to a good understanding of the steady-state characteristics of the rotor. However, in reality the flow across the rotor disc in a tidal stream is inherently unsteady [55]. Therefore, it is necessary to incorporate an environment that is much more representative of real tidal conditions in order to predict the dynamic performance of the rotor. Turbulence, for example, is often added to BEM codes using spectral models [56], subjecting the rotor to a spatiotemporally varying flow field in which interpolation methods are used to determine the velocity components at the position of each blade element. Similarly, wave induced currents add an unsteady component to the rotor flow and have been included in BEM models using linear wave theory [57], [58].

By modelling the turbine in these more realistic environments, it increases the likelihood of the rotor operating in regions where the static aerofoil properties do not accurately predict performance. This includes dynamic stall events, in which the measured aerofoil lift and drag coefficients from an operating wind turbine have been found to differ to those obtained in wind tunnels [59]. Semi-empirical models have been developed to account for these effects [60].

Confidence in the BEM method has increased after a number of experimental validation studies, including the research in [61], [62], [63], where the results from an 800 mm diameter tidal turbine operating in a cavitation tunnel showed a good agreement with numerical predictions of rotor performance for a range of conditions. Of the BEM models that have been extended to include wave effects, laboratory scale experiments have shown that the numerical predictions can capture the mean [57] and time-varying [58] rotor loads well, while [64] concluded that a dynamic stall model is necessary to estimate the forces from extreme conditions (high and steep waves).

The level of interest in tidal stream energy has increased to the point that commercial BEM based numerical models have become available, most notably DNV GL's Tidal Bladed software [65]. This product builds on the company's pre-existing Bladed software for modelling wind turbines [52]. The rotor hydrodynamics within Tidal Bladed can account for all of the aforementioned modifications to the standard BEM code, and includes others such as buoyancy and added mass related rotor loading, as well as cavitation prediction and blockage effects from operating within a confined channel [48]. The rotor model is coupled to various other models of the turbine system, including the drivetrain, electrical system and controller, leading to an understanding of how the entire device performs.

Initial validations of Tidal Bladed in [62] suggested that the power performance of a model scale turbine was overestimated by the software. Thrust predictions, however, were in good agreement at all operational ranges. Further laboratory scale validations were performed on a floating, twin-rotor tidal turbine in [66]. The software reproduced much of the behaviour of a device that was able to move in pitch, roll and yaw, but it was acknowledged that these more complex devices must be structurally modelled to a high degree of accuracy to improve the numerical predictions.

The largest validation study of Tidal Bladed, and indeed any numerical model of a tidal turbine, was performed as part of the Energy Technologies Institute (ETI) sponsored Reliable Data Acquisition Platform for Tidal (ReDAPT) research project. This involved installing and testing an 18 m diameter, 1 MW turbine at EMEC and comparing measured performance data with Tidal Bladed predictions. Comprehensive detail on the dynamic effects included in the setup of the model are not publicly available, but power curves from both Tidal Bladed and the operating turbine are shown to compare well in [37] and [67]. Further to this, the measured mean and dynamic blade bending moment results agreed favourably with the numerical predictions [68]. These validation studies have allowed DNV

GL to proclaim that Tidal Bladed is the "only validated, industry-standard tool for simulating tidal turbines at the design stage."

While BEM based methods have become the numerical tool of choice for the design of tidal turbines, there are a number of complex effects that they cannot accurately model. This includes many of the previously discussed BEM modifications, some of which are reliant on empirical corrections that may not be applicable in all scenarios. In addition to this, BEM models are not capable of predicting the effect that a turbine rotor has on the local flow environment. This is in contrast to numerical models based on computational fluid dynamics (CFD), which are suited to broad range of problems. This includes turbine wake behaviour, with the research in [69] showing that CFD simulations were capable of capturing much of the downstream flow characteristics behind a porous disc.

A number of CFD research studies have investigated the effect that turbine support structure geometry has on rotor performance. For example, the research in [70] compared several tower geometries and concluded that a square support structure leads to detrimental amounts of developed rotor power and thrust when compared with a circular geometry. This research was extended by further CFD analyses in [71], where rotor performance was shown to improve with separation distance from the support structure. Furthermore, this research showed that a turbine operating downstream of the support structure, i.e. in the wake of it, was subject to significantly greater blade root bending moment transients than in the upstream orientation. It should be noted that a number of BEM based models do include the capability to model interaction effects between the rotor and the support structure based on empirical work, e.g. [49]. The research in [72] showed that the predicted interaction effects from this simplified model agree well with those from CFD simulations, although the former is only applicable to cylindrical support structures, i.e. a geometry not dissimilar to a wind turbine tower. This simplified model would not have been suitable for the assessment of flow around a semi-submerged platform hosting 36 tidal turbines in [73], where CFD was instead used.

CFD methods have also been applied to a number of other challenging problems in tidal energy research, including blade deflection effects [74], [75], the performance of ducted rotors [76], [77], and array studies [78]. This versatility means that CFD is an attractive option for most numerical investigations, but it comes at the cost of significant computational expense. In [79] it was reported that it took 6 days to simulate a single rotation of a tidal turbine using CFD. Coupled BEM and CFD models appear to be one promising method for meeting the needs of numerical sophistication without adding significant computational expense [80], [81], [82]. This approach models the forces that the rotor imparts on the flow through the use of BEM methods, and combines it with a CFD domain to determine the effect that the turbine has on the local flow environment. The result is a hybrid model that does not need to incorporate detail on the rotor geometry, meaning that simulation times are several orders of magnitude lower than those from CFD alone. The BEM-CFD model in [80] took slightly more than one hour to complete a simulation.

2.2 Leading Environmental Characterisation Methods

Detailed and reliable environmental measurements are important at various stages of a tidal stream energy project. At the project feasibility stage, these measurements not only allow estimates to be made on the energy resource at a site of interest [83], but lead to an understanding of the unsteady environmental loads that a turbine will be subject to [55]. This information could, for example, be incorporated into any of the numerical methods described in Section 2.1 to improve the representation of the modelled environment. This approach was taken in [70], where the measured velocity shear profile from the Severn Estuary was used as the flow input to a CFD model of a tidal turbine. For research involving the testing of full-scale tidal turbines, reference measurements of the current velocities enable device performance to be measured and compared with numerical predictions [67], with any deviations from the norm a useful indication of the condition of the turbine. Environmental characterisation is equally important during scale model testing, allowing researchers to understand how certain flow properties can affect turbine performance in controlled laboratory settings, such as turbulence [84].

Currently the instrument of choice for tidal stream characterisation is the acoustic Doppler profiler (ADP), with this type of technology being used in tidal energy related research globally [55], [83], [85], [86]. An ADP transmits acoustic pulses from transducer beams into the water and “listens” for the returning signals. The transmitted sound scatters off small particulates, resulting in the reflected signal experiencing a frequency shift that is used to evaluate the water velocity via the Doppler effect [87], [88]. The inherent assumption here is that the scatterers travel at the same velocity as the water. The time it takes for the sound to return to the instrument is used to determine the distance at which the measurement was made. Returning signals are sorted into a number of distance intervals for averaging, often referred to as bins or cells. This leads to a profile of water velocities being developed at range. An ADP requires at least three diverging beams to resolve the 3-dimensional velocity, and assumes flow homogeneity across these beams.

The requirements of the ADP survey should be known before selecting the operating frequency of the instrument, as there is a trade-off between spatial resolution and range. Higher frequency instruments achieve the greatest spatial resolution, but have the lowest profiling ranges due to the increased absorption of sound in water with frequency. Additionally, the way in which the instrument is configured can influence the results obtained from a deployment. The chosen bin size dictates the spatial resolution of the measured flow profile. However, decreasing this parameter, thus increasing the spatial resolution, means that there are fewer returning measurements in each bin, and as a consequence the certainty of each derived average value decreases. The chosen sampling rate has a similar effect, and also influences the battery life of the instrument.

ADPs have developed over the years to not only obtain flow velocities, but now also provide simultaneous measurements of wave parameters. Modern ADPs can use as many as a combination of three methods to achieve this [89]. These are the measurements of orbital velocities below the sea surface, pressure measurements from inbuilt sensors, and direct surface tracking measurements from strong returning acoustic signals from any of the ADP’s beams. Some ADPs now include an additional vertically oriented beam to improve the accuracy of the latter [90]. Both linear wave theory and spectral methods can be used to determine wave parameters from these measurements. Under certain circumstances, some of these methods are more reliable than others. For example, the surface track method can become difficult when the surface is significantly disturbed by wind. Hence, the ADPs which have the greatest number of sensors offer more options for applying quality control to measurements. Other sensors that are commonly incorporated into in ADPs might be used to measure heading, pitch, roll, salinity and temperature. The last two of these are used to compute the speed of sound in water.

It is this combined capability of obtaining simultaneous current and wave measurements that makes ADPs the preferred instrument for tidal stream site characterisation. For research studies focusing on the energy resource at a site of interest, ADPs have been used as part of vessel transect surveys to understand the spatial variation of flow, identifying suitable locations for turbine deployment [91]. This is usually achieved by mounting the ADP off a small vessel such that it is oriented vertically downwards, and transecting across the site in a series of straight lines that are typically separated by less than 100 m. Normally each transect is performed in both directions to account for velocity biases that can be introduced through vessel motion. It is recommended that this total transect time, i.e. the time it takes for the vessel to return to the starting position, is no longer than 10 minutes, otherwise the velocities might have changed significantly due to the variations in the tidal cycle, while each transect should be repeated at various stages throughout the tidal cycle to capture this temporal variation [92].

The results from this type of survey illustrate the variation in the tidal resource both along the transect line and throughout the water column [83], leading to an understanding of the way in which bathymetry influences the flow. A research study performed at Ramsey Sound, for example, showed that an underwater pinnacle can produce wakes that extend beyond 400 m downstream [93], [94]. Similarly in [95], a series of vessel laps were performed in Puget Sound, USA, to characterise a region with an ADP, showing that the spatial variation in flow is independent of time of year. This research also highlighted the difficulty vessels have in perfectly repeating transects and maintaining a constant speed due to the wind, waves and tides.

To better understand the resource at an identified location, this last research study also emphasised the need for stationary observations. This could be obtained from a vessel holding its position or a seabed mounted arrangement, but the latter is preferred to achieve longer records. It is common practice to house an ADP in a small, low drag frame that sits on the seabed at tidal energy sites for resource assessments. Unless the ADP is powered via a cable to shore, the battery life of the instrument is the key limitation for this arrangement. For resource assessments, this constraint can be minimised by increasing the sampling period of the instrument, with the ADP performing short bursts of measurements at pre-configured intervals, e.g. 10 minutes, rather than constantly operating near the maximum sample rate. This configuration provides a good description of the mean flow conditions at the site of interest over considerable time periods. The industry guidelines on resource assessment recommend obtaining data for three months, or one month as a minimum [92]. This length of velocity record allows resource forecasts to be made over timeframes considerably longer than the survey period, through the use of harmonic analysis. The methodology uses Fourier methods to obtain a number of harmonic constituents that enable the reconstruction of the measured tidal currents, allowing predictions to be made for other time periods. The technique was used in [96] to predict the tidal currents from ADP surveys at EMEC and the Sound of Islay, showing a good correlation between measured and predicted data at the former, but did not fully capture the amount of variation in current direction.

Seabed mounted ADPs are also usually preferred for understanding the environmental loading that a turbine will be subject to. It is crucial to capture high frequency data for this type of survey, meaning that a separate and shorter ADP deployment is usually required for this purpose. This will often coincide with a large, spring tide to capture extreme conditions. Not only are the maximum currents of interest, but information on velocity shear, wave climate and turbulence are all important for turbine design and simulation. In [97], a methodology for determining turbulence metrics from ADP measurements is presented using data from Ramsey Sound. Interestingly, this work compared these parameters from two, separate surveys at the site, positioned less than 50 m apart. A considerable difference in turbulence properties between these surveys was found, emphasising the importance of obtaining measurements from the exact turbine location. It should be noted, however, that the surveys were not performed simultaneously, and the differences could be attributed to temporal variation. In [55] and [98], it is stressed that ADP measurements of turbulence intensity should be corrected for Doppler noise, a predicted standard error stated by the manufacturer due to inherent instrument noise. If uncorrected, measurements of standard deviation, and hence turbulence intensity, will be incorrectly high, leading to increased predictions of fatigue damage to a turbine.

Multiple ADPs have also been deployed in number at tidal energy sites to try and provide an extensive characterisation. As part of the ReDAPT project, seven ADPs were installed on top of a 500 kW tidal turbine along with an additional seabed mounted device [99]. This included the use of both single-beam Doppler instruments, capable of resolving 1-dimensional line of site velocities, as well as the more conventional multi-beam devices, with various profiling ranges and spatial resolutions configured. This research was extended in [100] by mounting 17 acoustic sensors on a larger turbine, including a single-beam in the turbine nose to face the flow approaching the rotor. Although most of the work from this research project is yet to be published, it should provide the most detailed picture of the environment in the vicinity of a tidal turbine. Similarly, as part of the Turbulence in Marine Environments (TiME) research project, arrays of ADPs were deployed at two other UK tidal energy sites, the Pentland Firth and Sound of Islay. The research aimed to measure, classify and predict the effect of turbulence on tidal energy resource assessment, turbine design and performance, and the yield from array projects. The ADPs were used in conjunction with non-acoustic instruments, leading to the publication of technical reports on recommended instrumentation selection, survey practices and data analysis procedures for the measurement of turbulence [101], [102], as well as a review of techniques available for simulation [103]. Lastly, a research project is underway in the Bay of Fundy, Canada, to attempt to overcome the difficulties in determining certain turbulence metrics from multi-beam acoustic devices, due to the averaging of measurements across diverging beams. This project is using a seabed platform to house five single-beams that are oriented such that their beams converge at desired positions above the platform. The arrangement is referred to as the Vectron and was tested in [85], showing that spectral velocity measurements agree well with other instruments.

The aforementioned assumptions and limitations of ADP technology suggest that for certain measurements, other instruments might be more suitable. Acoustic Doppler velocimeters (ADV), for example, also use acoustic beams and the Doppler principle to determine 3-dimensional flow. However, the ADV has beams which are oriented to converge just centimetres away from the probe to form a small sampling volume [87]. This provides a direct measurement of velocity at a position, rather than inferring this from measurements made at a number of separate locations from diverging beams, i.e. the ADP method. ADVs also contain much lower levels of Doppler noise than ADPs [55], [98] and can measure at higher sampling rates, enabling spectral analyses of turbulence to be performed at a greater range of frequencies. Thus, ADV flow measurements contain much higher accuracy and detail than those from an ADP, but are only formed at a single point. This key limitation makes them impractical in the field. An array of ADVs would be required to capture the spatial range of an ADP, which would be both challenging technically and cost considerably more than an ADP deployment. In [104], the possibility of placing multiple ADVs on a mooring line was considered for the purpose of obtaining detailed measurements over a rotor disc. It was shown that when coupled with an inertial motion unit, the mooring line motion could be used to correct ADV measurements affected by this non-fixed platform. This arrangement would be cheaper than installing a tower structure to position the ADVs.

ADVs are, however, regularly used for scale model testing of tidal turbines in the field [105] and laboratory [106]. At this scale the rotor diameter is small enough that a point measurement can be assumed to be representative of the flow experienced by the entire rotor disc. In addition, ADPs are not suited to the laboratory due to the possibility of interference from signals reflecting back from the shallow water depth and the confined space created by the test tank walls. There are also concerns relating to the lack of debris and particulates generally found in laboratory tanks compared with the sea, meaning that an ADP will have fewer backscatters to determine the flow velocity. This can also be a problem for ADVs, but is often overcome through the usage of a seeding material in the test tank. In addition to these benefits for the laboratory application, the ADV is a comparatively light and portable instrument, which makes it easy to move and obtain measurements from another area of interest. One study utilised this to measure the wake behind a 0.5 m diameter turbine to within 0.05 m resolution in the span-wise direction [106], i.e. across the width of the flume tank and perpendicular to the flow direction. These measurements were made at various downstream distances and vertical positions, leading to a detailed understanding of both the mean and turbulent flow field behind a turbine. Similarly, ADV measurements obtained from multiple depths within a laboratory flume have been used to verify predictions of wave induced currents from linear wave theory, before assessing the effect that this unsteady flow had on a model turbine [107].

While ADPs and ADVs are used extensively in tidal energy research, there is a developing interest in non-acoustic based instrumentation for flow measurements. Radar systems, for example, can determine currents and wave properties at a site of interest from radio waves that are Bragg scattered off small ripples on the sea surface. The key advantage of these systems is that there is no requirement for an offshore survey. They are instead often housed in shore based stations, meaning that the instrument can be easily installed and accessed without the cost associated with marine operations. In addition, from this shore based position it is possible to scan across a site to cover areas in excess of several square kilometres. Unlike the previously described vessel based ADP technique, surveying an area of this size with a marine radar system does not introduce temporal variation to measurements, resulting in an accurate picture of the entire site at any point in time within the survey period. In [108], two marine radar systems were positioned on the Western Brittany coast to survey the surface currents of the Iroise Sea in an area extending out to 140 km offshore. The results of this study not only identified two areas that have a suitable resource for tidal stream energy generation, but highlighted asymmetries between phases within the tidal cycle.

The main drawback of marine radar is the lack of sub-surface information on flow velocity, meaning that it is difficult to determine the conditions that a turbine rotor would experience. Marine radar measurements of surface velocity obtained from the EMEC test site were observed to be consistently higher than those from a simultaneous seabed ADP deployment [109], in which the flow velocities were depth averaged. This result was not entirely unexpected, given that the flow tends to be highest near the surface. The vertical flow profile can be predicted by assuming it follows a logarithmic or power law relationship, as in [110], but these expressions are often site dependent and require an offshore survey to establish the relationship in the first instance. Lastly, marine radars cannot always be relied upon in certain weather conditions. For example, in calm seas where there are light winds and low wave heights, the instrument will have difficulty resolving the near-flat surface properties. Similarly, the backscatter from rainfall can disrupt measurements.

Lastly, shear probes have recently seen some usage in tidal energy research for detailed turbulence measurements [101], [111]. These instruments measure turbulent velocity fluctuations at high spatial and temporal resolutions from the microscopic bending of its piezo-ceramic sensors [112]. The instrument ultimately obtains point measurements, but it can be used in a glider to obtain water profiles.

2.3 Physical Testing of Tidal Turbines

Due primarily to the high cost associated with large-scale testing of tidal turbines at sea, it is common practice to perform a degree of testing at a smaller scale first, providing the opportunity to evaluate key concepts of a particular design, or validate numerical models. This first step is often performed in laboratory tanks. These facilities are attractive because they provide a controlled and repeatable environment in which experiments can be designed to yield a high volume of accurate results within the order of days. Towing tanks are one such facility that are being used to test model scale tidal turbines. This comprises a tank of water that is significantly longer than it is in both the depth and width dimensions, with many of these tanks in excess of 100 m in length. Models are affixed to a towing carriage that moves back and forth along the length of the tank to simulate a flow. Some of these facilities may include a machine capable of generating waves from one end of the tank to study these effects. Historically these laboratories were built to test model ships and offshore structures, but the achievable carriage speeds and precision to which these are known makes them suitable for tidal turbine research. In [113], a 1:20 scale tidal turbine was towed up to speeds of 1 $m \cdot s^{-1}$ in a tank 76 m long. The tests established rotor performance related criteria to an uncertainty of less than 5%. Towing tanks have also been used to study more complicated problems, including misaligned flow [114], wave-induced currents [57], and the motions of a floating turbine [66].

Any model in a towing tank is subject to very low levels of turbulence since the water is still. This is unlike the tidal stream environment, in which turbulence intensities exceeding 10% have been reported [55], [100], and presents a limitation in using a towing tank for studying these effects. A flume tank is better suited for this requirement. In these facilities, water is driven through a channel to pass a stationary model turbine, either supported by a structure overhanging the tank or attached to its floor. Usually the water is recirculated underneath the tank to provide a consistent flow. This moving water contains a level of vertical non-uniformity and turbulence, both of which can be modified by placing upstream grids or flow straighteners. The turbulence intensity in a recirculating flume was reduced from 15% to 3% through the use of upstream honeycomb grid to study the effect of turbulence on both a single turbine [84] and two interacting turbines [115]. It should be noted that grids can be held in front of a model turbine in a towing tank to create turbulence, but it is harder to achieve the desired result. Flume experiments also tend to take less time as the water can be left flowing, rather than the stop-start nature of towing tests. A direct comparison of flume and towing tank experiments was performed in [116], where a tidal turbine was tested in two of each of these facilities. The mean performance related results were found to be in good agreement in each of the four tanks, but the standard deviations were higher in the flume tanks. This was attributed to the increased turbulence.

For floating tidal turbines, a wave tank may also be used to evaluate the response of the device to extreme wave conditions that may not be possible to replicate in a flume or a towing tank. Wave tanks are typically comparable in both length and width dimensions, with flap or piston wavemakers installed along one or more of the tank walls. These facilities are usually not equipped with current generating capabilities and are instead used in studies where these effects are of little interest, e.g. testing wave energy devices. One notable exception is the FloWave TT facility, a circular tank that can produce waves and currents in any direction [117], [118], making it suitable for a wide variety of applications in complex conditions.

To relate the results of a scale model turbine test to a full-scale device, a number of similarity levels must be satisfied for a complete comparison [119], [120]. These are geometric, kinematic and dynamic similarities, ensuring that not only all of the model's dimensions are correctly scaled, but the velocity and force ratios are held constant for the fluid and model. It is, however, impossible to satisfy all force ratios and hence full similitude cannot be achieved with scale model testing. As a consequence of this, it is necessary to select the force ratio that is most relevant to the application. Generally the Froude (inertial/gravitational forces) or Reynolds (inertial/viscous forces) number is the most applicable force ratio for hydrodynamic situations. The former is relevant when the effects of buoyancy and gravitational forces are significant, while the latter is appropriate when hydrodynamic loading and viscous effects dominate. Reynolds scaling is usually the most relevant for assessing the power performance and structural loading of tidal turbines [119]. It is, however, significantly challenging to test scale turbines at equivalent Reynolds numbers. For an aerofoil, the Reynolds number, Re, may be expressed as:

$$Re = \frac{\rho \cdot v_r \cdot \mathrm{c}}{\mu} \tag{2.1}$$

Where ρ is the density of the fluid, v_r is the relative flow velocity, c is the chord length of the aerofoil, and μ is the dynamic viscosity of the fluid. It is clear from this relationship that reducing the scale of the turbine rotor will decrease the Reynolds number. Only by using impractically high flow velocities or a fluid with substantially different properties would it be possible to achieve a consistent Reynolds number. As a result of this, it is common practice to measure the performance related characteristics of a scaled turbine at various flow velocities to determine the significance of Reynolds effects. For example, in [121] a 0.5 m diameter turbine was tested in flows between 0.5 – 1.5 $\mathrm{m \cdot s^{-1}}$, corresponding to a Reynolds number range $1.3 \times 10^5 - 3.8 \times 10^5$. The study concluded that above a Reynolds number of 2.4×10^5 the effects on performance were insignificant for this configuration.

Testing at low Reynolds numbers decreases the lift and increases the drag of an aerofoil [122], resulting in reduced power performance. While this behaviour is reasonably well understood, it becomes more difficult to account for Reynolds number effects with decreasing model size due to a lack of reliable aerofoil lift and drag data in this range. This is a key consideration for any scale model test campaign. In [123], it was argued that rotor geometries should be modified for scale model testing to obtain a better performance at low Reynolds numbers, such that comparable momentum extractions and representative wake behaviour is achieved. This study tested a 1/70th scale rotor with aerofoil sections that differed from its full-scale equivalent, and modified the blade chord lengths and twist angles to achieve comparable thrust characteristics.

Another consideration for scale model testing arises from the effects of blockage, occurring when the area of the turbine rotor occupies a significant proportion of the cross section of the flow in the test facility. In such circumstances, the flow is constrained by the boundaries of the tank dimensions and a full wake expansion behind the turbine rotor is not achieved. This results in the flow passing through the rotor at a greater rate than it would in unbound conditions, leading to enhanced power performance and increased thrust loading. It has been recommended that a blockage ratio (the swept area of the turbine rotor relative to the cross-section of the passing flow) of less than 10% should be sought to minimise these effects [124]. However, a blockage correction method was developed in [114] after testing a model turbine in conditions with a 17.5% blockage ratio. This resulted in reductions of 18% and 11% for power and thrust in thrust respectively. The method has since been applied to similar laboratory scale research studies of both tidal [125] and wind [126] turbines.

The EquiMar research project published extensive guidelines on best practices and limitations of testing laboratory scale tidal turbines [119], [127]. These are supported by subsequent work published from the MaRINET project, encouraging standardisation of test methodologies and practices across test centres [120], [122], [124], [128], [129].

In order to minimise the aforementioned limitations of laboratory scale testing, increasingly now tidal turbines are being tested at an intermediate scale in outdoor environments. This option is attractive because testing can take place in realistic flow conditions without the cost associated with full-scale grid connected projects, and provides experience of working in the offshore environment. Some of these intermediate scale tests have used vessels to support turbines. For example, a 1/10th scale turbine was tested in towed conditions from a bespoke catamaran in [130]. Subsequently the same catamaran was used to test a 1.5 m diameter turbine from a moored position within Strangford Narrows, Northern Ireland, subjecting the device to tidal flows [105]. The study compared the performance of the turbine to results obtained separately from towing tests in a steady lake environment. It was suggested that the turbulent conditions experienced in the tidal environment were detrimental to turbine power performance, but the authors stressed that there is less certainty in the unsteady results. The same catamaran was used to further study the interaction of two of these turbines in various array configurations [131], showing significant power reductions from spacing the devices 6 rotor diameters apart and in-line with the flow compared with adjacent arrangements.

A number of similar tests have been performed by SCHOTTEL during the development of its technology, starting with the towing of a 4 m diameter turbine off the front of a tug boat in a harbour [132], [133]. This proved to be a suitable configuration to evaluate the performance of the turbine and its control strategy, before further testing was performed from a moored barge in a tidal stream [134]. Unlike the findings in [105], the power performance was found to be comparable between the two test environments. However, greater mean thrusts were observed in the tidal stream tests, although the authors state that this is not a conclusive result given the differences in test setups.

Estuaries with a considerable tidal range also provide a suitable environment for testing turbines at intermediate scale. The Itchen River, Southampton, is one such example in the UK that is expected to soon host a tidal turbine, operating in flows up to 0.6 $m\cdot s^{-1}$ during spring ebb tides [135]. This approach was used during the development of the Sabella turbine [136], [137], where a 3 m diameter rotor device was installed in the Odet estuary in South Brittany. Not only did this lead to an understanding of the operational characteristics of the turbine, but it proved that marine growth on the rotor could be controlled with an antifoul coating. Other environmental effects and concerns were also studied during this project.

Meanwhile EMEC has a nursery tidal turbine site aimed at bridging the gap between laboratory and full scale testing, known as the Shapinsay Sound tidal test site [138]. This non-grid connected site features low peak tidal currents of 1.5 $m\cdot s^{-1}$, providing a relatively benign environment to test various aspects of a particular design. Nautricity, for example, tested the interaction between its 10 m diameter contra-rotating tidal turbine and mooring system at Shapinsay Sound [139], stating that the site was chosen for this purpose because no consents associated with exporting power were required, accelerating its technology development process.

Only full-scale grid connected testing, however, is capable of providing the complete experience of operating a commercial tidal turbine. The SeaGen project in Strangford Lough provided one of the first insights on the operational performance of a full-scale turbine [32]. The twin 16 m diameter rotor device reached its rated 1.2 MW power output in flows of approximately 2.5 $m\cdot s^{-1}$, corresponding to an overall system efficiency in the range 40 – 45%. Interestingly the performance was found to be slightly better during ebb flows, speculated to be due to flow enhancements from the upstream rotor supporting cross-beam on this tide.

The SeaGen performance was evaluated against standards published by EMEC [140]. These guidelines outline a methodology that attempts to guarantee consistency in the measurement of power performance of tidal turbines. The document recommends that turbine operations are split separately for ebb and flood tides into periods of 10 minutes, in which the measurements are averaged to determine the mean performance. It also recommends that the flow, as measured from a vertically oriented ADP in proximity to the turbine, is subject to a rotor weighted average. The method applies more weight to ADP measurements made near the rotor centre and less to those near the top and bottom of the rotor centre. This differs from wind turbine standards, where the wind speed at the hub-height only is used to assess performance [141]. The EMEC standard then recommends sorting the results into velocity bins of 0.1 $m \cdot s^{-1}$, before averaging further all measurements within each bin range. This amount of averaging and data sorting increases certainty on the power curve derived at the end of this process.

The EMEC standard was subsequently expanded upon in the International Electrotechnical Commission's (IEC) Technical Specification for tidal energy converter power performance assessment [142]. The specification provides a full description on the measurements that should be made, the analytical procedures for deriving results, and the required information that should be present in the final report on the power performance of a tidal turbine. This includes the recommendation that ADPs should be placed between 2 and 5 rotor diameters upstream of a tidal turbine on both ebb and flood tides (requiring 2 ADPs), and within 0.5 rotor diameters of the principal flow direction. Alternatively, a lateral arrangement of ADPs may be used, positioned between 1 and 2 rotor diameters adjacent from the edge of the rotor disc (requiring an ADP either side of the turbine). These requirements ensure that representative measurements of the flow velocity experienced by the turbine are obtained.

This arrangement of ADPs could not be satisfied for both tidal directions during the performance assessment of the Alstom 1 MW turbine at EMEC [37], with one ADP positioned 1.1 rotor diameters from the principal flow direction instead of the required 0.5. However, a subsequent deployment of ADPs was used in this work to show that the power curve derived from an ADP outside the IEC target area shows very few differences to results obtained from within it [67]. The ADP in question exceeded the 5 rotor diameter upstream limit by half a diameter. The derived Alstom power curves also showed differences on ebb and flood flows, similar to results found during the testing of SeaGen and further highlighted the importance of separating data by tidal state. In this instance, the variation was attributed to differing unsteady characteristics of each tide.

This IEC specification was also applied during the aforementioned testing of the SCHOTTEL turbine [143], in which the power curve was obtained up to flows of 2.1 $m \cdot s^{-1}$ using 4 minute temporal averaging of the data. This is lower than the IEC recommended 10 minute averaging. A sub-clause in the guidelines states that data sets may optionally be processed to averaging periods greater than or equal to 2 minutes, as long as an integer divisor of 10 minutes or 600 seconds is used.

More recently, the IEC guidelines were applied to a 10 m diameter version of the Sabella turbine despite the lack of ADP measurements [39]. The flow was instead derived from a calibrated oceanographic model. In agreement with findings elsewhere, the performance of the turbine differed between ebb and flood tides, but the authors could not explain this feature in the absence of flow measurements.

Despite the growing number of reported results from the sea trials of some of the largest tidal turbines, most test campaigns were by no means trouble free. For example, all of the blades broke off one of the SeaGen rotors as a result of an incorrect control action that pitched the blades in the opposite direction [32], providing a reminder of the forces generated from fast flowing water. Blade failures are not unique to SeaGen, with problems encountered at sites elsewhere on a number of other turbines [38], [144].

2.4 Tidal Turbine Control Strategies

As a result of the physical, mechanical and electrical similarities between wind and tidal turbines, it should come as no surprise that they also share many of the same control strategies, with the overall objective of maximising power production while preventing damage to the device from excessive mechanical loading. All turbines fall under one of the following categories [145]:

- Fixed-speed fixed-pitch (FS-FP)
- Fixed-speed variable-pitch (FS-VP)
- Variable-speed fixed-pitch (VS-FP)
- Variable-speed variable-pitch (VS-VP)

In each of the fixed-speed scenarios, the turbine generator is connected directly to the grid such that its speed is synchronised with the network frequency. This configuration is attractive because no additional components are required to manipulate the exported power, ensuring that the system is both simple and low-cost. The performance of fixed-speed turbines, however, tends to be low [145], [146], [147], particularly in the FS-FP case. This is due to their inability to track the point of maximum rotor efficiency, which only occurs at a certain ratio of rotor to wind speed (see Chapter 3). Since there is no control over the turbine rotational speed, it cannot track this point as the wind speed varies. Hence only during the specific circumstances in which the correct wind speed occurs will the turbine achieve optimum power performance. Furthermore, because the reactive torque from the generator is used to hold the speed constant, this requires large surges of torque in high and/or turbulent wind conditions, leading to concerns on fatigue.

The usage of fixed-speed wind turbines has been in decline since the beginning of the 21st century [148], while no applications have been identified for tidal stream energy. Instead, by decoupling the generator from the grid, most commercial wind turbines are now variable speed. This can be achieved through direct AC to AC frequency converters, or through power electronics which first convert the AC power to DC, before converting back to AC at the grid frequency [149]. There are cost and reliability implications associated with these additional components, but these are usually outweighed by the increased revenue from the improved energy capture of the variable speed turbine.

In the VS-FP case, power regulation above the rated wind speed is achieved by stalling the rotor. This occurs by limiting or slowing the rotor speed near the rated power point, increasing the angle of attack beyond the point of maximum lift. While this method can result in good overall power performance, slowing the rotor in high winds leads to thrust and torque transients not dissimilar to those experienced by fixed-speed devices. In the absence of empirical data, the behaviour of an aerofoil in deep stall is inherently unpredictable [150], [151].

There is, however, an alternative to stall for VS-FP turbines, namely overspeed control, and this is the control strategy adopted by TEL in its DeltaStream^{TM} turbine. The speed of the rotor in this control philosophy is not limited once the turbine reaches its rated power output, and is instead allowed to accelerate with a corresponding decrease in generator torque to ensure that power is held constant [152]. This decreases the angle of attack to a region where the aerofoil characteristics are better understood, unlike stall. In [153] and [154], blade design methodologies are presented for the development of rotors that have thrust limiting properties in the overspeed region, thus allowing a turbine to utilise this control strategy without penalties on structural loading. The SHOTTEL turbine was developed with this control strategy [132], and has demonstrated that its rotor has a decreasing thrust characteristics in the overspeed region [133], [134]. Similarly, the research in [155] describes how a 110 kW turbine with these characteristics can be influenced by the inclusion of tip modifications, or winglets, predicting that the decrease in thrust with overspeed is enhanced.

Greater control flexibility can be achieved through the addition of a pitch system, in which the rotor blades are pitched to change the inflow angle, altering the performance characteristics of the turbine. Usually this is achieved by electronic or hydraulic actuators, with systems that pitch the blades simultaneously or independently [146]. In high flows the blades are usually pitched to feather, i.e. decreasing the angle of attack, such that the lift is decreased, although pitch to stall is also used [145]. The pitch activity is usually reserved until the turbine reaches rated power, thereafter the torque and speed are held constant using the pitch system. Pitch systems are advantageous because the mechanical loading can be actively controlled, reducing the size of the transients that the fixed-pitch turbine is subject to. Additionally, in extreme conditions with the turbine shutdown, the blades can be pitched out of the flow to prevent damage. This option was used by the SeaGen tidal turbine to safely stop and park the rotor in full flows [32]. In [156], a numerical analysis compared the performance of a variable speed stall and pitch regulated turbine with the same aerofoil geometry and radial chord distribution, but differing radial twist. While the power performances of both turbines were found to be comparable, the stall regulated turbine exhibited greater rotor loading.

The main drawback of the pitch system is that it adds further complexity to the turbine, which has implications on the cost and reliability of the device. Research on wind turbines have shown that pitch faults [157] and failures [158] are significant contributors to operational downtime. In [159], the reliability of 350 pitch regulated wind turbines of rated powers greater than 850 kW was investigated. This study revealed that the pitch system is the turbine sub-system with the greatest normalised failure rate, plus it contributes the most to downtime. Despite this, pitch systems are now ubiquitous on most commercial wind turbines, with research suggesting that their inclusion reduces the number of failures of other components [160], namely the blades, generator and gearbox.

The adoption of pitch control systems is not necessarily widespread for the tidal stream application, as shown in Table 2.1 where the choice of rotor has been summarised for some of the larger turbines. It would appear as if pitch systems are generally found on the largest machines, similar to the wind industry. Plus, there is evidence to suggest that some of the advanced projects are shifting towards their usage, with Atlantis choosing to equip its 1.5 MW turbine with a pitch system after previously testing a smaller fixed-pitch device. There are, however, enough MW scale fixed-pitch turbines to suggest that this design is not confined to smaller devices, with Scotrenewables being a noteworthy proponent that has constructed at both scales. This lack of agreement is believed to be due to the cost associated with offshore maintenance operations, which are significantly greater than those for onshore wind turbines. Additionally, some research has suggested that the achievable pitch rates are lower in the tidal application, making the system less effective [31].

Table 2.1: Rotor comparison of some of the largest tidal turbines

Fixed-Pitch Tidal Turbines	**Generator Size [MW]**	**Variable-Pitch Tidal Turbines**	**Generator Size [MW]**
Scotrenewables SR250 [161]	0.125[*]	Alstom DEEP-Gen III [162]	0.5
Tocardo T2 [163]	0.2	SeaGen [32]	0.6[*]
TEL DeltaStream	0.4	Alstom DEEP-Gen IV [37]	1
Voith Hydro HyTide [164]	1	ANDRITZ HYDRO Hammerfest HS1000 [165]	1
Scotrenewables SR2000 [166]	1[*,#]	GE Oceade [167]	1.4[#]
Atlantis AR1000 [168]	1	Atlantis AR1500 [169]	1.5[#]

[*] Device features two of these generators; [#] Device in construction

This lack of conversion on rotor power regulation across tested tidal devices is also seen in the choice of adopting a yaw mechanism, with again the design decision being driven by factors relating to cost, performance and reliability. Since most tidal stream sites feature currents which have two dominant directions, the yaw requirement is not as crucial as it is in wind turbines. This is particularly true if the currents at the turbine site are approximately rectilinear, such as the Fall of Warness at EMEC [100]. Some turbines that do not yaw have been designed with symmetrical blades to operate in both flow directions [137], [170]. Such a turbine would be required to operate downstream of its supporting structure on one tide, which, as previously mentioned, has been shown to have both detrimental [71] and beneficial [32] effects on device performance. Of the tested tidal turbines that do have yaw capability, this has been achieved in seabed mounted devices through the usage of controllable thrusters in the rear of the nacelle [162] as well as electrical methods [169], while a floating turbine has been designed to passively yaw about its mooring system from the current forces [161]. It is expected that the requirement to yaw will increase as more tidal stream sites are developed for power generation. The research in [171] predicted that the flow varies to in excess of 15^o from perfectly rectilinear at a number of potential tidal stream energy sites around the U.K., with this condition often occurring around headlands. Turbines without a yaw system at these sites would be expected to underperform during the misaligned tide [172].

It is clear that pitch and yaw systems are key considerations for the control of any turbine design, but there is increasing interest in advanced techniques as a result of improvements in sensor technology. In the wind industry, the usage of light detection and ranging (LiDAR) systems has led to a better understanding of the wind in the vicinity of turbines [173], [174]. These instruments have been mounted inside the turbine hub to provide detailed measurements of the upwind conditions [175], leading to the possibility of developing a feedforward control system that performs yaw corrections in advance of the event of an approaching misaligned wind. Experimental research in [176] has shown that a feedforward pitch controller informed by LiDAR measurements can reduce turbine loads.

Since tidal turbine technology is less mature than its wind counterpart, fewer research efforts have been made towards achieving controller sophistication, although during the ReDAPT project the inclusion of low-cost inclinometers were used to inform the control system of excessive loading from transient events [177]. The controller responded by reducing the turbine power set point, resulting in a decrease in the mean, peak and variation in loading. Crucially this allowed the turbine to safely operate through large waves and turbulent tides without the need to shut down. There is also research interest in the usage of flexible turbine blades [133], [178], [179], which passively alleviate rotor loading due to the blades bending in high flows.

3. Mathematical Modelling

In order to estimate the operational characteristics of a tidal turbine in the absence of physical measurements, it was necessary to develop a mathematical model to form theoretical predictions. This chapter describes the historical methods that have been used to numerically model the DeltaStream™ turbine, before detailing the development of a new model. The resulting model is then validated against the commercially available Tidal Bladed software. This chapter concludes with a discussion on the strengths and limitations of the developed model.

3.1 External Modelling of the DeltaStream™ Turbine

Through the use of both BEM and CFD based numerical models, the DeltaStream™ rotor was designed by researchers at Cranfield University [180], a partner on TEL's Ramsey Sound project since 2007. This met the required criteria of TEL's thrust control patent [181], whereby the rotor has power and thrust shedding characteristics at high tip speed ratio, λ, the ratio of rotor tip speed to flow velocity, v:

$$\lambda = \frac{\omega \cdot R}{v} \tag{3.1}$$

Where:

R - Rotor radius

ω - Rotor rotational speed

Thus power and thrust can be regulated by allowing the rotor to overspeed to a high λ. The iterative design process led to a rotor comprising NACA0015 aerofoils, a symmetrical geometry with a 15% thickness to chord ratio. A 1:16 scale rotor (0.75 m diameter) was subsequently built and tested in the IFREMER wave-current circulation tank in Boulogne-sur-mer, France, in 2011. Figure 3.1 shows both the NACA0015 aerofoil geometry and the 1:16 scale rotor.

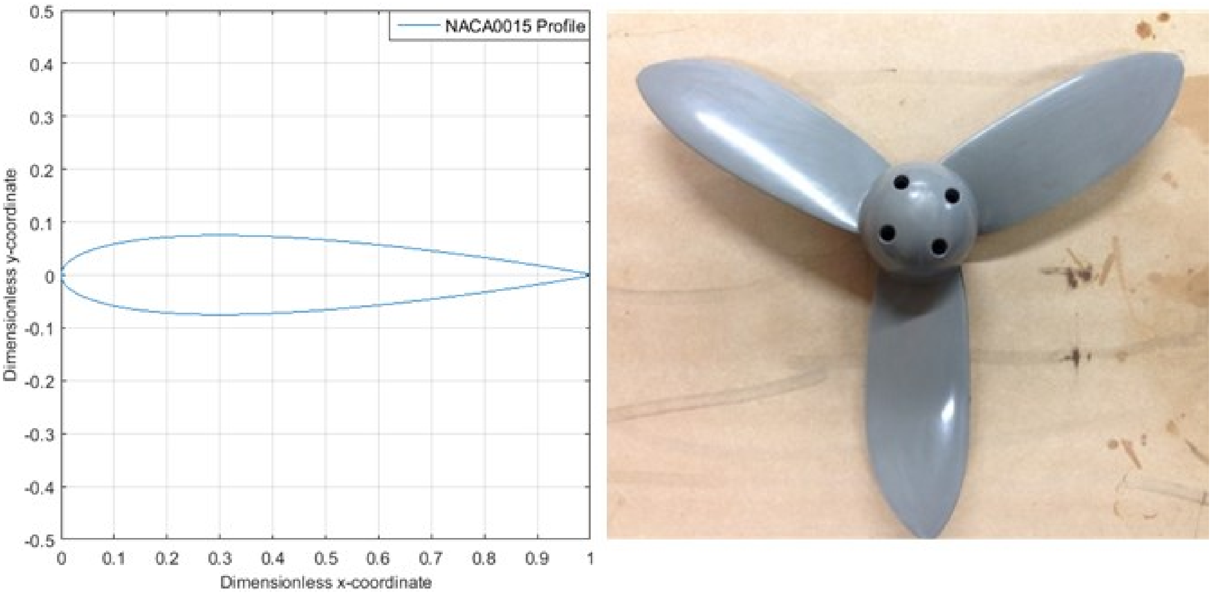

Figure 3.1: *NACA0015 dimensionless aerofoil geometry (left) and the 1:16 scale DeltaStream™ rotor (right)*

The experimental results from the IFREMER tests were found to be in good agreement with BEM predictions made by Cranfield, as shown in Figure 3.2 where the dimensionless rotor power, c_p, and thrust, c_t, coefficients are shown with respect to λ. c_p and c_t are defined as follows:

$$c_p = \frac{P_{rot}}{\frac{1}{2} \cdot \rho \cdot \pi \cdot R^2 \cdot v^3} \tag{3.2}$$

$$c_t = \frac{Hub\, F_x}{\frac{1}{2} \cdot \rho \cdot \pi \cdot R^2 \cdot v^2} \tag{3.3}$$

Where:

P_{rot} - Power developed by the rotor

ρ - Water density

$Hub\, F_x$ - Rotor (hub) thrust

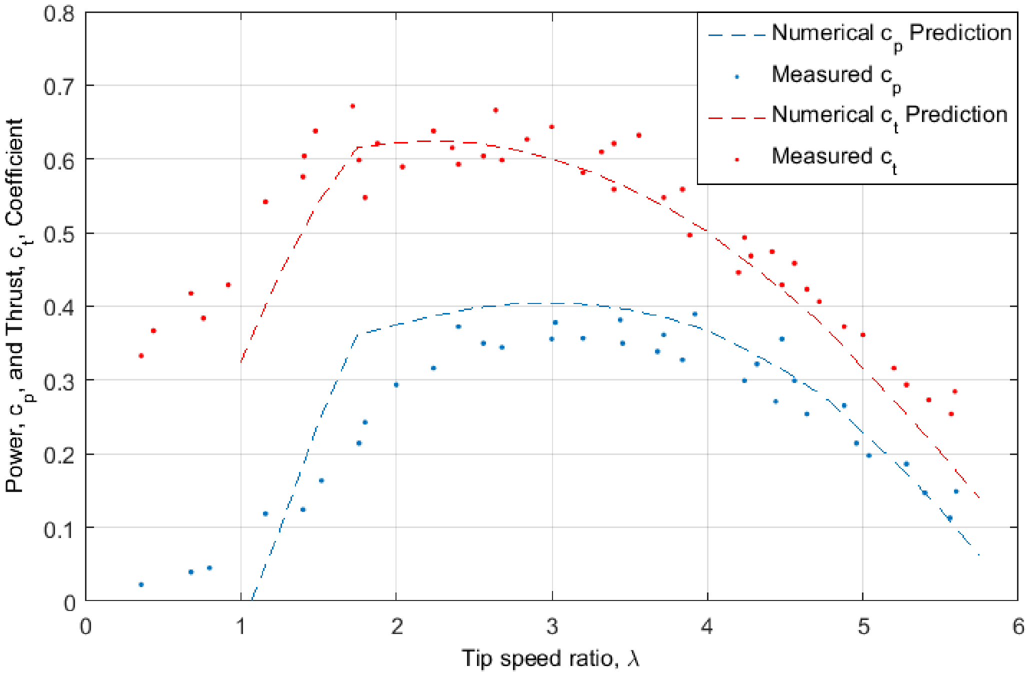

***Figure 3.2:** Steady-state rotor performance predicted by a BEM code developed at Cranfield University, compared with experimental results obtained at IFREMER, 2011*

The majority of the numerically predicted rotor c_p values in Figure 3.2 are greater than those obtained experimentally. This was attributed to efficiency losses encountered in the test rig set-up, with power measured electrically at the motor used to drive the turbine rather than at the rotor. The important point to note is that the BEM model developed by Cranfield adequately predicted the steady-state hydrodynamics of the TEL rotor, highlighting the suitability of the theory for this application.

The results from these studies suggested that the rotor has a peak c_p of 0.4 at a λ of 3, while c_t at this operational point is 0.6. Using the BEM code, it was possible for Cranfield to predict the steady-state operational regime for a 12 m diameter turbine with a 400 kW generator. The conclusion was that after accounting for efficiencies in the drivetrain, the device would achieve its rated power in flows exceeding 2.6 $\text{m}\cdot\text{s}^{-1}$, with a corresponding peak rotor thrust of 240 kN.

These initial predictions were made under idealised conditions and do not take into account dynamic phenomena that can affect performance, including the effects of turbulence and waves. The Cranfield predictions, therefore, would be insufficient to establish the structural design parameters for a full-scale tidal turbine. These were instead determined by Garrad Hassan, now DNV GL, using its Tidal Bladed software, in which dynamic simulations of a turbine operating in conditions similar to those experienced at Ramsey Sound were performed. This work was also very iterative. For example, one of the original turbine designs featured a cylindrical support tower. The simulations of this configuration suggested that tower shadow effects would have adverse consequences on the rotor fatigue life. TEL subsequently adopted an open tower structure.

The design loads were established from simulations with extreme environmental conditions and/or fault cases, including a scenario in which the turbine loses its connection to the grid. For historical reasons, these were calculated for a 15 m diameter turbine with a rotor geometry that has slightly different characteristics to those shown in Figure 3.2. As a result, the built structure to support the 12 m rotor installed by TEL in 2015 was over-engineered, but could host a larger turbine in the future.

DNV GL were contracted again ahead of the installation of the 12 m rotor to predict its operational loading and performance, providing TEL with a dataset to compare the results from testing at Ramsey Sound to. As shown in Figure 3.3, the mean results from this study demonstrate good agreement with the steady predictions from the Cranfield model. This should not be surprising since both models use a BEM code to predict the hydrodynamic behaviour. Only the dynamic simulations in Tidal Bladed capture the variation in loading, however, with peak rotor thrusts approximately twice that predicted from steady-state BEM. Note that the DNV GL results show slight variations on ebb and flood simulations due to differing levels of turbulence and velocity shear modelled for each tide. This is discussed in more detail in Section 3.2.

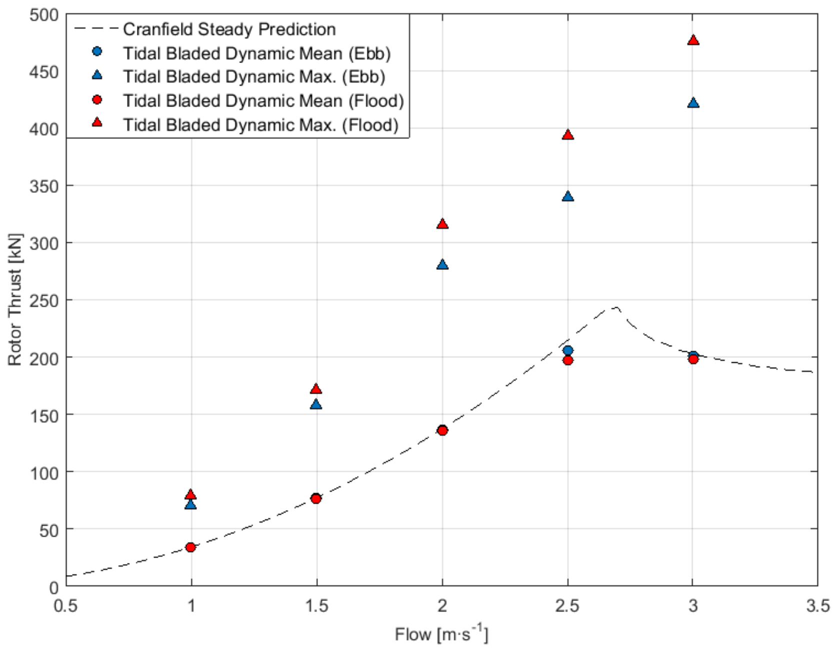

Figure 3.3: *Predictions of rotor thrust from modelling work by Cranfield University and DNV GL*

In 2013, TEL was provided with a Simulink® model of the turbine from its electrical systems supplier, GE, allowing the control system to be tested numerically before implementation on the real device. The model consists of three primary subsystems that continuously interface with each other, namely: the rotor; the mechanical systems; and the electrical systems and control. The model is shown in block diagram form at the top-level in Figure 3.4, illustrating how the subsystems interact with each other.

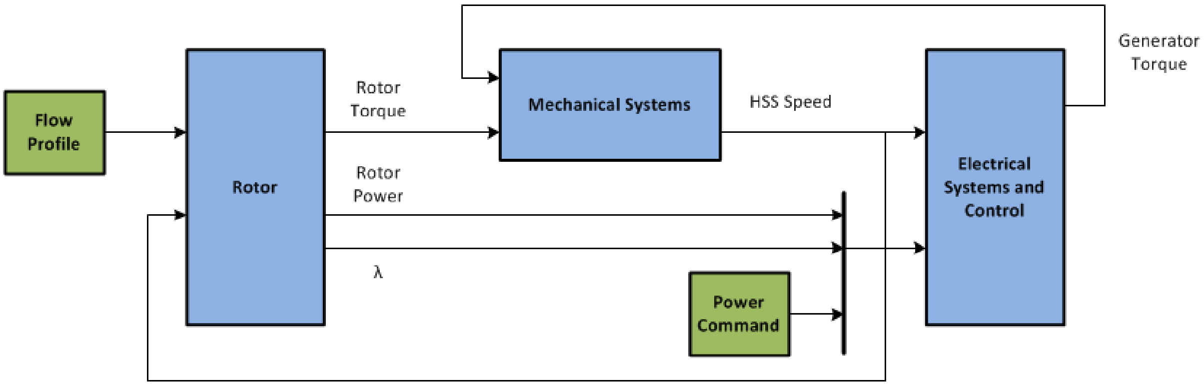

Figure 3.4: *GE Simulink® model of the turbine*

Starting with the left hand side of Figure 3.4, it can be seen that flow velocity and high speed shaft (HSS) speed are inputs to the rotor subsystem. By firstly determining λ from these inputs via Equation 3.1, the block calculates rotor power and torque from a lookup table of the Cranfield $c_p - \lambda$ curve (Figure 3.2). The rotor torque is sent into the mechanical systems block along with the reactive torque from the generator. This block represents the turbine drivetrain, modelled as a 2-mass system, similar to that described in [145]. The response of the drivetrain is calculated by relating these torques to the inertias of the gearbox, generator and rotor, along with the stiffness and damping of the HSS. The resulting HSS speed from the mechanical systems block is fed directly into a squirrel cage induction generator in the electrical systems and control block. This subsystem also contains the transmission network and the variable voltage variable frequency (VVVF) drive used to control the turbine.

Initial testing of the GE model revealed two areas of concern with regards to the control system objectives. Firstly, simulations showed that the turbine was operating near $\lambda = 2$ in below rated flow conditions. As seen in Figure 3.2, this would result in less than optimum power production and higher rotor thrust, although the latter is not considered in the GE model. Secondly, after reaching the rated power of 400 kW and with the flow speed still increasing, the generator would begin to lower its power output, rather than sustaining it. Both of these issues were communicated with GE and an updated version of the model was subsequently provided.

The finalised model allows the user to input a time varying flow profile to assess the dynamic response of the turbine's electrical systems. Through the inclusion of a power command input (see Figure 3.4), there is also scope to study the effect of altering the default control strategy. Essentially this allows the user to request a rated generated power lower than the default 400 kW at any point during the simulation, resulting in the turbine overspeeding to the thrust control region in flows lower than the rated velocity. This capability is illustrated in Figure 3.5, in which the same simulation is run three times with varying power commands. The aim here is to perform a simple demonstration on how these modifications might affect rotor thrust, which was calculated using the curve formed by the

Cranfield steady-state prediction (Figure 3.2 and Equation 3.3). The blue line shows the default control strategy where the turbine tracks $\lambda = 3$ until a flow disturbance at 22 seconds results in a brief period of rated power output, causing a small overspeed and a 265 kN peak in rotor thrust.

In contrast to this, the capped control strategy, as represented by the black line, places a limit of 270 kW on the generator power just before the flow disturbance occurs, leading to much more overspeed activity. A reduction in peak thrust occurs by adopting this control variation, although at the expense of power.

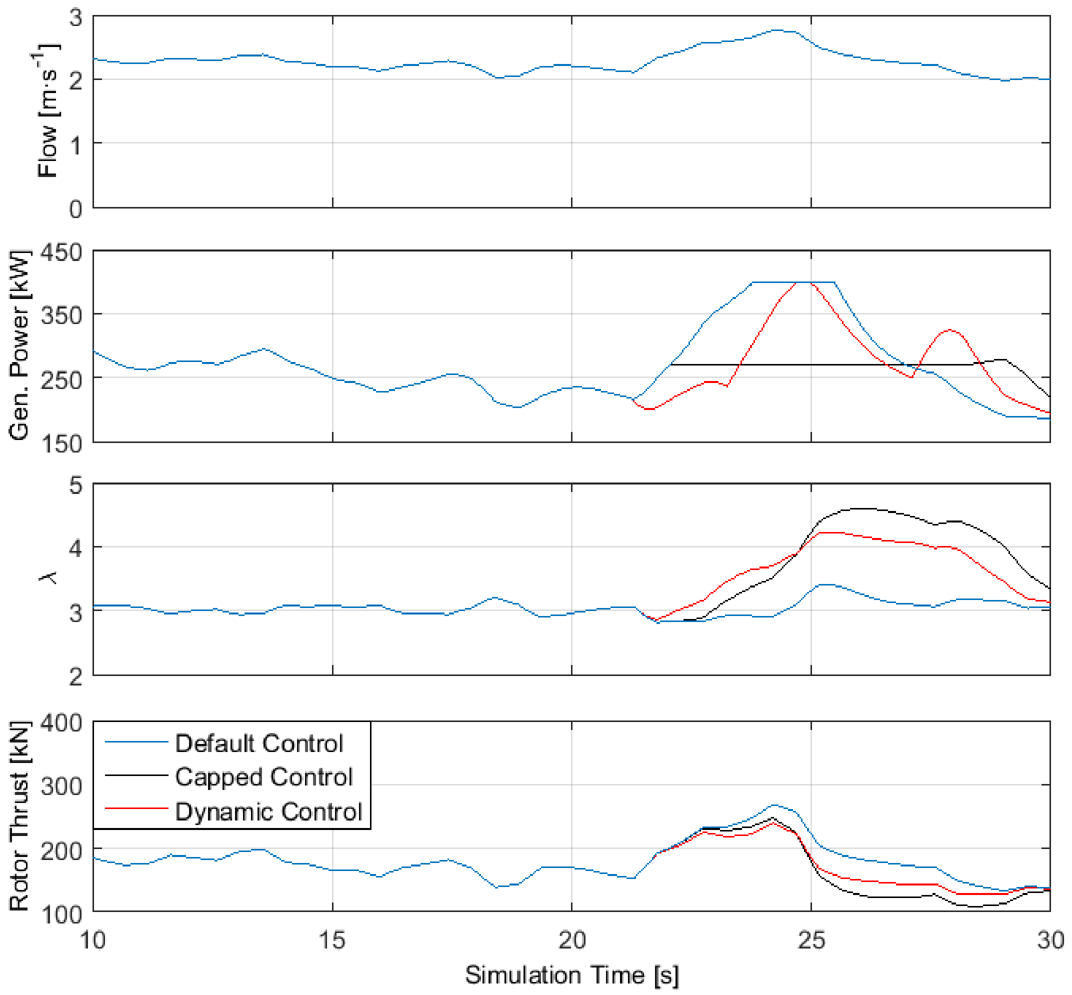

Figure 3.5: Demonstration of varying the default control strategy in the GE model

The red line, labelled dynamic control, attempts to minimise this power deficit by dynamically varying the power command during the flow disturbance. This results in better power capture and comparable thrust loading to the capped control variation. Thus, the simplified example in Figure 3.5 illustrates that the default controller in the Simulink model can be modified to achieve other objectives, which in this case involved minimising mean rotor thrust forces.

While the GE model is a good representation of the electrical and control aspects of the turbine, i.e. the systems it supplied to TEL for the physical device, it is weak at modelling a number of other areas. The hydrodynamics are the most noteworthy. As mentioned previously, the rotor subsystem uses a single flow velocity and the steady-state characteristics to predict performance. This is an inadequate description of the complex tidal environment and the interaction it has with the rotor. It is, therefore, incapable of providing an insight on the dynamic performance of the turbine and would be insufficient to fully evaluate a design or design modification. The drivetrain representation is also believed to be dubious, although not because of the modelling approach used. Instead, the source of the mechanical properties in the model of the drivetrain is uncertain, including the values of the HSS damping and stiffness. These were not supplied by TEL and it is speculated that GE chose them based on its experience of modelling wind turbines, or used values that prevented simulation instabilities.

In addition to these modelling concerns, the degree of flexibility with the turbine control system is lower than desired. The VVVF controller is represented in Simulink® through the use of a protected block of code (S-function), meaning that it is not possible to view how it has been modelled and is essentially a ‘black box’. This is due to the fact that aspects of the controller fall under intellectual property owned by GE.

3.2 Development of an Enhanced Turbine Model

Of the numerical models described in the previous section, only Tidal Bladed sufficiently captured the considerations required for turbine design, while the others showed some aspects in which they are strong. Tidal Bladed is, however, only available on a commercial basis. Thus there was a desire to develop in-house modelling capabilities for the purposes of this research project. This resulted in a search for an open-source model that exhibited many of the same capabilities as Tidal Bladed, culminating in the adoption of the FAST (Fatigue, Aerodynamics, Structures, and Turbulence) code developed by the National Renewable Energy Laboratory's (NREL) National Wind Technology Center (NWTC) [182]. The tool, developed for wind turbines, combines models of aerodynamics, hydrodynamics (offshore wind), control and electrical systems, and structural dynamics to perform simulations. The complexity and detail of the required simulations dictates the number of these models that are activated. The turbine itself is modelled as a combination of rigid and flexible bodies. The former includes the nacelle and hub, while the latter includes the blades, tower and drive shaft. The rigid and flexible bodies are connected with several degrees of freedom, including blade bending, nacelle yaw, rotor teeter (two bladed turbines), and drive shaft torsional flexibility. These degrees of freedom can also be activated based on the requirements of the model.

The aerodynamics in FAST are calculated using a model called AeroDyn [183], [49], an unsteady BEM model that computes the blade and rotor loads from elemental forces at various blade sections in a time-varying, 3-dimensional, turbulent, wind field. If activated, the resulting turbine deflections from these loads are considered during the calculation process, leading to an aeroelastic interaction. A number of other dynamic effects can also be modelled to provide further sophistication to the BEM code, many of which are considered in Tidal Bladed [65]. This includes loss calculations associated with the rotor hub and tip, tower interaction effects, and dynamic stall. The latter relates to changes in the lift and drag characteristics on aerofoil sections due to unsteady angle of attack time histories caused by the variation in wind velocity over the rotor.

FAST was evaluated by Germanischer Lloyd (GL) WindEnergie, since merged to become DNV GL, concluding that it is suitable for the calculation of onshore wind turbine loads for design and certification [184], after a code comparison study [185]. Subsequent work also showed that the aero-elastic modelling in FAST agreed very well with Bladed [186], DNV GL's wind turbine equivalent of Tidal Bladed.

One drawback of FAST is that the generator models available are very simple. However, it is possible to interface FAST with generator models created in the Simulink® environment [187]. This hybrid configuration allows the proven aerodynamic and mechanical models of FAST to be combined with the extensive electrical modelling options available in Simulink®, resulting in a greater amount of overall modelling capability. This arrangement was chosen to allow the coupling of FAST to the GE model mentioned in the previous section. The electrical and control aspects of the GE model would be maintained, while a FAST model (version 7.0) with a modified AeroDyn (such that the turbine operates in water) would be used to replace the rotor and mechanical subsystems.

The modified block diagram for this coupled model is shown in Figure 3.6. It can be seen that the only requirement to run the FAST model from Simulink® is generator torque, as generator power is not used in the calculation process [187]. The FAST block instead just records this in its output file. There are also blocks which can be used to create pitch and yaw controllers within Simulink®. However, since the TEL turbine does not pitch, and yaw activity was of no interest for this study, these blocks were inactive in the simulations presented in the following section. The GE electrical systems and control subsystem has not been modified, while the option to influence the control strategy is still possible through the power command block. It was necessary to create a series of initialisation parameters to start simulations, as represented by the orange initialisation block. During the first 20 seconds of simulation time, this block prevents the FAST signals from entering the GE block and instead sends pseudo values. This ensures that there are no instabilities during the start-up of the generator. After this period, the true values from FAST are sent through the initialisation block and the two models are fully coupled. This can cause a small disturbance to the simulation, resulting in a step change of both generator speed and torque. The size of the disturbance, both in amplitude and time, is dictated by the difference between the true and pseudo values at the coupling point. Typically the model settled within 5 seconds of coupling. The first 30 seconds of every simulation were always removed during post-processing to ignore the initialisation behaviour in the analysis.

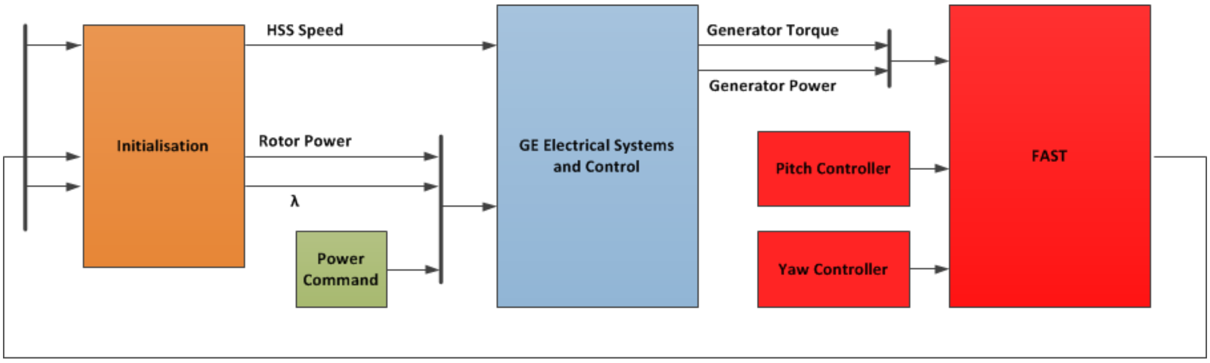

Figure 3.6: *The GE model of the electrical systems and control coupled with FAST*

To create the FAST model of the TEL turbine, input parameters were kept consistent with those used by DNV GL in their Tidal Bladed simulations where possible. This information was sourced by opening the Tidal Bladed simulation files in a demo version of the software. The setup includes modelling the turbine as a rigid structure, meaning that there are no blade deflections and the drivetrain is stiff. Only the AeroDyn and variable speed control modules were activated in the developed FAST model.

The most crucial component of the model is the rotor detail, which is built in sections using data relating to the aerofoil properties and geometry. Figure 3.7 shows the chord length and twist distribution along the 4.86 m modelled turbine blades, which were defined by 17 NACA0015 sections (Figure 3.1). These values were interpolated along the profile from the as built drawings of the blades provided by the manufacturer. The built rotor features a degree of flaring near the blade root to provide added strength, meaning that the increased thickness of these sections results in them differing from a NACA0015 profile. This was ignored here and in the Tidal Bladed modelling since it is the outermost blade sections that contribute most to rotor performance. The effects from this discrepancy are expected to be minimal. Note that the Tidal Bladed model used just the 9 sections from the built drawings to define the blades. A 3D drawing of the modelled blades is shown in Figure 3.8.

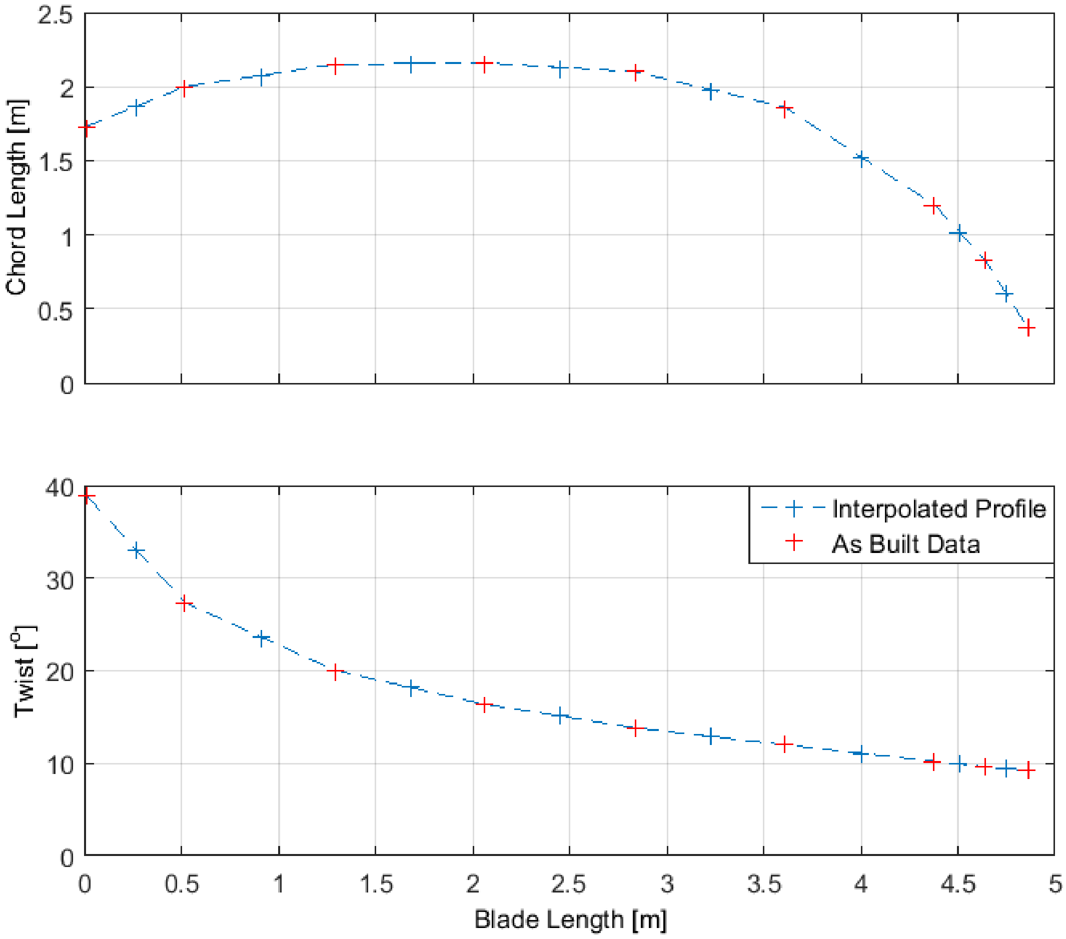

Figure 3.7: *Radial blade chord and twist distribution*

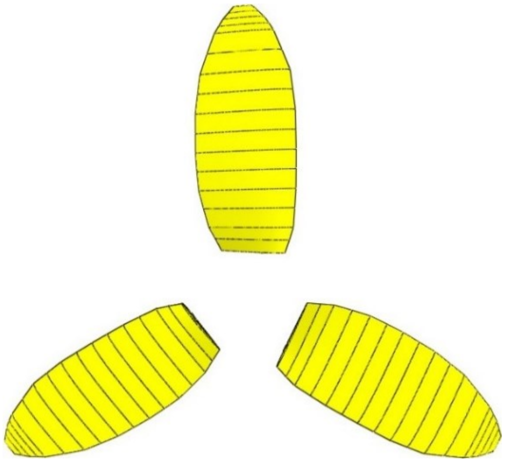

Figure 3.8: *Modelled rotor blades comprising of 17 NACA0015 sections*

The NACA0015 aerofoil lift, C_L, and drag, C_D, coefficient data used are shown in Figure 3.9 for three Reynolds numbers, covering the expected operational range of the turbine. An option within AeroDyn was enabled to allow interpolation between these datasets rather than using just one, ensuring that the calculations consider the variation of Reynolds number across the rotor and over the course of a simulation. This requires the kinematic viscosity of water to be defined in the setup file, specified as 1.48×10^{-6} $m^2 \cdot s^{-1}$ to agree with the Tidal Bladed simulations. Tidal Bladed was also configured to use an aerofoil interpolation scheme with exactly the same lift and drag data in Figure 3.9.

The full environmental and turbine parameters required by FAST are specified in Table 3.1, which again agree with those used in the Tidal Bladed simulations. The hub centre is at 12.1 m (tower height + tower to HSS) and the rotor overhang is the distance between the tower centre and the rotor plane. The overhang is required for blade-tower interactions, although these effects were disabled. This is because the AeroDyn tower shadow model is based on potential flow around a cylinder [49], which is considerably different to the open tower configuration adopted by TEL. When these effects were modelled in Tidal Bladed, which also uses a potential flow method [65], the tower was defined as a series of closely packed small diameter cylinders. Unfortunately this could not be replicated in FAST. The gearbox efficiency accounts for power losses between the rotor and HSS, while the generator inertia prevents the rotor speed from approaching infinity when FAST is decoupled from the GE model during initialisation.

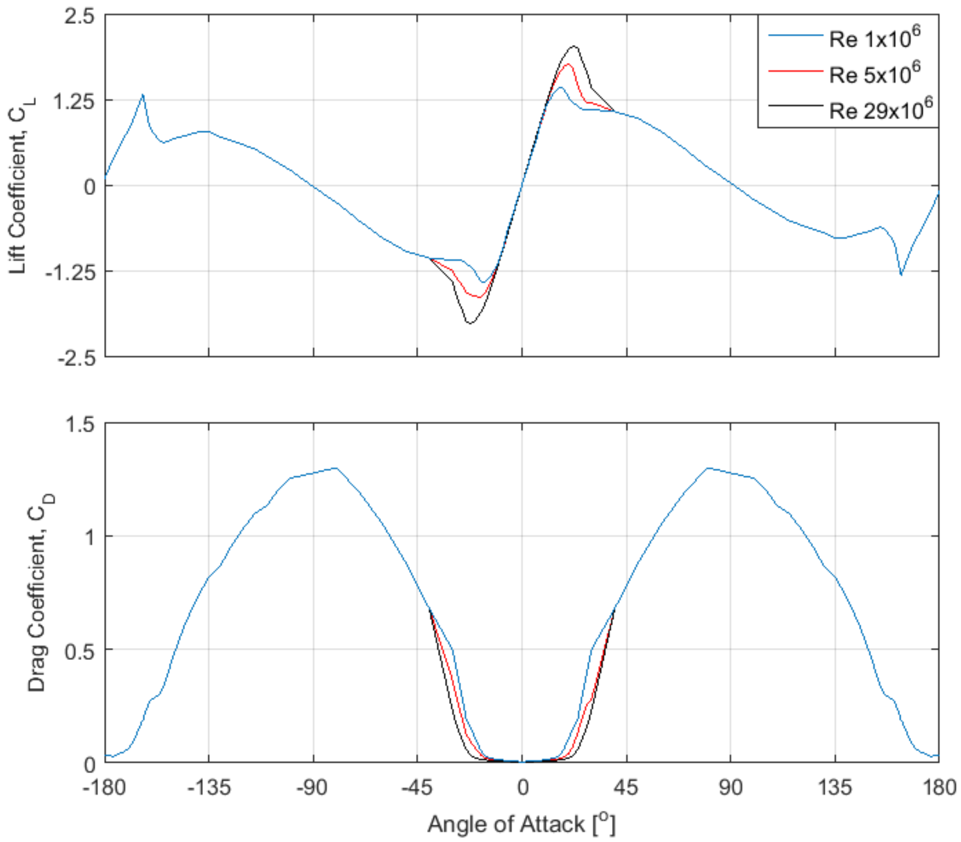

Figure 3.9: *NACA0015 aerofoil lift (top) and drag (bottom) coefficient data*

Table 3.1: *Environmental and turbine parameters specified in the FAST model*

	Parameter	**Value**	**Unit**
Environment	Gravitational Acceleration	9.81	$m \cdot s^{-2}$
	Water Density	1025	$kg \cdot m^{-3}$
	Kinematic Water Viscosity	1.48×10^{-6}	$m^2 \cdot s^{-2}$
Turbine Geometry	No. of Blades	3	-
	Rotor Radius	5.96	m
	Hub Radius	1.1	m
	Tower Height	10.6	m
	Tower to HSS	1.5	m
	Rotor Overhang	3.383	m
Drivetrain	Gearbox Ratio	74.05	-
	Gearbox Efficiency	0.96	-
	Generator Inertia	68.4	$kg \cdot m^2$

During FAST simulations, AeroDyn reads a time series flow file to make its calculations. These files can be hub height values only, or a plane of velocities that cover the rotor area. TurbSim [56], [188], another code developed by NREL, was used to generate 2D grids of 3-component turbulent flows using spectral models. These flows cover a field that is 15 x 15 m and centred on the hub height (12.1 m), i.e. from 4.6m above the seabed to 19.6m. The grid resolution is 1 m within this field, although TurbSim generates an extra point at the hub centre. The code features a number of turbulence spectral models that can be used to generate these flow fields, including a 'tidal' model based on measurements obtained from Puget Sound, USA. However, the Von Karman (VK) spectral model from the IEC standard [189] was selected for the modelling requirements here since the Tidal Bladed simulations also used a VK model.

The TurbSim code creates these time series flow fields based on a specified mean velocity at the hub height and turbulence intensity, which is the ratio of the standard deviation of hub height velocities to the mean value, expressed as a percentage. The option to specify a turbulence seeding number ensures that TurbSim input files with the same mean flow and turbulence intensity are output with different time histories. It is also possible to define a velocity shear profile within TurbSim using standard power and logarithmic relationships. In the Tidal Bladed simulations, custom shear profiles were used based on the analysis of ADCP measurements from Ramsey Sound. This level of flexibility is not available in the TurbSim code. Instead a power law profile was found to be in good agreement with the Tidal Bladed profile used for ebb simulations. This is shown in Figure 3.10.

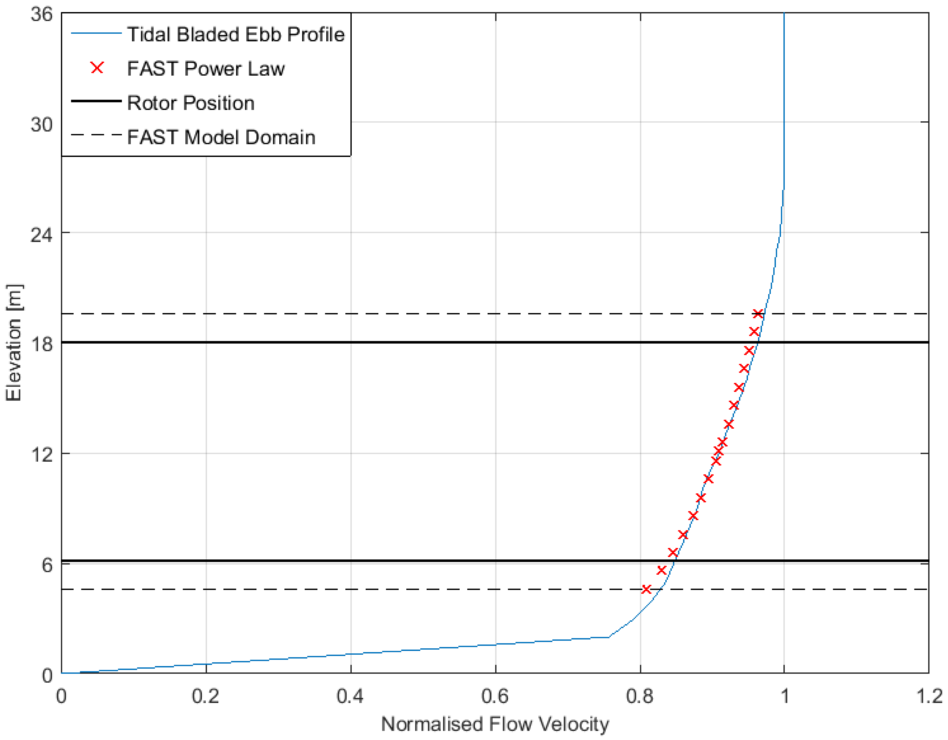

Figure 3.10: *Comparison of the flow shear profiles used in the Tidal Bladed and FAST simulations*

The shear profiles generated for the FAST simulations follow this relationship:

$$\bar{v}(z) = \bar{v}(z_{ref}) \cdot \left(\frac{z}{z_{ref}} \right)^{\gamma} \tag{3.4}$$

Where:

$\bar{v}(z)$ - Mean flow velocity at height, z

$\bar{v}(z_{ref})$ - Mean flow velocity at reference (hub) height, z_{ref}

γ - Power exponent

An exponent of 0.12 showed the best agreement with the Tidal Bladed profile. This is approximately equivalent to a 1/8th power law, and close to the 1/7th value that is often used to describe tidal profiles.

Flow files were created in TurbSim at mean hub velocities between 1 – 3 $m \cdot s^{-1}$, with the simulation time in each configured to have a duration of 10 minutes. For all simulations the turbulence intensity was set to 15%. A further two flow files were created at each mean hub velocity, but the turbulence seeding number was changed in the TurbSim input file to ensure that every simulation was different. This approach to flow field file preparation is consistent with that adopted by DNV GL, although the total number of Tidal Bladed simulations is twice that performed in FAST. Additionally, TurbSim is limited in its description of turbulence length scale. It defines this as 70% of the hub height, corresponding to 8.47 m in this case. The Tidal Bladed simulations, meanwhile, used 15 m. Other than a comment which stated that this value was based on its "experience" of tidal energy sites in the accompanying report that TEL received from DNV GL upon the completion of the simulations, it is unclear how this was derived.

Figure 3.11 shows the typical variation of the u-component velocity over the rotor (y – z) plane at flows between 1·5 – 3 $m \cdot s^{-1}$, as generated by TurbSim. Note that a u, v, w convention is adopted by TurbSim to define the longitudinal, lateral, and vertical directions respectively. It is clear from Figure 3.11 that the flow across the rotor disc, as depicted by the dashed line, is not constant, unlike the modelling described in Section 3.1 by Cranfield University and GE. Compared with these previous modelling efforts, this is an improved representation of the unsteady tidal environment, and will allow an understanding of the unsteady performance of the turbine.

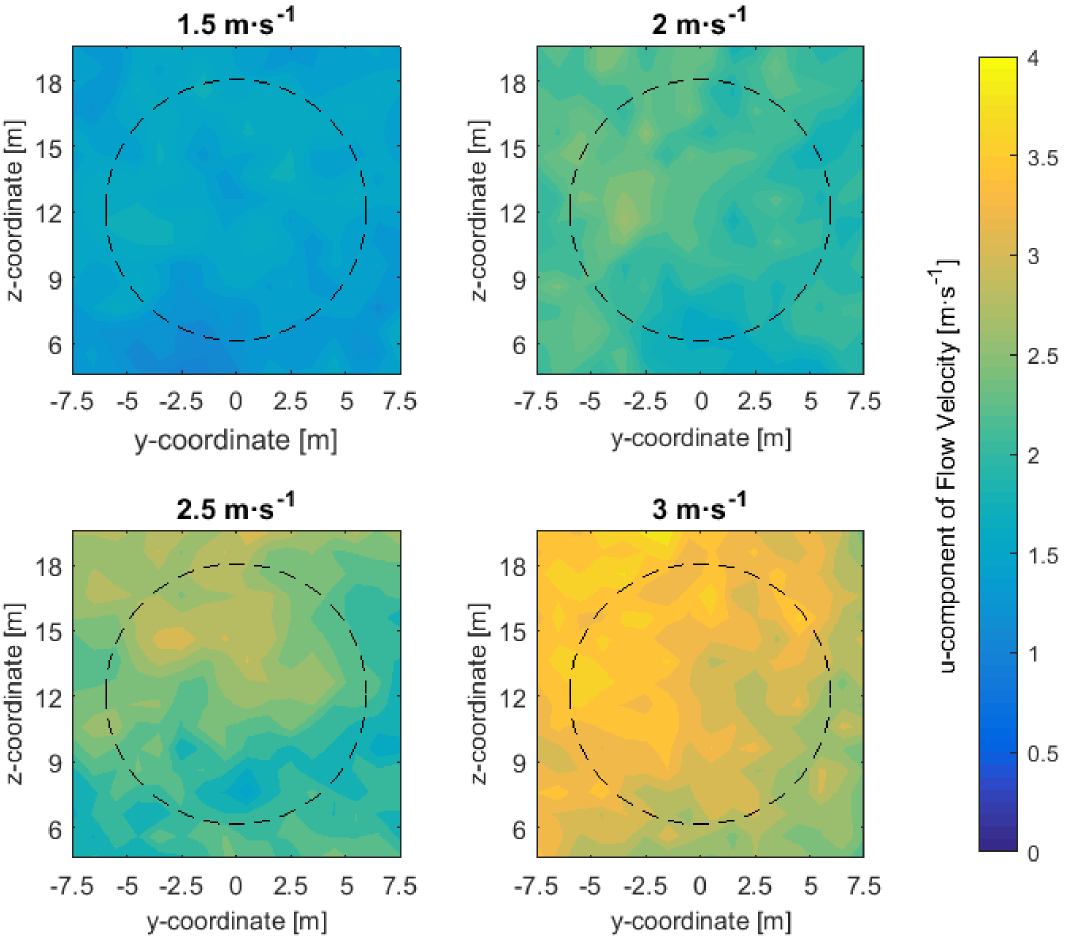

Figure 3.11: *Typical spatial variation of the u-component of flow velocity over the rotor disc for the FAST simulations*

Since the rotor performance would be evaluated in these complex flow fields, the dynamic stall model was activated in the AeroDyn setup files to account for unsteady blade effects. This is the Beddoes and Leishman model [60]. Lastly, the Prandtl hub and tip loss calculations [54] were also enabled to model the effects that vortices shed from the blade tips and rotor hub have on the induced velocity distribution at the rotor.

3.3 Validation of the FAST-Simulink® Model

In order to firstly verify that the environment and rotor have been configured correctly within FAST, the model was decoupled from Simulink® to evaluate the steady-state rotor characteristics. A uniform TurbSim flow file, featuring no turbulence or velocity shear, was created for this purpose. The FAST code was run directly from a command prompt, with each input file specifying a different fixed rotor speed to obtain results for a range of λ. These were found to compare very well with the Cranfield University BEM code, as shown in Figure 3.12.

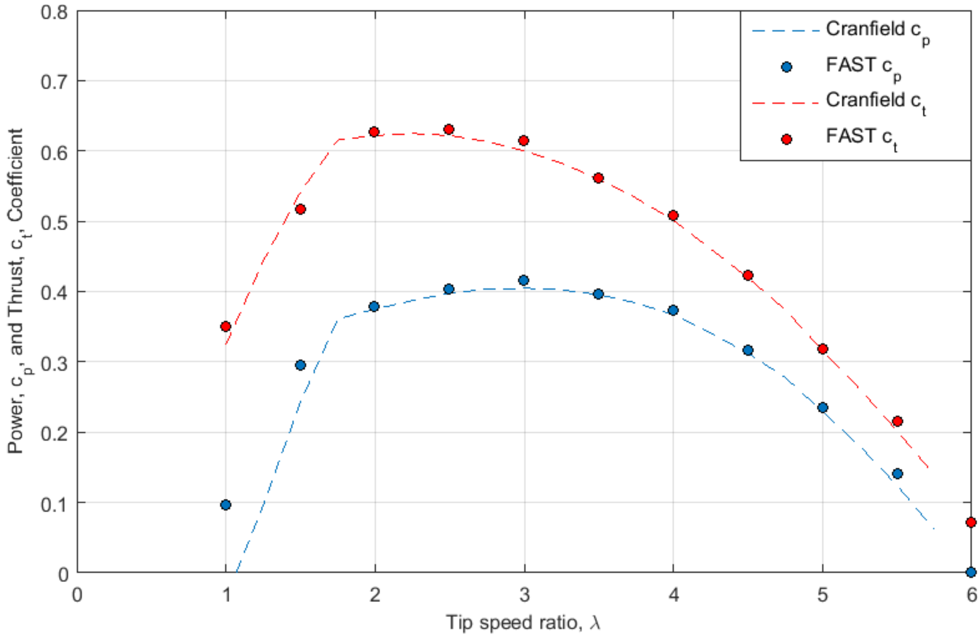

Figure 3.12: *Comparison of power (blue), c_p, and thrust (red), c_t, coefficient predicted by the Cranfield University BEM code and FAST*

Small discrepancies between the models are found at low λ when the turbine is stalling. This is unsurprising given the difficulty of predicting aerofoil performance at high angles of attack, due to a lack of empirical data at this range. Often extrapolation methods are used to predict the aerofoil characteristics at these angles, such as in [190]. Since the aerofoil data were sourced from the Tidal Bladed simulations (Figure 3.9), it is uncertain how the coefficients at these large angles have been derived. It is entirely possible that they differ from the aerofoil data used by Cranfield University.

This successful validation of the steady-state turbine performance allowed the recoupling of FAST and Simulink® to take place without any concerns on the rotor hydrodynamics. The initial simulations were then assessed on the ability of the hybrid model to follow the controller objectives in an unsteady environment. This ensures that the turbine tracks the peak rotor power coefficient, $c_{p_{max}}$, at the optimum tip speed ratio, λ_{opt}, in below rated flow conditions, and thereafter exports the rated 400 kW in high flows. Thus, there are two control regions in which the generator torque and speed must be controlled. The relationship between these quantities in the first region is found by rearranging the steady-state turbine power equation (Equation 3.2), with rotor power expressed as the product of torque, τ, and rotor speed, ω:

$$\tau = \frac{c_p \cdot \rho \cdot \pi \cdot R^2 \cdot v^3}{2 \cdot \omega} \tag{3.5}$$

Currently, Equation 3.5 is dependent on v, but this can be simplified for turbine parameters only by replacing v with the expression for λ (Equation 3.1). Furthermore, by dividing ω by the gearbox ratio, G_{ratio}, it is possible to arrive at generator equivalent values (τ_{gen} and ω_{gen}):

$$\tau_{gen} = \frac{c_p \cdot \rho \cdot \pi \cdot R^5 \cdot \omega_{gen}^2}{2 \cdot \lambda^3 \cdot G_{ratio}^3} \tag{3.6}$$

For variable speed drives, Equation 3.6 is often simplified to:

$$\tau_{gen} = k_\lambda \cdot \omega_{gen}^2 \tag{3.7}$$

Hence, the relationship between generator torque and speed is quadratic, with a k_λ gain term:

$$k_\lambda = \frac{c_p \cdot \rho \cdot \pi \cdot R^5}{2 \cdot \lambda^3 \cdot G_{ratio}^3} \tag{3.8}$$

By inserting the values of $c_{p_{max}}$ and λ_{opt} (Figure 3.12) into Equation 3.8 along with the values for the other constants (Table 3.1), k_λ is found to equal 0.44 $\text{N·m·rad}^{-2}\text{·s}^2$. However, since the gearbox efficiency is 96%, this is reduced to 0.42 $\text{N·m·rad}^{-2}\text{·s}^2$ to account for the loss of torque across this component. Applying this gain to the controller results in the turbine tracking $c_{p_{max}}$. Once the generator rated power, P_{rated}, is achieved, the second control region follows this objective:

$$\tau_{gen} = \frac{P_{rated}}{\omega} \tag{3.9}$$

This ensures that generator torque and speed are balanced such that P_{rated} is kept constant. For TEL's thrust control system [181], the controller allows the turbine to overspeed while the generator torque reduces in this region. In both regions only generator speed is the required input to the control system logic, keeping the complexity of the controller to a minimum.

In Figure 3.13, the idealised generator torque-speed curve is plotted using Equations 3.7 and 3.9 with a k_λ constant of 0.42. It can be seen that a peak torque 4.1 kN·m occurs at a speed of 98 rad·s^{-1}, corresponding to the rated power point and the crossover of control regions. The modelled generator torque-speed data are also shown for all of the Tidal Bladed and FAST-Simulink® simulations. These represent 1 second moving average values.

The results from the developed model scatter about the idealised curve, clearly demonstrating the transition from tracking $c_{p_{max}}$ to overspeed. The scatter appears to be slightly shifted to the left of the idealised curve in the below rated control region, however, suggesting that k_λ has been set slightly too high by GE in the Simulink® model. This was confirmed by running a steady-state simulation, from which it was back-calculated that the gain must be near 0.46 N·m·rad^{-2}·s^{2}. Unfortunately it is not possible to view how k_λ is calculated in Simulink® due to the 'black box' nature of the controller coding. The controller performance appears to agree better with the idealised curve above the rated point.

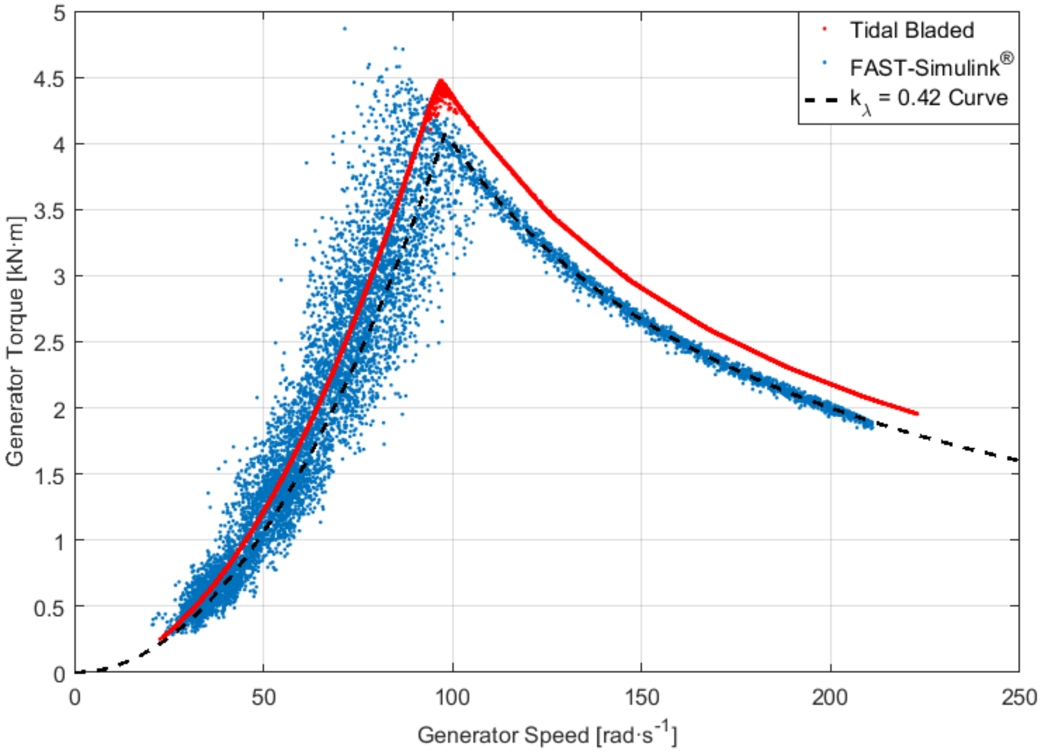

Figure 3.13: *Generator torque-speed curves obtained from Tidal Bladed (red) and the developed model (blue), compared with the idealised controller curve (black)*

The generator torque-speed results obtained from the Tidal Bladed simulations also broadly follow the idealised curve, but again there is some variation. Unlike the developed model, this is believed to be due to the inclusion of a generator efficiency curve in the Tidal Bladed simulations, which was obtained by extrapolating measurements made by the manufacturer from dry testing the generator (Figure 3.14). The efficiency relates to losses encountered during the mechanical to electrical power conversion and is a function of generator speed. This means that at the rated point the product of the generator speed and demanded torque will be greater than 400 kW, but electrically the rated power is output after accounting for losses. As a consequence, the Tidal Bladed results show greater amounts of torque in the above rated region when compared with the idealised curve. It would, however, appear as if the Tidal Bladed controller demanded higher generator torques in the below rated region too. This is surprising as it has the effect of slowing the turbine down below λ_{opt} and to a position of lower generator efficiency. It is suspected that the generator efficiency curve was incorrectly applied in this region to amend the controller gain. The final point to note is the narrower scatter observed in the Tidal Bladed results, implying that the modelling of its controller response time is quicker than that in the developed model.

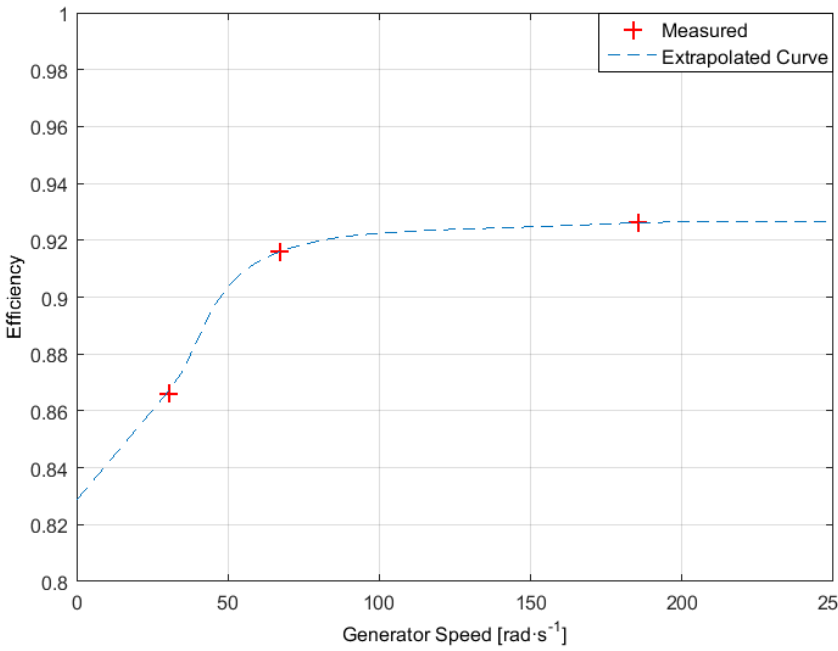

Figure 3.14: *Generator efficiency curve extrapolated from measurements obtained during testing*

The findings in Figure 3.13 are supported by further analysis in Figure 3.15, in which the rotor speed from both models is plotted as a function of hub flow magnitude. As before, these are 1 second moving average values. The gradient of the dashed black line is equal to λ_{opt}, i.e. $\lambda = 3$. Both models scatter closely about this line until approximately 2.7 m·s^{-1}, where the transition to the second control region occurs and the rotor overspeeds. The developed model enters this region slightly earlier than

Tidal Bladed since it does not model the generator efficiency. This is confirmed in Table 3.2 where the mean rotor speeds for each simulation case are compared. Due to turbulence, simulations at mean hub flow magnitudes 2.5 m·s^{-1} and higher feature periods in which the rated power is achieved, resulting in overspeed activity that shifts the mean λ above 3. The rotor speeds in the developed model are higher during these simulations. The two models agree well below the rated point, but the developed model is slightly closer to the desired λ_{opt}. Both operate just below λ_{opt} because their controller gains were set too high, as seen in Figure 3.13.

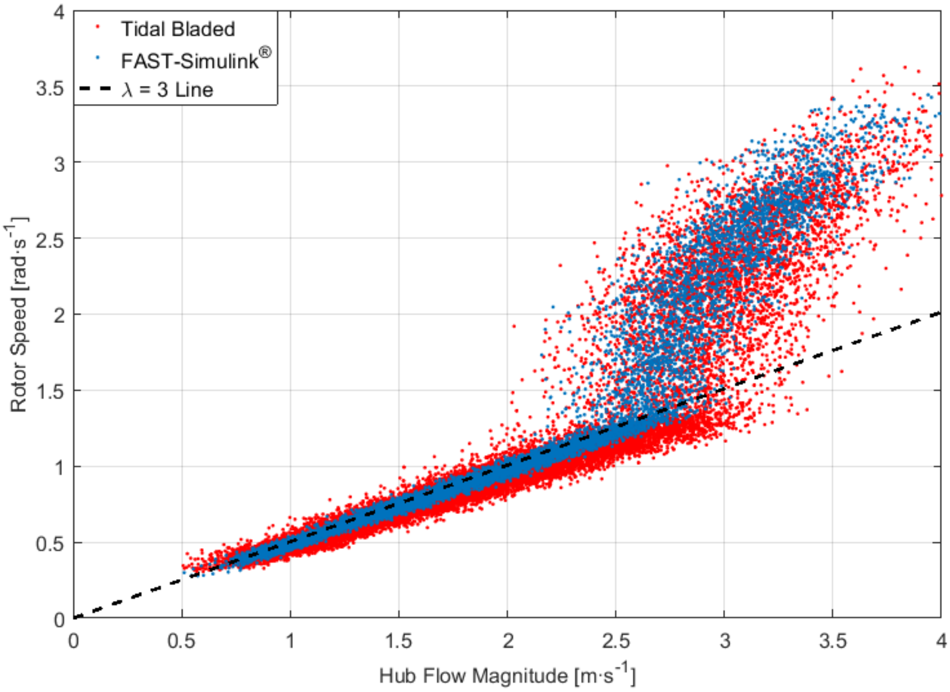

Figure 3.15: *Rotor speed as a function of hub flow magnitude obtained from simulations in Tidal Bladed (red) and the developed model (blue). The line of* λ_{opt} *(black) is also plotted.*

Table 3.2: *Comparison of mean rotor speeds from the Tidal Bladed and FAST-Simulink® simulations for each mean hub flow magnitude*

	Tidal Bladed		**FAST-Simulink®**	
Mean Hub Flow Magnitude [m·s^{-1}]	**Rotor Speed [rad·s^{-1}]**	**λ**	**Rotor Speed [rad·s^{-1}]**	**λ**
1	0.48	2.87	0.49	2.93
1.5	0.71	2.83	0.74	2.95
2	0.95	2.84	0.98	2.93
2.5	1.30	3.10	1.47	3.50
3	2.25	4.47	2.38	4.72

While Figures 3.13, 3.15 and Table 3.2 have shown that the models exhibit some deviation from the idealised controller objectives, the turbines in both operate close to the desired curves and the differences can be deemed insignificant. The most important finding is that both models show good agreement with each other below the rated point, and hence a validation of the developed model against Tidal Bladed is possible in this region. This is more difficult to achieve in the above rated region since the generator efficiency was not considered in the GE Simulink® model, and as a result the turbine speeds show greater variation in these conditions. Figure 3.16 highlights this, where the developed rotor thrust curves from each model are presented, defined as the 'Hub F_x' force as per the fixed coordinate system (Figure 3.17) in the GL convention *[191]*. The error bars represent ± 1 standard deviation, σ, and the scatter 1 second moving average values. The steady-state curve is also plotted from Figure 3.3.

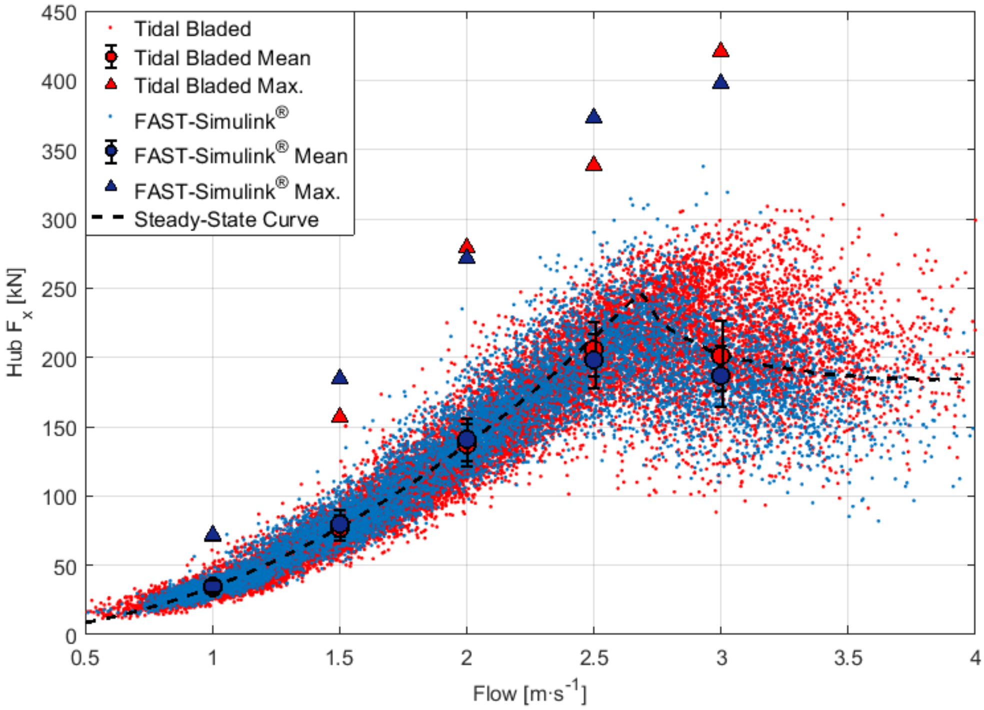

Figure 3.16: *Dynamic rotor thrust curves obtained from simulations in Tidal Bladed (red) and the developed model (blue)*

The dynamic results from both models demonstrate good agreement up until and including simulations at 2 m·s^{-1}, as seen by the similar mean and maximum values, and the variation shown by the error bars and scatter. Thereafter, the mean values in the developed model are found to be lower than those in Tidal Bladed as a consequence of the turbine speed difference. The predicted maximum thrust in the developed model is also lower, but this too will be influenced by the speed differences. Additionally, half as many simulations were run in the developed model. It is possible that greater values would have been observed if an equivalent number of simulations were performed.

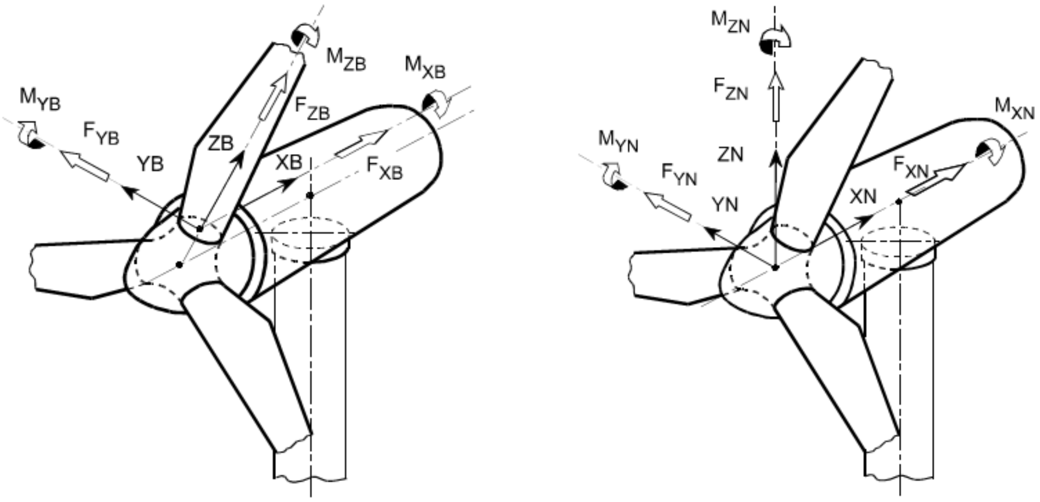

Figure 3.17: *Blade root (left) and fixed-hub (right) coordinate system in both models, adopted from the GL convention [191]*

Both models have demonstrated the thrust shedding characteristics of the rotor as a result of overspeed activity, evident from the reduced mean loading in high flows. The rate at which the dynamic loading increases has also decreased, with the scatter no longer following a quadratic relationship with flow velocity. Similarly, the maximum values broadly follow this relationship at simulations between 1 – 2 $m{\cdot}s^{-1}$, but the thrust shedding has prevented these values from becoming excessive.

Table 3.3 summarises the results of some of the other dynamic loads at the blade root and hub. Consistent with the rotor thrust findings in Figure 3.16, all of the mean loads in both models agree well in below rated conditions, and the FAST-Simulink® values are lower in higher flows. Generally the standard deviations in both models are of comparable magnitude below rated, with the blade root M_x and F_y loads being the only exceptions. These anomalies are believed to be due to buoyancy effects modelled in Tidal Bladed, and are discussed in more detail in section 3.4. Apart from the blade root M_x and F_y loads, the maximum values of all of the other loads derived from both models are within 20% of each other in flows 1 – 2 $m{\cdot}s^{-1}$, i.e. the simulations in which the mean rotor speeds are approximately the same (Table 3.2).

The blade root M_z and F_z loads did not compare well with Tidal Bladed. The root M_z moment contributes to the hub overturning (hub M_y) and yawing (hub M_z) moments, meaning that these too do not show an agreement. Similarly, the differing root F_z forces have resulted in disagreements on the hub forces perpendicular to rotor thrust. These are the hub F_y and F_z loads. The potential sources of these discrepancies are discussed in section 3.4.

Table 3.3: *Blade root and hub loads compared from the Tidal Bladed and FAST-Simulink® simulations*

Blade Root Loads					
Mean Hub Flow Magnitude [m·s^{-1}]	**Load**	**Tidal Bladed**		**FAST-Simulink®**	
		Mean ± 1σ	**Max.**	**Mean ± 1σ**	**Max.**
1	Root M_x [kN·m]	10.6 ± 4.7	30.2	11.0 ± 33.5	73.5
1.5		23.9 ± 9.3	67.5	24.0 ± 34.6	111.6
2		42.5 ± 14.8	119.6	44.0 ± 36.3	140.1
2.5		61.4 ± 21.5	157.2	55.8 ± 38.5	197.8
3		46.2 ± 31.9	194.8	39.8 ± 40.5	193.2
1	Root M_y [kN·m]	31.0 ± 10.1	74.0	31.7 ± 9.6	78.8
1.5		70.1 ± 22.5	167.0	73.3 ± 21.7	193.1
2		124.3 ± 36.5	309.2	128.9 ± 33.8	261.5
2.5		186.7 ± 56.4	436.5	178.9 ± 48.2	397.1
3		177.8 ± 110.5	724.2	162.3 ± 68.8	524.0
1	Root F_x [kN]	11.4 ± 3.6	26.3	11.6 ± 3.4	28.5
1.5		25.7 ± 8.1	61.6	26.7 ± 7.8	72.1
2		45.7 ± 13.0	114.4	47.0 ± 12.1	95.2
2.5		68.7 ± 19.7	155.9	66.1 ± 16.9	143.9
3		66.7 ± 36.7	250.7	62.1 ± 22.9	183.2
1	Root F_y [kN]	-4.5 ± 2.2	1.7	-4.7 ± 15.8	20.6
1.5		-10.1 ± 3.9	0.3	-10.5 ± 16.2	18.3
2		-18 ± 6.0	-1.1	-18.6 ± 16.8	17.6
2.5		-26.2 ± 8.4	14.2	-24.4 ± 17.4	16.1
3		-20.9 ± 11.7	37.7	-19.1 ± 18.0	26.7
Hub Loads					
1	Hub M_x [kN·m]	46.6 ± 11.3	101.2	47.4 ± 12.0	101.2
1.5		105.0 ± 25.7	211.2	109.8 ± 27.6	245.0
2		186.7 ± 41.4	384.1	193.0 ± 42.4	351.1
2.5		270.5 ± 51.5	467.4	247.5 ± 55.4	446.5
3		208.2 ± 66.9	449.6	182.9 ± 63.7	483.7
1	Hub F_x [kN]	34.1 ± 8.3	70.8	34.7 ± 8.9	72.3
1.5		77.1 ± 18.9	157.4	80.1 ± 20.1	184.7
2		137.0 ± 30.1	279.3	141.0 ± 31.1	271.6
2.5		206.1 ± 38.9	339.0	197.9 ± 39.0	372.8
3		201.5 ± 50.3	420.9	186.7 ± 44.1	398.4

Since the hub M_x moments, equivalent to rotor torque, and the turbine speeds have been found to be in good agreement in both models during below rated operation, the power developed by the rotors is also consistent. Figure 3.18 shows this by comparing the generator power curves of both models, with the data processed in the same way as that in Figure 3.16. The plotted steady-state curve is derived from the rearrangement of Equation 3.2 and a c_p of 0.4, while it also accounts for the gearbox (Table 3.1) and generator (Figure 3.14) efficiencies. The Tidal Bladed results show a very good agreement with the steady-state curve, whereas the developed model achieves a performance that exceeds this. This is due to the absence of the generator efficiency. Both models scatter closely about the rated power in high flows, suggesting good power capture in this region.

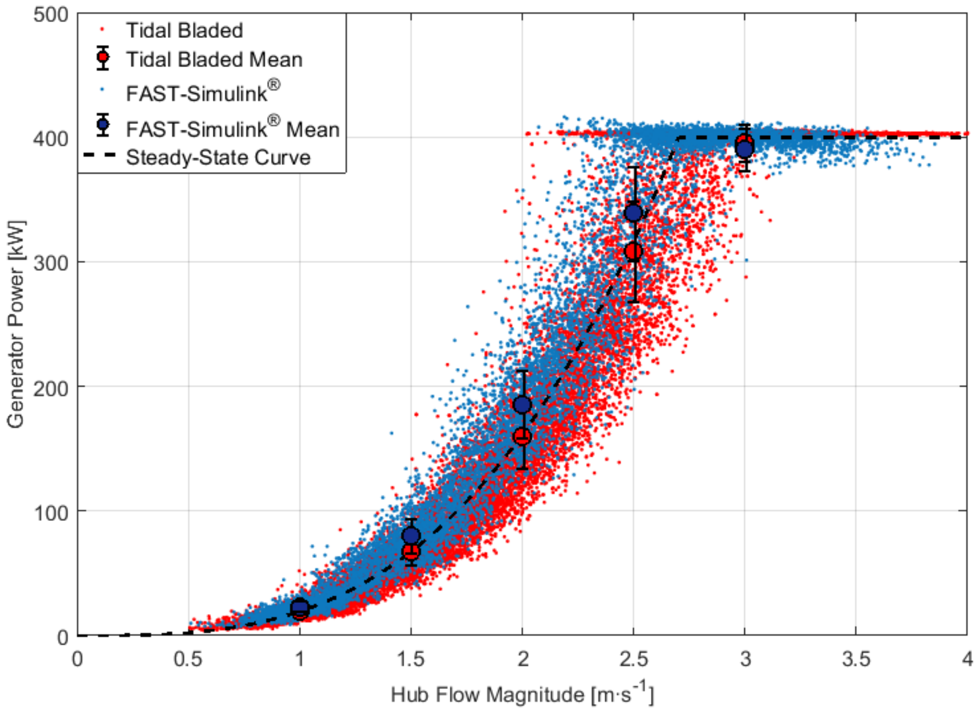

Figure 3.18: *Dynamic generator power curves obtained from simulations in Tidal Bladed (red) and the developed model (blue)*

3.4 Strengths and Limitations of the Developed Model

The previous sections in this chapter have described the development of a numerical model of the TEL turbine, by coupling an existing model of the electrical systems and controller with a BEM based code of the rotor hydrodynamics. The resulting hybrid model was benchmarked against the leading, commercially available Tidal Bladed software package, by comparing simulation results of the turbine operating in ebb tidal conditions representative of Ramsey Sound. Mean and dynamic rotor power and thrust results have been shown to be in very good agreement with Tidal Bladed, leading to the conclusion that the developed model sufficiently calculates the two key parameters that are of greatest interest in this study. Thus, a degree of validation has been established in the capabilities of the developed model, allowing it to be used with confidence to assess how performance related criteria are affected in configurations that differ to those simulated in Section 3.3. This could include changes to the environment, such as stronger and/or more turbulent flows, or the effects of modifying the turbine itself. For example, larger turbines and/or new rotor geometries could be assessed, as well as variations to the control strategy. The option to create pitch and yaw controllers within the FAST-Simulink® environment further demonstrates the flexibility of the developed model.

A situation in which there might be potential benefits to modifying the existing TEL turbine control strategy was shown in Figure 3.5 using a steady-state simulation, in which the turbine sacrificed some power production to reduce rotor loading. While this was a fairly simple analysis, it can be expected that similar benefits would be found if a similar simulation was run in an unsteady environment in the developed model. There is scope here to simulate the turbine with an idealised upstream flow measuring system that informs the controller of any approaching disturbances, allowing the turbine to react in advance of the event to minimise loading, i.e. feedforward control. The simulations could support the development of such a system, leading to an understanding of the required time that the controller would need in order to make feedforward actions in advance of the disturbance. Similar analyses have been performed in wind turbine research to assess the perceived benefits of a feedforward system informed by upwind LIDAR measurements [192].

The Simulink® aspects of the developed model were, however, written for the current turbine configuration by GE. Due to the ‘black box’ nature of the controller, this introduces a number of limitations that prevent modifications to the turbine’s electrical systems and control strategy. This includes sizing the generator itself, which cannot be increased from the 400 kW default. The model will correctly recalculate the generator torque gain parameter, k_λ, according to Equation 3.8 should the gearbox ratio, rotor diameter or water density change, but altering the c_p - λ curve in the accompanying MATLAB script required to run the model has no effect. This means that a new rotor design with a differing c_p - λ curve would continue to operate at $\lambda_{opt} = 3$ in the GE model, regardless of where its actual λ_{opt} value occurs. It would appear as if the c_p - λ curve is only being used to compute the steady-state rotor power in the model's original configuration (Figure 3.4). To summarise, smaller or larger turbines scaled from the rotor geometry of the existing 12 m diameter turbine can be modelled up to 400 kW only using the current GE model. The model does not permit the usage of larger generators and it will fail to track the point of optimum operation if it differs from that of the existing rotor design. Furthermore, should the user wish to model a turbine with a control strategy not based on overspeed, e.g. pitch or stall, the GE model will not allow the required speed regulation. This is a considerable limitation of the developed model. A customisable model of the electrical systems and controller is required if the FAST-Simulink® arrangement is to be used for other turbines.

The FAST elements of the developed model are not without their own limitations. These are primarily a result of the model being built specifically for wind turbines, and as a consequence a number of effects exclusive to the tidal application are not considered. The first of these are the influences that wave induced currents have on turbine performance, which have been shown to create cyclical time histories of turbine loading and power [57], [58], [193]. It should be noted that the results from the Tidal Bladed simulations in Section 3.3 do include the effect of waves, derived from a linear airy wave model [65]. The waves were, however, configured with small heights and low wavelengths that are representative of those in Ramsey Sound's sheltered environment, meaning that any effects from the induced currents will be negligible. Hence the increased variation of loading and power was insignificant during the model comparison study. If there was a desire to model the turbine at a site with a more extreme wave climate, it would be necessary to modify FAST to include these effects.

In Table 3.3, it was shown that there were discrepancies in the amount of variation exhibited on the blade root M_x and F_y loads. According to [194], these loads are calculated as follows:

$$M_{x_{root}} = M_{x_{hydro}} + M_{x_{grav}} + M_{x_{iner}} \tag{3.10}$$

$$F_{y_{root}} = F_{y_{hydro}} + F_{y_{grav}} + F_{y_{iner}} \tag{3.11}$$

From Equations 3.10 and 3.11, it can be seen that there are terms relating to hydrodynamic (aerodynamic for wind turbines), gravitational and inertial components that contribute to the net root load. In the rotating blade root coordinate system (Figure 3.17), the gravitational contributions are calculated according to Equations 3.12 and 3.13.

$$M_{x_{grav}} = m_b \cdot g \cdot z_{cm} \cdot sin\,\theta \tag{3.12}$$

$$F_{y_{grav}} = -m_b \cdot g \cdot sin\,\theta \tag{3.13}$$

Where:

m_b	-	Blade mass
g	-	Gravitational acceleration
z_{cm}	-	Centre of blade mass in z-direction
θ	-	Azimuth position of blade

Thus the gravitational terms are clearly periodic with amplitudes that depend on blade mass. In the Tidal Bladed setup files used to model the TEL turbine, m_b was defined as 2604 kg while z_{cm} was derived by integrating the sectional mass per unit length, $\frac{m}{L}$, values of the blade along its length, z:

$$z_{cm} = \frac{\int z \cdot \frac{m}{L} \cdot dz}{m_b} \tag{3.14}$$

This yielded a value of 1.48 m. Therefore, it would be expected that the periodic components of the blade root M_x and F_y loads have amplitudes of 37.8 kN·m and 25.5 kN respectively. However, upon the analysis of a steady flow simulation, i.e. no turbulence or waves, the amplitudes were found to be considerably smaller. This is shown in Figure 3.19 by the blue lines, where both loads are shown to have amplitudes less than 5. Note that the loading magnitudes increase during the simulation because the flow is linearly increasing. It is believed that the periodic components of the loads are not as high as expected due to buoyancy forces, as this option was selected in the setup files. The buoyancy contribution was determined by calculating the blade volume, through numerical integration of each aerofoil's area along the blade length. This was found to be 2.3 m^3, meaning that m_b in Equations 3.12 and 3.13 in effect reduces to 246.5 kg after subtracting the buoyancy term, which itself is the product of the blade volume and water density. Therefore, the blade root M_x and F_y loads should instead have amplitudes of 3.6 kN·m and 2.4 kN. This is confirmed by the red lines in Figure 3.19, which show the root loads with the gravitational/buoyancy term subtracted from the net value. The sinusoidal variation in loading is no longer present. The only remaining periodic component in the time-series is due to tower shadow effects, which result in small load reductions at a frequency equivalent to the rotor speed.

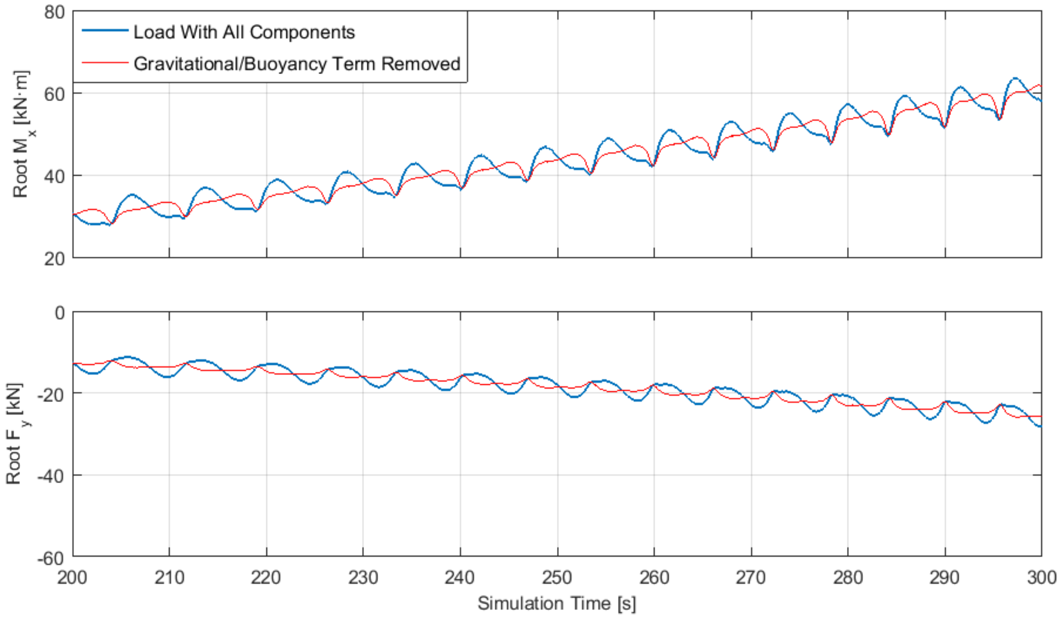

Figure 3.19: *Blade root* M_x *and* F_y *loads from Tidal Bladed. The net loads (blue) are subject to cyclical, gravitational/buoyancy components. The red line removes these components.*

During the setup of the FAST model the blade mass was not considered, and was instead obtained by modifying a pre-existing file packaged with the model that contained generic mass properties. This resulted in a blade mass of 2254 kg and a centre of mass of 2.1 m. These are both larger than those used by Tidal Bladed after accounting for buoyancy, explaining the greater variations experienced by the developed model in blade root M_x and F_y loads (Table 3.3). FAST does not have the capability to include buoyancy effects, but it would be possible to define false blade mass properties in order to achieve the correct variation in these loads.

It should be stated that the inertial components in Equations 3.10 and 3.11 are also dependent on blade mass. However, these loads are insignificant since they are a function of rotor acceleration, which is always considerably lower than 1 rad·s^{-2}. They are more significant for the blade root F_z forces, where they are instead a function of the square of rotor speed.

The modifications to the blade root F_z forces in Tidal Bladed are less clear, since there appeared to be no agreement with FAST. Similar to Equation 3.11, the net blade root F_z force is made up of 3 terms, including a cyclical gravitational/buoyancy related component, $F_{z_{grav}}$. These are expressed as follows:

$$F_{z_{root}} = F_{z_{hydro}} + F_{z_{grav}} + F_{z_{iner}} \tag{3.15}$$

$$F_{z_{grav}} = -m_b \cdot g \cdot cos\,\theta \tag{3.16}$$

It would, therefore, be expected that the amplitude of the sinusoidal variation of $F_{z_{root}}$ is equivalent to that of $F_{y_{root}}$, i.e. 2.4 kN. Instead the $F_{z_{root}}$ root forces show much larger cyclical variations about a mean value approximately equal to -230 kN, i.e. acting downwards on the blade. Unlike the other root loads, the mean $F_{z_{root}}$ appears to remain almost constant at this value irrespective of flow speed, except in the highest flows when the rotor is overspeeding and the inertial forces are significant. This would suggest that there is a consistent force contribution that is considerably larger than all other terms. It is believed that this comes from hydrostatic pressure on the blade. The contribution has been estimated by integrating the hydrostatic pressure over the sectional aerofoil areas that make up the blade, both when the blade is pointing vertically up and down. These orientations correspond to the points of minimum and maximum hydrostatic pressure, capturing in the expected range of force variation.

Using the turbine geometry data (Table 3.1 and Figure 3.7) and the specified seabed depth of 36 m in the Tidal Bladed model, it is possible to calculate the hydrodynamic pressure, p, at the aerofoil heights, h, below the sea surface according to:

$$p = \rho \cdot g \cdot h \tag{3.17}$$

The hydrostatic force, F_p, is then derived using the following integration over the aerofoil areas, A:

$$F_p = \int p \cdot dA \tag{3.18}$$

This yielded forces of -198 and -265 kN for the blade in the upwards and downwards orientations respectively, suggesting that the hydrostatic term fluctuates about -232 kN. Thus this calculation adds weight to the suspicion that the $F_{z_{root}}$ forces in the Tidal Bladed are primarily due to hydrostatic pressure. Again, since FAST was created to model wind turbines, the hydrostatic contribution is not considered. Only through modification of the source code would it be possible to include these effects.

The blade root pitching moments, $M_{z_{root}}$, calculated by FAST also did not appear to show an agreement with Tidal Bladed. Upon closer inspection of the setup files for the latter, it was realised that a table of pitching moment coefficient data was being used. This dataset is similar to the lift and drag data shown in Figure 3.9, covering ±180° angles of attack for three Reynolds numbers. In the AeroDyn module of FAST, it is also possible to include the pitching moment coefficient data for these calculations. This was not realised at the time of running the simulations presented in Section 3.3, but subsequently some of the simulations were repeated with the pitching moment coefficient data used by Tidal Bladed. While this improved the results, the $M_{z_{root}}$ values calculated still appeared to be approximately half of those obtained in Tidal Bladed. One potential source of this difference could be added mass effects, caused by the acceleration of the blades through water. Wind turbines do not need to consider these effects due to the comparatively low density of air. It is known that Tidal Bladed considers added mass in its modelling [65].

As mentioned previously, the rotor hub loads are derived from those at the blade roots. Therefore, it would be firstly necessary to apply tidal modifications to the blade root loads before attempting to correctly calculate the hub loads. After which, it is expected that these improved hub load calculations will require further modification to account for nacelle buoyancy and hydrostatic related forces.

This chapter, therefore, has outlined the development of a numerical model that can be used to reproduce many of the predicted dynamic loads from the leading Tidal Bladed software (Table 3.3). However, it is clear that a number of modifications are required to standard BEM codes to comprehensively understand tidal turbine loading. This includes the rotor overturning, $Hub\ M_y$, and pitching (yawing), $Hub\ M_z$, moments (Figure 3.17), both of which are key during the assessment of foundation stability. While Tidal Bladed does consider many effects from the subsea operation of a horizontal-axis turbine, as discussed in this section, there is very little information publicly available on the validity of these modelling approaches. This can only be realised through experimental verifications.

4. 1:30 Scale Model Testing

The numerical results in the previous chapter predicted that desirable operational characteristics are achievable from the overspeed based control strategy. The next step was to demonstrate these on a physical turbine to appraise the system further with experimental evidence. For this reason, a 1:30 scale model of the turbine was developed and tested in a laboratory ahead of the installation of the full-scale device. This chapter details the test arrangement and evaluates the obtained results against numerical predictions. The chapter concludes with a discussion that reviews the test campaign.

4.1 Test Arrangement

A turbine rig developed by researchers at Cardiff University was obtained for the test campaign, comprising of a Baldor brushless AC servomotor and a controllable drive. By fitting a rotor to the turbine rig, the hydrodynamic torque it developed could be opposed by applying a resistive load from the servomotor. A regenerative resistor was used to absorb the power developed by the rotor. The software accompanying the drive allowed the turbine speed or torque to be controlled [195]. These quantities were recorded to measure turbine power. The test rig has previously been used for several tests with a 0.5 m diameter turbine [121], [125]. Full details of the turbine rig can be found in [196].

The turbine was tested at Cardiff University's Hydro-environmental Research Centre, in a 1.20 m W x 0.66 m D recirculating flume. This cross-sectional area placed a constraint on the rotor size. If the rotor was too large it would be subject to considerable blockage effects, whereas if it was too small the performance characteristics would be dissimilar to a full-scale equivalent due to significant Reynolds number differences. As a compromise, a 1:30 scale rotor diameter of 0.4 m was selected. This would lead to a blockage ratio of 16% that could be accounted for in the post-processing of data, while the achievable flume speeds (> 1 $\mathrm{m \cdot s^{-1}}$) in the tank would ensure that the turbine operated at a Reynolds number where any performance disparities would be minimal.

The hub accompanying the test rig had a fixed diameter of 0.1 m, meaning that it could not be scaled accurately without manufacturing a new one. The 2.2 m hub diameter on the commercial turbine should have been scaled to 0.07 m. Instead it was decided to remove the bottom sections of the scaled blades in the region where the larger hub occupied, since this region of the blade contributes the least to the developed rotor torque. Consequently, the size ratio of the hub to the rotor was greater than that of the commercial turbine, i.e. the model had an oversized hub. Even though this did not represent true geometric scaling, the model was expected to maintain performance characteristics similar to that of the larger device, albeit with reduced hydrodynamic loading and rotor power capture. This was confirmed by running steady-state simulations of this rotor in the FAST model to produce the c_p and c_t curves with respect to λ, as shown in Figure 4.1.

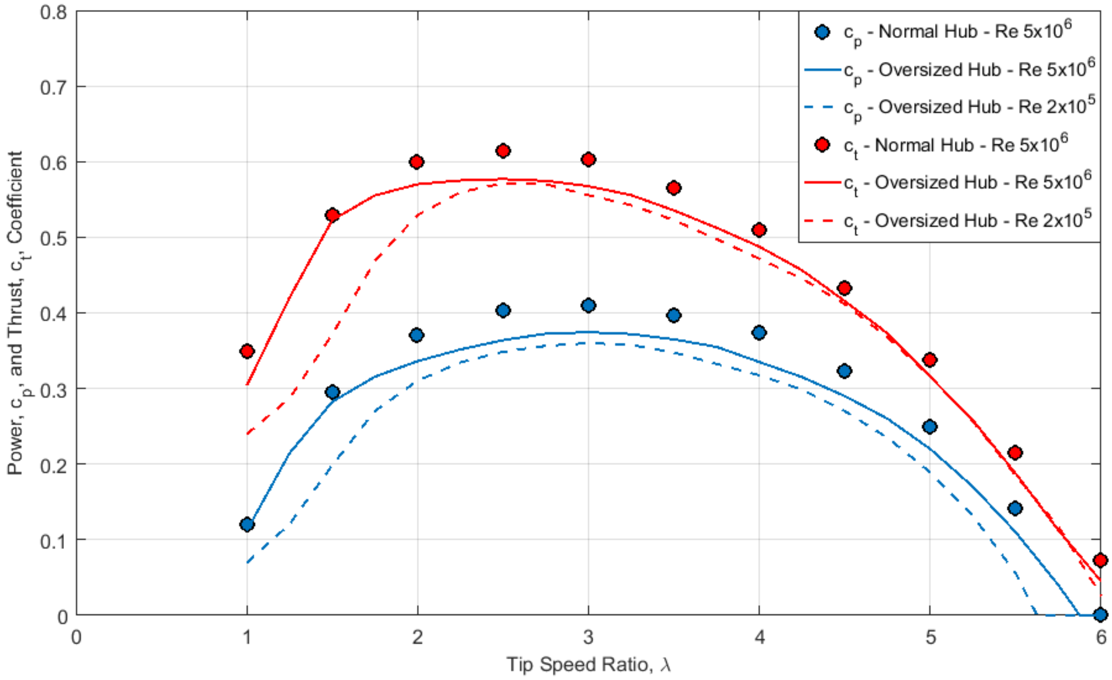

Figure 4.1: *Predicted modifications to the c_p and c_t curves with respect to λ as a result of oversizing the hub and Reynolds number effects*

It can be seen from Figure 4.1 that the $c_{p_{max}}$ still occurs at λ_{opt} = 3 for the rotor with the oversized hub, but its magnitude has reduced to a value of 0.37 at the representative full-scale Reynolds number of 5 x 10^6. Similarly, the c_t at λ_{opt} has reduced to 0.57 at this Reynolds number. Crucially, however, the oversized hub was predicted to maintain the thrust shedding characteristics at high λ, allowing the effectiveness of the overspeed control strategy to be assessed despite the differing geometries.

For the 1:30 scale turbine, the rotor characteristics are predicted for a Reynolds number of 2 x 10^5 in Figure 4.1. The reasoning for this Reynolds number choice is described in Section 4.2. The c_p and c_t values at λ_{opt} are predicted to reduce further to 0.36 and 0.56 respectively for the 0.4 m diameter rotor.

The model turbine blades were geometrically scaled from the commercial device, resulting in a 0.15 m blade length comprising of a maximum chord and thickness of 0.07 m and 0.01 m respectively. These were 3-D printed and fitted with circular pins to position into holes on the circumference of the turbine hub. The correct pitch angles were set by resting the blades on 3-D printed moulds that aligned with the back of the hub. Once the pitch angle was set, grub screws inside the hub were tightened to prevent the pins from moving. The blade and mould are shown in Figure 4.2.

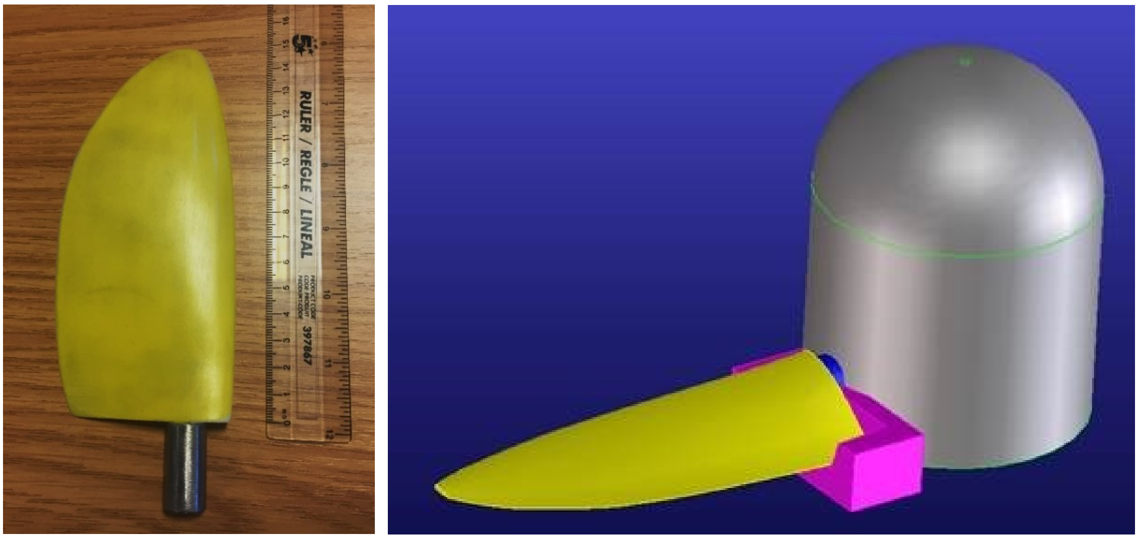

Figure 4.2: *The 3-D printed blade (left) and pitch angle setting mould (right)*

The turbine was supported by a Y-shaped frame that was fixed to a platform resting above the flume, leaving the rotor positioned approximately in the centre of the tank cross-section. The support frame was allowed to pivot under loading exerted on it by the flow. These forces were measured using a 10 kg load cell that was affixed to the turbine support pole. Through the evaluation of the lever arm moments formed on the support pole (see Section 4.2), it was be possible to relate the force at the load cell to the equivalent load at the turbine position, providing a measurement of rotor thrust. A drawing of the general arrangement of the turbine and support structure is shown in Figure 4.3.

A pump power dial in the test facility provided manual control over the flow speed. This was measured using a Nortek Vectrino acoustic Doppler velocimeter (ADV), positioned upstream of the rotor with its transducer probes at a comparable depth to the hub centre. For the calibration tests (Section 4.2), the ADV was configured to sample at 25 Hz using the accompanying Vectrino software. Maximum flow speeds of approximately 1.2 $m \cdot s^{-1}$ were reached during testing.

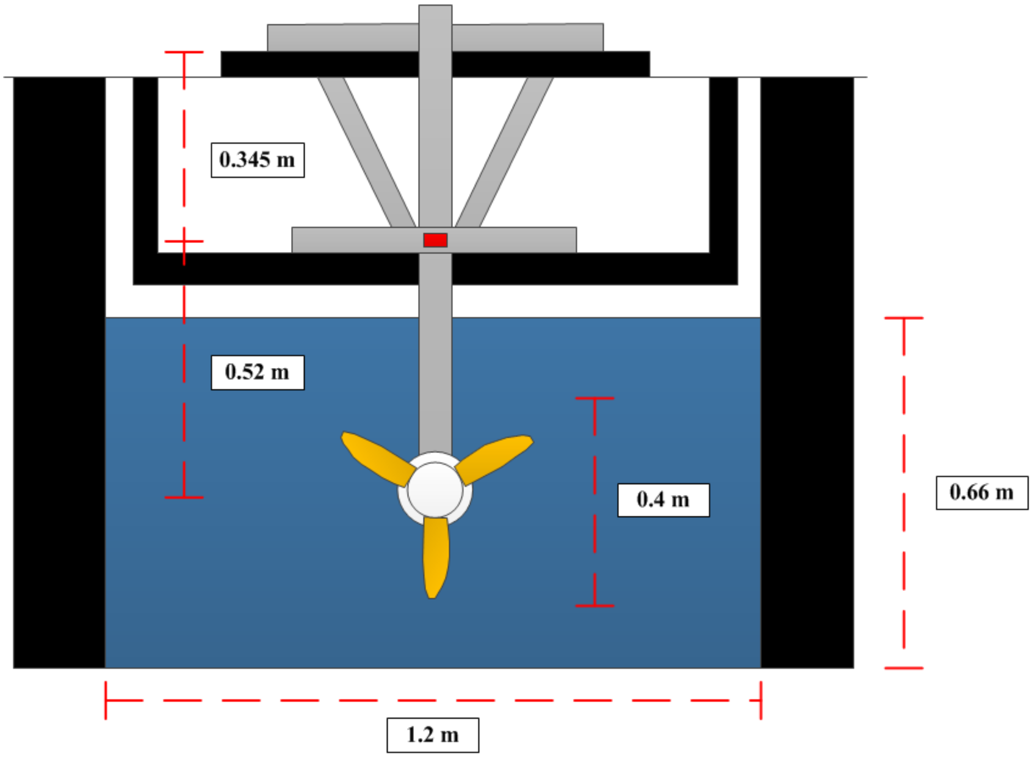

Figure 4.3: *Schematic of the test arrangement. The rectangular square on the turbine support pole indicates the position of the load cell*

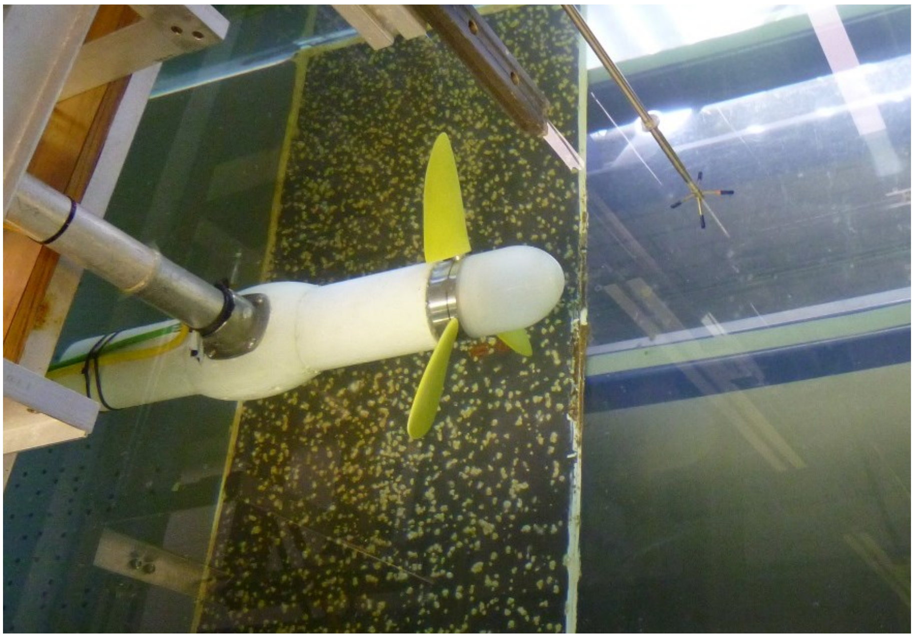

Figure 4.4: *Turbine installed in the flume with the upstream ADV probes visible*

4.2 Preparatory Tests

ADV measurements were obtained 3 rotor diameters (1.2 m) upstream of the turbine and were quality controlled for low correlation and signal to noise ratios (SNR). The former is a measure of signal quality and is expressed as a percentage, while the latter is the amplitude of the signal relative to the noise level, defined in decibels (dB). Measurements with correlations less than 40% or SNRs lower than 15 dB were removed in post-processing, as recommended by Nortek [197]. Additionally, measurements found to be outside ± 3 standard deviations from the mean value within an averaging period were removed. The flow turbulence intensity, *TI*, was determined from the ratio of the root-mean-square velocity fluctuations to the mean values:

$$TI = \sqrt{\frac{\frac{1}{3} \cdot (u'^2 + v'^2 + w'^2)}{\bar{u}^2 + \bar{v}^2 + \bar{w}^2}} \tag{4.1}$$

Where u, v and w represent the x, y and z components of velocity, with the overbar and apostrophe denoting the mean and fluctuating values respectively. *TI* was found to be consistently within the region 9 - 12% during testing. These measurements were not corrected for Doppler noise as the standard error of the ADV was unknown. However, the work in [98] suggests that this concern is more important for ADPs, where *TI* was reduced from 22 – 10% upon applying the correction. In contrast, the ADV measurements from the same field survey were reduced from 12 – 11%.

To determine the thrust on the turbine, two conversions were required to relate the load cell measurements to axial forces on the rotor. The first accounts for drag associated with the turbine support structure. This was determined by removing the blades from the turbine hub and measuring the drag with respect to flow velocity. Figure 4.5 shows the relationship. The measurements correspond to mean values obtained over two minute periods in which the pump power was constant, producing consistent flume speeds. It can be seen that the structural drag is approximately linear at these flow velocities, demonstrated by the high coefficient of determination (R^2) on the fitted line. The equation of this line was used in all subsequent analysis to evaluate the drag force, F_d, as a function of flow velocity, v. The drag corrected force, F_c, is derived from the raw measurement, F, as follows:

$$F_c = F - F_d \tag{4.2}$$

Where:

$$F_d = 33.8v - 11.3 \tag{4.3}$$

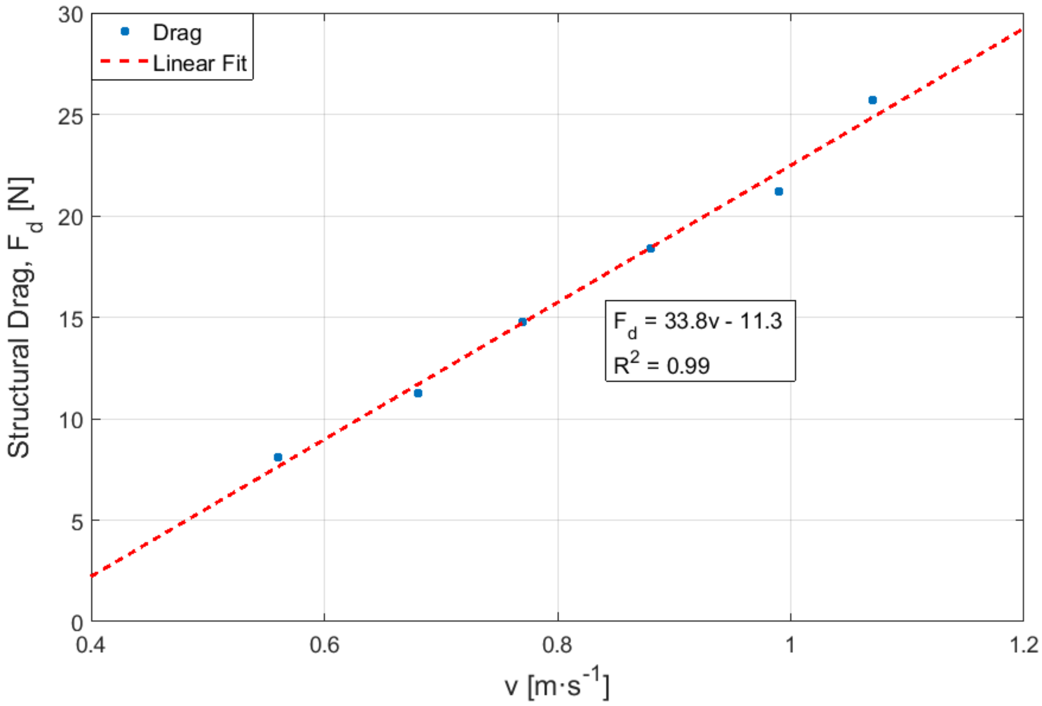

Figure 4.5: *Measured drag force on the turbine support structure and the fitted line used for subsequent calculations of rotor thrust*

The second conversion relates the F_c to the thrust developed by the rotor, F_x. The turbine support pole forms a lever arm, meaning that careful measurements of both its length and the position of the load cell allow the relevant moments to be evaluated. The dimensions are illustrated in Figure 4.3. The load cell was measured to be at 0.345 m from the pivot point (y_1) and 0.52 m from the rotor centre (y_2). Using these measurements it can be found that F_x is approximately 40% of F_c after applying the following conversion:

$$F_x = \frac{F_c \cdot y_1}{(y_1 + y_2)} \tag{4.4}$$

With a methodology established to determine the turbine speed, power and thrust, as well as the upstream flow velocity, it was possible to experimentally derive the non-dimensional rotor characteristics. These were measured in constant flows with the turbine operating in a speed controlled mode, where it was commanded to step through a number of targeted rotor speeds in order to achieve a λ range between 1 and 6. The procedure allowed the rotor to firstly free wheel in the flow without any opposing torque, before the servomotor applied a resistive load to slow the rotor down in steps until the lowest demanded speed was reached. Subsequently the turbine was stepped back up to the free wheel condition. The methodology is similar to that in [121], [196].

Since the load cell was on a separate data acquisition (DAQ) system to that of the ADV and servomotor, a manual trigger event was created on a spare channel to mark the position in its time-series at the point where the servomotor torque was first applied for each test, enabling data synchronisation. Upon studying the load cell data, a distinct peak in force was always present at the same time as the trigger event, clearly marking the point at which the servomotor drive was activated. The issue of data synchronisation is described in more detail in Section 4.3.

Each speed step lasted for a period of 1 minute, with measurements of flow, rotor speed, support structure load and drive current all averaged within steps. The manufacturer states that the motor torque is related to the drive current through a proportionality constant of 0.906 $\mathrm{N{\cdot}m{\cdot}A^{-1}}$ [198]. Measurements obtained within ± 5 seconds of the step changes were discarded to allow the rotor some settling time about the transition point. The aforementioned quality control techniques for the ADV measurements were also applied here. λ, rotor c_p and c_t were calculated using Equations 3.1, 3.2 and 3.3 respectively with a freshwater density, ρ, of 1000 $\mathrm{kg{\cdot}m^{-3}}$. However, due to the rotor occupying 16% of the flume cross-sectional area, its power performance was artificially enhanced due to blockage effects. Thrust loads and λ were also affected. Therefore, it was necessary to use the iterative blockage correction method detailed in [114] to estimate the unconstrained performance of the device, allowing comparisons to be made with numerical predictions and the operational results of the full-scale device. The blockage correction method yields a factor that is defined as the ratio of the measured tank flow speed, v, to a free stream equivalent, v_F, i.e. a flow representative of unblocked conditions. The unconstrained λ, c_t, and c_p are all obtained by using this blockage factor to correct the blocked results, denoted by the $blocked$ subscripts, in the following way:

$$\lambda = \lambda_{blocked} \cdot \left(\frac{v}{v_F}\right) \tag{4.5}$$

$$c_t = c_{t_{blocked}} \cdot \left(\frac{v}{v_F}\right)^2 \tag{4.6}$$

$$c_p = c_{p_{blocked}} \cdot \left(\frac{v}{v_F}\right)^3 \tag{4.7}$$

Typically, the blockage factor was found to be approximately equal to 0.97, resulting in 3, 6 and 9% reductions in λ, c_t, and c_p respectively. The corrected results are shown in Figures 4.6 and 4.7.

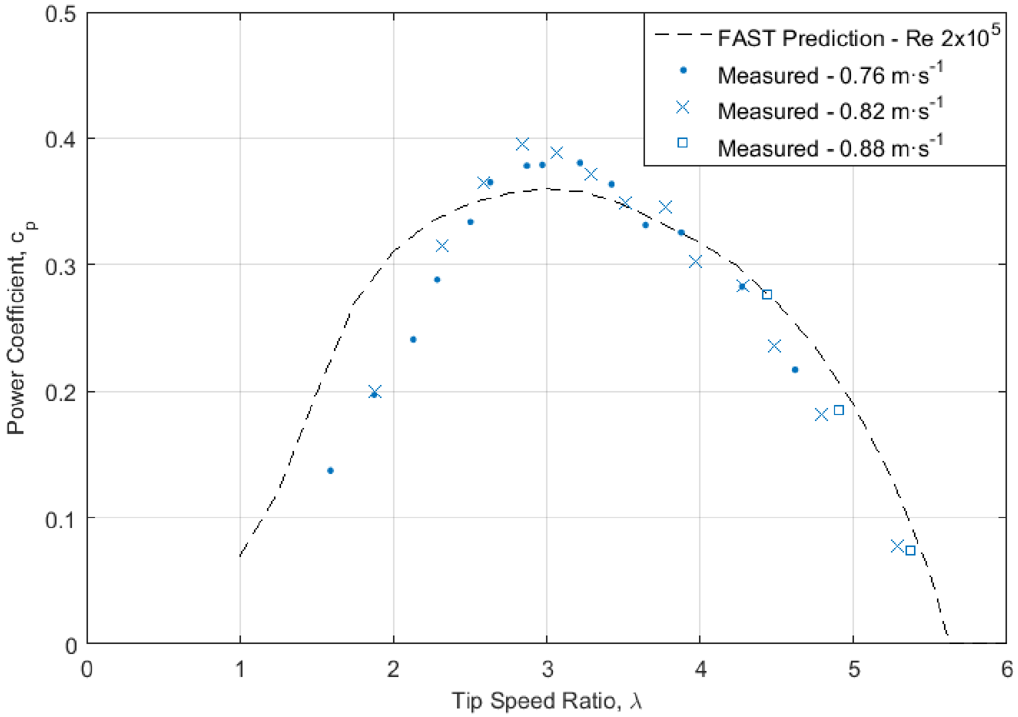

Figure 4.6: *Measured c_p - λ curves compared with numerical predictions from the FAST model*

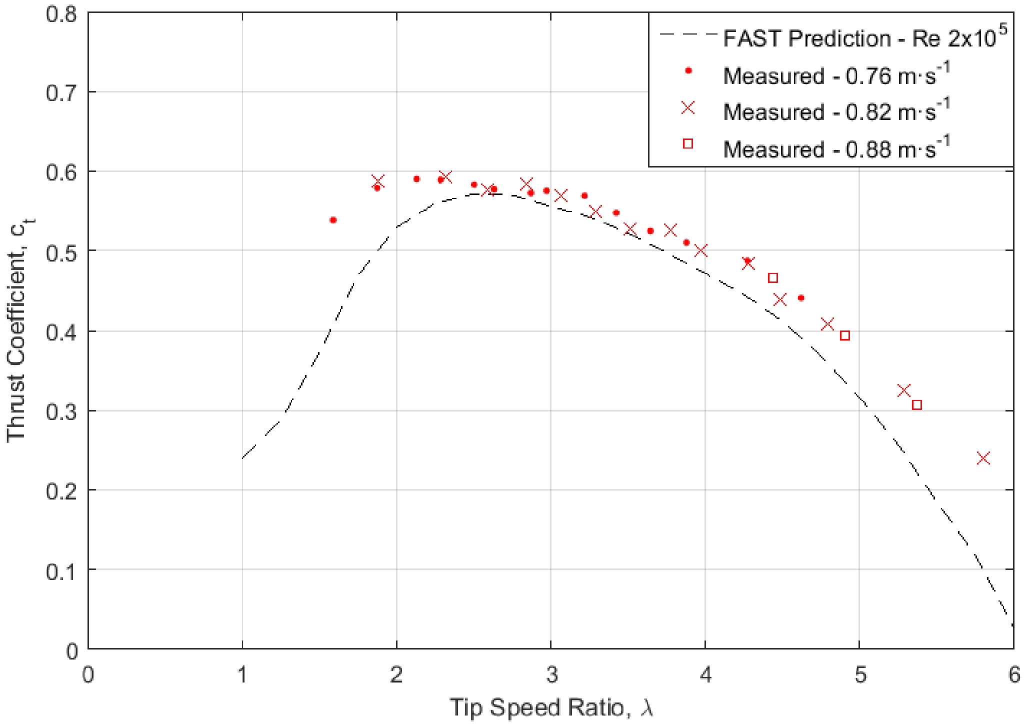

Figure 4.7: *Measured c_t - λ curves compared with numerical predictions from the FAST model*

As seen in Figures 4.6 and 4.7, the results obtained in mean flows of 0.76, 0.82 and 0.88 m·s^{-1} are consistent with each other. The tests performed at 0.88 m·s^{-1} only yielded three usable measurements since the limit on the load cell (10 kg) was breached at low values of λ, meaning that the blockage correction method, which depends on thrust measurements, could not be applied to these results. However, the uncorrected rig measurements of c_p at low λ in this flow speed were found to be consistent with the other flume conditions prior to applying the blockage correction. The results, therefore, can be deemed conclusive for the turbine operating across this range of Reynolds numbers.

The numerical FAST predictions in Figures 4.6 and 4.7 are made with the scale model rotor geometry and the inclusion of aerofoil lift and drag data for the Reynolds number 2 x 10^5, obtained using the XFOIL solver and extrapolation methods within the QBlade environment [199]. This was the lowest Reynolds number at which a stable solution on the aerofoil properties could be found, but it does fall within the range at which the turbine operated at. This is shown in Table 4.1, where Reynolds number is calculated using Equation 2.1 with a dynamic viscosity of water equal to 1.1 x 10^{-3} N·m^{-2}·s^{1}. Also, the chord length and relative velocity values at 70% of the rotor radius were used in this calculation, as per the International Towing Tank Conference (ITTC) recommendations on the evaluation of model propellers [200].

Table 4.1: *Model turbine operational Reynolds number range*

	Min.	**Max.**
Flow [m·s^{-1}]	0.76	0.88
λ	1.6	5.8
Reynolds No.	0.7 x 10^5	2.3 x 10^5

The measured c_p - λ curves (Figure 4.6) show a reasonable agreement with the numerical predictions, with both showing that $c_{p_{max}}$ occurs at λ = 3. Generally the numerical predictions are greater than those that have been measured, possibly as a consequence of the efficiency of the servomotor. Specification data from the manufacturer state that the motor output power has an efficiency of > 95% [195], which could account for some of the small differences between experimental and theoretical results observed at λ > 4. However, the motor efficiency alone cannot account for the larger differences seen in the stall region at λ < 2. As mentioned in Chapter 3, the confidence in BEM based predictions is lower in stall operation due to greater uncertainty in the aerofoil lift and drag characteristics at these angles of attack. The experimental and numerical comparison of c_p – λ curves in Figure 3.2 also showed the lowest agreement in the stall region.

For the same reason, the confidence in the numerical c_t - λ curve (Figure 4.7) is also low at $\lambda < 2$, and the measured behaviour is visibly different in this region. Elsewhere the measurements trend well with the numerical predictions, demonstrating the thrust shedding characteristics of the rotor at high λ. The agreement is particularly good in the λ range 2.5 – 4. Measured thrust is, however, consistently greater than that predicted, especially at the higher λ range. This could be due to uncertainties associated with the geometrical accuracy of the rotor and/or the blockage correction method. Both of these are discussed further in Section 4.5. Additionally, there are a number of factors that contribute to the uncertainty of the thrust measurement itself. Firstly, the load cell was calibrated by suspending a bucket containing measured volumes of water from it and recording the corresponding force, taking into account the weight of the bucket. The human error associated with these volume measurements is less than 5%. Secondly, the lever arm positions used to convert load cell forces to rotor equivalents (Figure 4.3) have measurement errors within ± 0.01 m. Lastly, the structural drag correction (Equation 4.3) was dependent on the flow velocity measurement. A data sheet from Nortek states that the ADV has an accuracy of ± 1% of the measured value [201]. After considering all of these sources of error associated with the thrust measurement, its resulting error would propagate to in excess of 6%.

Since c_p, c_t and λ are all functions of flow velocity, their respective errors are all affected by the accuracy of the ADV. The ADV contribution to the net error is the largest for c_p as a consequence of its cubic dependence on flow velocity (Equation 3.2). It is difficult, however, to determine these errors without any knowledge of the accuracy of the blockage correction method used to derive the non-dimensional parameters.

4.3 Control Strategy Implementation

The servomotor could also be controlled within the LabVIEW environment using the ActiveX framework [202], enabling much more flexibility over the control of the drive than the time-based speed (or torque) commands available within its accompanying software. This option was pursued to provide a physical demonstration of the overspeed control strategy at model scale. The developed LabVIEW program was written to continuously measure the motor speed, ω, in order to calculate and apply the correct amount of opposing torque, τ_{dem}, from the servomotor, resulting in the rotor tracking λ_{opt} or overspeeding if the predefined rated speed, ω_{rated}, was exceeded. The overspeed criteria ensures that motor torque and speed are balanced such that a constant rated power, P_{rated}, is produced in this region. The LabVIEW controller logic is based on Equations 3.7 and 3.9 from Section 3.3 and is shown in block diagram form in Figure 4.8.

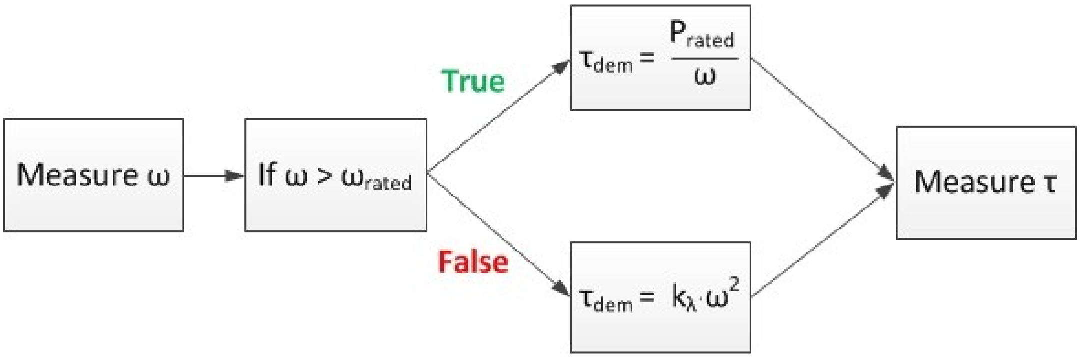

Figure 4.8: *Controller logic defined in LabVIEW for the model turbine*

The controller gain, k_λ, was calculated from Equation 3.8 with the laboratory parameters, i.e. $\rho = 1000$ kg·m^{-3}, $R = 0.2$ m, and $G = 1$ since the model does not have a gearbox. From the measured $c_p - \lambda$ curve (Figure 4.6), a $c_{p_{max}}$ of 0.375 occurs at $\lambda_{opt} = 3$. Thus a k_λ of 7 x 10^{-3} N·m·rad^{-2}·s^{2} was derived.

The turbine would aim to reach the rated point in flows of 0.8 m·s^{-1}, chosen such that a sufficient amount of data could be obtained to assess its performance in both control regions. Additionally, there was a possibility of the load cell limit being exceeded if the rated point was much higher than this, as found in Section 4.2. This meant that rated values of 12 rad·s^{-1} and 11.6 W were defined for ω_{rated} and P_{rated} respectively in the controller logic (Figure 4.8), corresponding to a peak τ_{dem} of 0.97 N·m.

Unlike the tests in the previous section, the turbine was subject to a time varying flow in order to evaluate its dynamic performance. Starting with a still tank, this was achieved by steadily increasing the pump power dial until flows of approximately 1.2 m·s^{-1} were reached, after which they were slowly returned to the still conditions. This would take the turbine through a cycle that is broadly similar to the generating patterns experienced at a tidal energy site. Since a varying flow condition was used, it was crucial to synchronise the ADV measurements with the turbine rig to perform the dynamic assessment. This was achieved by controlling the ADV in the developed LabVIEW program using the PdCommX ActiveX control function interface [203]. The LabVIEW program recorded the rig and flow measurements at 10 Hz, saving the data as text files with the PC time reference.

The load cell, however, was operated from a separate PC and required a different synchronisation method. Similar to Section 4.2, a trigger based method was used to achieve this. This time a LED was positioned above the monitor of the LabVIEW program, which was configured to clearly display its PC time, i.e. the time reference for the rig and ADV measurements. Whenever the LED was triggered to flash, it created a mark on the load cell's secondary channel. These events were filmed with both the flash and PC time in view, allowing the synchronisation to take place upon analysis of the recordings.

Figure 4.9 shows the real-time data monitoring for these tests, with the operating turbine visible in the background. The graphs and dials on the LabVIEW monitor display measurements coming from the ADV and turbine. The PC time is visible in the top left corner of this monitor, with the LED taped just above it. The laptop to the left of the monitor was used to acquire the load cell measurements.

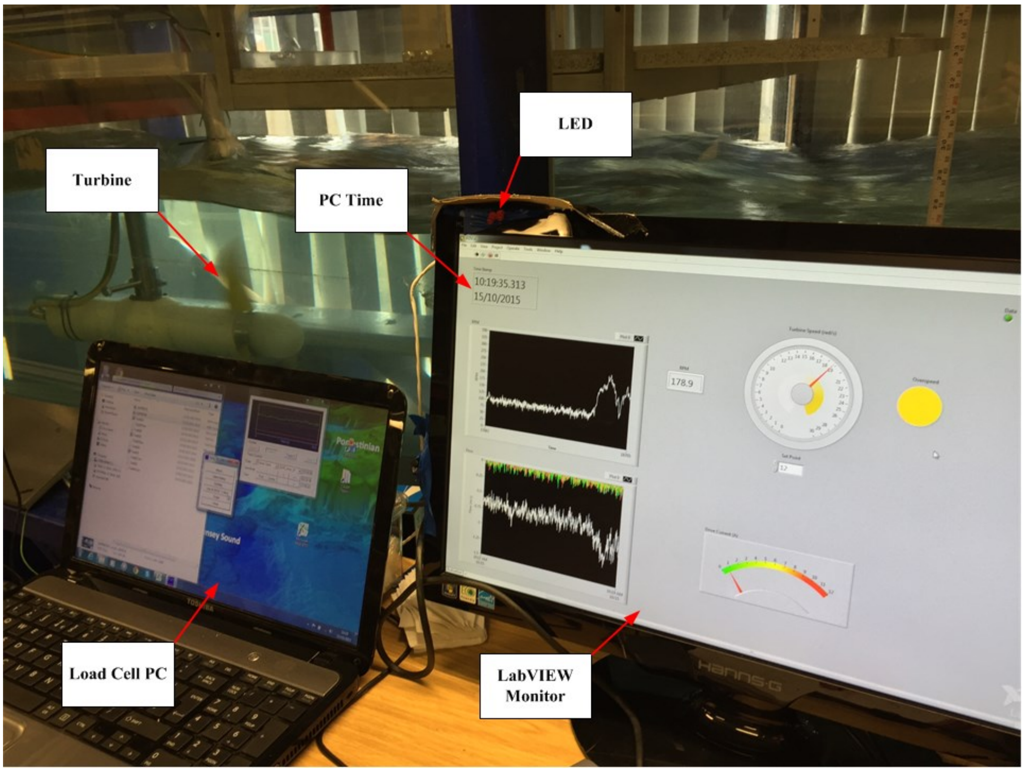

Figure 4.9: *Real-time data monitoring arrangement for the dynamic tests*

4.4 Results

The turbine controller performance was firstly assessed on its ability to follow the idealised torque-speed curve, defined by the logic in Figure 4.8. The results are shown in Figure 4.10. It is clear that the turbine follows the control strategy well, as can be seen by the narrow amount of measured scatter about the idealised line. The transition from λ_{opt} tracking to overspeed at 12 rad·s^{-1} also does not appear to cause any instabilities in the controller performance, with a maximum measured torque occurring at 1 N·m. In the overspeed region the scatter shows a degree of broadening about the idealised line, but this should be expected given that the turbine by this point is operating at high speed in the strongest flows while its torque is decreasing.

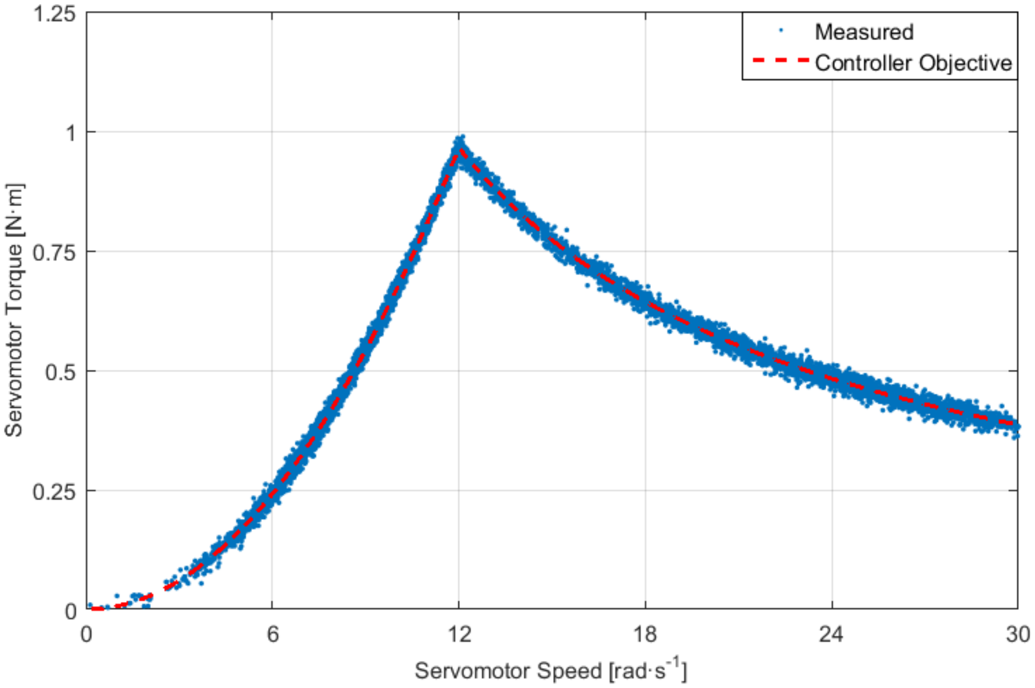

Figure 4.10: *Measured servomotor torque as a function of speed (blue) compared with the idealised controller objective (red)*

The time-series results from one of the controller tests are shown in Figure 4.11, both the instantaneous 10 Hz data and 10 second moving average values. However, only the latter is presented for rotor thrust (Hub F_x) due to the difficulty in using instantaneous flow measurements for the support structure drag calibration (Equation 4.3 and Figure 4.5). The instantaneous flow features considerable variation and would lead to the prediction of erratic support structure drag. The moving mean values are much more reliable for the calibration. Using the same method in Section 4.2, the mean thrust measurements were corrected for blockage effects to obtain the free stream rotor values, but the measured servomotor variables were not. This decision was made in order to assess these aspects of the turbine from an electrical perspective, since the controller logic was written to regulate the power from the servomotor rather than the rotor.

Due to the resistance provided by the servomotor, the turbine did not start rotating until the flow reached near 0.5 m·s^{-1}. As a result, the first 300 seconds of this test are not shown in Figure 4.11 while the flow speed built up from a still tank. Between 300 and 480 seconds, the flow (top plot) is seen to steadily increase to 0.8 m·s^{-1}. During this time the turbine tracks $\lambda_{opt} = 3$ well, as shown on the second plot. Servomotor torque (third plot), power (fourth plot) and rotor thrust (bottom plot) all increase with flow speed in this time period, with the latter approximately doubling from 10 to 20 N.

Peak torque is then reached at 480 seconds and the turbine can be seen to move to a λ greater than λ_{opt}, entering overspeed. As the flow increases further, so too does λ and the torque begins to decrease, balanced such that power is capped at 11.6 W. Thrust continues to increase when the rotor overspeeds, but the rate at which it does so has reduced significantly. By 700 seconds, the thrust peaks at 24 N in flows of 1.1 m·s^{-1}, just a 4 N increase from the value measured at 0.8 m·s^{-1}. During this maximum flow, λ is as high as 5.3 and torque is down to 0.5 N·m. When the flow is decreased from 1.1 m·s^{-1}, the torque steadily increases again until it reaches the peak value for a second time at 900 seconds. At this point the flow has reduced back to the rated value of 0.8 m.s^{-1}. This also marks the point at which the turbine is no longer producing its rated power.

The last 200 seconds of this test sees the flow continue to decrease, along with both torque and power. The turbine has reverted back to tracking λ_{opt} during this period. Finally, it stops rotating once the flow drops to 0.4 m·s^{-1}.

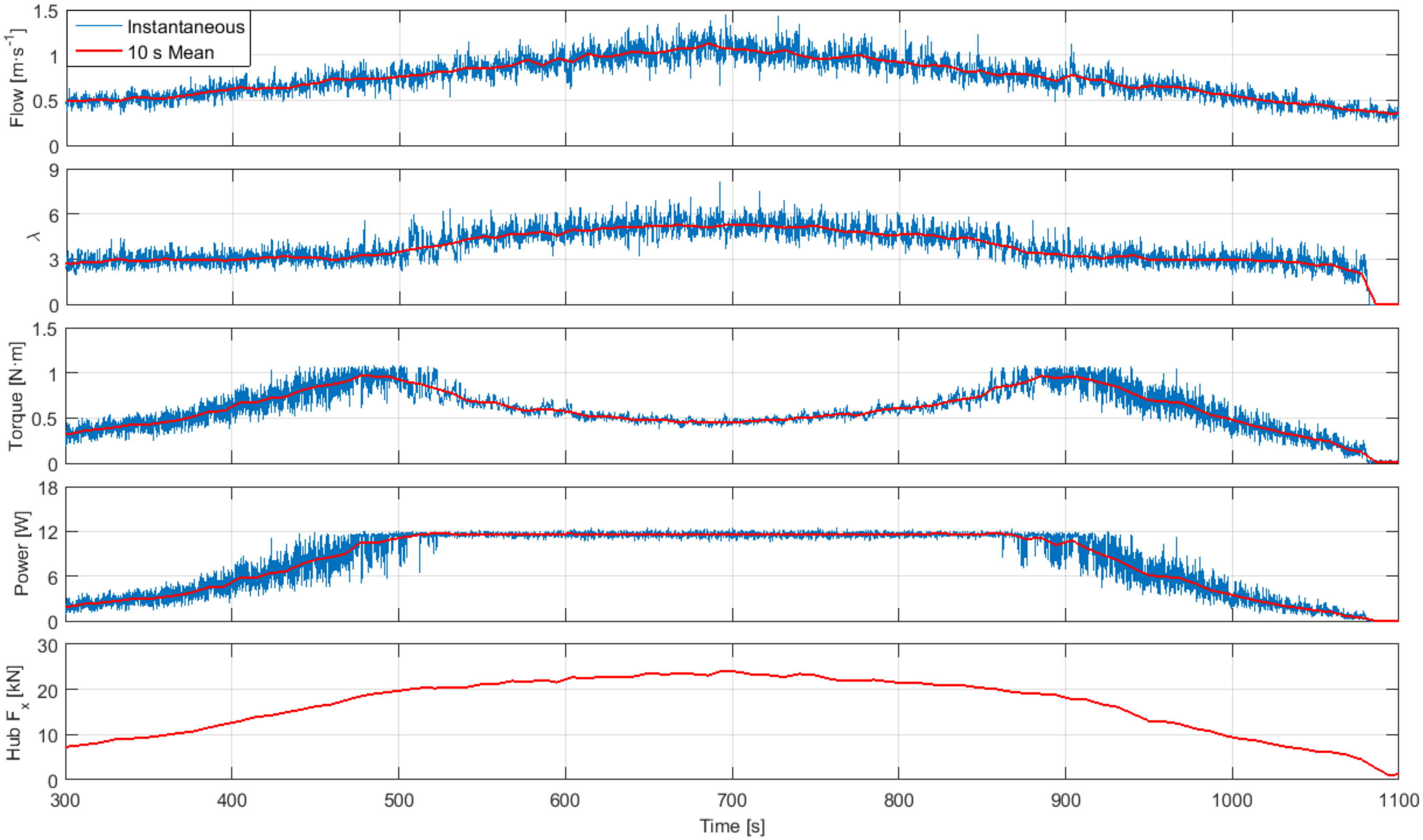

Figure 4.11: *Time-series of the test data. From top to bottom: flow velocity; tip speed ratio; torque; power; and rotor thrust*

A further two tests similar to that in Figure 4.11 were performed. The 10 second average values from all of these tests have been used to create dynamic plots of the servomotor power, speed and rotor thrust with respect to flow velocity, as shown in Figure 4.12. The power plot includes a steady-state curve made by rearranging using Equation 3.2 with the peak rotor c_p of 0.375 from Figure 4.6, and is capped at 11.6 W. In general the dynamic results scatter closely about this line, indicating that the turbine performed well in both the λ_{opt} tracking region and in overspeed. Arguably in the below rated region the majority of the scatter is slightly above the steady curve, although this should be expected since the peak c_p without a blockage correction is greater than 0.375. In contrast to this, the majority of the scatter lies below the steady-state curve in flows of less than 0.5 $m \cdot s^{-1}$. At these low flows this could be a consequence of operating at low Reynolds numbers. In addition to this, this flow region corresponds to the start-up conditions in which the turbine begins rotating. It is believed that the turbine just had enough energy to rotate in this region, but not enough to consistently track λ_{opt}, resulting in a lower power capture efficiency. This is confirmed by studying the same region on the servomotor speed curve, where it can be seen that the turbine operated below the line of λ_{opt} during these flows. Elsewhere the servomotor speed scatters closely about this line, before the overspeed behaviour in the higher flows takes the turbine to in excess of double its rated 12 $rad \cdot s^{-1}$.

The blockage corrected thrust data in Figure 4.12 are compared against a steady-state curve made using Equation 3.3 with a rotor c_t of 0.56, as predicted in Figure 4.7 at $\lambda_{opt} = 3$. The measurements closely scatter about the steady-state curve up until the rated point, as expected from the successful λ_{opt} tracking shown on the servomotor speed plot. Above the rated point, the measurements are prevented from following the steady-state curve due to the overspeed activity. Instead, the rate at which thrust increases with flow reduces significantly. For example, a maximum thrust of 24 N was measured in flows of 1.1 $m \cdot s^{-1}$, whereas the steady-state curve, which varies with the square of flow velocity, would predict a value just under 43 N. Therefore, this physical demonstration of the control strategy has shown good power production and effective management of structural loading in all flows, both of which are desirable characteristics for any tidal turbine. However, unlike the numerical results presented in Section 3.3, the control strategy has not prevented the mean rotor thrust loads from increasing entirely in the overspeed region. Possible explanations for this are given in the Section 4.5.

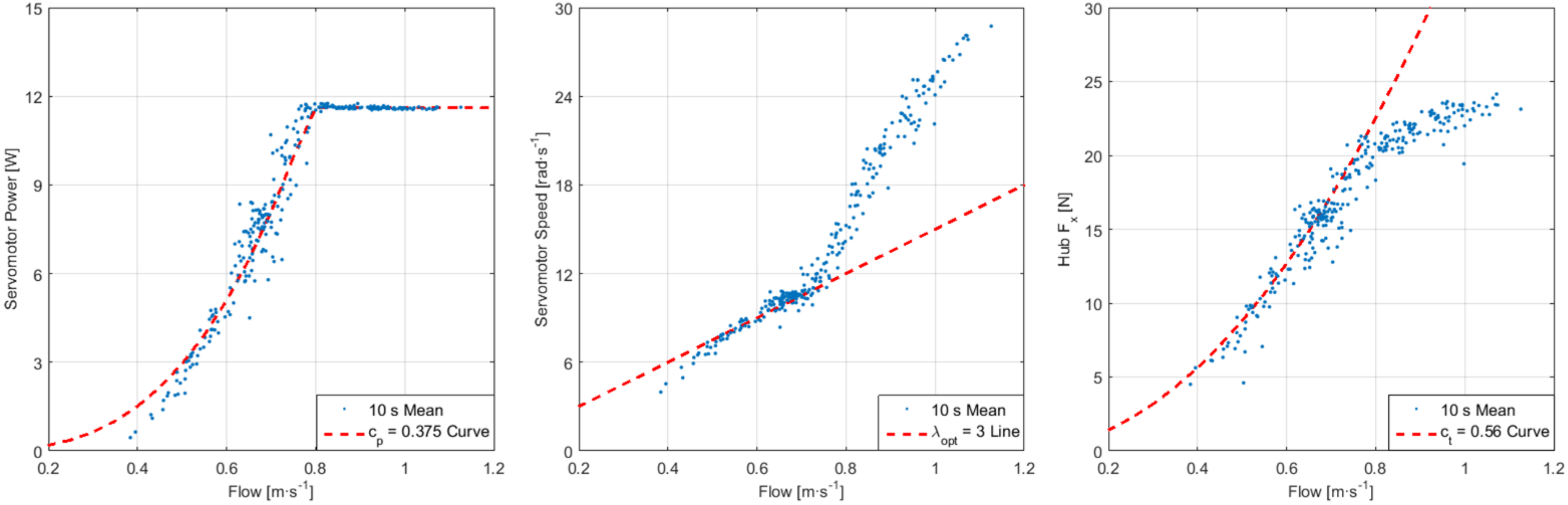

Figure 4.12: *Dynamic plots of servomotor power (left), speed (middle) and rotor thrust (right)*

Two variations were made to k_λ to assess its influence on turbine performance. k_λ was both decreased and increased from the previously derived optimal value of 7 x 10^{-3} N·m·rad^{-2}·s^{2}, resulting in the turbine rotating faster and slower below the rated point respectively. To compare these variations with the optimal control strategy, the same P_{rated} of 11.6 W was maintained. This means that each control strategy has identical overspeed behaviour. The servomotor torque-speed curves for these alternative control strategies are shown in Figure 4.13, compared with the optimal strategy. It can be seen that peak torque has reduced to approximately 0.75 N·m and occurs at 16 rad·s^{-1} on the reduced gain strategy (k_λ = 3 x 10^{-3} N·m·rad^{-2}·s^{2}), while it has increased to 1.2 N·m and occurs at 10 rad·s^{-1} on the increased gain variation (k_λ = 11 x 10^{-3} N·m·rad^{-2}·s^{2}).

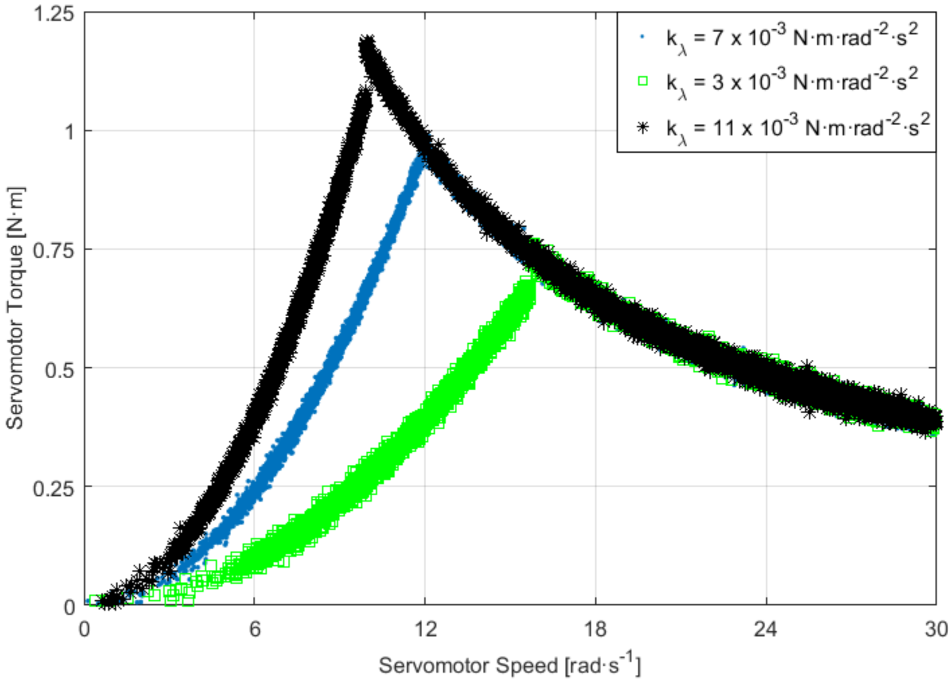

Figure 4.13: *Servomotor torque-speed curves measured by reducing (green) and increasing (black) the controller gain from the default control strategy (blue)*

The dynamic servomotor power, speed and rotor thrust curves for each k_λ variation are displayed in Figure 4.14, again compared relative to the default control strategy. Due to the fact that both of these controller variations have moved the operational point away from λ_{opt}, it is not surprising to see that the turbine underperforms from a power perspective, with the majority of the scatter falling below that of the optimal control strategy and the c_p = 0.375 steady-state curve. The servomotor speed curves clearly show that the controller variations have moved the λ away from the the λ_{opt} = 3 line, with the increased and reduced gain strategies operating nearer λ = 2 and 4 respectively. The reduction in power capture is most pronounced when using the increased gain strategy, particularly at the lowest flows. This result should be expected given the asymmetric $c_p - \lambda$ curve of the rotor displayed in

Figure 4.6, in which a measured c_p of 0.3 was observed at $\lambda = 4$, compared with 0.22 at $\lambda = 2$. Interestingly, the results suggest that the reduced gain strategy begins rotating, and hence producing power, in flows lower than the optimal strategy, despite obtaining fewer measurements from these tests. In contrast to this, the turbine does not start rotating until higher flows in the increased gain strategy. Thus there are benefits, albeit small, from reducing the demanded torque gain during turbine start-up.

In terms of rotor thrust, reducing the controller gain has decreased the axial loading on the rotor, with most of the measurements found to be lower than optimal strategy's $c_t = 0.56$ steady-state curve. This is expected given that the measured c_t was shown to be near 0.5 at $\lambda = 4$ in Figure 4.7. The effect that increasing the controller gain has on thrust is less clear, with the results appearing to be similar to those obtained with the optimal control strategy. Figure 4.7 suggested a slight increase in c_t to 0.58 at $\lambda = 2$, but not enough measurements have been obtained to prove that this has contributed to greater dynamic thrust loading when the controller gain was increased.

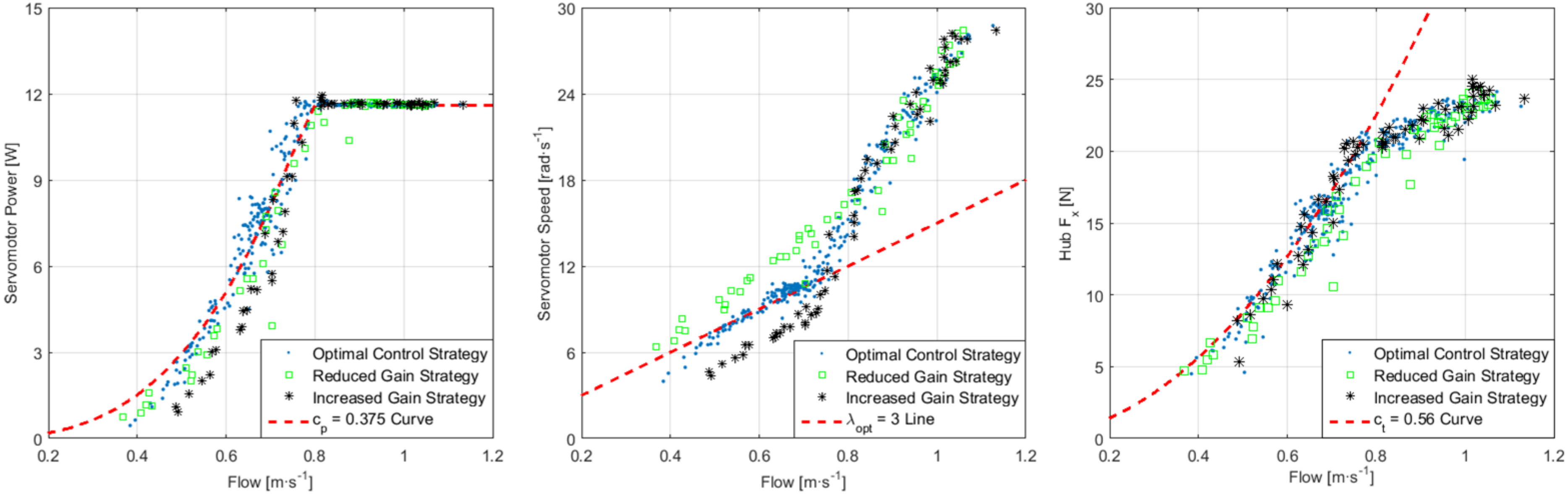

***Figure 4.14:** Dynamic plots of servomotor power (left), speed (middle) and rotor thrust (right) compared for all controller gain variations*

4.5 Reviewing the Test Campaign

The test arrangement described in Section 4.1 was successful in demonstrating the DeltaStream^{TM} turbine's concept of operation at 1:30 scale, achieving the primary objective of this chapter. The developed LabVIEW program was key to this success, enabling the required level of flexibility in the control of the servomotor to test the model turbine under dynamic conditions. By also integrating the ADV system into the LabVIEW program, full data synchronisation of the servomotor and flow measurements was achieved, removing any uncertainty over this issue and simplifying the analysis of test results. This arrangement also enabled the servomotor and laboratory parameters to be monitored in real-time during tests, providing the operators with the key information relating to any faults or operational limits they should be aware of. There are, in fact, a number of parallels between this test arrangement and that of the full-scale turbine (Chapter 6), albeit at a considerably smaller scale.

If the test arrangement was to be used again for future research, there are areas in which it could be improved upon to increase the quality of results. A key weakness of this test campaign was the measurement and synchronisation of rotor thrust. While the latter was achieved manually upon the analysis of trigger events in the load cell data, it was a laborious process. Integration of the thrust measurements to the LabVIEW program would be a clear improvement to the test arrangement. In terms of the measurement itself, positioning the load cell on the support structure meant that direct measurements of thrust were not possible, with it instead inferred using the calibrations and conversions outlined in Section 4.2. This could be improved upon by placing a sensor on the turbine itself. For example, other scale model test campaigns have used dynamometers [114], [58] or strain gauges in the blade roots [113] to measure thrust.

The thrust results were further complicated by the 16% blockage ratio in the laboratory, as were measurements of rotor power and λ. Even though a prevalent blockage correction method [114] was used to derive the free stream equivalent values, the accuracy and validity of this technique is unknown. The method has only been used to compare corrected results obtained under differing blockage ratios [114], or with numerical predictions of a free stream rotor [61]. To the author's knowledge, blockage corrected measurements from a model turbine have never been compared with results of the same device operating in free stream conditions. Future test campaigns should strive to minimise these effects by operating in a tank with a larger cross-sectional area, reducing the blockage ratio. The research in [113] decided that a correction to results was not necessary since the blockage ratio was less than 5%.

Similarly, the degree to which Reynolds number effects have had on results is uncertain. Results were compared against numerical predictions made at a Reynolds number of 2×10^5. Table 4.1, however, showed that there were conditions in which the model operated below a Reynolds number of 1×10^5. In contrast to this, the 12 m diameter commercial turbine will consistently operate at Reynolds numbers exceeding 1 x 10^6. The results in Figures 4.6 and 4.7 did not appear to show any variation with flow velocity, and hence Reynolds number, but this could be due to the narrow range (0.76 – 0.88 $m \cdot s^{-1}$) in which the tests were performed. Research in [121] found that Reynolds number effects above a value of 2.4 x 10^5 had a minimal effect on results, while in [125] CFD was used to show that Reynolds number insensitivity occurs at a value of 5 x 10^5, although it was stated that 3 x 10^5 could be taken as the critical value. It would be preferable in future test campaigns to test at a larger scale in order to reduce the uncertainty around Reynolds number effects. A 1 m diameter rotor (1:12 scale), for example, would operate at the aforementioned critical Reynolds number in flows of 0.8 $m \cdot s^{-1}$ and at a $\lambda = 3$, whereas the 1:30 scale tested rotor operated at 1.2 x 10^5 under the same conditions. This would also reduce the difficulty in forming comparisons with numerical predictions at low Reynolds numbers. While it was possible to obtain stable NACA0015 lift and drag data at a Reynolds number of 2 x 10^5 in this chapter, this may not be possible for other aerofoils.

The measured non-dimensional rotor curves in Figures 4.6 and 4.7, in general, agreed well with the BEM predicted behaviour, both in terms of the magnitude and shape of the curves. Disagreement at low λ was accounted for by the reduced accuracy of the BEM method in this region, whereas at high λ the theory is more reliable. However, above $\lambda = 4$ the measured c_t showed a decreasing agreement with the BEM prediction, with the measured values found to be consistently higher. The accuracy of any of the previously mentioned methods used to derive the rotor thrust could be accountable for these differences. It is also entirely possible that any minor geometrical differences between the modelled and built turbine will have influenced results. The printed accuracy of the blades at model scale is unknown, and any discrepancies associated with this would dramatically change the performance characteristics of the rotor. Similarly, any blade flexing or incorrectly set pitch angles would have an effect on performance, despite the best efforts made to prevent the latter.

When the model turbine was configured to follow a control strategy similar to the commercial device, it successfully operated close to the idealised controller objectives (Figure 4.10) at all ranges under dynamic conditions. This highlighted the simplicity of the control system, requiring only turbine speed as an input. By calculating an appropriate gain parameter for the controller, the results in the time-series (Figure 4.11) showed how torque and speed were balanced to ensure that the turbine extracts the maximum amount of power in all flows, leading to the development of a dynamic power curve (Figure 4.12) that scattered closely about the theoretical prediction. These dynamic results also showed that rotor thrust was prevented from becoming excessive in the highest flows, although the mean loads did continue to increase despite the turbine overspeeding, unlike the numerical predictions in Section 3.3. This observed difference is a consequence of the disagreement of measured and modelled $c_t - \lambda$ curves at high λ. To prove this, a curve has been fitted to the blockage corrected λ data in the overspeed region (flows > 0.8 $m \cdot s^{-1}$), as shown by the dashed magenta line on the left plot in Figure 4.15. The plot on the right shows the region that this corresponds to on the measured (magenta) and modelled (green) $c_t - \lambda$ curves. The former is a part of a curve that was fitted to all of the measured data, represented by the dashed blue line.

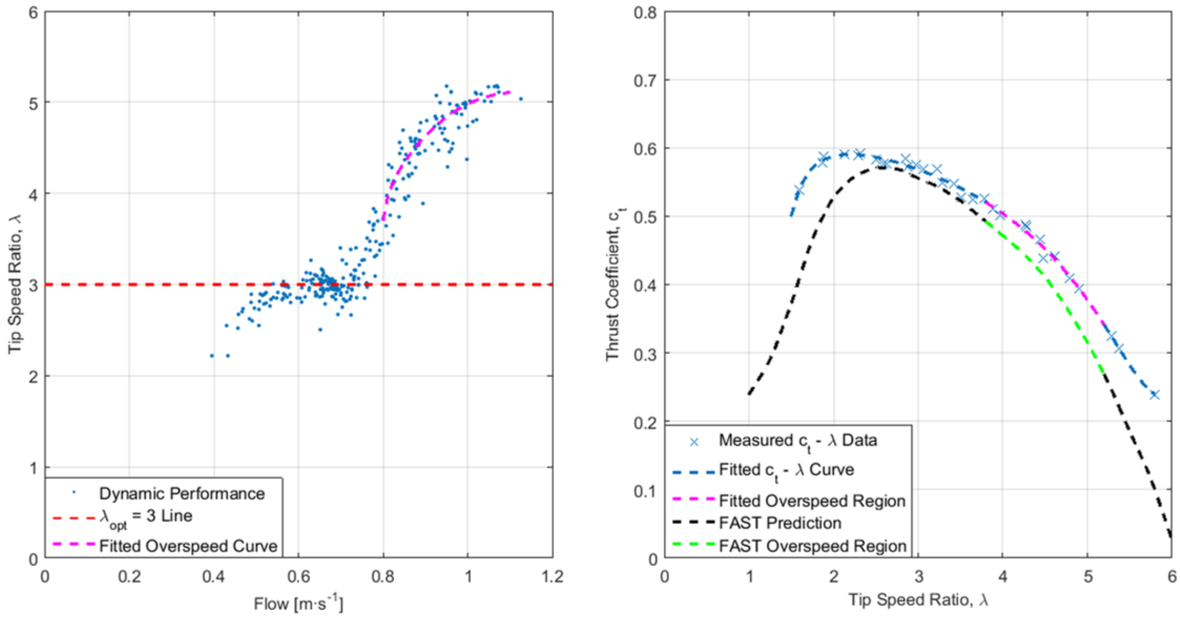

Figure 4.15: *Curve fit applied to overspeed data (left) and the corresponding region on the measured (magenta) and modelled (green) c_t - λ curves (right)*

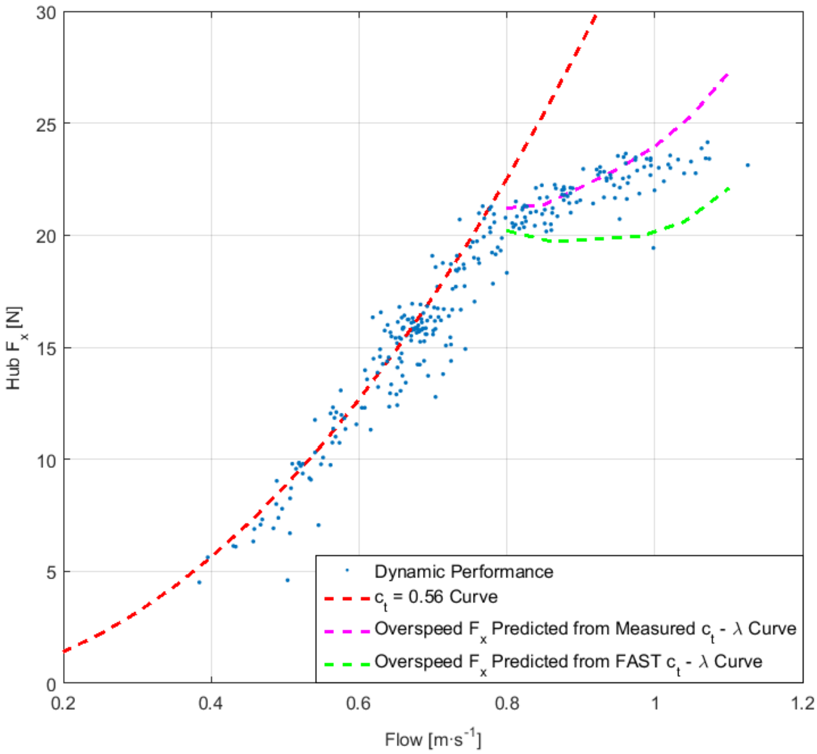

Figure 4.16: *The predicted overspeed behaviour using the measured (magenta) and modelled (green) c_t - λ curves*

By using the highlighted overspeed regions in Figure 4.15, it is possible to predict the above rated rotor thrust, as shown in Figure 4.16. The curve fit on the measured $c_t - \lambda$ data predicts thrust behaviour that agrees well with that observed during the dynamic tests, as would be expected. This curve, therefore, only predicts a change in the rate at which thrust increases with flow velocity, and does not suggest that the mean loads will decrease. The modelled $c_t - \lambda$ curve, however, does predict that mean thrust will not increase from the rated value between 0.8 – 1.0 $m \cdot s^{-1}$, remaining fairly constant at 20 N. Thereafter the thrust does begin to increase, but by this point the flow is in excess of 25% of the rated 0.8 $m \cdot s^{-1}$. For comparison, this would correspond to mean flows of 3.4 $m \cdot s^{-1}$ for the commercial turbine (rated at 2.7 $m \cdot s^{-1}$), a condition which is not experienced at the device location in Ramsey Sound. In addition, due to efficiencies associated with the drivetrain components, the commercial turbine will overspeed to a higher λ than the scale model, resulting in better thrust regulation. The analysis in Figure 4.16 has, however, highlighted the sensitivity of the overspeed behaviour to the shape of the $c_t - \lambda$ curve, showing that a steep reduction in c_t is required in order to achieve effective thrust regulation in high flows.

The results from modifying the controller gain parameter from its optimal value were used to show that this leads to reduced power performance (Figure 4.14), although fewer drawbacks were found while using the reduced gain control strategy for this rotor geometry. This implies that if there was a desire to operate away from the optimal point, it would be preferable for the gain to be reduced rather than increased. An example of which would be the decision of overspeeding or stalling the rotor. Variable speed stall could be used to regulate the power output of this turbine just as effectively as overspeed, but the rotor thrust would be greater. Given that DeltaStream^{TM} has been designed around a gravity-based foundation, it would require extra ballast weights to prevent seabed movement as a result of the increased loading, incurring financial penalties. Additionally, a full-scale turbine utilising stall control would need to be equipped with a larger gearbox to handle the increased torque required to limit the rotor speed, again adding cost to the system. Therefore, for the tested fixed-pitch rotor geometry, there are a number of clear benefits from adopting an overspeed based control strategy instead of conventional stall regulation.

5. Flow Instrumentation Tests

The previous chapter showed that a point based flow measurement was a sufficient reference of the environmental conditions experienced by the model rotor. This type of instrument, however, would not be used during the testing of the full-scale device, as there was interest in both the upstream and vertical flow profiles in the vicinity of the turbine. The tidal stream environment would instead be characterised using seabed and turbine mounted ADPs. This chapter reports on two separate test campaigns that took place with these instruments prior to their installation with the turbine. The tests were designed to establish the capabilities of each sensor to understand how they can be used to assess the performance of a tidal turbine (see Chapter 6). The chapter concludes with a review of the findings with consideration of the principles of operation of each instrument

5.1 Instruments Tested

The first ADP is a 4-beam, 600 kHz instrument, manufactured by Teledyne RDI and pictured in Figure 5.1. This type of instrument is suitable for seabed or vessel mounted deployments, and is capable of determining flow velocities along a vertical profile by sorting the measurements into range (elevation) bins. The beams are oriented at 20^{o} from vertical in order to compute the 3-D velocity components, using trigonometric relations and the implicit assumption that the flow is uniform across each sampling volume [88]. Depending on the specified vertical resolution, the instrument can profile to a range extent of 38 – 51 m [204]. Since the instrument can also determine flow direction and wave properties, it was selected as the primary environmental sensor to support operations of the full-scale turbine. Additionally, it meets the minimum data collection requirements for a current profiler in the IEC’s power performance technical specification [142]. It is hereafter referred to as the RAMP (remote acoustic monitoring platform) ADCP, for reasons explained in Chapter 6.

Figure 5.1: *Teledyne RDI Workhorse Sentinel ADCP*

While the RAMP ADCP is a versatile instrument capable of measuring a number of parameters of interest, it obtains all of this information from a fixed position when installed in a stationary frame. In order to obtain a detailed characterisation of the approaching flow upstream of the turbine rotor, a secondary ADP would be required. A 1 MHz Nortek Aquadopp® current profiler was selected for this purpose, as shown in Figure 5.2. It will be mounted inside the turbine nosecone to profile the oncoming flow in horizontal bins to a range of 20 m, with full rotation enabled via a slip ring. The instrument was fitted with a bespoke single-beam transducer head with no offset angle, unlike the standard 3-beam configuration advertised by the manufacturer [205]. This would allow the currents to be measured without any requirement to resolve the velocity components, or the need to account for a rotating reference frame. However, only the along beam, i.e. line-of-sight, component of the currents can be measured in this configuration. Information on the net current direction or magnitude is not possible. Additionally, in a horizontal arrangement the instrument can only profile the flow from one height in the water column, equivalent to the rotor centre in the turbine mounted application.

Figure 5.2: *Nortek Aquadopp® Single-Beam Current Profiler*

In addition to the ADPs, a 720 kHz, multi-beam sonar system was used during some of the testing discussed in this chapter. This instrument was acquired for marine mammal identification and tracking purposes, allowing the behaviour of such species to be studied in the vicinity of the turbine. Its capabilities and measurements are not considered in this study, and the instrument was instead used as part of a separate research project run simultaneously.

5.2 Pembroke Dock Sea Trials

In April, 2014, the instruments were tested in the Port of Pembroke Dock, situated in the Cleddau estuary in south-west Wales. The region features an appreciable tidal range that exceeds 7 m, and can leave some areas of the harbour to dry out during periods of low water on spring tides. This property was exploited for the installation and recovery of test equipment on the seabed. Additionally, there are regions in the harbour where the tidal flow is accelerated around obstructions created from piers extending into the estuary. One of these piers was built with arches in its wall, creating a considerable acceleration in flow as it funnels through, particularly on ebb tides. This pier is conveniently located near a storage yard owned by TEL, providing a source of power for test equipment. Thus the site provided a low risk environment in which the instruments could be tested in real sea conditions.

Figure 5.3 shows the layout of the Pembroke Dock test site. The red arrows indicate the directionality of the flow on ebb and flood tides, heading perpendicular to the arches found underneath the narrower pier section. A cabin was positioned on this pier to house all of the PCs used to control and monitor the instruments, with power provided from a 100 m long cable running back to the storage yard. All of the instruments were placed to the west of the pier, downstream of the stronger ebb flows coming through the arches. The single-beam was supported by an 8 m ladder that was mounted off the pier wall and in front of one of the arches. The instrument was oriented to profile the flow both through the archway and to the western side of the pier, by rotating the device 180° during a period of low water. As for the RAMP ADCP and sonar system, these instruments were placed in a gravity frame on the seabed. Their cables were buried and fed along the ladder to shore. The motion sensors in a smartphone were used to ensure that all of the instruments rested level.

The control cabin, gravity frame and ladder are all visible in Figure 5.4, taken during a period of low water. The subsequent flood tide fills this region of the harbour to in excess of 5 m, almost entirely submerging the archway in which the ladder was placed in front of. The gravity frame was positioned within the profiling range of the single-beam, with the 4-beam measured to be 15.5 m away. This would allow simultaneous measurements of the same volume of water from both instruments. The single-beam and RAMP ADCP transducer heads were measured at 2.1 m and 0.6 m above the seabed, as shown in planar form in Figure 5.5.

In Figure 5.6, the test activities at the site are illustrated with respect to the tidal conditions. After preparing the test area, the support frames were firstly left at the site overnight on the 14th of April to ensure that they would not move with the tidal flow. On the 15th, the instruments were installed such that the single-beam profiled above the RAMP ADCP (orientation A), capturing the evening flood and ebb tides, as well as the following morning ebb on the 16th. The single-beam was then rotated to profile the next flood and ebb tides through the archway (orientation B), before all of the instruments were retrieved in the early hours of the 17th.

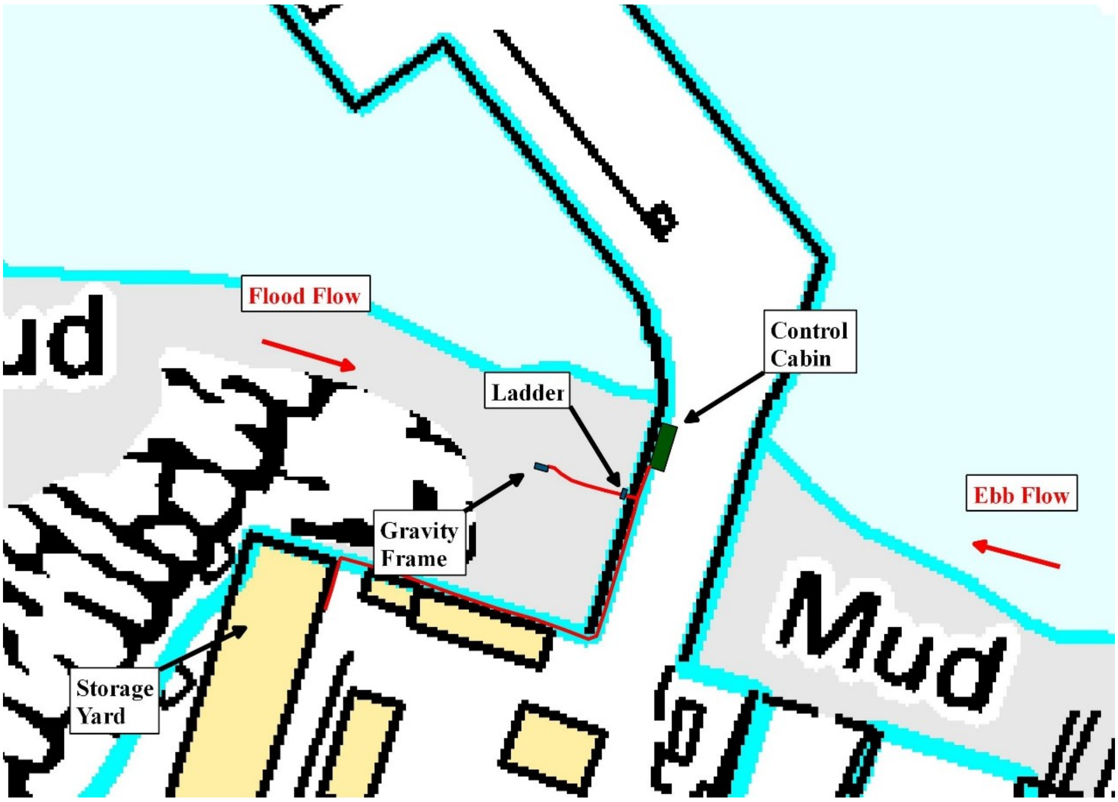

Figure 5.3: *Pembroke Dock test arrangement*

Figure 5.4: *Test arrangement viewed from the seabed*

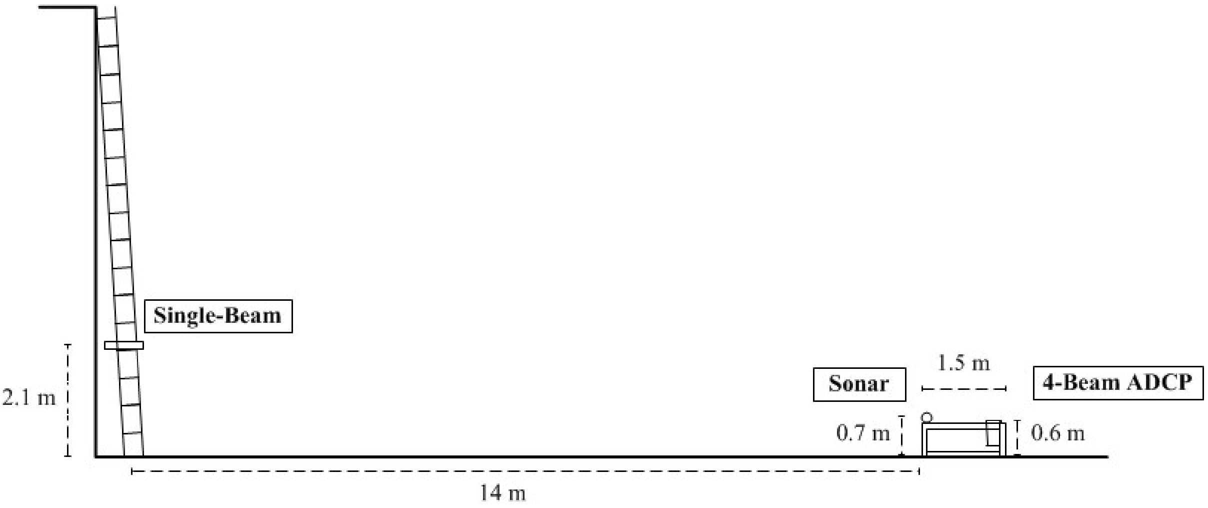

Figure 5.5: *Relevant dimensions for the Pembroke Dock tests*

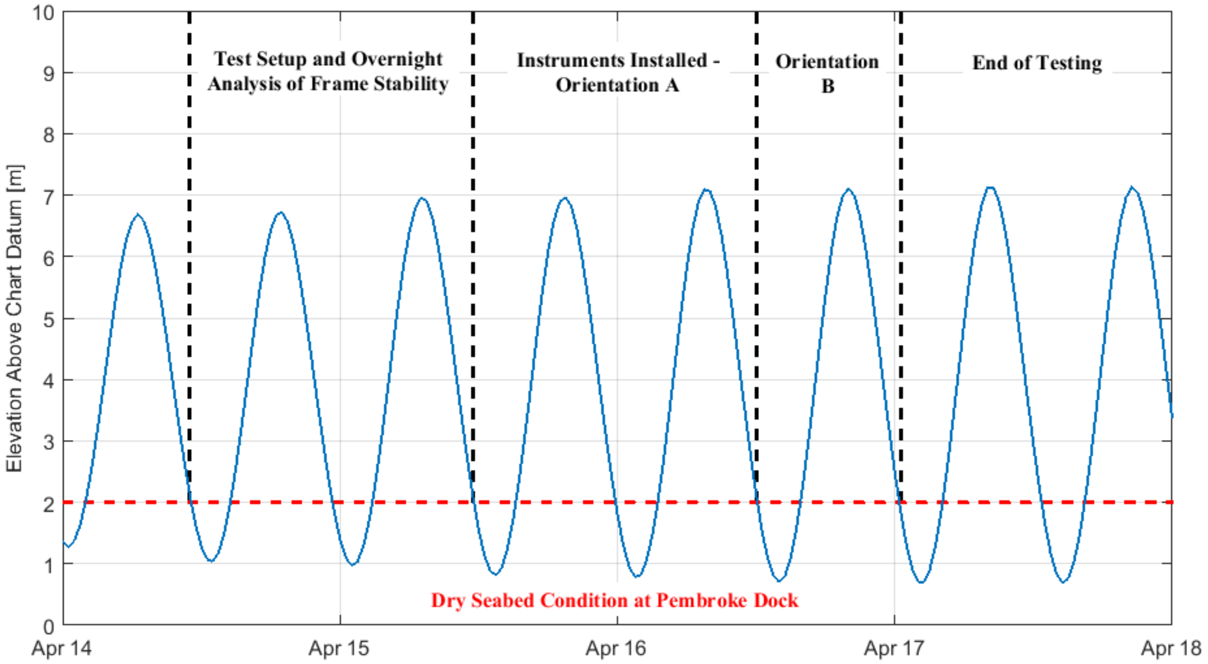

Figure 5.6: *Plot of tidal elevation at the nearby Milford Haven during the week commencing the 14th of April, 2014. The test area dried during periods in which the tidal elevation was less than 2 m (red dashed line). Test setup activities were planned around these periods.*

5.3 Results from the Sea Trials

All of the data presented in this section have been reduced to 10 minute average values, a period in which the flow is not expected to vary significantly from the derived mean value and in agreement with best practices published elsewhere in the tidal stream sector [142], [92]. The RAMP ADCP was configured to profile at a 0.5 m vertical resolution throughout testing, with the first measurement centred at 1.43 m above the instrument, and corresponding to 2.03 m above the seabed. Measurements obtained from this elevation alone are presented here, since it is approximately the same height at which the single-beam samples. Additionally, the measurements obtained above this elevation are limited to fewer recordings due to the rising and falling tidal elevation, and are more susceptible to sea surface data contamination effects. The recommendation of rejecting data obtained from the top 6% of the water column from the manufacturer [88] was followed to account for contamination of the first velocity bin. Both instruments sampled at 1 Hz.

A polar plot of the directionality and magnitude of the RAMP ADCP flow is shown in Figure 5.7. As expected the majority of the ebb flow heads in a 285^{o} direction, perpendicular to the heading of the pier wall (Figure 5.3). The flow reaches in excess of 1 $m \cdot s^{-1}$. There are, however, inconsistencies in the results observed on the first ebb tide, occurring on the evening of the 15th of April. During this tide the majority of the flow was measured to head towards 265^{o}, although the magnitudes are comparable. These measurements are highlighted in red in Figure 5.7. This is believed to be a consequence of the instrument being erroneously configured to operate in a narrowband mode during this period, rather than the broadband setting that was used for the remainder of testing. Broadband processing allows the instrument to use greater bandwidth, and hence access more information to form measurements, significantly reducing the variance [88]. The standard deviations were approximately 4 times larger when operating in the narrowband mode, confirming the influence that this parameter has on measurement uncertainty.

The measurements that are found below 0.5 $m \cdot s^{-1}$ and scatter between 150^{o} – 210^{o} were all obtained during flood periods, showing that this tide is both weaker and less directional. This is not surprising considering that there are no significant flow enhancing features of the harbour in this direction.

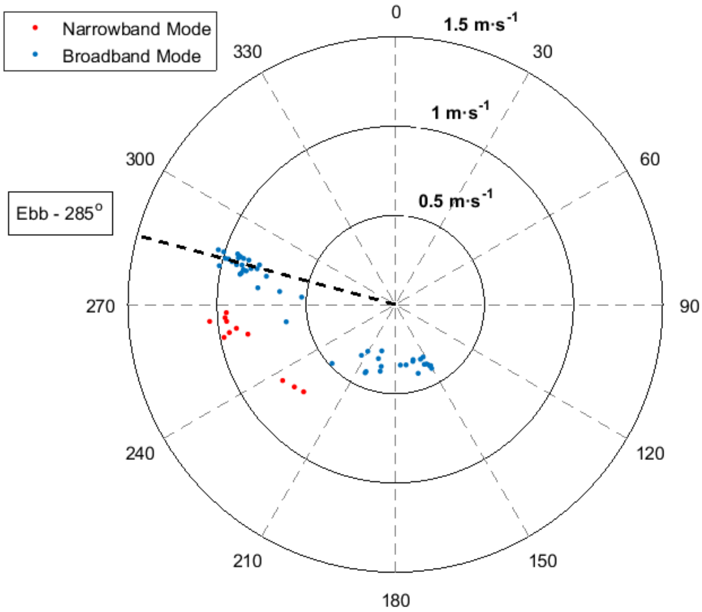

Figure 5.7: *Polar plot of flow measurements obtained from the RAMP ADCP. Data in red were recorded when the instrument was erroneously configured in a narrowband processing mode*

In order to compare the RAMP ADCP flow measurements with those obtained separately from the single-beam, the mean values of the latter were processed over the same time periods and in the range bin that sits above the former (15.5 m range). The spatial resolution of the single-beam was varied between 0.5 – 2 m during testing, meaning that it was not always possible to obtain a measurement centrally located above the RAMP ADCP. Instead, the measurement closest to the 15.5 m range was chosen. For example, 16.4 m was selected when the instrument was configured with a 2 m bin resolution. The volume in which the measurement is made is twice the length of the bin size [87], meaning that in this instance it is 4 m and covers the range 14.4 – 18.4 m.

The correlation between the instruments is shown in Figure 5.8 for both orientations of the single-beam. However, just 30 minutes of data are available for comparison in orientation B, since the RAMP ADCP was non-operational for the majority of the time during this configuration. This was to try and resolve some interference issues that the instrument was creating on the sonar system.

The results from orientation A consistently show that the single-beam measures a lower flow than the RAMP ADCP. This is believed to be mainly due to the difference in quantities measured by each instrument, with the single-beam only capable of measuring the line-of-sight velocity component, whereas the RAMP ADCP determines velocity magnitude. The difference is not thought to be due to velocity shear in the water column that, under certain circumstances, could create a bias as a result of the vertical averaging method used by the RAMP ADCP. Any variation in the flow would be expected to be low over a 0.5 m bin resolution. This was confirmed by evaluating the flow magnitudes in the adjacent bin, i.e. the measurement deduced at 0.5 m above the first bin. These were typically found to be no greater than 5% of the first bin, and in some instances the values were lower.

By comparison, the single-beam measurements are regularly lower by as much as 10 – 15% of the RAMP ADCP. This would correspond to a misalignment with the flow heading in excess of 25° ($\cos 25 = 0.91$). While the true single-beam heading is unknown, it was not believed to be offset by a margin as large as 25° to the ebb flow during testing. Previously it was shown in Figure 5.7 that the ebb flow contains a directional variability much lower than 25° when considering the broadband measurements only. However, this is based on the mean flow direction. The instantaneous variability of the ebb flow is shown as a histogram in Figure 5.9, again considering just the data obtained from the broadband configuration. While the distribution of measured directions is approximately symmetrical about 285°, only 67.5% of the data lie within 25° of this central value, i.e. the range 260° – 310°. Thus there are a considerable number of occurrences where the instantaneous flow has a heading outside 25° of the mean direction, meaning that during these periods the single-beam would measure a lower flow than the RAMP ADCP.

The agreement between the instruments appears to be particularly weak when the RAMP ADCP was configured to use the narrowband setting, but these results should be treated with caution given the aforementioned increased uncertainty of operating the instrument in this mode.

In contrast to orientation A, the single-beam flow is considerably greater than that measured by the RAMP ADCP in orientation B despite the low data return. These measurements were taken from 8 m upstream of the single-beam, near the middle of the archway. It is clear that the arch structure causes a local acceleration of the flow.

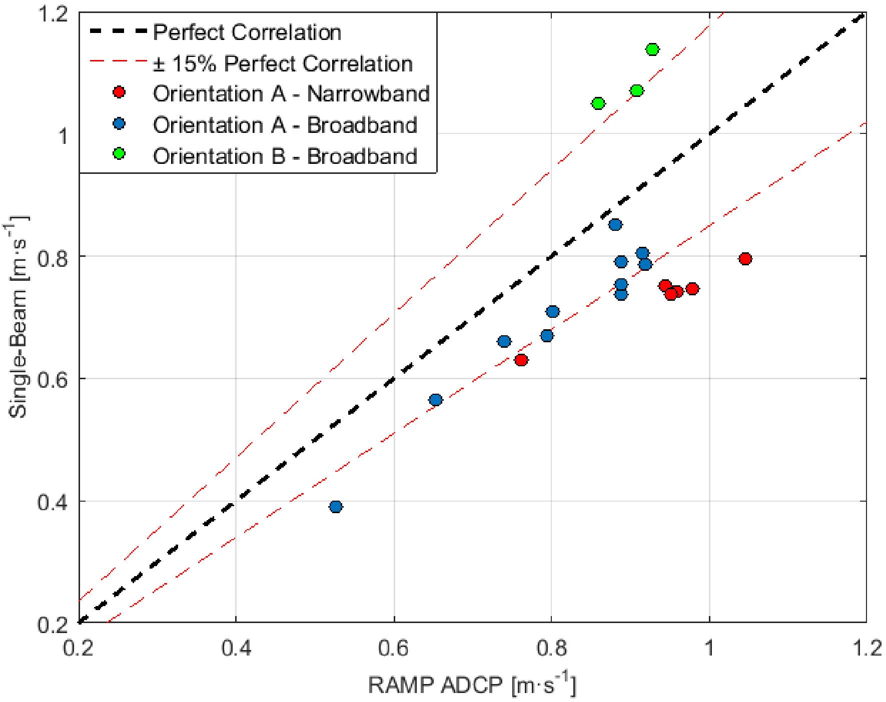

***Figure 5.8:** Comparison of RAMP ADCP and single-beam flow measurements*

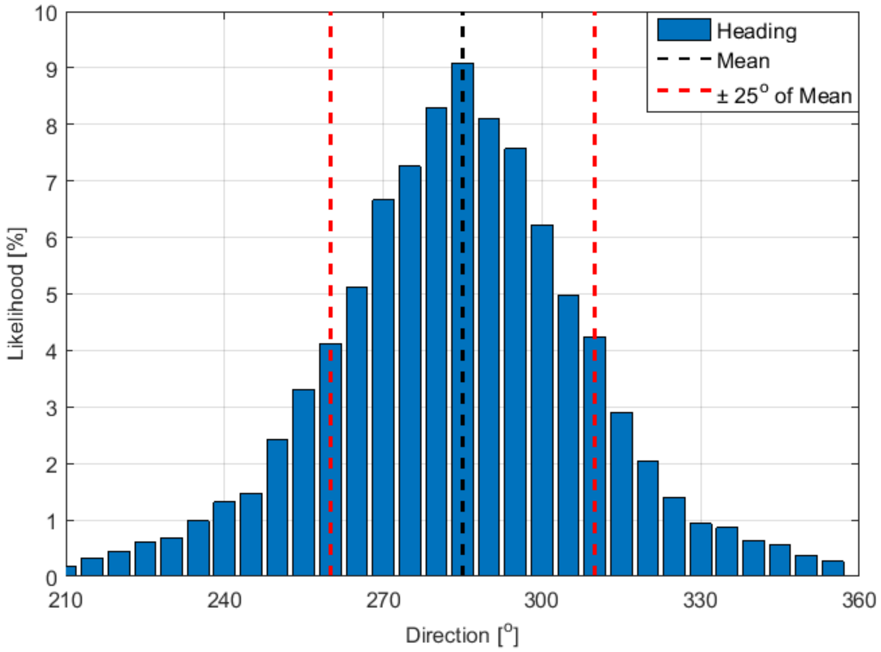

Figure 5.9: *Probability distribution of instantaneous ebb flow heading measurements*

In Figure 5.10, the mean and standard deviation of the flow is profiled along the range of the single-beam while configured in orientation B. These results were derived over four consecutive 10 minute periods, with the bin resolution changing in each. Both statistics are approximately constant in each period out to 10 – 12 m, before the mean values begin to decrease at the range extent where the initial acceleration zone is captured at the archway entrance. This also creates more variation in the flow, as seen by the rising standard deviation. The mean flow increases with decreasing bin size purely as a consequence of temporal variations in the current strength. The standard deviation, however, should not be affected in the same way. It is observed that this paramater increases with decreasing bin size, especially when reduced to a 0.5 m resolution. This is not a surprising outcome given that a reduction of the instrument resolution decreases the number of measurements that are available spatially to form the derived average value within each bin, but the erratic flow profile observed at 12 – 17 m from the 0.5 m test suggest this resolution will also lead to increased uncertainty on the absolute value of results. There does not appear to be as large a penalty from reducing the bin resolution from 2 to 1 m.

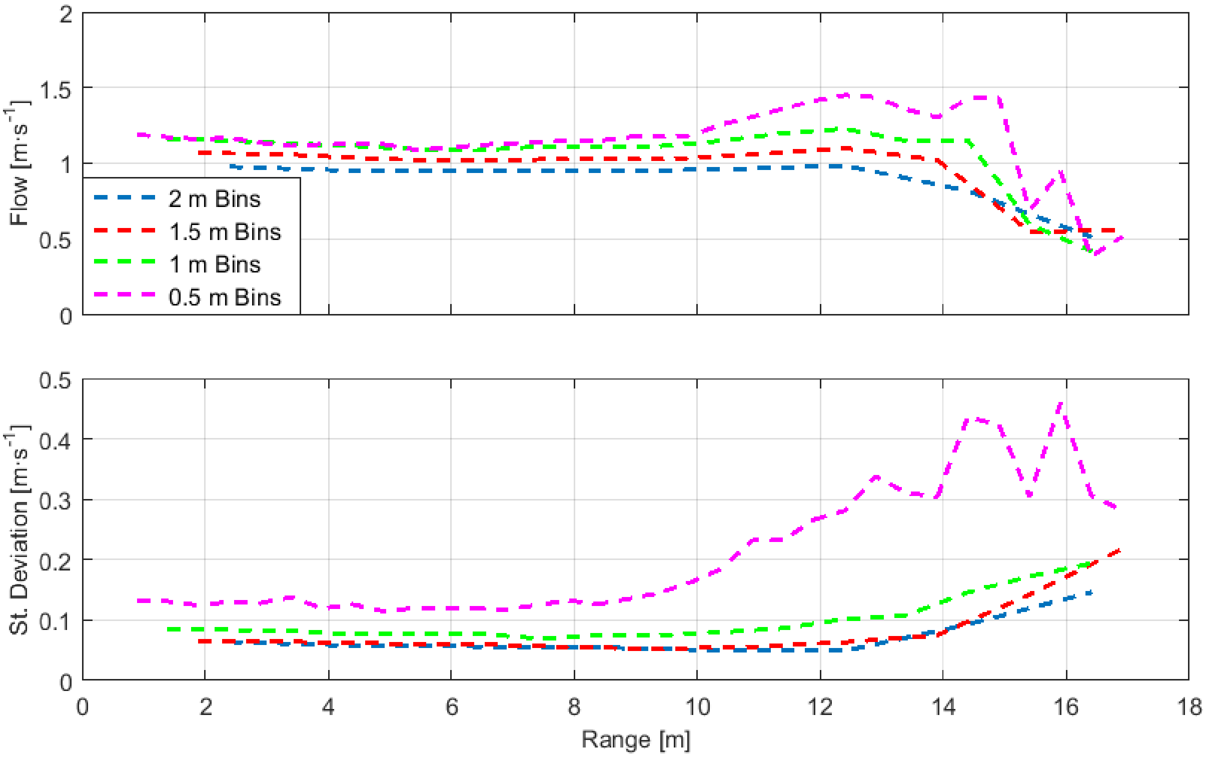

Figure 5.10: *Single-beam bin resolution tests*

5.4 *Strathclyde University Towing Tests*

The instruments were subsequently tested at the University of Strathclyde's Kelvin Hydrodynamics laboratory [206], a 76 m long towing tank. These tests aimed to further evaluate the capabilities of the single-beam under controlled, repeatable and well understood conditions, with specific attention on the uncertainty of the instrument. The tank depth was insufficient for the RAMP ADCP to obtain any measurements that are not susceptible to the aforementioned contamination effects. It was, however, used during the test period for some further interference related studies with the sonar system.

The tank measures 76 m (L) x 4.6 m (W) x 2.5 m (D), with a water depth of 2.1 m used throughout testing. At the upstream end is an absorbing wavemaker, capable of producing regular and irregular waves of heights up to 0.6 m. A beach at the other end of the tank is used to minimise wave reflections propagating back in the opposite direction, while lane markers can be raised between tests to reduce the settling time of the tank. A resistance based wave probe was positioned 10 m downstream of the wavemaker. This position also marks the extent at which the tow carriage can travel along the tank. Additionally, the carriage's default starting position was greater than 10 m away from the beach end, meaning that typically it would travel some 50 m during each run. The carriage itself can reach speeds in excess of 4 $m \cdot s^{-1}$, but 3.5 $m \cdot s^{-1}$ was never exceeded during these tests. Positional measurements were determined from a laser on the carriage that evaluates signal return time from a fixed target above the wavemaker. For each run, measurements of carriage speed, position and wave height were obtained using the facility's data acquisition system at a sampling rate of 74 Hz. The carriage speeds can be controlled to in excess of ITTC standards. The general arrangement of the test equipment in the laboratory is shown in Figure 5.11, with the towing carriage approaching the wavemaker.

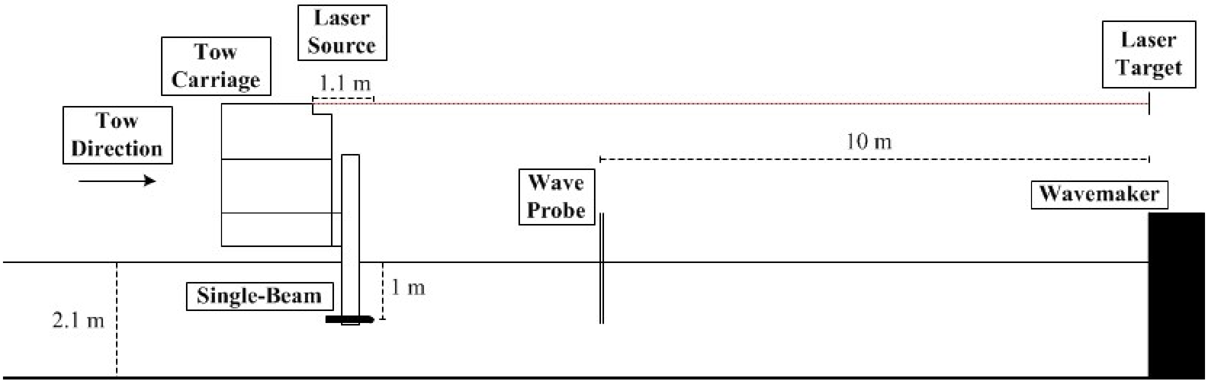

Figure 5.11: *General arrangement of the test equipment in the laboratory*

The instruments were mounted off a vertical support beam in front of the tow carriage and lowered 1 m below the water surface (Figure 5.12). The support beam was modified to minimise the drag forces acting on it. Cables from the instruments were fed back on the carriage, which also hosted all of the PCs used for control and monitoring. Since the results from the sea trials in Section 5.3 suggested that the single-beam achieves reliable measurements down to a bin resolution of 1 m, most of the tests were performed with the instrument configured in this setting. There was also interest in characterising wave induced flows spatially, and a bin size greater than this might mask some of the features. Some tests did, however, take place with the bin resolutions used previously. For all tests the instrument sampled at its maximum rate of 1 Hz.

Figure 5.12: *The single-beam (right) and sonar system (left) mounted off the front of the tow carriage*

Once in the instrument was placed in the tank its amplitude signal was checked, since this parameter provides an indication of the returning signal strength. If this is too low it is likely that the measurements will be questionable, and similar experiments with ADPs have struggled to attain high enough signal responses due to a lack of scattering material in laboratory tanks [207]. This did not prove to be a problem at this facility, with signal strengths trailing off to around 80 counts at the range extent, which is higher than the 20 – 30 count noise floor stated in the manufacturer's guidelines [87] and only slightly lower than that measured during the sea trials.

For any test in which the instrument was towed, data recorded from each run along the tank have been cut during the start and end of each test. This removed measurements made while the carriage was accelerating to the desired speed, as well as the subsequent deceleration to stop. Additionally, measurements were removed once the end of the tank was in the instrument's profiling range. This was achieved by identifying a clear peak in the amplitude signal once the wavemaker was in range, indicating the presence of a strong reflection. Figure 5.13 illustrates this data removal process for a tow run at 1 m·s^{-1}. The carriage is consistent at this speed after 19 seconds and does not start to decelerate until 60 seconds, but the amplitude signal returning from the outermost bin increases rapidly after 52 seconds, indicating the presence of the wavemaker. Therefore, the useable data (red) from this test consists of just over 30 measurements.

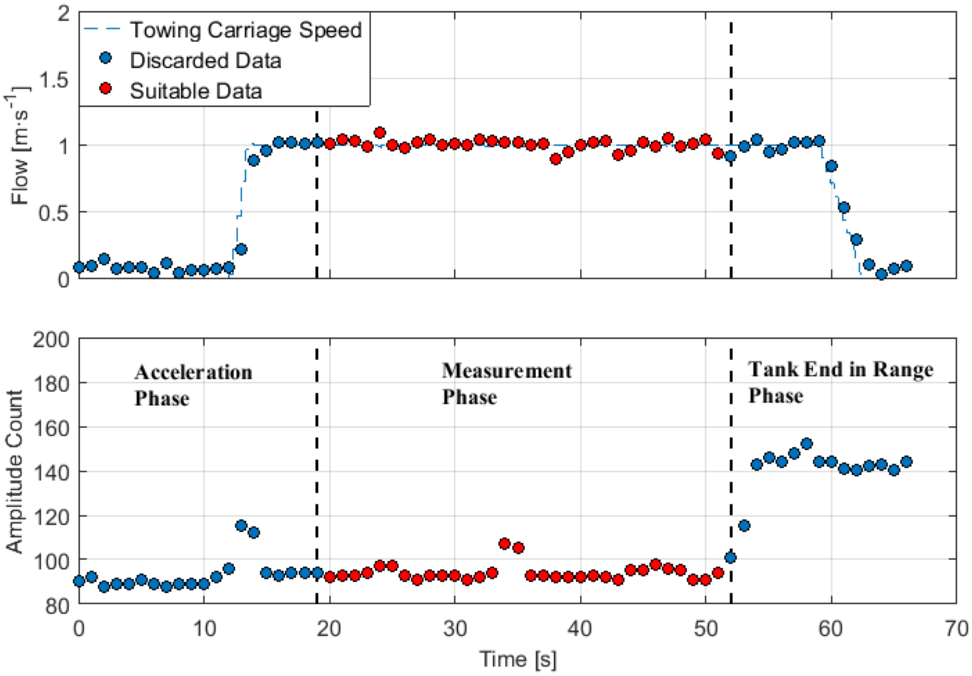

Figure 5.13: *Data filtering process for the towing tests*

5.5 *Results from the Laboratory*

The single-beam was towed at seven speeds between 0.5 – 3.5 m·s^{-1}. Since the number of useable measurements (Figure 5.13) is inversely proportional to the towing speed, it was necessary to perform more tests at higher speeds in order to make reasonable, statistical comparisons between results. Table 5.1 lists the number of measurements obtained at each towing speed. The instrument was towed 50 times, amounting to approximately 14 minutes of useable data, with at least one minute of cumulative data obtained at each of the speeds.

Table 5.1: *Number of measurements obtained at each towing speed*

Tow Speed [m·s^{-1}]	**No. of Tests**	**No. of Measurements**
0.5	4	254
1.0	5	142
1.5	4	70
2.0	8	102
2.5	8	83
3.0	9	74
3.5	12	78

Summary results from these runs are presented in Figure 5.14. It is clear that at ranges up to 12.4 m on all of the runs there is a significant discrepancy between the measured and true values. The difference tends to be greater the nearer the measurements are made to the instrument, and increases with tow speed. It is unclear what has caused this, but the fact that this feature was not seen during the sea trials suggests that these measurements should not be treated as representative of the instrument's true performance at this range. The amount of variation, represented by error bars of ± 1 standard deviation, σ, in these first few bins is also noticeably higher than it is elsewhere. In some cases, the standard deviations from the tow runs are 2.5 times greater than those seen during the sea trials (Figure 5.10), i.e. in unsteady conditions. These findings suggest that the data are questionable at this range. For this reason, the remainder of the discussion in this section will focus on the bins at ranges 12.4 m and greater, where the expected mean speeds were observed.

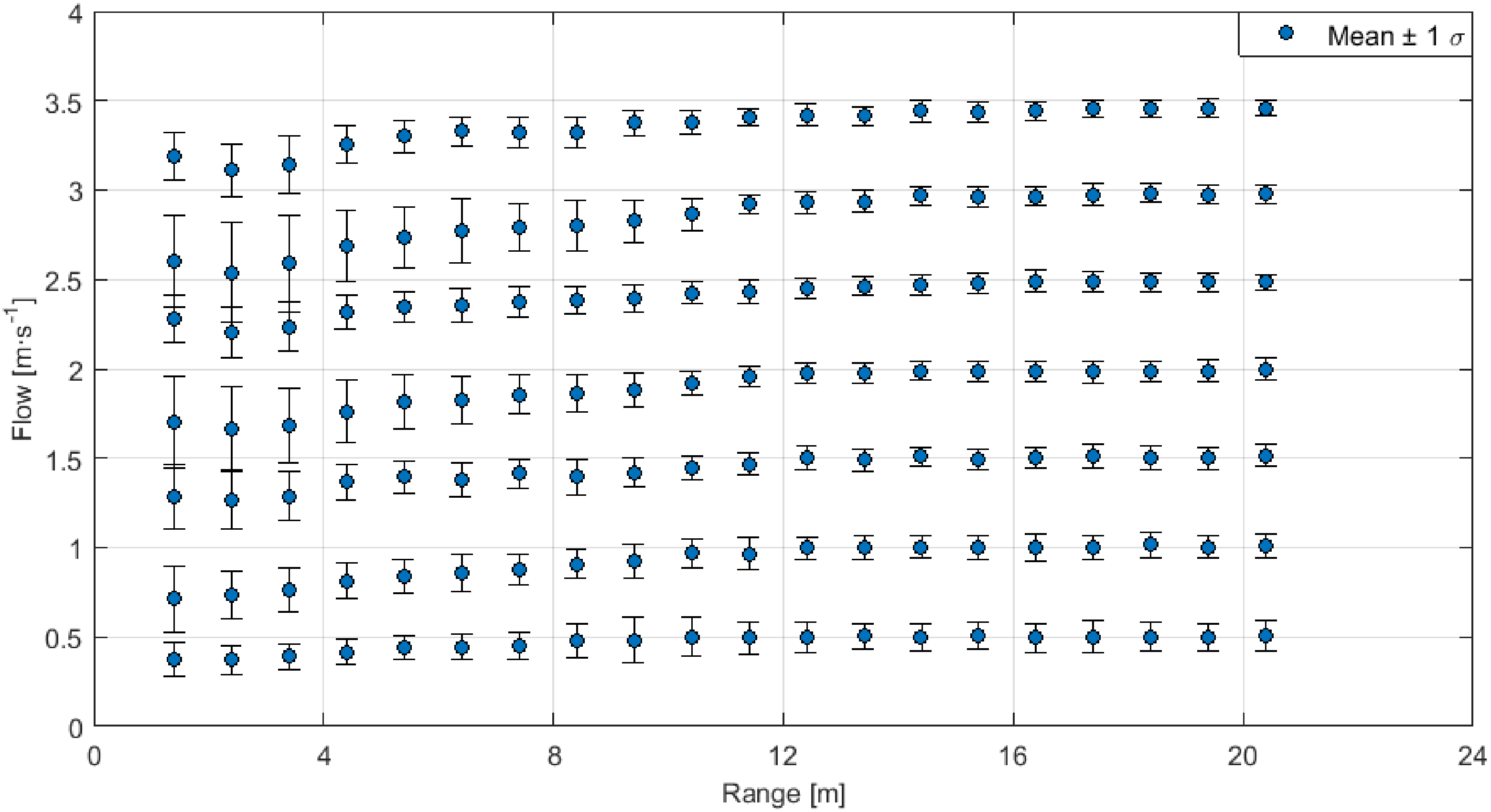

Figure 5.14: *Summary statistics from the constant speed tow tests*

The standard deviations do not appear to be affected by measurement range or tow speed. All standard deviations are within the range of 0.05 – 0.09 m·s^{-1}. The higher values tend to be found at lower tow speeds, but there is not enough evidence to suggest that there is more variation at these speeds. This result implies that the standard error, SE, should not vary with range or tow speed either, given that the standard error is the ratio of the standard deviation to the square root of the sample size, *N*:

$$SE = \frac{\sigma}{\sqrt{N}} \tag{5.1}$$

This quantity cannot be fairly compared between tow speeds due to its dependence on *N*, although Table 5.1 shows that four of the runs do have similar sample sizes (1.5, 2.5, 3 and 3.5 m·s^{-1}). Therefore, there is evidence to suggest that the standard error is unaffected by tow speed, meaning that the instrument's precision, or random error, is unaffected by range or speed. This also implies that the precision improves relatively with tow speed.

In terms of absolute error, i.e. the difference between the mean single-beam and carriage speeds, this tends to increase with tow speed and is unaffected by range. This is visibly apparent in Figure 5.14, where measurements of the target tow speed at 0.5 m·s^{-1} are within ± 0.02 m·s^{-1}, whereas at 3.5 m·s^{-1} the results are lower by as much as 0.08 m·s^{-1}. In relative terms, the absolute errors are never greater than 3.1%, but not enough measurements have been obtained to conclude if this parameter varies with tow speed.

To complement the work described in Section 5.3 in which the bin resolution parameter was modified to study the effect that this setting has on instrument performance, further constant speed tests were undertaken with the single-beam configured to profile at the same bin sizes tested during the sea trials. Each bin size was towed once only at 1 and 1.5 m·s^{-1}, with the data trimmed in post-processing such that an identical number of measurements were obtained at each speed. Table 5.2 shows the results.

As expected, the standard error increases with decreasing bin size due to the lower amount of spatial averaging. From Equation 5.1, the standard error would be expected to increase by 41% upon halving the sampling volume, and hence *N*, but not enough measurements were obtained to confirm this.

Accuracy was again determined by calculating the difference in mean tow and measured speeds. This quantity is also seen to improve with bin size. A maximum absolute error of 0.08 m·s^{-1} was recorded during the 0.5 m bin size tests, while the 2 m cell tests had an equivalent value of 0.02 m·s^{-1}. Again, the lack of data recorded from these tests means that it is difficult to quantify the reduction in this error with respect to bin size.

Table 5.2: *The effect of the single-beam bin size on measurement uncertainty*

Bin Size [m]	**Tow Speed [m·s^{-1}]**	**Max. Std. Error [m·s^{-1}]**	**Max. Abs. Error [m·s^{-1}]**
0.5	1	0.03	0.08
	1.5	0.06	0.08
1	1	0.01	0.04
	1.5	0.02	0.05
1.5	1	0.01	0.03
	1.5	0.01	0.02
2	1	0.01	0.02
	1.5	0.01	0.02

In order to assess the capabilities of the single-beam in unsteady flows, waves were sent down the tank to create profiles of induced currents. The tow carriage was held stationary at the midpoint along the tank for these tests, since the waves generated are of a better quality at this location and less susceptible to reflections from the beach end. The instrument was tested with 0.3 and 0.6 Hz regular waves. To determine the expected current profiles from these waves, the intermediate water depth equations of linear wave theory were applied. These are listed below:

$$k = \frac{2 \cdot \pi}{\lambda} \tag{5.2}$$

$$\omega = \sqrt{g \cdot k \cdot tanh(k \cdot h)} \tag{5.3}$$

$$v_{phase} = \sqrt{\frac{g}{k} \cdot tanh(k \cdot h)} \tag{5.4}$$

$$u_x = \omega \cdot a \cdot \frac{cosh\big(k(z + h)\big)}{sinh(k \cdot h)} \tag{5.5}$$

Where:

k	-	Wavenumber (m^{-1})
λ	-	Wavelength (m)
ω	-	Wave frequency (rad·s^{-1})

g - Acceleration due to gravity (9.81 m·s^{-2})

h - Water depth (2.1 m)

v_{phase} - Wave phase speed (m·s^{-1})

u_x - Maximum horizontal wave induced current velocity (m·s^{-1})

a - Wave amplitude (m)

z - Single-beam depth below water surface (-1 m)

Equation 5.3 was rearranged and solved iteratively to determine k, and hence λ and v_{phase}. It was necessary to estimate a from the wave probe measurements of surface elevation. This was achieved by applying a first order Fourier fit to the measurements, as shown in Figure 5.15 for the 0.3 Hz waves. The amplitude of the wave is then found from the square root of the sum of the cosine and sine multipliers squared in the derived equation of the fitted curve, resulting in an amplitude of 128 mm in this case.

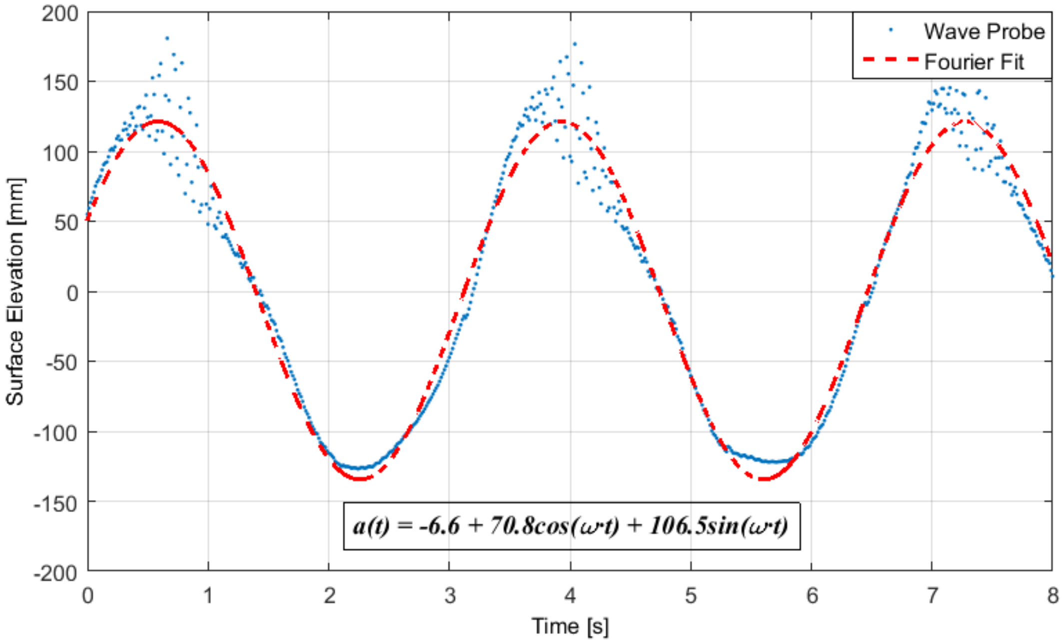

Figure 5.15: *Fourier fit applied to the wave probe measurements of 0.3 Hz waves*

The derived properties are listed in Table 5.3, showing that while the two tested waves have considerably different wavelengths, their maximum horizontal wave induced current velocities are both approximately 0.2 m·s^{-1} at the single-beam depth.

Table 5.3: *Derived wave properties for the 0.3 Hz and 0.6 Hz waves*

Property	0.3 Hz Waves	0.6 Hz Waves
λ [m]	13.21	4.32
a [m]	0.13	0.19
v_{phase} [m·s^{-1}]	3.96	2.59
u_x [m·s^{-1}]	0.23	0.18

Figures 5.16 and 5.17 shows the wave profiles measured by the single-beam during the 0.3 and 0.6 Hz tests respectively. These are plotted over four consecutive time steps, i.e. 1 second measurement intervals. Similar to Figure 5.15, a first order Fourier fit has been applied to each profile in order to derive the measured wave properties. In both sets of results, the expected progressing curves are observed to move towards the single-beam, showing the sinusoidal motion of the wave induced currents. As predicted, shorter wavelengths were measured in the 0.6 Hz results. The fitted curves do, however, have amplitudes lower than the predicted u_x in Table 5.3. For example, the maximum u_x observed in the 0.3 Hz results is just 0.16 m·s^{-1}. The tendency to underestimate this parameter should not be unexpected considering the instrument's principles of operation. Firstly, the instrument performs a spatial, weighted average of measurements around the central measurement location, and this averaging space is twice as large as the bin size (1 m resolution in this case). This implies that the instrument will never truly be able to capture the maximum induced currents because it is averaging around the peak values. Secondly, the instrument pings multiple times during each sample (1 Hz in this case), and the recorded measurement is an average of the returning pings. This temporal averaging also has consequences on the ability of the instrument in characterising a progressing disturbance, because it will have moved between each ping. Decreasing the cell size and increasing the sample rate might lead to a better characterisation, although this would increase the uncertainty of measurements, as shown earlier in Table 5.2.

It is also possible to estimate v_{phase} and λ from the results in Figures 5.16 and 5.17, with the former determined by evaluating the distance that the crest of the fitted curve moves between time steps. These estimates are also lower than those predicted in Table 5.3, although the results have improved in relative terms when compared with the measurements of u_x. A maximum v_{phase} of 3.8 m·s^{-1} and a λ of 11.8 m were obtained from the 0.3 Hz results, close to the predicted 3.96 m·s^{-1} and 13.21 m. These improved measurements should be expected considering that both v_{phase} and λ do not vary spatially or with respect to time.

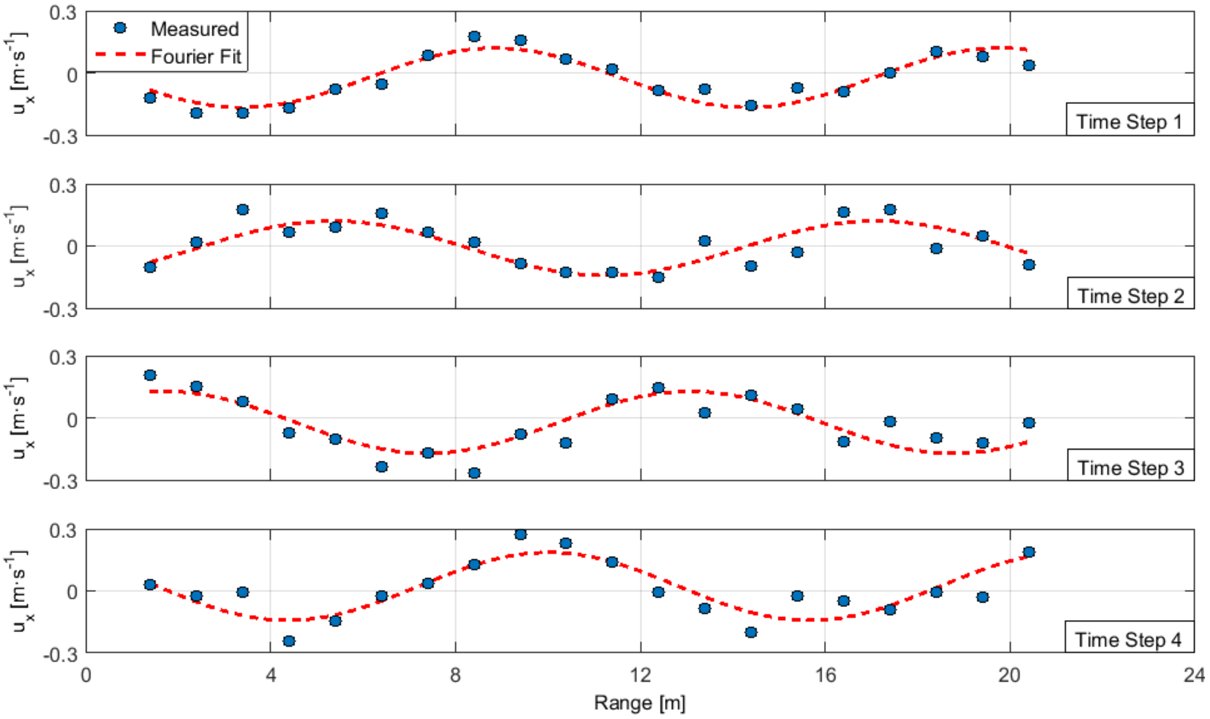

Figure 5.16: *Single-beam measurements of induced currents from 0.3 Hz regular waves*

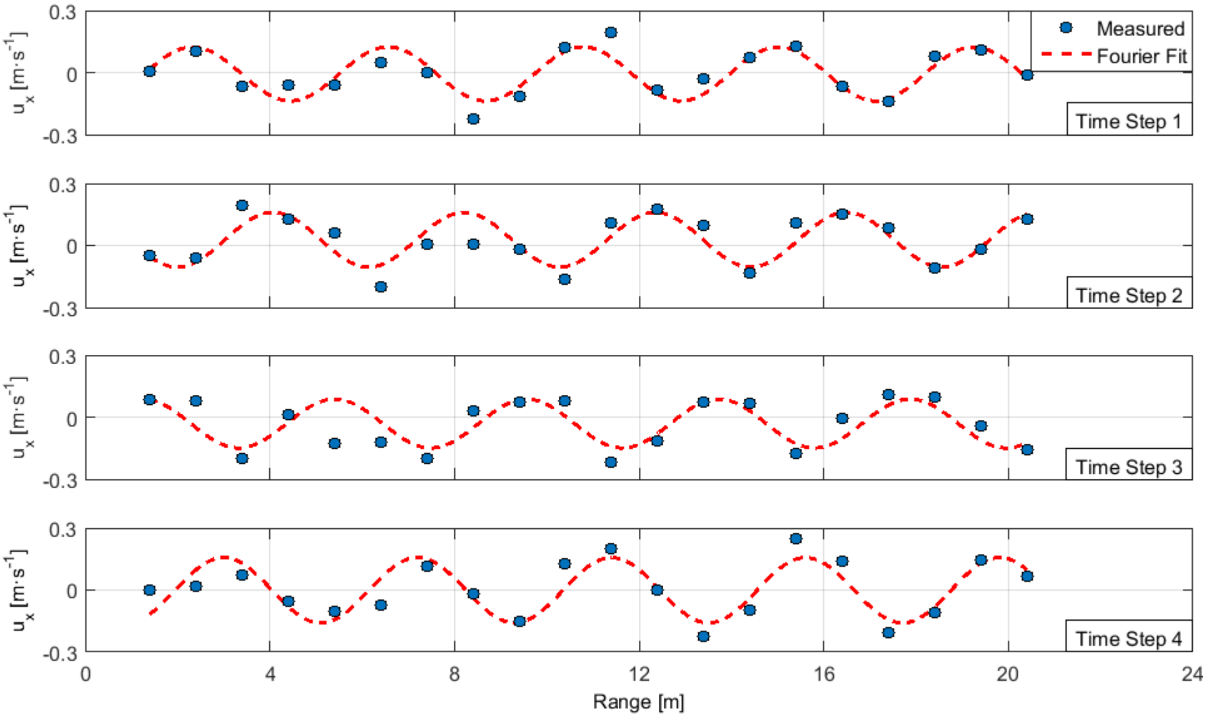

Figure 5.17: *Single-beam measurements of induced currents from 0.6 Hz regular waves*

5.6 Reviewing the Test Campaigns

The RAMP ADCP and single-beam are both instruments that will be used to characterise the environmental conditions that the full-scale turbine is subject to (Chapter 6). The test campaigns presented in this chapter provided invaluable operational experience with the instruments prior to the installation of the turbine, and were designed to evaluate their capabilities.

Multi-beam ADP technology has been used for decades now and their ability to characterise tidal stream sites is well documented [55], [83], [100], [102]. In this chapter the RAMP ADCP was used to show that the survey area in the Pembroke Dock harbour has an ebb flow in excess of 1 $m \cdot s^{-1}$ and heads in a 285^{o} direction, whereas the flood flow is significantly weaker and does not have a dominant heading. These findings are to be expected considering the surrounding features of the harbour, in which there are archways upstream of the ebb flow that act as both flow magnifiers and straighteners. The flood flow is not susceptible to these flow enhancements. When the instrument was erroneously configured to operate in a narrowband processing mode, the uncertainty of these flow properties was found to increase, with the directional measurements found to be particularly questionable. This is a consequence of the instrument having less information available to form measurements in this configuration. It is not a configuration recommended by the manufacturer.

In contrast to the RAMP ADCP, the single-beam is a non-standard product that to date has seen limited usage in tidal energy research [100], and it is also unrecognised in guidelines relating to tidal current measurement [92], [142]. Therefore, the tests in this chapter aimed to establish suitable configurational parameters for the instrument. Throughout testing the instrument was always configured to sample at its maximum rate of 1 Hz, for the reason that averaging the data temporally in order to reduce noise could take place in post-processing if necessary, essentially achieving the same goal as sampling at a lower rate. Since the instrument was always connected to a PC and powered to shore, this choice of sampling rate also had no consequences on data storage or battery life that would usually be considerations for remote deployments. The turbine application also benefits from these onshore resources (Chapter 6). The tests did, however, study the effect that the bin resolution parameter has on measurement uncertainty. It was found that both the absolute and standard errors are inversely proportional to bin size, an unsurprising result given the methods used by the instrument to derive measurements [87]. A 1 m bin size was selected as the preferred compromise between measurement certainty and spatial resolution.

The Pembroke Dock sea trials allowed the instruments to be configured such that they both measure the flow velocity in the same volume of water. The results suggested that the single-beam measures a mean flow typically in the region of 85 – 90% of that obtained from the RAMP ADCP. This is believed to be primarily due to the fact that the RAMP ADCP is capable of measuring flow magnitude, whereas the single-beam can only resolve the component along its beam. An assessment of the instantaneous directional variability in flow direction added weight to this argument, showing that nearly 1/3 of measurements lie outside 25° of the dominant flow direction. The single-beam, which was oriented such that it faced this direction, will measure a significantly lower flow during these instances of misalignment.

Subsequent testing of the single-beam under controlled and well understood laboratory conditions further disproved any concerns of measurement bias. Mean measurements of carriage tow speed were all found to be within 3.1% of the reference values, considerably lower than the discrepancies found during sea trials.

Throughout testing the single-beam demonstrated capabilities in identifying non-uniform flow features, including the flow acceleration zone near the archway entrance at Pembroke Dock. While this is perhaps unsurprising given the aforementioned low uncertainties on mean measurements, the single-beam also showed in the laboratory an ability to identify, track and characterise regular waves from its instantaneous observations of the flow velocity. Compared with theoretical predictions the single-beam tended to underestimate the wave properties, but this should be expected since the instrument averages both spatially and temporally to form each measurement. However, the results from this study have highlighted the potential of the instrument in characterising turbulent flows. For turbine mounted arrangements, this could be used to better understand instantaneous effects on device performance, or as an input to an advanced control system aiming to best prepare the turbine for approaching turbulent effects. Such a system would have parallels with ongoing wind energy research on the usage of turbine mounted LIDAR systems [175], [176].

Since the conclusion of the work in this chapter, it was revealed that some additional settings relating to the configuration of the single-beam could be modified after discussing the test results with the manufacturer. A previously inaccessible hardware configuration menu was made available in the software accompanying the instrument, allowing the maximum sampling rate to be increased to 2 Hz. The consequence of this is that the number of measurements available to derive each temporally averaged value will be halved as a result of doubling the sampling rate, due to the fact that the instrument was operating at its maximum ping rate, i.e. the number of times the transducer sounds to derive each sample. The effect is similar to reducing the bin resolution by a factor of two, resulting in the standard error increasing by 41% (Equation 5.1). However, it was realised that the ping rate could be increased due to the fact that the software had been configured for a 3-beam instrument, the standard Aquadopp product. This had led to the instrument pinging at just one third of its actual capacity, at 7 pings per measurement. With a single-beam it is possible to increase this to 21 for 1 Hz measurements. Therefore, 10 pings per measurement is achievable for 2 Hz measurements, an improvement on the tested configuration despite increasing the sampling rate. It is believed that this new configuration would lead to an improved characterisation of instantaneous and unsteady flows, without affecting measurement uncertainty.

6. Full-Scale Device Testing

With the scale model test results showing a general agreement with numerical predictions, and the preparatory ADP trials identifying suitable configuration parameters to characterise a number of environmental properties, the next step was to assess the operational performance of the full-scale turbine. DeltaStream^{TM} was installed at Ramsey Sound in December, 2015. While this is a considerably more challenging and complex environment than the laboratory, the device performance would not be subject to the same uncertainties attributable to testing at small-scale in a confined channel. This chapter begins by describing the Ramsey Sound test site and detailing the methods used to process environmental and turbine related measurements. Thereafter, the chapter reports on the power performance and rotor loading of the full-scale device from its initial operational trials in ebb flows, with all results compared against numerical predictions. Lastly, the chapter discusses the lessons learnt from this test period and makes a number of recommendations for future work.

6.1 Demonstration Project

The general arrangement and bathymetry of the Ramsey Sound test site are shown in Figure 6.1. The turbine is located to the north of the site, just over 1 km to the west of the Welsh Mainland and in a depth of 35 m. The subsea cable runs approximately 1.2 km to the onshore temporary power conversion compound (TPCC) and control centre. It can be seen that there are a number of notable bathymetrical features at the site. To the south of the turbine a trench runs through the site, with its depth reaching in excess of 75 m. East of this channel there is a long ridge that runs up towards the turbine. The ridge peaks some 700 m downstream of the turbine at Horse Rock, a pinnacle that pierces the surface during low spring tides. Further downstream and outside of the extent of the bathymetric survey, a reef of rocks, known as the Bitches, protrude out into the site from Ramsey Island. In comparison, the bathymetry to the north of the turbine shows much less variation, and as a consequence the southwards heading ebb tide is less turbulent than the flood, which is disturbed by the aforementioned features of the seabed. The flood flow is, however, considerably stronger than the ebb at the turbine location, meaning that there is a significant asymmetry at the site. A tidal ellipse of hub height (12.1 m) flow data is shown in Figure 6.2, obtained from a seabed mounted ADP survey near the turbine location prior to its installation. The scatter, which represents 10 minute average values, shows that during this survey the mean flood flow reached 2.7 $m\cdot s^{-1}$, whereas the maximum ebb was just 1.8 $m\cdot s^{-1}$. The flow is approximately bidirectional at the site, but the narrower scatter seen on ebb flows demonstrates that the directionality is more consistent on this tide. Again, this is a result of the bathymetry disturbing the flood flow.

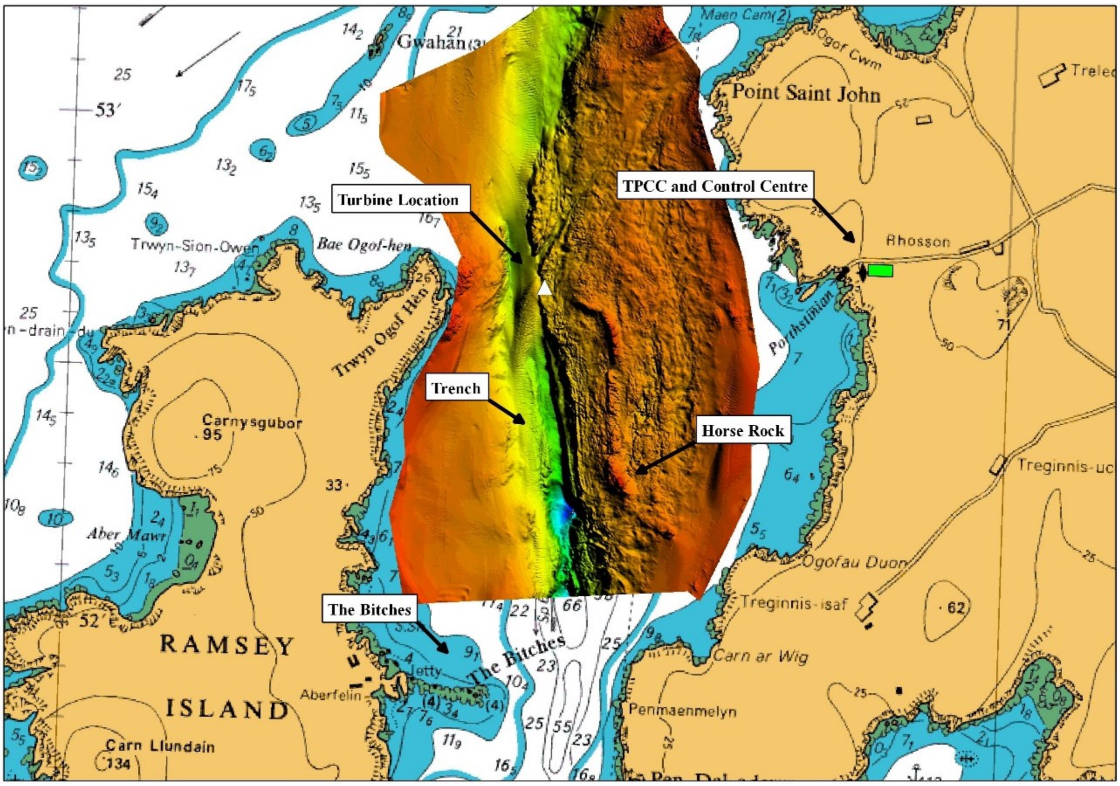

Figure 6.1: *Notable features of the Ramsey Sound bathymetry*

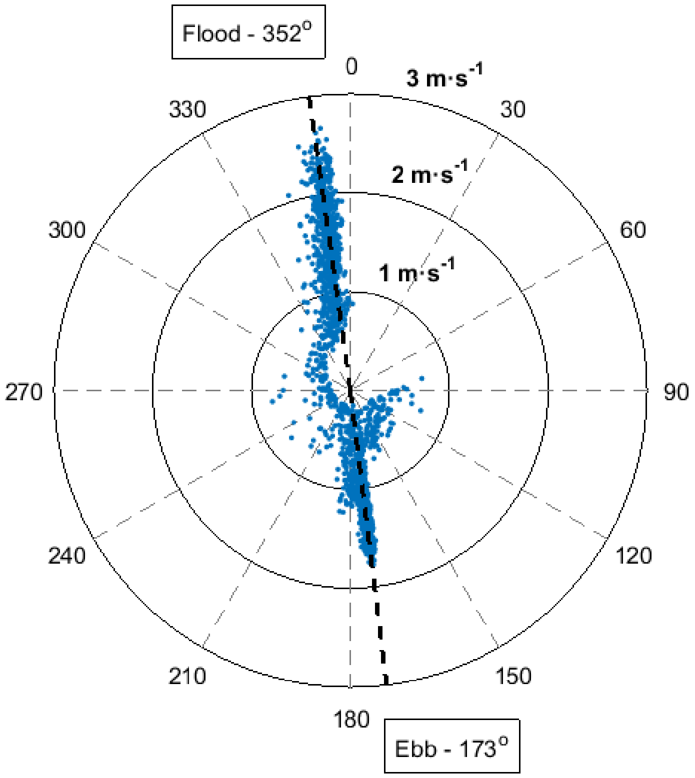

Figure 6.2: *Tidal ellipse of hub-height flow obtained near the turbine location*

The IEC power performance assessment guidelines [142] recommend surveying the bathymetry at the test site out to 5 equivalent rotor diameters (D) either side of the turbine, and 10 D upstream and downstream, covering an area of 10 D x 20 D. This region is shown in Figure 6.3, with the area offset by 8^{o} to align with the dominant flood flow. The turbine sits on the northernmost apex of its triangular frame with the rotor facing west when parked and non-operational. The yaw system range (± 100^{o}) is sufficient to allow the rotor to face the dominant directions of both tides, and accounts for the small offset frame installation angle from true north. The 4-beam ADCP was housed in a small seabed structure referred to as the remote acoustic monitoring platform (RAMP), pictured in Figure 6.4. RAMP also contained the sonar system and is located 35 m east of the turbine. It is cabled to the turbine, and hence the shore, to allow full operation of these sensors from the onshore control centre.

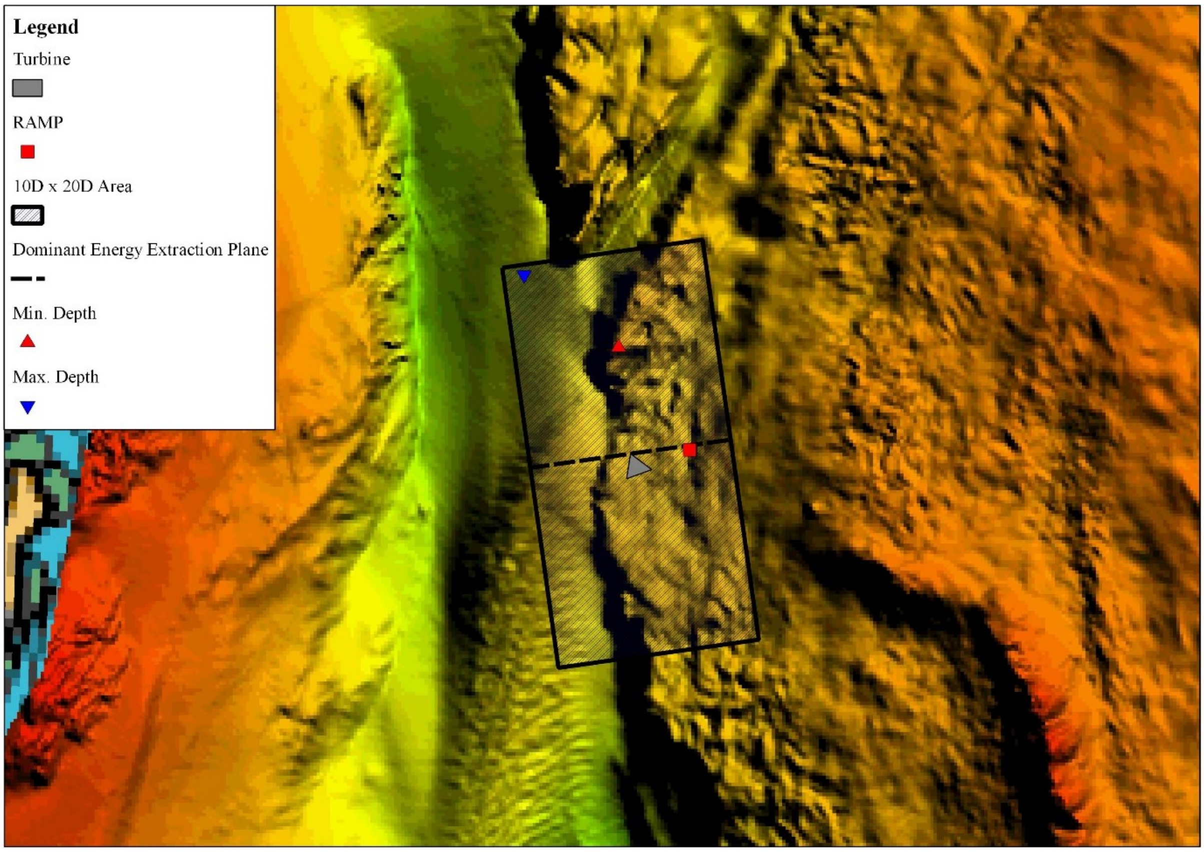

Figure 6.3: *Bathymetry within the vicinity of the turbine, showing the 10 D x 20 D area*

Figure 6.4: *The remote acoustic monitoring platform (RAMP)*

Within the 10 D x 20 D area there are no significant variations in depth immediately downstream or upstream of the turbine. A minimum depth of 31 m is found approximately 65 m north of the turbine, while a maximum depth of 44 m occurs near the North-West apex. The bathymetry was sampled along the dashed line, forming the dominant energy extraction plane that the rotor sits in when operational. This has been drawn to scale in Figure 6.5. The RAMP sits approximately 2 m south of this line, but there is a negligible variation in depth between these locations. Both the RAMP and the turbine sit at a depth of 35 m.

The IEC guidelines recommend that for this adjacent configuration of ADCPs, two measurement volumes are obtained within 1 - 2 D away from the extent of the rotor plane, which in this case is 18 – 30 m away from the rotor centre. The recommended extraction planes are displayed as dashed boxes in Figure 6.5, with the ADCP measurement volume (± 20^{o} beam spread) shown in red. Since the ADCP is 35 m away, the majority of its measurement volume lies outside of the recommended plane. The location for the RAMP, however, was dictated by the requirements of the sonar system, which needed to be at least this distance away in order for its beam spread to capture the rotor disc. The inclusion of a secondary ADCP to the west of the turbine is another condition of the IEC guidelines that could not be met during this test.

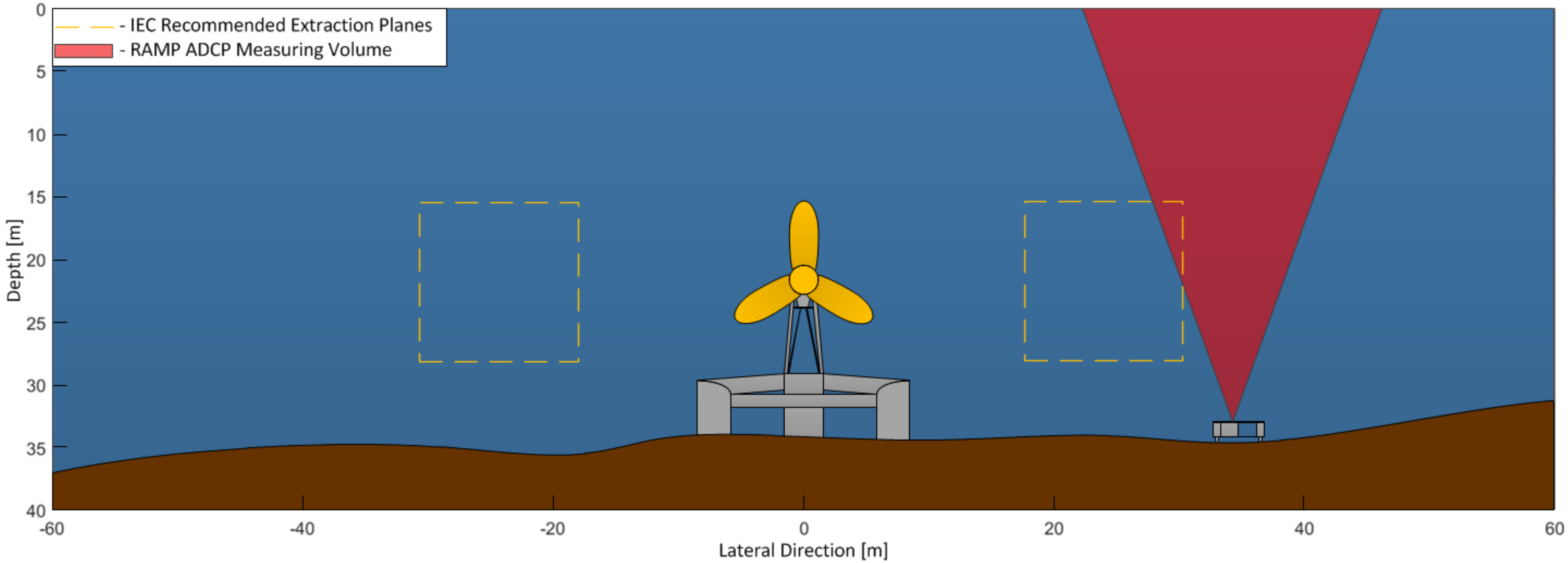

Figure 6.5: *The channel cross-section along the dominant energy extraction plane. The dashed yellow boxes show the areas in which the IEC guidelines recommend measuring flow velocity, while the red area shows where the RAMP ADCP sampled*

6.2 Processing Flow Measurements

Despite the previous section highlighting that the RAMP ADCP arrangement does not fully satisfy the requirements of the IEC guidelines, the data processing methodology outlined in the document was still adhered to. This process involves vertically integrating the flow measurements over the elevation in which the rotor is positioned to obtain a power weighted average velocity across the disc. Each measurement is assigned a weight based on the area it covers on the rotor disc, with the greatest weights being applied to the profiler bins that are at heights closest to the rotor centre. The ADCP transducer head sits 1.25 m above the seabed in the RAMP and its first profiler bin is centrally located at 1.86 m above the instrument. The ADCP spatial resolution was set to 0.75 m. Therefore, bins 5 – 21 cover the range 6.11 – 18.11 m, i.e. the rotor disc elevation. This information was used to numerically derive the elemental areas, A_k, that would be used as weights for each measurement, M, as illustrated in Figure 6.6. Each area spans ± 0.375 m about the central measurement location, apart from the outermost bins that lie on the edge of the rotor disc. The derived weights are not quite symmetrical about the rotor centre (12.1 m) due to the very slight offset in bin locations.

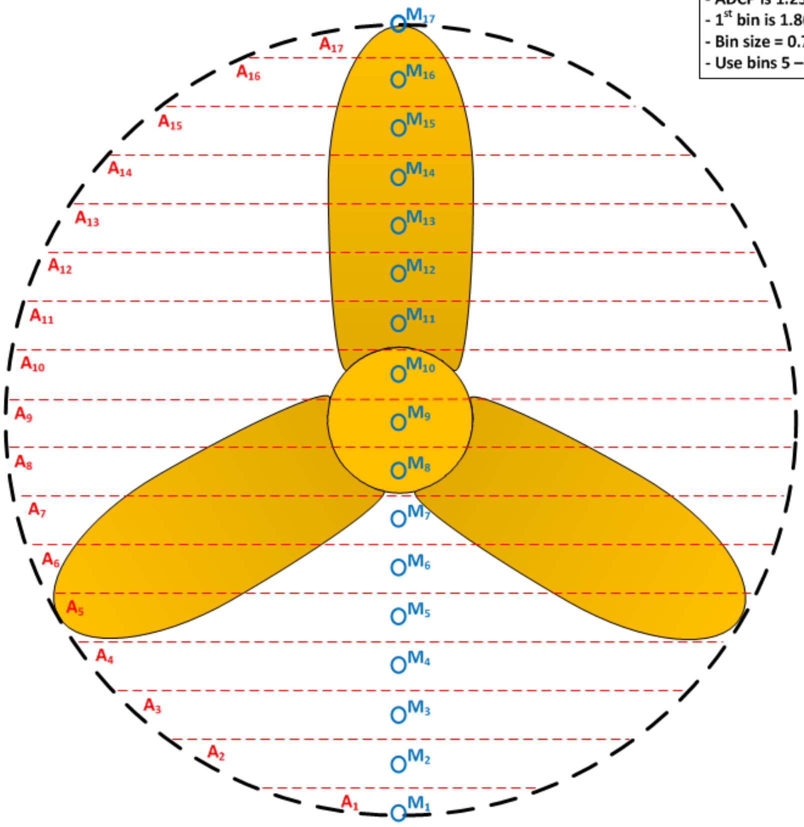

Note
- ADCP is 1.25 m above seabed
- 1^{st} bin is 1.86 m above ADCP
- Bin size = 0.75 m
- Use bins 5 – 21 to cover rotor area elevation (6.1 – 18.1 m)

ADCP Bin	Elevation (m)	Area Element	Area (m^2)
M_1	6.11	A_1	0.81
M_2	6.86	A_2	4.22
M_3	7.61	A_3	5.91
M_4	8.36	A_4	7.00
M_5	9.11	A_5	7.78
M_6	9.86	A_6	8.33
M_7	10.61	A_7	8.70
M_8	11.36	A_8	8.91
M_9	12.11	A_9	8.98
M_{10}	12.86	A_{10}	8.91
M_{11}	13.61	A_{11}	8.69
M_{12}	14.36	A_{12}	8.32
M_{13}	15.11	A_{13}	7.76
M_{14}	15.86	A_{14}	6.98
M_{15}	16.61	A_{15}	5.87
M_{16}	17.36	A_{16}	4.16
M_{17}	18.11	A_{17}	0.75

Figure 6.6: *Illustration of the weight assigning process to perform a weighted average of RAMP ADCP flow measurements*

The power weighted flow velocity in the IEC document is the first calculation in a series of three averaging steps that are applied in order to develop a power curve. The second calculation involves temporally averaging the power weighted data over a given time period, while the third sorts all of these measurements into a series of flow bins, before averaging all of the measurements that lie within each bin. This last step is described in more detail in Section 6.6. The power weighted flow velocity (first step) is calculated as follows:

$$\widehat{U}_{i,j,n} = \left[\frac{1}{A} \cdot \sum_{k=1}^{S} U_{i,j,k,n}^{3} \cdot A_k\right]^{\frac{1}{3}} \tag{6.1}$$

Where:

- i is the index defining the flow bin
- j is the index defining the instance in time at which the measurement was obtained
- k is the ADCP profiler bin index
- n is the index defining a data point within a flow bin
- A is the rotor area (113.1 m^2) and equivalent to the summation of elemental areas, A_k
- S is the total number of ADCP bins across the rotor area ($S = 17$)
- $\widehat{U}_{i,j,k,n}$ is the magnitude of the flow velocity at time j, in ADCP bin k, and flow sorted bin i, for data point n
- $\widehat{U}_{i,j,n}$ is the instantaneous power weighted flow velocity

The temporal averaging (second step) is then derived from Equation 6.2:

$$\widehat{U}_{i,n} = \left[\frac{1}{L} \cdot \sum_{j=1}^{L} U_{i,j,n}^{3}\right]^{\frac{1}{3}} \tag{6.2}$$

Where:

- L is the number of measurements within the averaging period
- $\widehat{U}_{i,n}$ is the temporally averaged power weighted flow velocity

The majority of the results that follow in this chapter were averaged over 10 minute periods, unless otherwise stated. The RAMP ADCP sampled at 1 Hz, yielding 600 measurements, L, within these averaging periods.

The single-beam ADP was mounted inside the rotor nosecone (Figure 6.7) to face the approaching flow. It was allowed to rotate with the rotor via a slip ring. Recall that the single-beam measures the line-of-sight component of the flow velocity only. Therefore, during all periods in which the turbine was non-operational with the rotor parked approximately 90° out of the dominant flow direction, the single-beam recorded very low velocities. Any yaw misalignments would also affect the strength of the flow measured by the instrument. A correlation study of the flow measured by the RAMP ADCP and single-beam is provided in the Section 6.4.

Figure 6.7: *The single-beam transducer head positioned at the centre of the rotor nosecone*

The single-beam profiled the incoming flow from the range 1.4 – 20.4 m upstream of the turbine at a resolution of 1 m. The initial analysis of the single-beam data revealed that the measurements closest to the rotor are subject to a considerable flow reduction, as a consequence of the presence of the turbine itself. The flow in this region decelerates as it attempts to move around the turbine. This is in agreement with findings from a similar turbine mounted single-beam arrangement used in the ReDAPT project [67], where flow reductions were observed out to 13 m in front of an 18 m diameter turbine. Here, mean flows were found to be near constant from ranges in excess of 10 m, and as a consequence the outermost bins have been length averaged in the range 11.4 – 20.4 m to provide an unbiased mean inflow from the single-beam. Example flow profiles are presented in Section 6.4 to justify the averaging criteria. Similar to the RAMP ADCP, the single-beam sampled at 1 Hz and its length averaged values were further averaged temporally over the same 10 minute periods. However, this was not power weighted by the cube as in Equation 6.2. Instead, the standard arithmetic mean was used.

6.3 Processing Turbine Measurements

The GE SCADA system recorded various turbine parameters, including the electrical properties and shaft speed (measured via an encoder). However, the turbine power measurement was made onshore at the TPCC, by which point it is subject to a number of losses due to power conversion and transmission. The chain of systems that the power developed by the rotor must pass through until it is measured is illustrated in Figure 6.8. Therefore, in order to determine the power from the generator, it was necessary to perform a series of backwards calculations that account for the losses in each system.

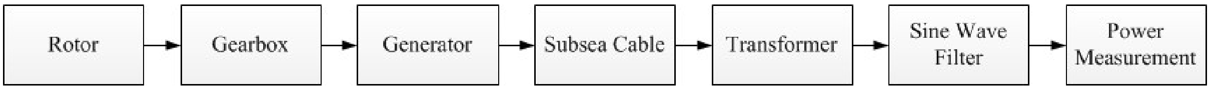

Figure 6.8: *Chain of turbine systems between the rotor and power measurement*

Information relating to the efficiency of the sine wave filter was provided by personal communication from GE. Table 6.1 lists this information, in which a maximum loss of 6.5 kW was quoted for the full load condition (400 kW). This information was used as a lookup table in order to calculate the sine wave filter losses via interpolation.

Table 6.1: *Efficiency of the sine wave filter*

Input Power [kW]	**Power Loss Across Sine Wave Filter [kW]**
40	3.25
100	3.90
200	4.55
300	5.53
400	6.5

The onshore transformer steps the 6.6 kV cable voltage down to 690 V. Its efficiency was derived from a test sheet provided by the manufacturer, stating that the losses are a function of power factor and load. The efficiency varies between 97.5% - 98.4%. For simplicity, a 98% efficiency was assumed for all conditions.

The efficiency of the subsea cable was calculated based on its physical properties and expected electrical characteristics. The Joule losses, $P_{loss_{Joule}}$, were calculated via the following equation:

$$P_{loss_{Joule}} = 3 \cdot I_{cable}^{2} \cdot R_{cable} \tag{6.3}$$

Where I_{cable} is the current and R_{cable} is the resistance. The specification sheet from the manufacturer stated a cable resistance per kilometre of 0.528 $\Omega \cdot m^{-1}$, meaning that R_{cable} is 0.63 Ω for the 1.2 km cable. The 3-phase power, $P_{cable,}$ equation was rearranged to calculate I_{cable}:

$$I_{cable} = \frac{P_{cable}}{\sqrt{3} \cdot V_{cable} \cdot cos\, \emptyset} \tag{6.4}$$

Where V_{cable} is the cable voltage and $cos\, \emptyset$ is the power factor. The operational power factors were in the range 0.9 - 1, but this only has a small influence on $P_{loss_{Joule}}$. This is confirmed in Figure 6.9, in which the relationship between V_{cable} and P_{cable} was determined from a steady-state simulation of the turbine using the GE Simulink model (Chapter 3). This relationship and the derived $P_{loss_{Joule}}$ curves are shown for power factors 0.9 and 1. The 6.6 kV cable limit is reached once the exported power from the turbine exceeds 150 kW, by which point $P_{loss_{Joule}}$ continues to rise as a result of increasing I_{cable}. At the 400 kW rated condition, maximum losses of 2.28 and 2.36 kW were estimated to occur for power factors 1 and 0.9 respectively. Since the difference is negligible, the $P_{loss_{Joule}}$ curve from the power factor equal to 1 condition was used as lookup table in the back calculation of generator power.

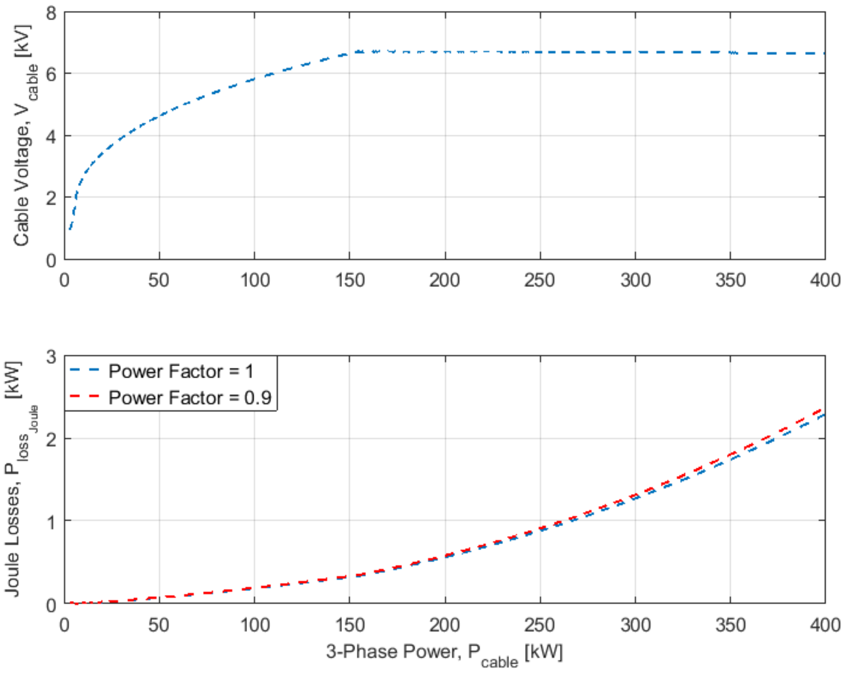

Figure 6.9: *Cable voltage (top) and Joule losses (bottom) as a function of generated power*

Most of the power results that follow in this chapter present the generator output, meaning that the cable efficiency calculation was the last step in the evaluation of losses. However, where there is interest in the rotor performance, the generator and gearbox efficiency data described in Chapter 3 were applied.

In contrast to the power measurement, the forces on the rotor were measured locally on the turbine. Each rotor blade is equipped with 10 strain gauges, five on both the compression and tension surfaces and positioned at radial positions between 1.2 – 4.0 m. These are fibre optic gauges that measure the wavelength of light, which is shifted when the sensor is subject to strain. An onshore calibration was performed with the manufacturer at Pembroke Dock prior to the turbine installation. The calibration involved laying the rotor on its back and individually applying a series of known loads to each blade. Measurements were also obtained for the unloaded condition of each blade, used as the reference to evaluate the difference in wavelength as a result of loading. The results of the calibration tests have been used to convert measurements of wavelength to bending moments, accounting for temperature and thermal properties of the sensor. The sampling rate of the system is approximately 16 Hz, resulting in the order of 500 measurements of strain every second across the entire rotor.

A methodology was developed to infer the blade root bending moments from the strain gauges, since these are of greater interest than the radial values. The procedure involves fitting a curve to the measurements and extrapolating back to radial position 1.1 m, the location of the blade root as defined in the numerical modelling (Chapter 3). Taking the derivative of the fitted bending moment profile about the root then allows the root axial forces on the blade to be determined, the summation of which yields the net rotor thrust force. The expressions for the root axial force, $Root\ F_x$, and rotor thrust, $Hub\ F_x$, are as follows:

$$Root\ F_{x,i} = \frac{dM_{y_{root,i}}}{dr} \tag{6.5}$$

$$Hub\ F_x = \sum Root\ F_{x,i} \tag{6.6}$$

A Matlab script was developed to perform this calibration and curve fitting procedure, using the *pchip* extrapolation method. The $Root\ F_x$ forces were found by calculating the gradient of the formed bending moment curve between extrapolated values found at radial positions, r, between 1.09 – 1.11 m. The methodology, however, required improvement due to some of the measurements appearing to be consistently spurious. This is thought to be a consequence of calibration difficulties at a transitional region in the blades, where the composite material changes in thickness. As a result of this, some of the measurements have been ignored completely in the curve fitting process, while others have had their weights modified. This is an imperfect solution, but the mean blade-to-blade statistics were found to agree well with each other, as would be expected over a sufficient time period. The uncertainties with this process are discussed further in Section 6.8.

Figure 6.10 shows the application of this extrapolation procedure at one instance in time to the measured bending moments, both on the compression and tension surfaces of the blades. The measurements that do not lie on the fitted curves have been ignored, while those that lie close to the curve have had their weights altered. Additional 'measurements' have been included at the blade tip, i.e. at 6 m, and correspond to the zero load experienced at this location. These were added to improve the extrapolation. Blade 2 shows the greatest amount of loading in this example, possibly as a consequence of it being oriented upwards and higher up in the water column where the flow is stronger (Section 6.4). In contrast, blades 1 and 3 agree well with each other. Since there are two measurements of blade root bending moment, the mean of these values was used in all of the analysis that follows.

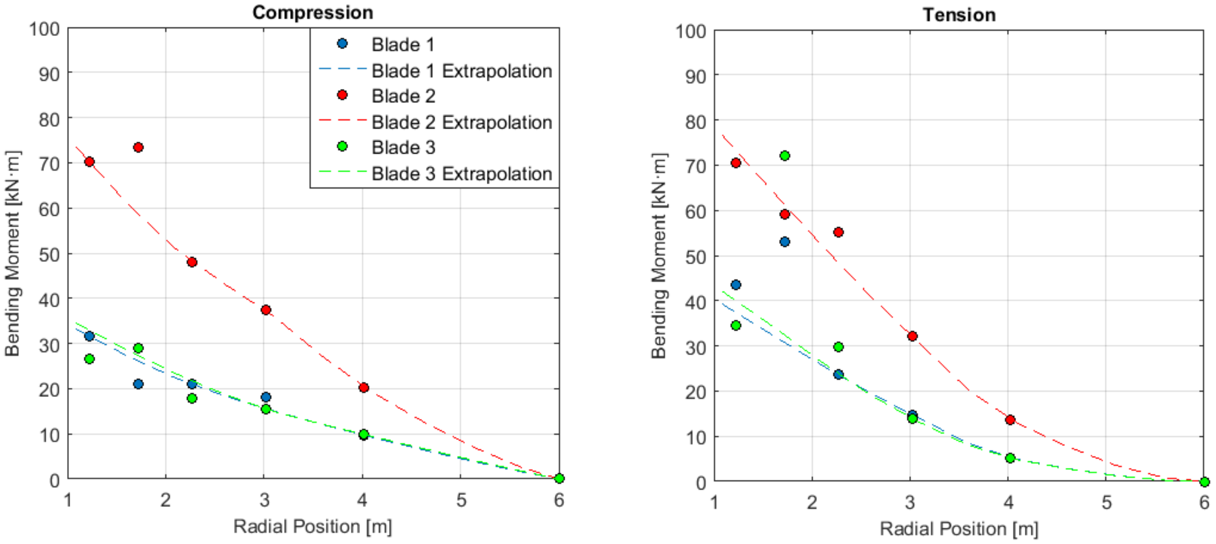

Figure 6.10: *Blade root bending moment extrapolation process*

The rotor strain measurements were recorded independently of the GE SCADA system. This meant that it was necessary to align the data in post-processing for synchronisation. This was achieved through the careful analysis of trends in the time-series results from both systems and manually shifting the data from the GE SCADA system by an identified offset, since the flow measurements were already synchronised with the strain gauges. The rotor thrust was the most reliable parameter to align with power because the individual blade loading measurements are subject to cyclical variations as they rotate. Figure 6.11 illustrates this synchronisation process for one dataset.

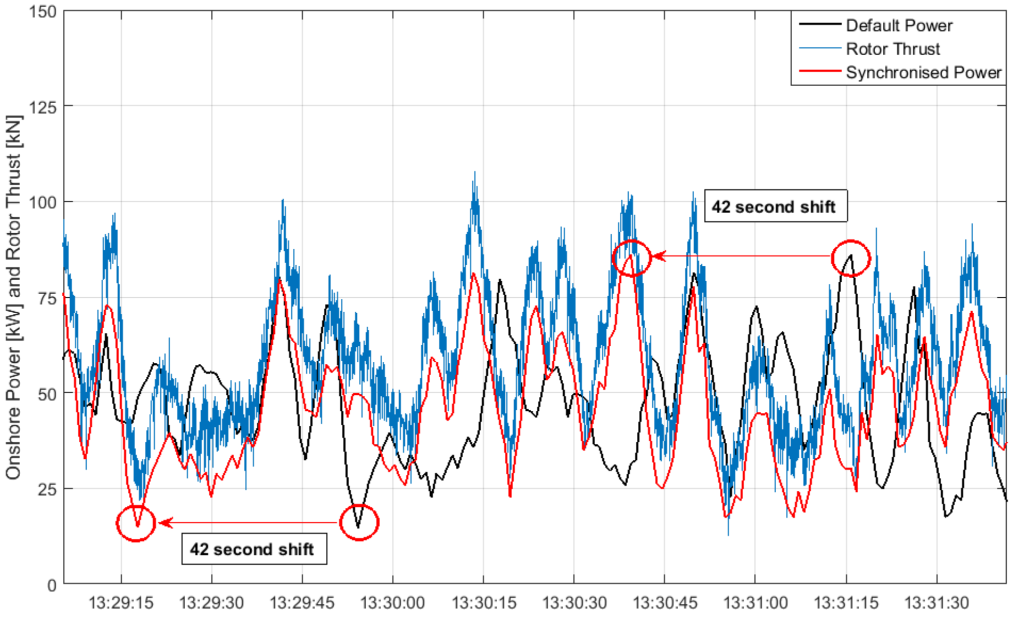

Figure 6.11: *The measured onshore power before (black) and after (red) synchronisation with rotor thrust (blue)*

From Figure 6.11 it can be seen that the peaks in power and thrust better align with each other after shifting the GE SCADA data by 42 seconds. The difference between the clocks was found to vary from day to day, with the root cause of this still being investigated. The synchronisation process presented adequately fixes the data, but is reliant on the strain gauges. It is possible that incoming disturbances measured by the single-beam could be used in a similar manner for data synchronisation in the event of the strain gauges failing. This approach, however, was never required during the test period.

6.4 Test Conditions

After a commissioning period that lasted until the 13th of January, 2016, the turbine began prolonged power production trials. The majority of which took place during ebb tides to increase confidence in operating the device in weaker conditions, before gradually the flood tides were utilised more regularly to test the turbine in higher flows. Since there is a larger dataset available for ebb tides, the results that follow in this chapter are presented for these conditions only. This amounts to in excess of 30 hours of ebb power production in January.

Figure 6.12 shows the tidal conditions for the entirety of January, as measured by the RAMP ADCP. There were two consistent power production periods during the month that occur towards the end of the spring tidal periods, with mean ebb flows reaching up to 1.6 m·s^{-1}. The turbine did not generate power on the week commencing the 18th of January as TEL sought clarification from regulators over the failure of one of its environmental monitoring sensors. Power production trials resumed on the 25th of January. There are some gaps in the dataset as a consequence of the ADCP software crashing. This never occurred during power production.

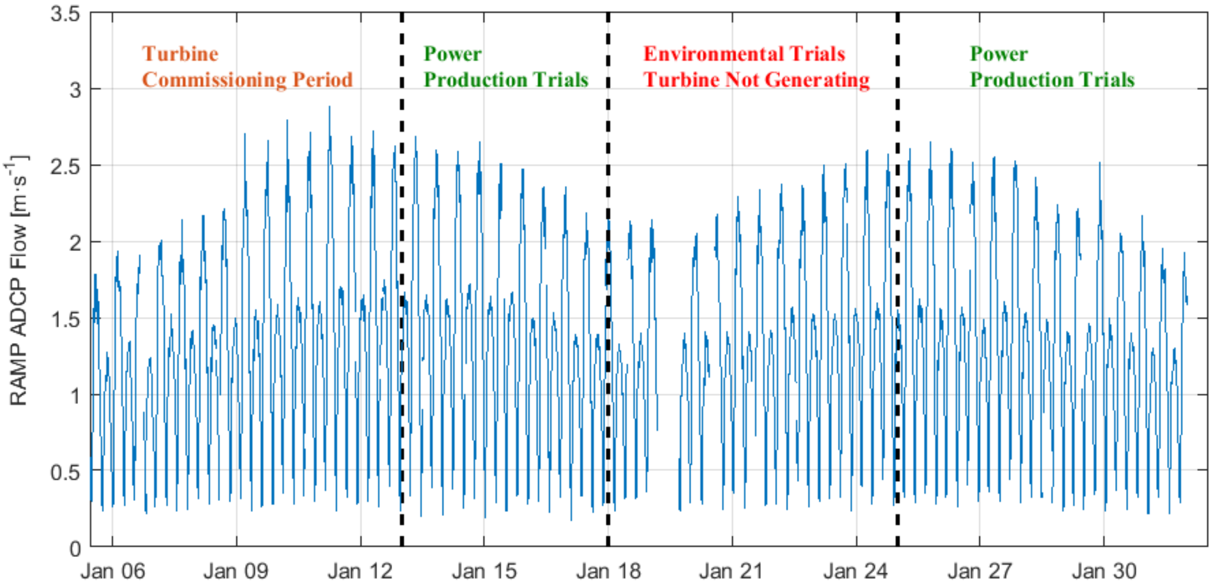

Figure 6.12: *RAMP ADCP flow conditions during January, 2016, and the status of the turbine*

Figure 6.13 shows an example of the flow profiles obtained from both the RAMP ADCP and single-beam during the same three phases of an ebb tide: rising from slack water; peak flow; and falling back to slack water. The spatial measurements have been temporally averaged over 10 minute periods. RAMP ADCP measurements are compared with the power weighted rotor average value (coloured dashed lines) derived using Equations 6.1 and 6.2. In addition, a 1/8th power law profile (black dashed line) is formed about the central measurement, allowing the profiles to be compared with the flow fields used in the numerical simulations (Chapter 3). The single-beam measurements are compared with the length averaged value (coloured dashed lines), as described in Section 6.2.

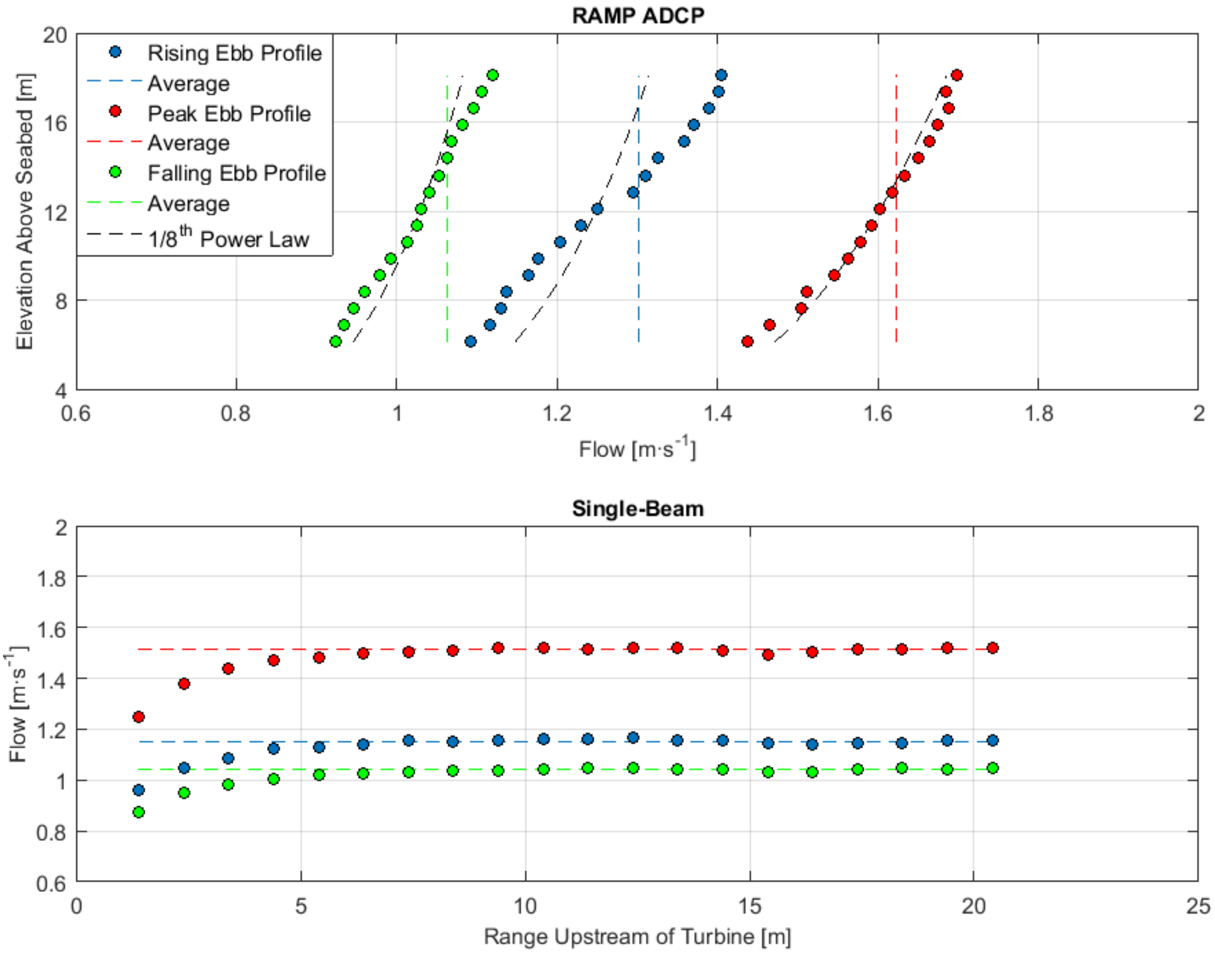

Figure 6.13: *Flow profiles as measured by the RAMP ADCP (top) and single-beam (bottom) during three phases of an ebb tide*

The shear profiles as measured by the RAMP ADCP consistently show greater variation between the bottom and top of the rotor than that of the 1/8th power laws, with a particularly low level of agreement found during the rising flow period. These results suggest that the power exponent is typically greater than 1/8th, although a further analysis on a larger number of samples would be required to conclude this. The derived average values are always greater than the central, hub height value, as a consequence of the power weighting applied in Equations 6.1 and 6.2. The difference is typically small, although this increases with the size of the shear profile, as can be seen on the rising ebb condition.

The single-beam profiles clearly show the aforementioned deceleration in flow near the rotor in all tidal conditions, justifying the length averaging of measurements obtained from 11.4 – 20.4 m upstream. These mean values are consistently lower than those derived from the RAMP ADCP. The power weighted average calculation of RAMP ADCP measurements accounts for some of this difference, but this instrument's mean hub height values are also consistently higher than those from the single-beam. This result was also found during the preparatory tests of the instruments at Pembroke Dock (Chapter 5), where it was attributed to the difference in quantities measured by each instrument, i.e. flow magnitude compared with one flow velocity component. To complement this work, the Ramsey Sound ebb flow correlation was studied further by comparing all of the derived average values from both instruments. The length of the single-beam record is approximately just 50% of that of the RAMP ADCP due to some periods of unrecognised downtime. The measurements that can be compared, which amounts to approximately 15 hours of operation, are shown in Figure 6.14.

Similar to the tests at Pembroke Dock, it can be seen that almost all of the single-beam measurements are lower than that obtained from the RAMP ADCP. There are a few exceptions, but the results do not suggest that the flow at the turbine is greater than that at the RAMP ADCP. However, unlike the previous tests, none of the measurements lie outside 15% of a perfect correlation, implying that the directional variation of flow is lower. This is confirmed in Figure 6.15, in which a distribution of instantaneous flow directionality is shown for an ebb tide. As much as 99% of the data lie within ± 25° of the dominant flow direction, compared with 67.5% from a similar analysis of the Pembroke Dock results.

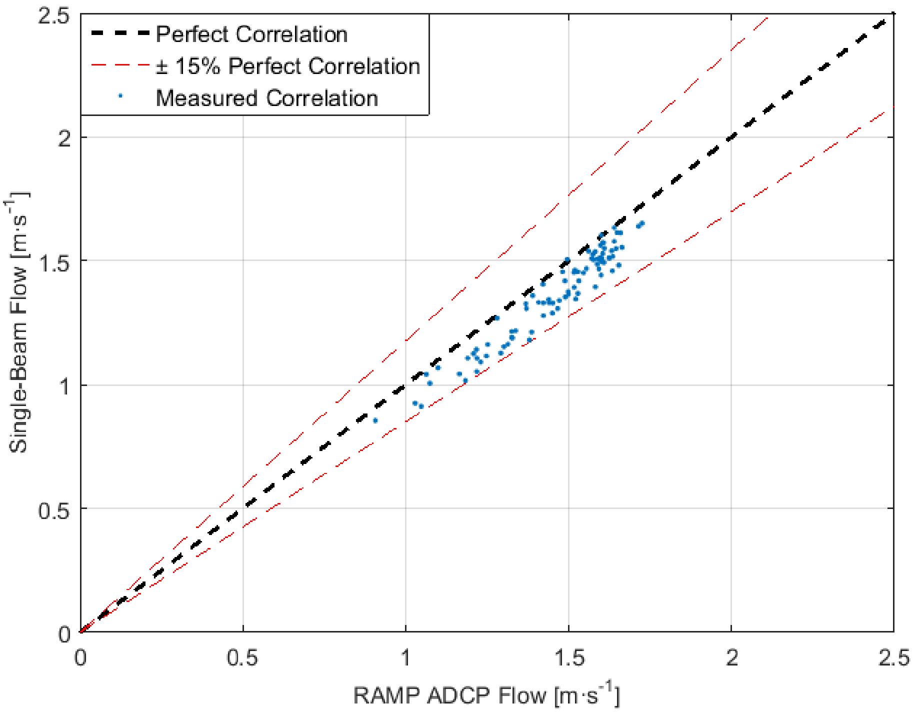

Figure 6.14: *Distribution of single-beam flow measured relative to the RAMP ADCP*

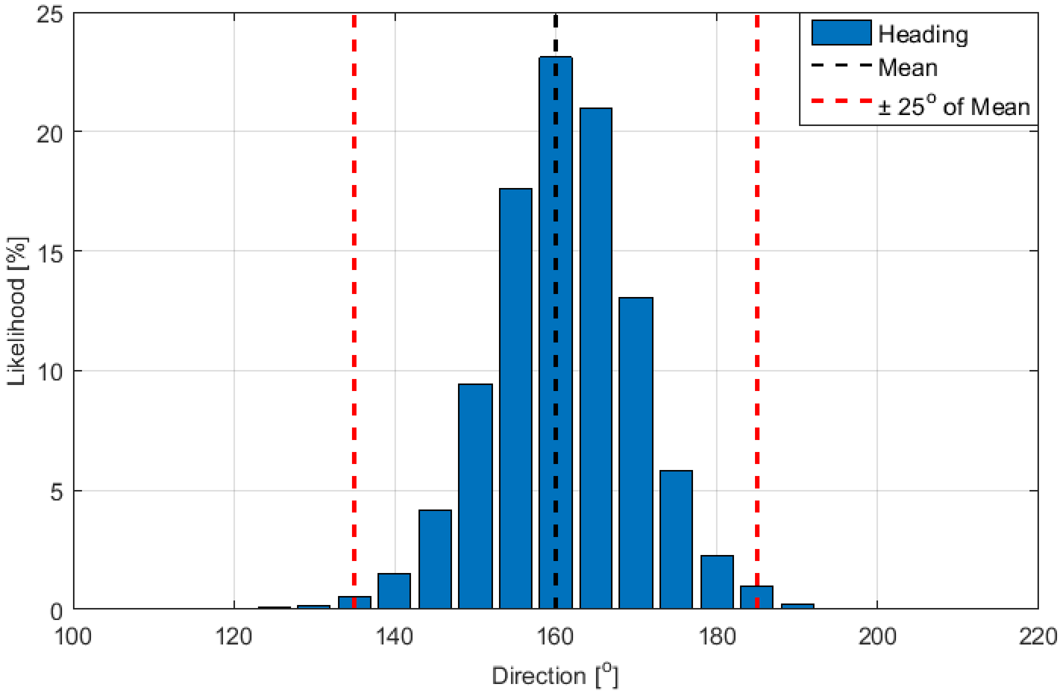

Figure 6.15: *Probability distribution of ebb flow heading measurements*

Therefore, the ability of the RAMP ADCP to capture flow magnitude accounts for the majority of the measured differences between the instruments, similar to the findings from the Pembroke Dock tests. This is despite the fact that the rotor, and hence single-beam, could be subject to an additional yaw error. The work during the commissioning phase identified a pair of yaw angles to default the turbine to for ebbs and floods, and typically operators would perform yaw corrections of less than 5° during power production if they thought there was a misalignment. This low level of yaw activity and the narrow spread of flow directionality shown in Figure 6.15 suggests that concerns relating to misalignment are thought to be low, although there will undoubtedly be periods in which they were significant.

The issue of spatial variability at the site is one other consideration that could have a considerable influence on flow correlation. The instruments do not derive flow measurements from the same volume of water, unlike the tests at Pembroke Dock. Instead, they are approximately 35 m away from each other. It is entirely possible that there are local variations in the flow between these two sites. Spatial variation in Ramsey Sound has already been demonstrated between the locations of two seabed ADP deployment sites in proximity to the turbine [97], separated by less than 50 m, while the transect survey work in [83], [93] showed that the flow across the site is considerably non-uniform. The differences between the measurements obtained from the instruments are discussed in more detail in Section 6.8.

6.5 Non-Dimensional Rotor Characteristics

There was a desire to understand the overspeed characteristics of the rotor in the relatively benign ebb conditions before testing this control region in the stronger flood tide. However, the turbine would never achieve rated power in ebb tides because of the flow conditions, with maximum ebb flows of less than 2 $m{\cdot}s^{-1}$. Therefore, it was necessary to de-rate the turbine in order for it to overspeed. This was achieved by overriding the control system to run the turbine in a speed mode, such that it could be commanded to step through various rotational speeds in a manner not dissimilar to the procedure used for the scale model tests in Chapter 4.

Figure 6.16 shows the time-series of flow and generator RPM from this test. The flow is subject to the spatial averaging methods described in Section 6.2, but no temporal averaging was performed at this stage. The test took place around the time of peak ebb flow, and it can be seen that the currents fluctuated about 1.5 $m{\cdot}s^{-1}$ on both sensors during this period. As before, the single-beam measurements are generally lower those on the RAMP ADCP. There are some notable instances where this is particularly evident, including at 15:00 where the flow on the single-beam decreases to in the region of 1 $m{\cdot}s^{-1}$. This could be a result of any of the considerations discussed in Section 6.4. The generator speed is incremented in steps of the order of 75 RPM, which equates to slightly more than 1 RPM on the rotor (gearbox ratio = 74.05). Each step lasted five minutes, with maximum and minimum generator speeds of 870 and 350 RPM achieved respectively.

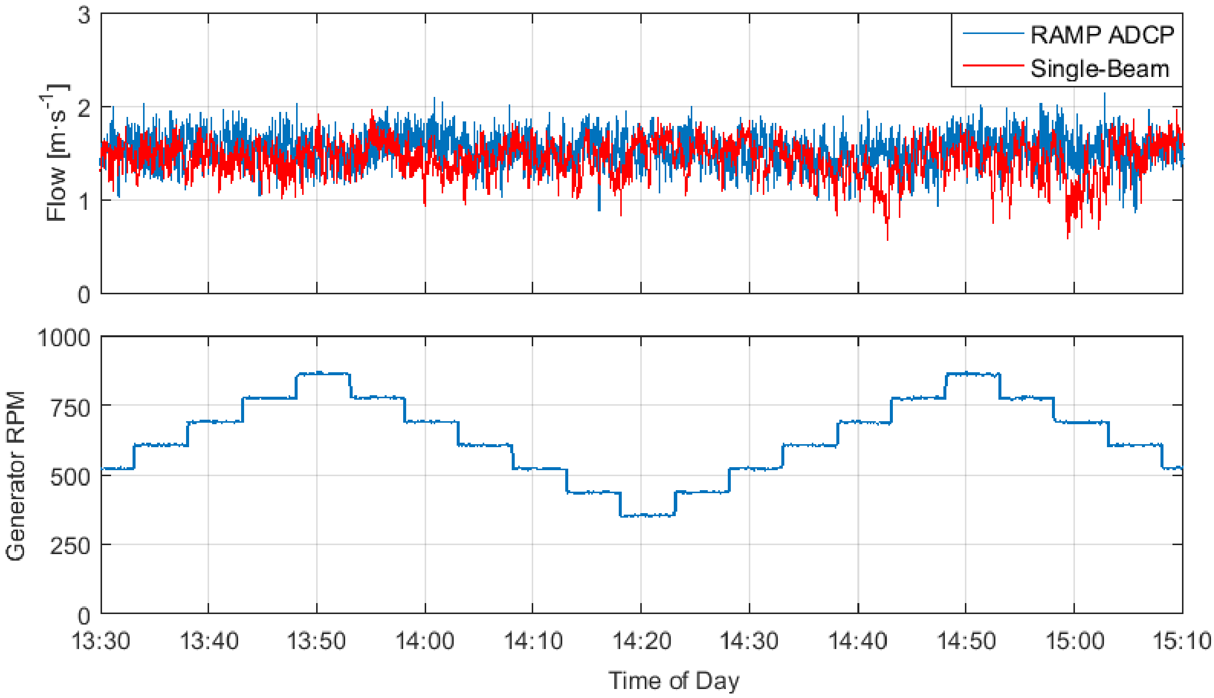

Figure 6.16: *Time-series of flow (top) and generator RPM (bottom) during the test aimed at determining the rotor characteristics*

Similar to the scale model testing, measurements were averaged within each stepping period, removing data that lie within ± 5 seconds of the stepping point. For the RAMP ADCP measurements, the temporal averaging method as described by Equation 6.2 was used. All of the non-dimensional parameters that follow are calculated relative to both flow instruments, providing two references.

The derived rotor $c_p - \lambda$ measurements are shown in Figure 6.17, compared with a numerical curve from the FAST model. The test covered the λ range 2 – 5.3, in which the general the shape of the predicted curve has been captured by the measurements, with a peak in c_p occurring near $\lambda = 3$ and a reduction thereafter. Most of the measurements, however, fall below the numerical curve and are subject to a considerable amount of variation. This is unlike the measured $c_p - \lambda$ curve from the scale model tests in Chapter 4, where the results were in better agreement with predictions. The measurements of both flow velocity and rotor power during these full-scale tests are subject to a greater amount of experimental uncertainty, and this is believed to be the main reason for the lower agreement. The calculation of c_p is particularly sensitive to the flow measurement, since c_p is inversely proportional to the velocity cubed (Equation 3.2). This could be problematic when using the RAMP ADCP reference, in which there is no consideration of spatial variation or yaw misalignment. Research from the wind industry has suggested that turbine power is affected by the cosine-squared of the yaw misalignment angle [208]. Thus it is believed that the RAMP ADCP often overestimated flow velocity. In contrast to this, some of the single-beam results suggest that this instrument occasionally underestimated flow velocity, given that c_p was measured to be as high as 0.53 using this reference.

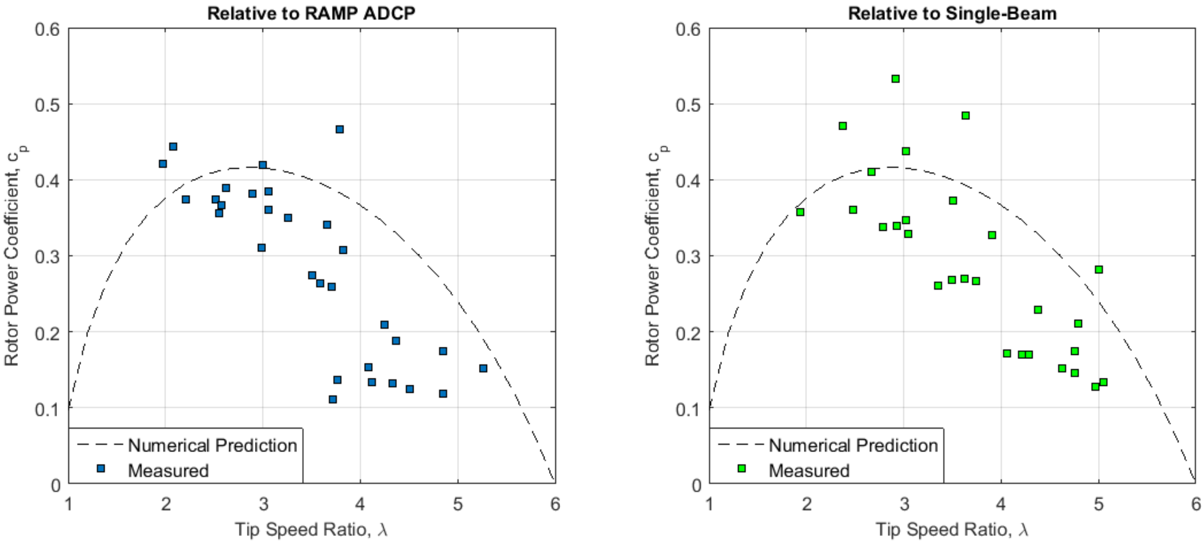

Figure 6.17: *The rotor power coefficient, c_p, as a function of tip speed ratio, λ, measured relative to the RAMP ADCP (left) and single-beam (right)*

In addition to this, some difficulties were encountered with power generation during these tests due to the low flow conditions. There were instances in which the turbine had to be motored in order to hold the desired speed as the flow was not strong enough. This usually occurred at high λ. Furthermore, the power loss back calculations detailed in Section 6.3 are mostly conservative so that power is not overestimated, implying that a more rigorous approach is required to better understand rotor power.

In terms of the non-dimensional loading characteristics, the first parameter of interest is the blade root bending moment coefficient, c_{M_y}. The normalisation is similar to the thrust coefficient, c_t, expression (Equation 3.3), except the cube of the rotor radius, R, is used instead:

$$c_{M_y} = \frac{Blade\ Root\ M_y}{\frac{1}{2} \cdot \rho \cdot \pi \cdot R^3 \cdot v^2} \tag{6.7}$$

The results are displayed separately for each blade in Figure 6.18, along with the mean value across all three blades. These are also compared with a curve predicted from FAST. It is clear that single-beam provides a better indication of the flow experienced by the rotor, demonstrated by the narrower and more consistent scatter. This was not as evident in the $c_p - \lambda$ results due to the indirect measure of rotor power, whereas the loads were obtained locally. The values derived relative to the single-beam also show a particularly good agreement with the theoretical predictions, scattering closely about the numerical curve. Both flow references display the diminishing c_{M_y} with increasing λ characteristics of the blades. Generally the individual blade measurements agree well with each other across the λ range, especially when comparing results from blades 1 and 3. Their agreement with blade 2 is usually good, but at high λ there are minor differences. This occurs when the loading is very low.

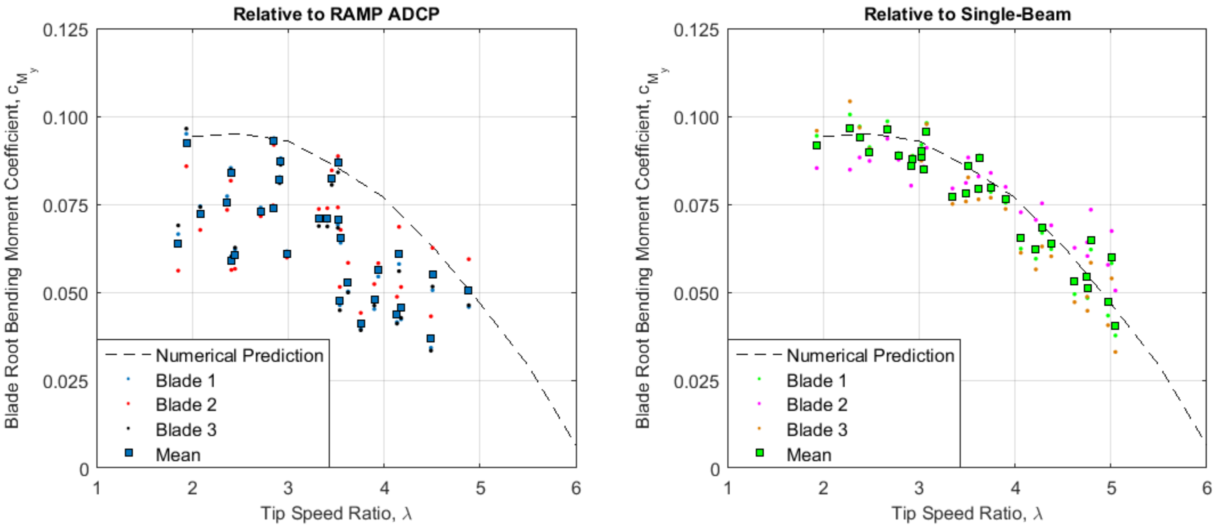

Figure 6.18: *The blade root bending moment coefficient, c_{M_y}, as a function of tip speed ratio, λ, measured relative to the RAMP ADCP (left) and single-beam (right)*

The measurements of root F_x force can be normalised in exactly the same way as rotor thrust to form blade root axial force coefficients, c_{F_x}:

$$c_{F_x} = \frac{Blade\,Root\,F_x}{\frac{1}{2}\cdot\rho\cdot\pi\cdot R^2\cdot v^2} \tag{6.8}$$

The root c_{F_x} results and FAST prediction are shown in Figure 6.19. Unlike the root bending moment coefficients, most of the measured root c_{F_x} are lower than the numerical predictions when determined relative to both instruments, although the single-beam results are closer. The shape of the curve is captured well on the single-beam, while there is evidence to suggest that c_{F_x} decreases at high λ in the RAMP ADCP results also. Contrary to the bending moment results in Figure 6.18, the agreement between the blades is greatest on blades 1 and 2. Blade 3 usually measured the lowest force, and has resulted in the mean axial force often being lower than that determined from blades 1 and 2. The measurements derived from blades 1 and 2 often appear to agree well with the numerical predictions using the single-beam reference.

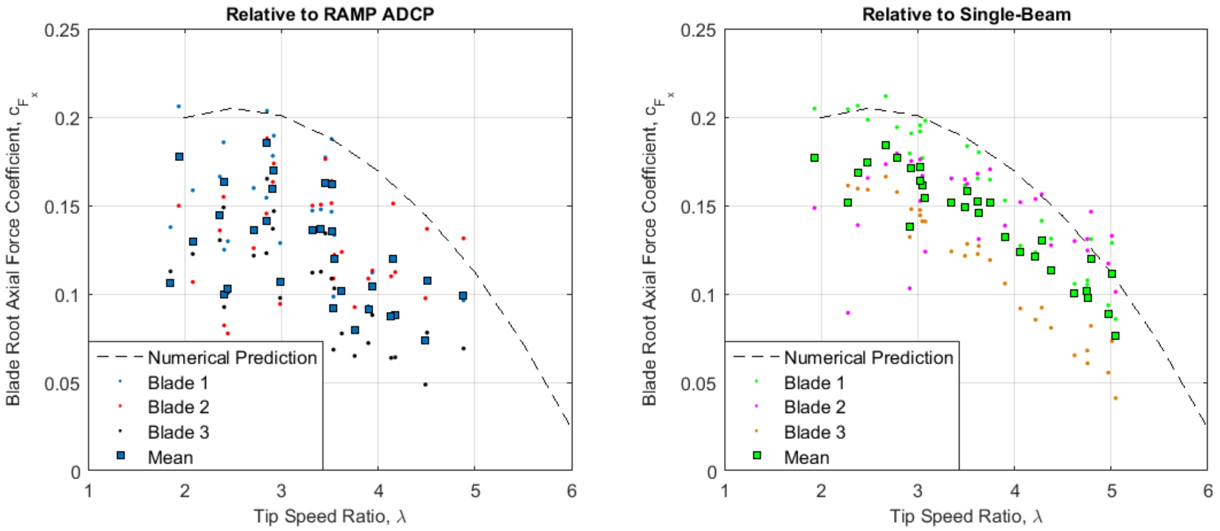

Figure 6.19: *The blade root axial force coefficient, c_{F_x}, as a function of tip speed ratio, λ, measured relative to the RAMP ADCP (left) and single-beam (right)*

The lower than expected measurements of root c_{F_x} have been attributed to the sensitivity of the curve fitting process on radial bending moments, as described in Section 6.3. While the results in Figure 6.18 suggest that the location of the blade root bending moment is identified well from the process, it is believed that often the curves do not form a steep enough gradient near the root, resulting in an axial force underestimate. The axial force blade-to-blade variation is also greater, highlighting further the difficulty of ensuring that the fitted curve forms the correct shape. This issue is discussed in more detail in Section 6.8, along with some suggested improvements to the process.

Since the blade root axial forces have been underestimated, it is unsurprising that the resulting net rotor thrust is also lower than predicted, as shown in Figure 6.20. Both of the measured curves again provide firm evidence of the predicted thrust shedding characteristics of the rotor, with the single-beam results suggesting about a 50% reduction in thrust loading by increasing the turbine λ from 3 to 5. This agrees well with the numerically predicted overspeed behaviour.

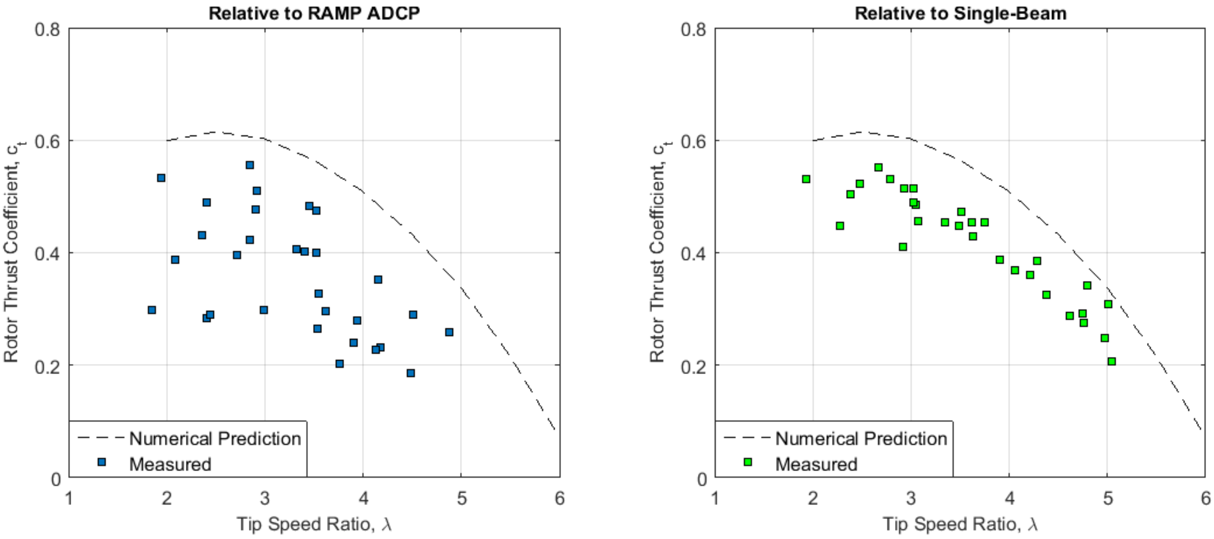

Figure 6.20: *The rotor thrust coefficient, c_t, as a function of tip speed ratio, λ, measured relative to the RAMP ADCP (left) and single-beam (right)*

6.6 Power Performance Assessment

The turbine controller objectives were described previously in Chapters 3 and 4, in which the generator torque is controlled based on the shaft speed to ensure that the maximum power from the device is extracted at all times. However, during the initial testing of the full-scale device, it was realised that a controller with a different philosophy had been supplied to TEL. The controller was instead using the mean flow measured by the RAMP ADCP to change the speed of the generator, such that the rotor operated at λ_{opt}. While in theory there is nothing wrong with this control strategy, the reality is that it is flawed for a number of reasons, and resulted in the turbine rarely following the generator torque-speed curve of optimum operation. To begin with, the RAMP ADCP is an inadequate reference of the flow conditions experienced by the rotor because it is not positioned upstream of the turbine. The results in Section 6.5 showed that there are local flow variations between the locations of the turbine and RAMP ADCP. Furthermore, the controller was using an average of the flow conditions obtained over the preceding one minute period. Not only is this information historical, but it places a limit on the update rate of the controller, i.e. one minute. As a direct consequence of this, the turbine would attempt to keep its speed constant for the entirety of this period. In reality the flow can vary considerably over this timeframe, meaning that under this controller the generator would be required to make large variations of reactive torque in order to keep its speed constant. Not only is this undesirable from a power performance perspective, but the large fluctuations in torque on the drivetrain will have consequences on its fatigue life. The result is a turbine that is neither fixed nor variable-speed, and is instead somewhere in between. The issues arising from this sub-optimal controller are discussed further in Section 6.8.

A controller upgrade was required to enable the desired full variable speed operation, as demonstrated by the scale model tests in Chapter 4. This could not be obtained during the month of January, meaning that the results presented in this section are all subject to the turbine operating sub-optimally. A methodology, however, has been developed to identify when the turbine, on average, operated close to the desired curve. The process is illustrated in Figure 6.21, which shows the measured 10 minute mean values of generator speed and torque. The black dashed line is the curve of the optimum controller performance, and is identical to that derived previously in Section 3.3. It can be seen that the majority of the measured data is found on the right hand side of this curve, suggesting that the generator was usually running too fast. Despite this, there are some periods in which the turbine on average operated near optimum, as shown by the measured data highlighted in red and lying within a 10% boundary (red dashed lines) formed about the idealised curve. This amounts to 30% of the data. In all subsequent analysis in this chapter, these near optimum periods are highlighted to separate these results from the other measurements.

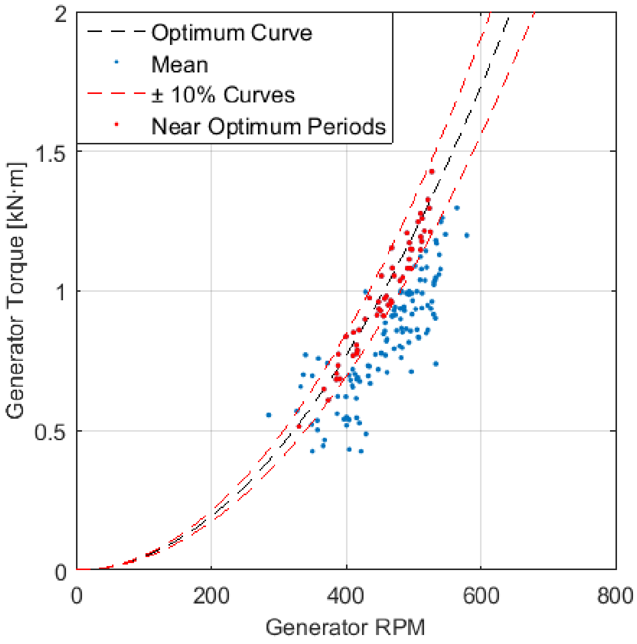

Figure 6.21: *Measured generator speed and torque (blue) compared with the curve of optimum operation (black). The data in red are periods where the turbine operated close to this idealised curve*

During these near optimum periods, the correlation between the single-beam and RAMP ADCP measurements was found to improve, as would be expected. This is shown in Figure 6.22, where a probability distribution of flow correlation from optimum operation periods is compared with an equivalent distribution for all ebb operations. Approximately 64% of the single-beam measurements lie within 0.94 – 1 of the RAMP ADCP during optimum operation, compared with 44% for all periods.

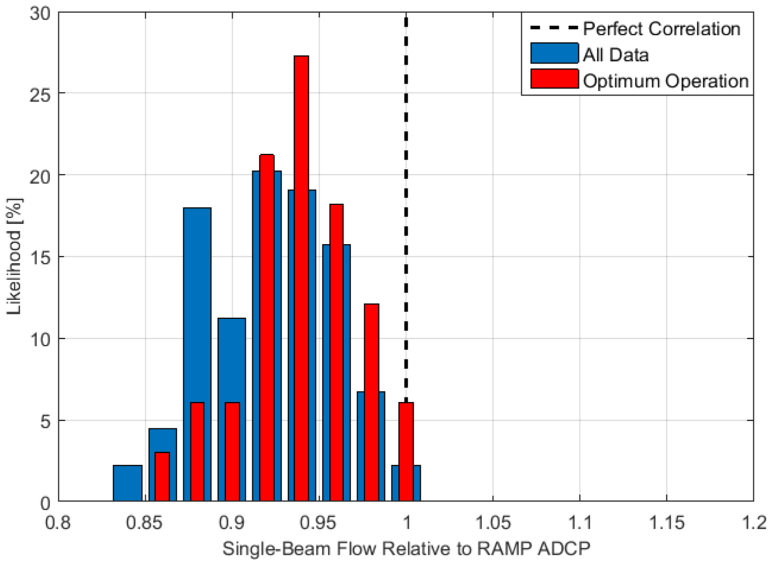

Figure 6.22: *Improved flow correlation observed during optimum periods of operation*

The mean recorded generator power is scattered in Figure 6.23, along with the maximum value measured in each 10 minute period. These results are compared with the numerically predicted performance curve from the mathematical modelling work in Chapter 3. The numerical maximum values from the Tidal Bladed ebb simulations at 1 and 1.5 m·s^{-1} are also plotted.

Due primarily to the usage of the sub-optimal controller, the majority of the scattered mean power measurements are lower than predictions. The conservative power efficiency calculations are also believed to account for some of this deficit. Results from the selected optimum periods of operation, however, consistently show an improved agreement with the theoretical curve, confirming that the rotor was closer to the maximum c_p during these times. This is particularly evident in the RAMP ADCP results, which are subject to a greater amount of variation than those measured relative to the single-beam, consistent with the findings in Section 6.5. This provides further evidence that the RAMP ADCP measurements regularly differ to those observed locally at the turbine as a result of either spatial variation or yaw misalignment. The scatter from the single-beam results, in contrast, is much narrower and closer to the numerical curve. The measured maximum values appear to be close to the numerical results at 1 m·s^{-1} but not 1.5 m·s^{-1}, where they are instead lower. This could be another consequence of the turbine rarely operating at the point of maximum c_p.

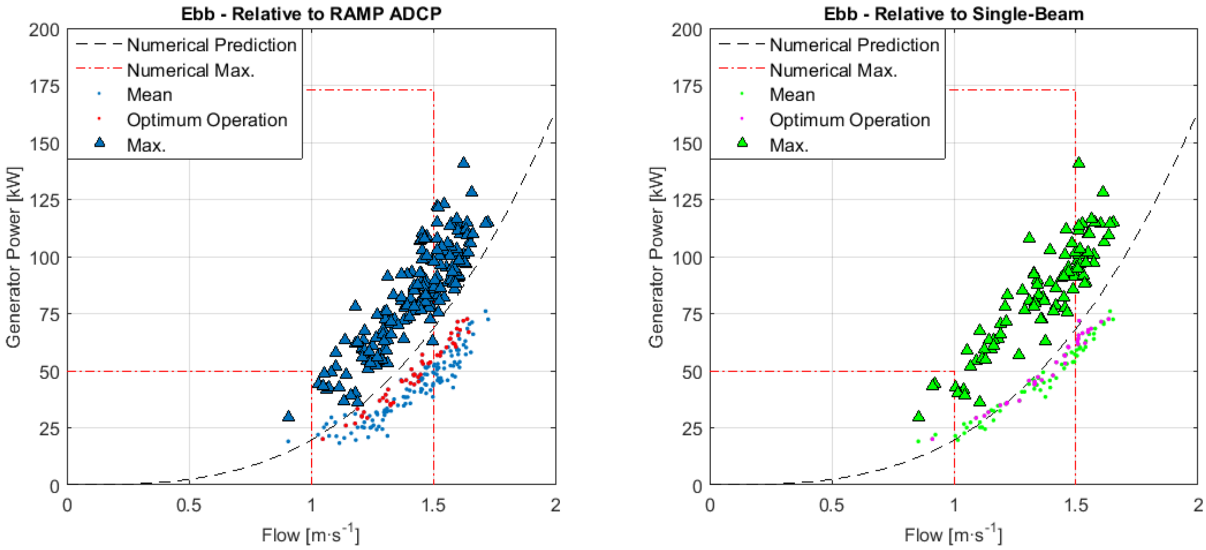

Figure 6.23: *Dynamic generator power curves relative to the RAMP ADCP (left) and single-beam (right)*

To develop a power curve from the results in Figure 6.23, the IEC guidelines recommend further averaging the data by sorting it into discrete flow velocity bins. This has been performed for the optimum data only to produce a curve that is more representative of the potential of the turbine. The calculations are as follows:

$$\bar{U}_i = \frac{1}{N_i}\sum_{n=1}^{N_i}\bar{U}_{i,n} \tag{6.9}$$

$$\bar{P}_i = \frac{1}{N_i}\sum_{n=1}^{N_i}\bar{P}_{i,n} \tag{6.10}$$

Where U_i and P_i are the mean weighted flow velocity and generator power measurements in bin i respectively, while N_i is the number of data points in bin i. An increment of 0.1 m·s^{-1} was chosen to ensure that at least three RAMP ADCP and single-beam measurements fall within each bin between 1.15 – 1.65 m·s^{-1}. This meets the minimum IEC recommended data capture requirement for each velocity bin. Table 6.2 lists the number of data points in each bin for both instruments. The single-beam also satisfies the minimum data requirement in the bin range 1.05 – 1.15 m·s^{-1}, but neither instrument captured enough measurements between 0.85 – 1.05 m·s^{-1}. In total, the amount of useable data for the RAMP ADCP totals just over 8 hours, while it is slightly more than 5 hours for the single-beam.

Table 6.2: *The number of measurements within each flow bin range. Values highlighted in red do not meet the minimum data capture requirement*

Flow Bin Range [m·s^{-1}]	No. of RAMP ADCP Points	No. of Single-Beam Points
0.85 – 0.95	0	1
0.95 – 1.05	1	0
1.05 – 1.15	1	3
1.15 – 1.25	6	3
1.25 – 1.35	8	6
1.35 – 1.45	12	3
1.45 – 1.55	9	13
1.55 – 1.65	14	4

The finalised generator power curves are shown in Figure 6.24. It is clear that despite only covering the lower region of the full power curve, the measurements broadly form the expected cubic relationship with flow velocity, although there are some fluctuating points that can be attributed to the sub-optimal controller. The measured curve would only be expected to take a cubic form if the turbine successfully tracked the maximum c_p. Instead, performance is down from prediction by as much as 20% in the RAMP ADCP reference and 14% relative to the single-beam. Some of measurements from the latter reference in the lowest flows are in good agreement with the numerical curve (< 1% difference) and even outperform prediction, but these occur in flow bins where just 3 measurements were obtained (Table 6.2), and hence the confidence in these results is low. This does, however, highlight that the potential performance of the turbine is in line with prediction, but it is necessary for the full variable speed control strategy to be implemented in order for the device to achieve it.

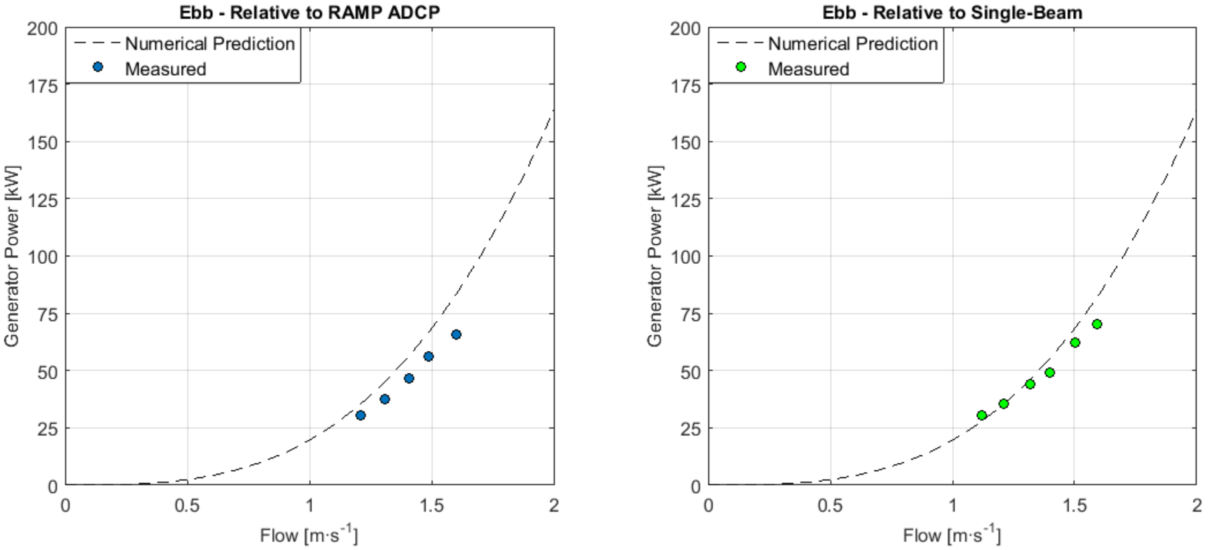

Figure 6.24: *Generator power curve measured relative to the RAMP ADCP (left) and single-beam (right)*

6.7 Dynamic Rotor Loading

The same process of separating the data based on the controller performance has been applied to the dynamic rotor loading results. The mean and maximum values from each 10 minute period are presented for the blade root loads and rotor thrust in Figure 6.25, relative to both flow sensors. Due to the volume of data on the blade root plots, the individual blade measurements are not separated by colour, as in Section 6.5. Instead all of the blade measurements are displayed using the same colour. As before, each plot contains the numerical steady-state curves and maximum values at 1 and 1.5 $m \cdot s^{-1}$.

Figure 6.25 would appear to suggest that the majority of the measured dynamic loads are lower than those predicted. This result should be expected, given that Figure 6.21 showed that the rotor spent the majority of the time overspeeding during these tests, and hence operating at a region where the respective loading coefficients are lower (Figures 6.18 – 6.20). In addition to this, the results in Section 6.5 suggested that the blade root axial forces and rotor thrust were being underestimated by the curve fitting process used to derive these loads.

The measured loading does, however, consistently show an improved agreement with the numerical curves during periods of optimum operation, similar to the power performance results. Furthermore, the agreement is always better using the single-beam flow reference, again consistent with results presented earlier in this chapter. The blade root bending moments (top plots) measured relative to this instrument show the greatest agreement with theory, scattering closely about the numerical curve. This is consistent with the non-dimensional rotor loading results in Figures 6.18 – 6.20.

In contrast to this, the blade root axial forces (middle plots in Figure 6.25) exhibit a much broader scatter. This is particularly evident in the lowest flows, where it is possible to see the blade-to-blade variation in loading in currents less than 1 $m \cdot s^{-1}$ despite the uniform colouring. Since these are mean loads, this level of variation across the blades is unexpected, and this result is instead believed to due to the aforementioned sensitivity of the curve fitting process. However, the blade-to-blade variation decreases in higher flows, implying that the consistency of the curve fitting process improves when the blades are subject to greater loading. In addition to this, the agreement with the numerical curve increases at higher flows. These findings are believed to be a consequence of difficulties encountered during the onshore calibration of the strain gauges, where there was increased uncertainty around the calibration data obtained when the blades were lightly loaded. A significant number of the ebb loads presented in Figure 6.25 fall within the region where there were calibration issues. The turbine was designed to operate under much higher loading in the stronger flood tides. Lastly, the net rotor thrust (bottom plots in Figure 6.25) findings are similar to the blade root axial forces, with the measurements showing an improved agreement with theory at higher flows.

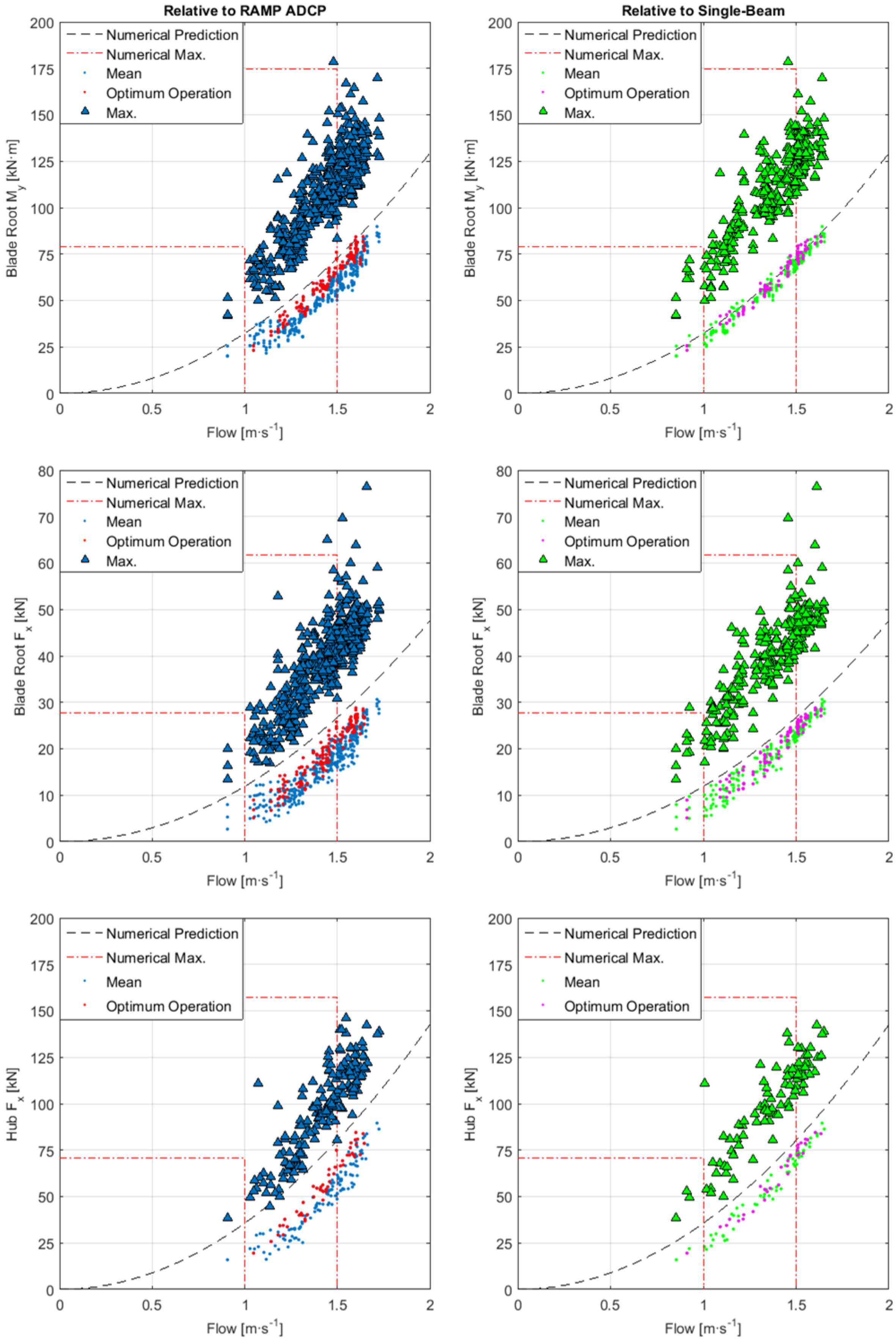

Figure 6.25: *Dynamic rotor loading in ebb flows measured relative to the RAMP ADCP (left column) and single-beam (right column). From top to bottom: blade root M_y; blade root F_x; and rotor thrust*

For all of the loads in Figure 6.25, the measured maximum values generally appear to be lower than those predicted numerically. Just one measured root bending moment lies outside the numerical maximum in flows of 1.5 m·s^{-1}. Since this point is considerably higher than the other maximum values recorded around this flow, it could be a questionable measurement. There are also a couple of root axial force measurements that lie outside the predicted maximum values. Again, these appear to be dubiously higher than the majority of other nearby values. This, however, is not a comprehensive comparison with the Tidal Bladed results. If this was to be studied further, it would be necessary to compare the flow conditions of the model and test site, with specific attention to turbulence. It is possible that the levels of turbulence during testing were greater than those in the simulations. Furthermore, the total simulation time at these flows amounts to just two hours, considerably shorter than the operational time. If further simulations were performed, it is possible that higher maximum values would have been found.

Similar to the mean loading, the lower than predicted maximum values could also be a consequence of the rotor usually running too fast (Figure 6.21), although there were periods in which it ran slow. Therefore, it is difficult to form a fair comparison in dynamic loading without the turbine following a control strategy similar to that modelled.

Using the exact same method of binning the data as described in Section 6.6, the mean loads were averaged further to develop finalised curves. As before, this was only applied to the measurements obtained during periods of optimum operation. These results are presented in Figure 6.26, and are labelled separately for each of the blade root loads.

By averaging the data further the relative strengths of each flow measuring instrument are no longer as apparent, with the results relative to both the RAMP ADCP and single-beam now visibly showing a better agreement. The latter is, however, still consistently closer to the numerical predictions. The blade root bending moments, for example, all lie within 9% of the numerical predictions relative to the single-beam, while they are all within 22% relative to the RAMP ADCP. This is an impressive result considering there are fewer single-beam measurements to form these mean values, since it was not operational during some of the test period.

As observed previously in Figure 6.25, the agreement with the numerical predictions increases with loading. In the two highest single-beam flows (1.5 m·s^{-1} and above) the measurements agree to within 3, 11 and 9% of the theoretical predictions for the blade root bending moments, the blade root axial forces, and the rotor thrust respectively. The blade-to-blade agreement of root bending moments is good in all flows, although blade 3 consistently measures slightly higher values. For the root axial forces, the improved blade-to-blade agreement with increased loading is now visibly clearer than in Figure 6.25. The behaviour of blades 2 and 3 are found to be the least predictable in low flows, whereas blade 1 is usually the closest to the numerical curves.

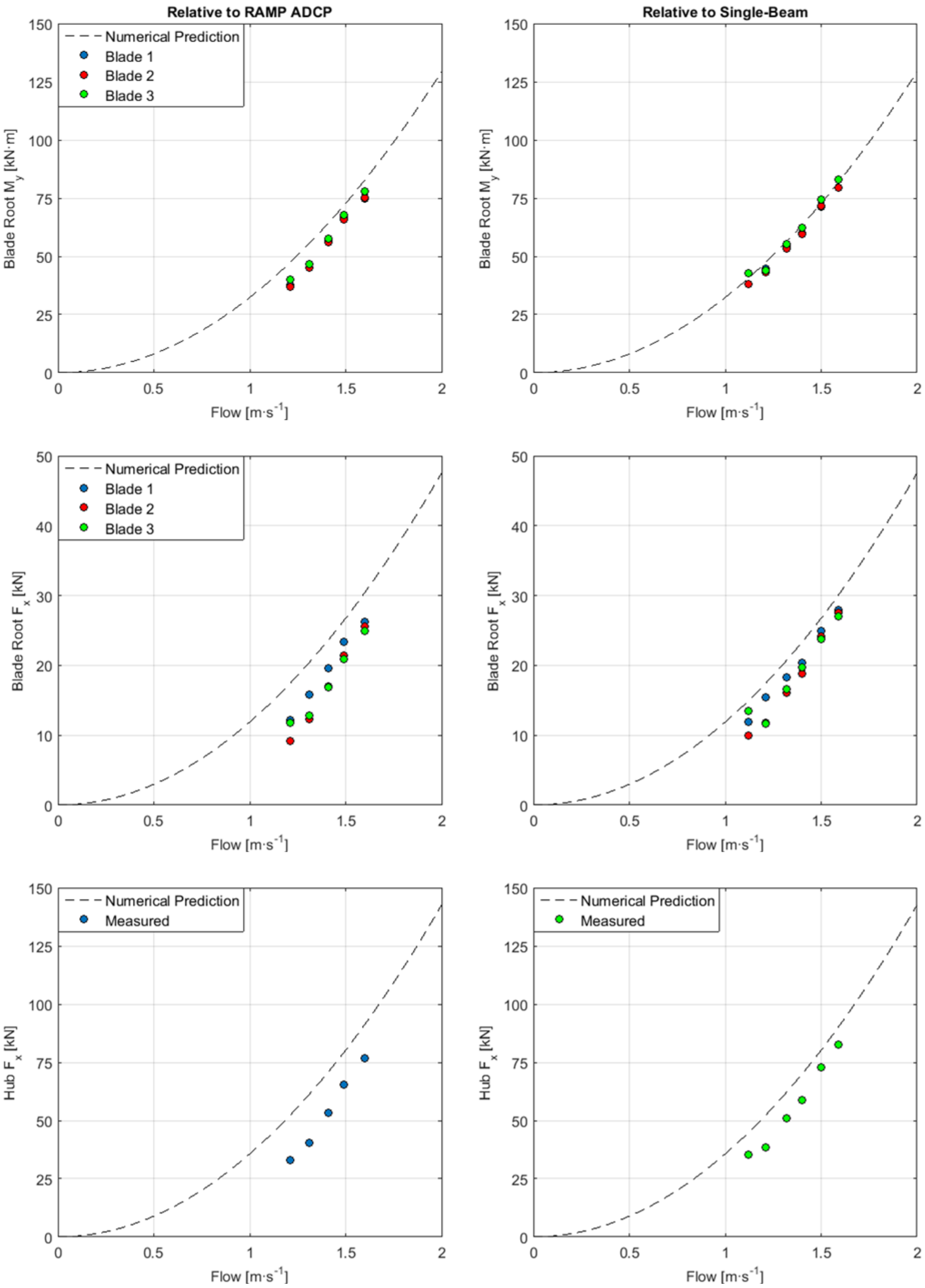

Figure 6.26: *Finalised rotor loading curves in ebb flows measured relative to the RAMP ADCP (left column) and single-beam (right column). From top to bottom: blade root* M_y*; blade root* F_x*; and rotor thrust*

6.8 Recommendations for Future Work

The 12 m DeltaStream^{TM} turbine was successfully installed at Ramsey Sound in December, 2015, with first power exported to the local distribution network soon afterwards. This chapter has reported on the measured power performance and rotor loading from the early operational trials in ebb flows. The results were found to be broadly in line with predictions obtained in earlier chapters on numerical modelling and scale model testing. The majority of the observed differences can be attributed to the sub-optimum controller used during this test period, as well as uncertainties on a number of the environmental and turbine related measurements. These issues are discussed in more detail here.

In Section 6.6, the majority of the flaws of the controller used during this test period were attributed to the way in which the RAMP ADCP flow was used an input to the system. While the concerns relating to any spatial differences in the flow observed at the turbine location could be minimised by using the single-beam measurements as an input instead, this would only result in minor improvements in device performance. The reality is that the control system supplied is overcomplicated with the addition of the flow measurement input, to the point where the performance of the turbine has been hampered as a direct consequence. In Chapter 4, the desired variable-speed control philosophy was demonstrated at 1:30 scale and proved that flow speed is not a required input to the system, only generator speed is. This same technique is common practice in the wind industry. Measurements of the flow/wind are usually reserved for advanced control techniques, such as yaw corrections [175] and feedforward methods [176].

As mentioned earlier there are also a number of reliability related concerns associated with the tested control system. This is particularly true if the flow measured is considerably lower than reality, leading to the turbine operating at a λ below optimum and where the loading is higher. It is perhaps fortunate that the results presented in this chapter showed that the turbine was generally overspeeding (Figure 6.21). In addition to this, a complete failure of the flow sensors would have restricted operations under this control system, affecting the availability of the device. While it is possible to control the turbine manually, as shown in Section 6.5, this mode of operation is not recommended in the most energetic tidal phases without a reference of the flow conditions. In contrast to this, it is feasible that a turbine could continue to operate safely under such circumstances using the conventional variable-speed control strategy, given the predictability of the tidal resource. However, this would not be a desirable situation and may still impose operational limits.

While the controller has been identified as an area that needs immediate attention, there are a number of other aspects of the test arrangement that could be improved on for subsequent tests. The first of which is the location of the RAMP ADCP, which has consistently throughout this chapter shown that it measures a greater flow than the single-beam. Figure 6.14 showed that the single-beam measured flows as low as 85% of that obtained from the RAMP ADCP. This difference is greater than that which would be expected from the contrasting averaging methods used to process the data from each sensor, as described in Section 6.2. The likelihood is that this is either a consequence of yaw misalignment or spatial differences in the flow. It is difficult to comment on the former without extending the analysis here to compare the mean flow and yaw angles from within each averaging period. This has not been performed because the problem is further complicated by the absence of reliable flow directionality measurements, since the ADCP could not utilise its compass in the ferrous frame it was placed inside. Its heading was instead manually set during installation using a variety of information available, including the compass bearings from a remotely operated vehicle (ROV) used during the process. Comparing the flow directionality results in Figures 6.2 and 6.15, the dominant ebb direction from this test campaign is offset by 8^{o} from a historical survey, although the two surveyed locations are not identical. Even if the measurement of flow directionality could be improved upon, the results would still be subject to uncertainty relating to spatial variation. Not only is the location of the ADCP outside the defined separation distance in the IEC guidelines [142], as illustrated in Figure 6.5, but the recommendations also state that positioning the instrument adjacent to the turbine is the least preferred arrangement. The 2 – 5 D upstream and in-line with the dominant flow direction is instead the favoured configuration, while for both arrangements it is recommended that two seabed mounted instruments should be used. As mentioned earlier, the location of the RAMP was based on constraints relating to the sonar system. The findings in this chapter suggest that this either needs to be relaxed to increase the confidence of results, or that the ADCP needs to be placed in a separate frame that lies within the IEC recommended locations, although there are cost implications with the latter option. Despite this, Figures 6.24 and 6.26 suggested that differences in results between the flow sensors reduced after applying the final averaging step to develop the performance curves, i.e. the method of bins. Perhaps if more data were available for this analysis, it might have been possible to conclude this and reduce the significance of the IEC recommendations.

Throughout this chapter the single-beam results consistently showed the best agreement with numerical predictions, even though it yielded a lower data return and is not an instrument recognised by the IEC guidelines. It also showed considerably lower levels of variation between results obtained during optimum and sub-optimum periods of operation. Similar findings have been observed in wind energy research, where power performance measured relative to rotor mounted LiDAR systems have shown to display significantly lower levels of scatter than a hub-height cup anemometer [175]. The single-beam results found here suggest that if the rotor was subject to a yaw misalignment, it would be observed as a reduction in flow velocity on the instrument, negating the influence of the orientation error. The rotor would still, however, underperform in such circumstances since it would be overspeeding relative to this reduced inflow velocity component, but the difference in expected performance would always be greater when using the RAMP ADCP reference as it measures flow magnitude. All of the dynamic RAMP ADCP results in this chapter exhibited a much broader scatter as a consequence of this and the aforementioned spatial differences. Further to this, the single-beam also proved to be a better reference for establishing the non-dimensional rotor characteristics in Section 6.5, showing that even within a relatively short period of averaging (5 minutes) its results are in-line with expectations. This conclusion could not have been justified with only the RAMP ADCP measurements. The instrument, therefore, has proven to be a valuable addition to the turbine system. Further usage and testing of this instrument would be of benefit to the industry in order to help understand turbine performance, despite the research in the ReDAPT project suggesting its performance related results were optimistic when using an upstream single-beam flow reference [67]. This is believed to be due to the combination of a shorter instrument profiling range (13 m) and an increased rotor diameter (18 m) used in this research, leading to an extended flow deceleration zone in front of the turbine that had not fully recovered within the measurement volume of the single-beam. The work described here showed that inflow uniformity occurs at ranges in excess of 10 m upstream of a 12 m diameter turbine, suggesting that the profiling range of the single-beam needs to be of a comparable magnitude to the rotor diameter. Future research should compare the measurements obtained at these longer profiling ranges with those from an upstream ADCP in order to further evaluate the single-beam. This should include further work on assessing the suitability of the instrument in highly sheared environments, as the results in Figure 6.13 showed that the difference between the vertically averaged RAMP ADCP flow and the hub height value increased with shear. The single-beam has no knowledge of this, but it is possible that a calibration could be applied to its measurements to account for velocity shear.

The flow measurements were used to assess the turbine power performance despite neither instrument meeting the IEC requirements. One of the tests aimed to establish the non-dimensional power characteristics using a similar methodology to that used during the scale model tests (Chapter 4). To the author's knowledge, this is the first time that these performance related measures have been reported on for a full-scale tidal turbine. The results captured the expected shape of the $c_p - \lambda$ curve, but revealed the difficulty in accurately obtaining these characteristics at full-scale primarily as a consequence of the increased uncertainty on the measurement of rotor power. There are as many as five systems between the rotor and the onshore measurement of power, each with their own associated conversion or transmission efficiency. Attempts were made to account for these losses, but this is an area that needs further work and justification in order to accurately recover the rotor power. It is recommended that a power sensor is placed nearer to the rotor in the turbine system, removing the number of back calculations required to establish rotor power. For example, current and voltage sensors could be placed at the output terminals of the generator. Alternatively, rotor torque, and hence power, could be derived from the strain gauges in the blades, removing the need for an additional sensor. The analysis presented earlier in this chapter could be extended to include this, although this measure of rotor power would be subject to its own, and potentially larger, sources of uncertainty, discussed later in this section. The issue of measuring the rotor power characteristics was further complicated by the requirement to occasionally motor the turbine during instances of weak flow. While this had no effect on the rotor loading measurements, the test should take place in a higher mean flow if it was to be repeated to better understand non-dimensional rotor power.

The dynamic power results were filtered to identify periods in which the turbine operated close to the desired control strategy. These results consistently showed an improved agreement with the predicted performance. It is expected that the remaining power deficit will be recovered upon implementation of a variable speed controller similar to that tested in Chapter 4.

The inclusion of strain gauges in the rotor blades provided further insight on the performance of the turbine. The results in Section 6.5 proved the load shedding characteristics at high λ, while the dynamic results in Section 6.7 provided supporting evidence to show that the rotor was usually overspeeding during sub-optimum operational periods, as seen by the lower than expected measured loads. The results were found to be more in-line with predictions during the identified near-optimum periods, providing further evidence that the full potential of the device was not achieved. However, as with the measurement of rotor thrust during the scale model testing in Chapter 4, the rotor loads here are again inferred indirectly. Section 6.3 detailed this curve fitting and extrapolation process used to determine the blade root loads. In principle this should be a fairly reliable approach, but some of the results have shown that the root loads are often underestimated and there is considerable blade-to-blade variation. This is particularly true of the blade root axial forces, which are sensitive to the gradients of the fitted curves. Often these were underestimated as a result of difficulties encountered during the calibration of the strain gauges. It is recommended that the calibrations are repeated, or improvements in the robustness of the curve fitting process are sought. The latter was performed to a degree in this work by ignoring or weighting some of the measurements to reduce the influence of spurious values. While this had the desired net effect of improving the fitted curves, it also meant that there were fewer values available to form the curves. The spurious values are thought to occur at a material transitional region in the blades. Future applications of this arrangement should carefully consider the location of each strain gauge.

Despite the sensitivity of deriving the axial forces, the root bending moments, which were found by locating the value of the extrapolated curve at the root position, were in good agreement with theory and demonstrated lower blade-to-blade variation. Both of these agreements improved further with increased rotor loading found in higher flows. These results were also found on the blade root axial forces, implying that the uncertainty of the curve fitting process reduces with loading. This is believed to be due to improved signal to noise ratio (SNR) at this region. Each sensor is subject to an inherent level of white noise, and the relative contribution of signal contamination arising from this is greater when the signal strength is weak, i.e. when the loading is low. The results, therefore, could be improved by incorporating a noise filter during the data processing, but since there is more interest in the highest loads for structural reasons, this may not be necessary once the turbine is evaluated against stronger currents.

In terms of other future areas of research stemming from this test period that could be pursued to evaluate aspects of the numerical modelling work in Chapter 3, both tower shadow and wave effects could be investigated. For the former, the individual blade loads were sampled at a frequency (16 Hz) considerably higher than the tower pass frequency, meaning that a spectral analysis would reveal the significance of these periodic effects. The technique could also be applied to waves, which again were of a frequency much lower than the sampling rate of the rotor strain gauges. The wave properties were measured during testing by the RAMP ADCP. In addition to this, the loading analysis in this chapter did not consider the out-of-plane rotor moments key to turbine stability, i.e. the pitching and yawing moments. These were shown in Chapter 3 to be a function of tidal effects in the Tidal Bladed simulations, including buoyancy and hydrostatic pressure. An analysis of the measured moments would provide further insight on the accuracy of the model. The methodology required to establish the out-of-plane rotor moments would need to be capable of identifying the orientation of each blade. This was not directly measured, although using a combination of the rotational speed of the turbine and the blade-to-blade variation in loading it should be possible to identify the location of each blade. The time-series results of blade loading were observed to vary periodically at the rotor frequency, with the blades 120^o out of phase with each other.

7. Discussion

7.1 Tidal Turbine Numerical Modelling Developments

The numerical model developed in this thesis has been validated against the leading, commercially available tidal turbine design code, and with experimental measurements from tidal turbines at both 1:30 scale and full-scale. In all of these validation studies, the model adequately captured the steady and unsteady dynamics of turbine power, thrust and blade root bending moment within the bounds of numerical and experimental uncertainty. This highlights the potential of modifying codes available from wind energy research for tidal applications, providing weight to similar arguments made elsewhere [48], [209].

However, unlike most other research in this area, the modelling here included the turbine control system. This is often neglected in numerical assessments and instead the rotor is configured to operate at a fixed-speed during simulations [58], [193]. Since most tidal turbines are variable speed machines (Section 2.4), a fixed-speed simulation would misrepresent the dynamic performance of devices. This was realised in the research here upon the comparison of numerical predictions with full-scale testing results, where the physical turbine operated somewhere between fixed and variable speed. As a result, the numerical predictions overestimated device performance because a fully variable speed turbine was modelled, and hence consistently operated closer to the point of maximum power capture. Thus the control system is an important consideration that should be modelled accurately if the numerical results are to be used for turbine design purposes.

The developed model did not agree well with the commercial code for the blade root out-of-rotor-plane forces and pitching moments, believed to be a consequence of tidal effects that were not included in the former, e.g. added mass, buoyancy and hydrostatic pressure. This resulted in a disagreement on rotor overturning and pitching moments. These rotor moments could be derived from the experimental measurements of blade root bending moment on the full-scale turbine to provide a physical comparison, but this is beyond the scope of the research here. Without this information it is difficult to comment on the validity of these aspects of numerical modelling. The rotor moments are key drivers for the design of the turbine support structure and are rarely reported on in tidal energy research, implying that future efforts should aim to clarify how these are influenced by tidal effects, and how wind turbine codes should be modified to include them.

7.2 Furthering Scale Model Testing Best Practices

The results from the scale model testing provided an invaluable insight into the dynamic performance of the turbine in each control region. While the available literature on scale model experiments is extensive in comparison to that on full-scale testing (Section 2.3), few studies have investigated the importance of testing the turbine control system. It is envisaged that the test setup presented in this thesis could be replicated to perform similar experiments on assessing the merits of a stall or pitch based control system, or indeed other aspects of turbine control in a time varying flow.

There are a number of parallels with the developed LabVIEW program used to control the model turbine and the SCADA system used to control the full-scale turbine. These both provided a real time graphical and numerical output of key turbine parameters for monitoring purposes, and acted as a platform for the synchronisation of measurements. In some respects the scale model tests acted as a preparatory exercise for the full-scale tests, as did the flow instrumentation tests (Chapter 5). For research on the development of SCADA systems, this thesis has demonstrated that the laboratory provides a low risk environment in which the integration of hardware and software in the turbine system can be tested before an offshore installation at sea.

Without the inclusion of low Reynolds number aerofoil lift and drag data in the BEM aspect of the numerical model, the agreement with the scale model tests would have been weaker. Therefore, the usage of a BEM code with a Reynolds number interpolation scheme was justified. Some research efforts have shown experimentally and numerically the effect of Reynolds number on rotor performance [121], [125], but often BEM codes use aerofoil data from just one Reynolds number [64], [210]. This simplification could affect the validity of numerical predictions if Reynolds number varies during simulations.

The blockage correction method described in [114] was used in this research to estimate the free stream turbine performance. Applications of the method have been used to correct blockage ratios of 17% and 8% in [114], and 16% in [125]. Given that the corrected results from the 16% blocked condition in this research were found to agree well with numerical predictions, confidence in the suitability of the method has increased. This is encouraging for researchers concerned about these effects, although it is stressed that efforts should always be made to minimise blockage if the free stream performance is of interest.

In both the 1:30 scale and full-scale testing, there is an element of uncertainty associated with the measurement of rotor thrust, as a consequence of the load being indirectly inferred. This complicates any comparative studies with numerical predictions, and is a key area of improvement required to obtain accurate loading information for design purposes, as well as confidence in any mathematical modelling work.

7.3 Site Characterisation Relevance

The Pembroke Dock and laboratory tests with the acoustic instruments (Chapter 5) were designed to better understand the capabilities of each sensor. Without these tests, false conclusions on the full-scale device performance might have been arrived at, such as pessimistic results relative to the RAMP ADCP. The reality is that both instruments measure different quantities, with the single-beam the only sensor that experiences a flow reduction due to rotor misalignment, and hence effectively accounts for the resulting performance deficit. This same feature was observed during the Pembroke Dock trials when the single-beam tended to obtain a lower flow velocity than the RAMP ADCP despite occupying the same measurement volume, a consequence in this instance of the flow being subject to considerable directional variation. Meanwhile the laboratory tests showed that the single-beam achieves highly accurate measurements, confirming that comparisons with the RAMP ADCP are not due to instrument bias. Thus the single-beam complements the turbine system, particularly for the tested arrangement in which an upstream seabed mounted instrument was not used.

It is believed that further testing of the single-beam could lead to the development of enhancements to the turbine control system. The discussed flow differences with the RAMP ADCP could be used to inform the controller of a suspected yaw error, while the flow disturbance tracking capabilities shown in the laboratory could lead to the development of feedforward control actions that aim to minimise the effects from approaching turbulent conditions. These are both active research areas in the wind industry that are being pursued through the usage similar rotor mounted sensors [175], [176], with the ultimate aim of improving turbine performance and reliability.

The strengths of the single-beam do not, however, undermine the importance of the RAMP ADCP, since currently these are the only type of instruments recommended by industry guidelines for the assessment of turbine performance [142]. Furthermore, the RAMP ADCP is capable of obtaining many of the parameters key to the configuration of the simulated environment in any numerical modelling work, e.g. shear profile, turbulence intensity and wave properties. While a comprehensive comparison of the numerical and experimental environments was beyond the scope of the research in this thesis, this type of analysis would help understand if these effects are modelled appropriately. This is particularly true for waves since research on their inclusion in numerical models is ongoing [57], [58], [64], [193].

7.4 Understanding Full-Scale Tidal Turbine Performance

As stated earlier, presently there are just a few reports available on the operational performance of full-scale devices in tidal energy research, while the literature available on any comparative work with numerical modelling or scale model tests is even scarcer. Therefore, the research in this thesis increases the current level of understanding on these aspects, with the general conclusion being that the leading methods adopted by researchers who are not testing at full-scale are suitable for the prediction of many aspects of device performance in a tidal stream environment.

In terms of recommendations for other research projects on full-scale devices, the inclusion of strain gauges in the turbine system was found to be a particularly useful measure of performance, and provided the only unimpeded rotor measurement. In contrast to this, the power measurement was made onshore and subject to the losses of at least five systems from the rotor, and consequently it proved to be difficult to accurately determine rotor power. Evidence from the scale model testing in this thesis would suggest that if experimental measurements of rotor loading are broadly in line with numerical predictions, it would be expected that so too should the measurements of rotor power. This, however, should not be relied upon and future efforts should strive to achieve greater certainty on the measurement of power.

Performance uncertainty also arose in the full-scale test campaign due to the location of the RAMP ADCP, which was subject to spatial variations in the flow. This was particularly evident when using shorter temporal averaging intervals to measure device performance, such as the assessment of the non-dimensional rotor characteristics when five minute averaging periods were used. In comparison with the single-beam, the RAMP ADCP results were consistently subject to more scatter which often made it difficult to form conclusions from this reference alone. Similarly, when the same tests were performed at scale in the laboratory the flow velocity was captured well by the upstream ADV despite temporal averaging of just one minute, as demonstrated by the highly repeatable results. These findings support the preference of an upstream ADP placement in the IEC recommendations [142], although it has been observed that by using longer averaging intervals (10 minutes) and further data sorting via the binning process (Sections 6.6 and 6.7), the RAMP ADCP results were in better agreement with both the single-beam and numerical predictions. This should provide some confidence for test campaigns where an upstream ADP arrangement cannot be achieved, such as this one.

To fully understand the behaviour of the overspeed control strategy, the turbine now needs to be tested in stronger flows to allow it to reach the rated point. This is an ongoing area of research by TEL. The encouraging results obtained numerically and from scale model testing show promise for this control methodology, while there is enough evidence from full-scale testing to show that by overspeeding the rotor, the loads acting on it decrease.

8. Conclusions

A new coupled numerical model of a tidal turbine has been developed, which to the author's knowledge has not previously been used elsewhere in tidal energy research. This hybrid model allowed the hydro-mechanical-electrical interaction of a tidal turbine to be simulated in an unsteady environment representative of a tidal stream, with the device following the objectives of an overspeed based control strategy. Mean and dynamic simulation results were found to be in good agreement with those obtained separately from the commercially available Tidal Bladed software. Thus the numerical model has shown potential for evaluating a number of aspects of tidal turbine design.

Further validation of the developed numerical model was achieved after testing a 1:30 scale tidal turbine in a laboratory flume, with the measured dimensionless rotor characteristics agreeing well with theoretical predictions. These tests also provided the first physical demonstration of the overspeed control strategy, in which the model turbine closely followed the controller objectives in dynamic flow conditions, leading to the development of performance curves in line with theoretical predictions.

Two ADP instruments were tested in harbour, laboratory and tidal stream environments. One is a standard multi-beam instrument that proved its capabilities in resolving the 3-components of flow velocity at profiled ranges in the vertical direction, while the other is a single-beam instrument that obtains very accurate line-of-sight measurements to a range of in excess of 20 m, showing an ability at identifying and tracking unsteady flows along this range profile. When the two instruments operate alongside a tidal turbine it is possible to characterise the environment for the purposes of assessing device performance, as well as comment on the likelihood of suspected yaw errors and spatial variation in the flow that could result in sub-optimum performance.

The power performance of a full-scale tidal turbine has been assessed in accordance to industry guidelines using data from the first operational hours of the device. This was complemented by an evaluation of the rotor loading after developing a methodology to infer this information from strain gauges placed in the turbine blades. There is enough evidence from these initial tests to conclude that the turbine performance is in agreement with predictions made from the aforementioned numerical and scale model testing work, although a control system update and a reduction in experimental uncertainty are required to fully realise this.

Using the numerical and experimental methods described, overspeed control has been shown in this thesis to be a simple method of achieving good power performance without structural loading implications in a range of environmental conditions, i.e. the desirable characteristics of any turbine control strategy. Since this can achieved without the requirement of a pitch system, it is believed that there may be significant cost and reliability benefits associated with the adoption of such a control system. Further testing of overspeed control at full-scale is an ongoing area of research.

References

[1] International Energy Agency (IEA), "Key world energy statistics," IEA, 2015.

[2] BP, "BP statistical review of world energy," BP, 2016.

[3] The Royal Society and the US National Academy of Sciences, "Climate change evidence and causes," The Royal Society and the National US Academy of Sciences, 2014.

[4] World Health Organization (WHO), "Climate change and human health," WHO, 2003.

[5] Parliament of the United Kingdom, "The climate change act 2008," The Stationery Office, London, 2008.

[6] Renewable Energy Policy Network for the 21st Century (REN21), "Renewables 2016 global status report," REN21, Paris, 2016.

[7] World Nuclear Association, "World nuclear performance report 2016," World Nuclear Association, 2016.

[8] W. Poortinga, N. F. Pidgeon, S. Capstick and M. Aoyagi, "Public attitudes to nuclear power and climate change in Britain two years after the Fukushima accident - synthesis report," UKERC, London, 2014.

[9] Department of Energy and Climate Change (DECC), "DECC public attitudes tracker - wave 14," DECC, 2015.

[10] Organisation for Economic Co-operation and Development (OECD) Nuclear Energy Agency (NEA), "Public attitudes to nuclear power," OECD-NEA, 2010.

[11] World Nuclear Association, "The economics of nuclear power," World Nuclear Association, 2008.

[12] Greenpeace, "The economics of nuclear power," Greenpeace, 2007.

[13] Department of Energy and Climate Change (DECC), "Electricity generation costs," DECC, 2012.

[14] Nuclear Energy Agency, "Projected costs of generating electricity," IEA, 2015.

[15] Directive 2009/28/EC of the European Parliament and of the Council of 23 April 2009 on the promotion of the use of energy from renewable sources and amending and subsequently repealing Directives 2001/77/EC and 2003/30/EC, OJ L 140/16, 2009.

[16] A. Bartle, “Hydropower potential and development activities,” Energy Policy, vol. 30, pp. 1231-1239, 2002.

[17] The Energy Technology Systems Analysis Program (ETSAP) and the International Renewable Energy Agency (IRENA), “Hydropower technology brief,” IEA-ETSAP and IRENA, 2015.

[18] The International Renewable Energy Agency (IRENA), “The power to change: solar and wind cost reduction potential to 2025,” IRENA, 2016.

[19] The International Renewable Energy Agency (IRENA), “Renewable energy technologies: cost analysis series, Volume 1: Power sector, Issue 5/5, Wind power,” IRENA, 2012.

[20] The International Renewable Energy Agency (IRENA), “Renewable power generation costs in 2014,” IRENA, 2015.

[21] F. Tait, “Transition by consent, meeting Britain's energy needs together,” Fabian Society, London, 2015.

[22] Department for Business Energy and Industrial Strategy (BEIS), “BEIS's energy and climate change public attitudes tracking survey,” [Online]. Available: https://www.gov.uk/government/collections/public-attitudes-tracking-survey. [Accessed August 2016].

[23] Offshore Renewable Energy (ORE) Catapult, “Cost reduction monitoring framework 2015,” ORE Catapult, 2015.

[24] Eurostat, “Energy from renewable sources,” 2016. [Online]. Available: http://ec.europa.eu/eurostat/statistics-explained/index.php/Energy_from_renewable_sources. [Accessed August 2016].

[25] S. Waters and G. Aggidis, “Tidal range technologies and state of the art in review,” Renewable and Sustainable Energy Reviews, vol. 59, pp. 514-529, 2016.

[26] F. O. Rourke, F. Boyle and A. Reynolds, “Tidal energy update 2009,” Applied Energy, vol. 87, pp. 398-409, 2010.

[27] R. H. Charlier, “Forty candles for the Rance River TPP tides provide renewable and sustainable power generation,” Renewable and Sustainable Energy Reviews, vol. 11, pp. 2032-2057, 2007.

[28] Department for Business Energy and Industrial Strategy (BEIS), “Wave and tidal energy: part of the UK's energy mix,” 2013. [Online]. Available: https://www.gov.uk/guidance/wave-and-tidal-energy-part-of-the-uks-energy-mix. [Accessed August 2016].

[29] British Hydropower Association (BHA), “La Rance tidal power plant, 40 year operation feedback - lessons learnt,” in BHA Annual Conference, Liverpool, U.K., 2009.

[30] The International Renewable Energy Agency (IRENA), “Tidal energy technology brief,” IRENA, 2014.

[31] A. I. Winter, “Differences in fundamental design drivers for wind and tidal turbines,” in Oceans '11 IEEE Santander Conference, Santander, Spain, 2011.

[32] P. L. Fraenkel, “Development and testing of Marine Current Turbine's SeaGen 1.2 MW tidal stream turbine,” in 3rd International Conference on Ocean Energy (ICOE), Bilbao, Spain, 2010.

[33] P. Bornens, J. F. Daviau, M. K. Decrin, L. Gaillard, D. Grosdemange, F. Guéna, A. Kerebel, H. Majastre and J. Ruer, “The Sabella tidal turbine,” in 2nd International Conference on Ocean Energy (ICOE), Brest, France, 2008.

[34] R. Fabre, F. Trarieux, F. Fiore and R. Starzmann, “Turbine performance enhancement on the PLAT-O taut moored underwater tidal energy converter,” in 11th European Wave and Tidal Energy Conference (EWTEC), Nantes, France, 2015.

[35] The European Commission, “SEAFLOW pilot project for the exploitation of marine currents,” The European Commission, 2005.

[36] The European Marine Energy Centre (EMEC), “Tidal clients,” 2016. [Online]. Available: http://www.emec.org.uk/about-us/our-tidal-clients/. [Accessed August 2016].

[37] Alstom Ocean Energy, “ReDAPT MC7.1 - initial power curve,” The Energy Technologies Institute (ETI), 2014.

[38] OpenHydro, “Nova Scotia Power and OpenHydro reach next project milestone,” 2010. [Online]. Available: http://www.openhydro.com/news/OpenHydroPR-171210.pdf. [Accessed August 2016].

[39] S. Paboeuf, P. Y. K. Sun, L.-M. Macadré and G. Malgorn, “Power performance assessment of the tidal turbine Sabella D10 following IEC62600-200,” in 35th ASME International Conference on Ocean, Offshore and Arctic Engineering, Busan, South Korea, 2016.

[40] Verdant Power, “Improved structure and fabrication of large, high-power KHPS rotors,” Verdant Power, 2013.

[41] Tocardo, "Tidal power plant delta works Netherlands," 2016. [Online]. Available: http://www.tocardo.com/wp-content/uploads/2016/06/Deltaworks-Tidal-Power-Plant.pdf. [Accessed August 2016].

[42] The Crown Estate, "UK wave and tidal key resource areas project," The Crown Estate, 2012.

[43] The Carbon Trust, "Accelerating marine energy," The Carbon Trust, 2011.

[44] The Department of Energy and Climate Change (DECC), "Sub-national electricity and gas consumption statistics," DECC, 2015.

[45] RenewableUK, "Wave and tidal energy in the UK, conquering challenges, generating growth," RenewableUK, 2013.

[46] M. Limited, "The project," 2016. [Online]. Available: http://www.meygen.com/the-project/. [Accessed August 2016].

[47] OpenHydro, "The first two OpenHydro tidal turbines on EDF's Paimpol-Bréhat site successfully deployed," 2016. [Online]. Available: http://www.openhydro.com/news/OpenHydroPR-2016-01-20.pdf. [Accessed August 2016].

[48] G. McCann, R. Rawlinson-Smith and K. Argyriadis, "Load simulation for tidal turbines using wind turbine experience," in 1st International Conference on Ocean Energy (ICOE), Bremerhaven, Germany, 2006.

[49] P. J. Moriarty and A. C. Hansen, "AeroDyn theory manual, NREL/TP-500-36881," National Renewable Energy Laboratory (NREL), 2005.

[50] W. M. J. Batten, A. S. Bahaj, A. F. Molland and J. R. Chaplin, "The prediction of the hydrodynamic performance of marine current turbines," Renewable Energy, no. 33, pp. 1085-1096, 2008.

[51] I. Masters, J. C. Chapman, M. R. Willis and J. A. C. Orme, "A robust blade element momentum theory model for tidal stream turbines including tip and hub loss corrections," Journal of Marine Engineering and Technology, vol. 10, no. 1, pp. 25-35, 2011.

[52] G. McCann and R. Rawlinson-Smith, "Development of a design tool for tidal current turbines," in 6th European wave and tidal energy conference (EWTEC), Glasgow, U.K., 2005.

[53] T. M. Nevalainen, C. M. Johnstone and A. D. Grant, "An unsteady blade element momentum theory for tidal stream turbines with Morris method sensitivity analysis," in 11th European Wave and Tidal Energy Conference (EWTEC), Nantes, France, 2015.

[54] H. Glauert, "Airplane propellers," in Aerodynamic Theory, Berlin, Springer Verlag, 1935.

[55] J. Thomson, B. Polagye, V. Durgesh and M. C. Richmond, "Measurements of turbulence at two tidal energy sites in Puget Sound, WA," IEEE Journal of Oceanic Engineering, vol. 37, no. 3, pp. 363-374, 2012.

[56] N. D. Kelley and B. J. Jonkman, "Overview of the TurbSim stochastic inflow turbulence simulator, NREL/TP-500-41137, Version 1.21," National Renewable Energy Laboratory (NREL), 2007.

[57] N. Barltrop, K. S. Varyani, A. Grant, D. Clelland and X. Pham, "Investigation into wave-current interactions in marine current turbines," IMechE Journal of Power and Energy, vol. 221, no. 2, pp. 233-242, 2007.

[58] P. W. Galloway, L. E. Myers and A. S. Bahaj, "Quantifying wave and yaw effects on a scale tidal stream turbine," Renewable Energy, vol. 63, pp. 297-307, 2014.

[59] A. C. Hansen and C. P. Butterfield, "Aerodynamics of horizontal-axis wind turbines," Annual Revision of Fluid Mechanics, vol. 25, pp. 115-149, 1993.

[60] J. G. Leishman and T. S. Beddoes, "A semi-empirical model for dynamic stall," Journal of the American Helicopter Society, vol. 34, no. 3, pp. 18-29, 1989.

[61] W. M. J. Batten, A. S. Bahaj, A. F. Molland and J. R. Chaplin, "Experimentally validated numerical method for the hydrodynamic design of horizontal axis tidal turbines," Ocean Engineering, vol. 34, no. 7, pp. 1013-1020, 2007.

[62] A. S. Bahaj, W. M. J. Batten and G. McCann, "Experimental verifications of numerical predictions for the hydrodynamic performance of horizontal axis marine current turbines," Renewable Energy, vol. 32, pp. 2479-2490, 2007.

[63] W. M. J. Batten, A. S. Bahaj, A. F. Molland and J. R. Chaplin, "The prediction of hydrodynamic performance of marine current turbines," Renewable Energy, vol. 33, pp. 1085-1096, 2008.

[64] C. Faudot and O. G. Dahlhaug, "Prediction of wave loads on tidal turbine blades," Energy Procedia, vol. 20, pp. 116-133, 2012.

[65] DNV-GL, "Theory Manual, Tidal Bladed, Version 4.6," DNV-GL, 2014.

[66] S. Way, M. Thomson and J. Goldsmith, "Modeling a floating, multiple-rotor tidal energy converter using Tidal Bladed," in 1st Marine Energy Technology Symposium (METS), Washington, DC, U.S.A., 2013.

[67] J. McNaughton, S. Harper, R. Sinclair and B. Sellar, "Measuring and modelling the power curve of a commercial-scale tidal turbine," in 11th European Wave and Tidal Energy Conference (EWTEC), Nantes, France, 2015.

[68] DNV-GL, "ReDAPT: Full-scale validation study of Tidal Bladed," 2015. [Online]. Available: http://www.eti.co.uk/project/redapt/. [Accessed August 2016].

[69] M. E. Harrison, W. M. J. Batten, L. E. Myers and A. S. Bahaj, "Comparison between CFD simulations and experiments for predicting the far wake of horizontal axis tidal turbines," IET Renewable Power Generation, vol. 4, no. 6, pp. 613-623, 2010.

[70] A. Mason-Jones, D. M. O'Doherty, C. E. Morris and T. O'Doherty, "Influence of a velocity profile and support structure on tidal stream performance," Renewable Energy, vol. 52, pp. 23-30, 2013.

[71] C. Frost, C. E. Morris, A. Mason-Jones, D. M. O'Doherty and T. O'Doherty, "The effect of tidal flow directionality on tidal turbine performance characteristics," Renewable Energy, vol. 78, pp. 609-620, 2015.

[72] M. Arnold, F. Biskup, D. Matha and P. W. Cheng, "Simulation of rotor-foundation-interaction on tidal current turbines with computational fluid dynamics," in 11th European Wave and Tidal Energy Conference (EWTEC), Nantes, France, 2015.

[73] I. P. Jones, A. K. Wells, R. Starzmann and S. Bischof, "CFD simulations of the TRITON tidal energy platform to analyse the surrounding flow pattern," in 11th European Wave and Tidal Energy Conference (EWTEC), Nantes, France, 2015.

[74] C. E. Morris, D. M. O'Doherty, T. O'Doherty and A. Mason-Jones, "Kinetic energy extraction of a tidal stream turbine and its sensitivity to structural stiffness attenuation," Renewable Energy, vol. 88, pp. 30-39, 2016.

[75] M. Arnold, F. Biskup and P. W. Cheng, "Impact of structural flexibility on loads on tidal current turbines," International Journal of Marine Energy [In Press], 2016.

[76] P. Muller, F. Sainclair, A. Carlisle and C. Delafosse, "Tidal current turbine optimisation using CFD simulation," in 11th European Wave and Tidal Energy Conference, Nantes, France, 2015.

[77] R. Luquet, D. Bellevre, D. Fréchou, P. Perdon and P. Guinard, “Design and model testing of an optimized ducted marine current turbine,” International Journal of Marine Energy, vol. 2, pp. 61-80, 2013.

[78] W. Hunter, T. Nishino and R. H. J. Wilden, “Investigation of tidal turbine array tuning using 3D Reynolds-averaged Navier-Stokes simulations,” International Journal of Marine Energy, vol. 10, pp. 39-51, 2015.

[79] I. Afgan, U. Ahmed, D. D. Apsley, T. Stallard and P. K. Stansby, “CFD simulations of a full-scale tidal stream turbine: comparison between large-eddy simulations and field measurements,” 2014. [Online]. Available: http://www.eti.co.uk/project/redapt/. [Accessed August 2016].

[80] R. Malki, A. J. Williams, T. N. Croft, M. Togneri and I. Masters, “A coupled blade element momentum - computational fluid dynamics model for evaluating tidal stream turbine performance,” Applied Mathematical Modelling, vol. 37, pp. 3006-3020, 2013.

[81] I. Masters, R. Malki, A. J. Williams and T. N. Croft, “The influence of flow acceleration on tidal stream turbine wake dynamics: a numerical study using a coupled BEM-CFD model,” Applied Mathematical Modelling, vol. 37, pp. 7905-7918, 2013.

[82] M. Edmunds, A. J. Williams, I. Masters and T. N. Croft, “BEM-CFD: A revised model for accurate prediction,” in 11th European Wave and Tidal Energy Conference (EWTEC), Nantes, France, 2015.

[83] I. Fairley, P. Evans, C. Wooldridge, M. Willis and I. Masters, “Evaluation of tidal stream resource in a potential array area via direct measurements,” Renewable Energy, vol. 57, pp. 70-78, 2013.

[84] P. Mycek, B. Gaurier, G. Germain, G. Pinon and E. Rivoalen, “Experimental study of the turbulence intensity effects on marine current turbines behaviour. Part I: One single turbine,” Renewable Energy, vol. 66, pp. 729-746, 2014.

[85] A. H. Hay, L. Zedel, S. Nylund, R. Craig and J. Culina, “The Vectron: A pulse coherent acoustic Doppler system for remote turbulence resolving velocity measurements,” in IEEE/OES 11th Currents, Waves and Turbulence Measurement (CWTM) Workshop, St. Petersburg, FL, U.S.A., 2015.

[86] B. Sellar, S. Harding and M. Richmond, “High-resolution velocimetry in energetic tidal currents using convergent-beam acoustic Doppler profiler,” Measurement Science and Technology, vol. 26, 2015.

[87] Nortek AS, “Comprehensive Manual,” Nortek AS, 2013.

[88] Teledyne RD Instruments, “Acoustic Doppler current profiler principles of operation: A practical primer,” Teledyne RD Instruments, 1996.

[89] Teledyne RD Instruments, “Waves primer: Wave measurements and the RDI ADCP waves array technique,” Teledyne RD Instruments, Date unknown.

[90] A. Bouferrouk, J. Saulnier, G. H. Smith and L. Johanning, “Field measurements of surface waves using a 5-beam ADCP,” Ocean Engineering, vol. 112, pp. 173-184, 2016.

[91] P. Evans, A. Mason-Jones, C. Wilson, C. Wooldridge, T. O'Doherty and D. O'Doherty, “Constraints on extractable power from energetic tidal straits,” Renewable Energy, vol. 81, pp. 707-722, 2015.

[92] The European Marine Energy Centre (EMEC), “Assessment of tidal energy resource,” EMEC, 2009.

[93] P. S. Evans, S. Armstrong, C. A. M. E. Wilson, I. Fairley, C. F. Wooldridge and I. Masters, “Characterisation of a highly energetic tidal energy site with specific reference to hydrodynamics and bathymetry,” in 10th European Wave and Tidal Energy Conference (EWTEC), Aalborg, Denmark, 2013.

[94] P. Evans, E. Lazarus, A. Mason-Jones, D. O'Doherty and T. O'Doherty, “Wake characteristics of a natural submerged pinnacle and implications for tidal stream turbine installations,” in 11th European Wave and Tidal Energy Conference (EWTEC), Nantes, France, 2015.

[95] J. Epler, B. Polagye and J. Thomson, “Shipboard acoustic Doppler current profiler surveys to assess tidal current resources,” in MTS-IEEE OCEANS, Seattle, WA, U.S.A., 2010.

[96] A. S. Iyer, S. J. Couch, G. P. Harrison and A. R. Wallace, “Variability and phasing of tidal current energy around the United Kingdom,” Renewable Energy, vol. 51, pp. 343-357, 2013.

[97] I. Masters and M. Togneri, “The influence of micrositing on marine turbulence,” in ASRANet International Conference on Offshore Renewable Energy, Glasgow, U.K., 2014.

[98] J. Thomson, B. Polagye, M. Richmond and V. Durgesh, “Quantifying turbulence for tidal power applications,” in MTS-IEEE OCEANS, Seattle, WA, U.S.A., 2010.

[99] D. R. J. Sutherland, B. G. Sellar and I. Bryden, “The use of Doppler sensor arrays to characterise turbulence at tidal energy sites,” in 4th International Conference on Ocean Energy (ICOE), Dublin, Ireland, 2012.

[100] D. R. J. Sutherland, B. G. Sellar, S. Harding and I. Bryden, “Initial flow characterisation utilising turbine and seabed installed acoustic sensor arrays,” in 10th European Wave and Tidal Energy Conference (EWTEC), Aalborg, Denmark, 2013.

[101] K. Black, J. Ibrahim, J. McKay, T. H. Clark, N. Pearson, R. Moore, J. Hernon, D. Lambkin and B. Cooper, “MRCF-TiME-KS9a Turbulence: Best practices for measurement of turbulent flows. A guide for the tidal power industry,” Ocean Array Systems, 2015.

[102] T. Clark, K. Black, J. Ibrahim, N. Minns, S. Fisher, T. Roc, J. Hernon and R. White, “MRCF-TiME-KS9b Turbulence: Best practices for measurement of turbulent flows. A guide for the tidal power industry,” Ocean Array Systems, 2015.

[103] T. H. Clark, T. Roc, S. Fisher, N. Minns and R. White, “MRCF-TiME-KS10 Turbulence and turbulent effects in turbine and array engineering. A guide for the tidal power industry,” Ocean Array Systems, 2015.

[104] L. F. Kilcher, J. Thomson and J. Colby, “Determining the spatial coherence of turbulence at MHK sites,” in 2nd Marine Energy Technology Symposium (METS), Seattle, WA, U.S.A., 2014.

[105] P. Jeffcoate, B. Elsaesser, T. Whittaker and C. Boake, “Testing tidal turbines - Part I: Steady towing tests vs. tidal mooring tests,” in ASRANet International Conference on Offshore Renewable Energy, Glasgow, U.K., 2014.

[106] S. C. Tedds, I. Owen and R. Poole, “Near-wake characteristics of a model horizontal axis tidal stream turbine,” Renewable Energy, vol. 63, pp. 222-235, 2014.

[107] T. A. de Jesus Henriques, S. C. Tedds, A. Botsari, G. Najafian, T. S. Hedges, C. J. Sutcliffe, I. Owen and R. Poole, “The effect of wave-current interaction on the performance of a model horizontal axis tidal turbine,” International Journal of Marine Energy, vol. 8, pp. 17-35, 2014.

[108] M. Thiébaut and A. Sentchev, “Estimation of tidal stream potential in the Iroise Sea from velocity observations by high frequency radars,” Energy Procedia, vol. 76, pp. 17-26, 2015.

[109] P. S. Bell, J. Lawrence and J. V. Norris, “Determining currents from marine radar data in an extreme current environment at a tidal energy test site,” in IEEE Geoscience and Remote Sensing Symposium (IGARSS), Munich, Germany, 2012.

[110] M. L. Heron, “Mapping currents at tidal turbine sites using VHF high resolution ocean radar,” in MTS-IEEE OCEANS, Bergen, Norway, 2013.

[111] H. Torrens-Spence, P. Schmitt, P. Mackinnon and B. Elsaesser, “Current and turbulence measurement with collocated ADP and turbulence profiler data,” in 11th IEEE/OES Current, Waves and Turbulence Measurement (CWTM) Workshop, St. Petersburg, FL, U.S.A., 2015.

[112] R. Lueck, F. Wolk and K. Black, “Measuring tidal channel turbulence with a vertical microstructure profiler (VMP),” Rockland Scientific, 2013.

[113] D. A. Doman, R. E. Murray, M. J. Pegg, K. Gracie, C. M. Johnstone and T. Nevalainen, “Tow-tank testing of a 1/20th scale horizontal axis tidal turbine with uncertainty analysis,” International Journal of Marine Energy, vol. 11, pp. 105-119, 2015.

[114] A. S. Bahaj, A. F. Molland, J. R. Chaplin and W. M. J. Batten, “Power and thrust measurements of marine current turbines under various hydrodynamic flow conditions in a cavitation tunnel and a towing tank,” Renewable Energy, vol. 32, pp. 407-426, 2007.

[115] P. Mycek, B. Gaurier, G. Germain, G. Pinon and E. Rivoalen, “Experimental study of the turbulence intensity effects on marine current turbines behaviour. Part II: Two interacting turbines,” Renewable Energy, vol. 68, pp. 876-892, 2014.

[116] B. Gaurier, G. Germain, J. V. Facq, C. M. Johnstone, A. D. Grant, A. H. Day, E. Nixon, F. D. Felice and M. Costanzo, “Tidal energy "round robin" tests comparisons between towing tank and circulating tank results,” International Journal of Marine Energy, vol. 12, pp. 87-109, 2015.

[117] T. Davey, I. Bryden, D. M. Ingram, A. Robinson, J. L. Sinfield and A. R. Wallace, “The all-waters test facility - a new resource for the marine energy sector,” in 4th International Conference on Ocean Energy, Dublin, Ireland, 2012.

[118] D. Ingram, R. Wallace, A. Robinson and Bryden I, “The design and commissioning of the first, circular combined current and wave test basin,” in MTS-IEEE OCEANS, Taipei, Taiwan, 2014.

[119] EquiMar, “Deliverable D3.3: Assessment of current practice for tank testing of small marine energy devices,” EquiMar, 2010.

[120] Marine Renewables Infrastructure Network (MaRINET), “WP2: Marine energy system testing - standardisation and best practice. D2.2: Collation of tidal test options,” MaRINET, 2012.

[121] S. C. Tedds, R. J. Poole, I. Owen, G. Najafian, S. P. Bode, A. Mason-Jones, C. Morris, T. O'Doherty and D. M. O'Doherty, “Experimental investigation of horizontal axis tidal stream turbines,” in 9th European Wave and Tidal Energy Conference (EWTEC), Southampton, U.K., 2011.

[122] Marine Renewables Infrastructure Network (MaRINET), “WP2: Marine energy system testing - standardisation and best practice. D2.18: Tidal data analysis best practice,” MaRINET, 2012.

[123] J. I. Whelan and T. Stallard, “Arguments for modifying the geometry of a scale model rotor,” in 9th European Wave and Tidal Energy Conference (EWTEC), Southampton, U.K., 2011.

[124] Marine Renewables Infrastructure Network (MaRINET), “WP2: Marine energy system testing - standardisation and best practice. D2.7: Tidal measurement best practice manual,” MaRINET, 2013.

[125] A. Mason-Jones, D. M. O'Doherty, C. E. Morris, T. O'Doherty, C. B. Byrne, P. W. Prickett, R. I. Grosvenor, I. Owen, S. Tedds and R. J. Poole, “Non-dimensional scaling of tidal stream turbines,” Energy, vol. 44, pp. 820-829, 2012.

[126] T. Y. Chen and L. R. Liou, “Blockage corrections in wind tunnel tests of small horizontal-axis wind turbine,” Experimental Thermal and Fluid Science, vol. 35, pp. 565-569, 2011.

[127] EquiMar, “Deliverable D3.4: Best practice for tank testing of small marine energy devices,” EquiMar, 2010.

[128] Marine Renewables Infrastructure Network (MaRINET), “WP2: Marine energy system testing - standardisation and best practice. D2.16: Tidal test parameter overview,” MaRINET, 2013.

[129] Marine Renewables Infrastructure Network (MaRINET), “WP2: Marine energy system testing - standardisation and best practice. D2.23: Review of tow tank limitations,” MaRINET, 2014.

[130] M. Atcheson, P. MacKinnon and B. Elsaesser, “A large scale model experimental study of a tidal turbine in uniform steady flow,” Ocean Engineering, vol. 110, pp. 51-61, 2015.

[131] P. Jeffcoate, T. Whittaker, C. Boake and B. Elsaesser, “Field tests of multiple 1/10 scale tidal turbines in steady flows,” Renewable Energy, vol. 87, pp. 240-252, 2016.

[132] R. Starzmann, M. Baldus, E. Groh, N. Hirsch, N. A. Lange and S. Scholl, “A stepwise approach towards the development and full-scale testing of a marine hydrokinetic turbine,” in 1st Marine Energy Technology Symposium (METS13), Washington, DC, U.S.A., 2013.

[133] R. Starzmann, M. Baldus, E. Groh, N. Hirsch, N. A. Lange and S. Scholl, “Full-scale testing of a tidal energy converter using a tug boat,” in 10th European Wave and Tidal Energy Conference (EWTEC), Aalborg, Denmark, 2013.

[134] R. Starzmann, P. Jeffcoate, S. Scholl, S. Bischof and B. Elsaesser, "Field testing a full-scale tidal turbine. Part 1: Power performance assessment," in 11th European Wave and Tidal Energy Conference (EWTEC), Nantes, France, 2015.

[135] K. Shah, T. Blackmore, L. Blunden, L. Myers and A. Bahaj, "From lab to field: deployment of a scale turbine in a tidal estuary," in 11th European Wave and Tidal Energy Conference (EWTEC), Nantes, France, 2015.

[136] P. Bornens, J. F. Daviau, M. K. Decrin, L. Gaillard, D. Grosdemange, F. Guéna, A. Kerebel, H. Majastre and J. Ruer, "The Sabella tidal turbine," in 2nd International Conference on Ocean Energy (ICOE), Brest, France, 2008.

[137] P. Bornens, J. F. Daviau, L. Gaillard, A. Guerrier and J. Ruer, "The Sabella tidal turbine - Test results and further development," in 3rd International Conference on Ocean Energy (ICOE), Bilbao, Spain, 2010.

[138] The European Marine Energy Centre (EMEC), "Scale test sites," 2016. [Online]. Available: http://www.emec.org.uk/facilities/scale-test-sites/. [Accessed August 2016].

[139] The European Marine Energy Centre (EMEC), "Case study: Benefits of real sea testing at EMEC," 2016. [Online]. Available: http://www.emec.org.uk/about-us/our-tidal-clients/nautricity/. [Accessed August 2016].

[140] The European Marine Energy Centre (EMEC), "Assessment of performance of tidal energy conversion systems," EMEC, 2009.

[141] International Electrotechnical Commission (IEC), "IEC/TS 61400-12-1. Wind turbines - Part 12.1: Power performance measurements of electricity producing wind turbines," IEC, 2005.

[142] International Electrotechnical Commission (IEC), "IEC/TS 62600-200. Marine energy - Wave, tidal and other water current converters - Part 200: Electricity producing tidal energy converters - Power performance assessment," IEC, 2013.

[143] P. Jeffcoate, R. Starzmann, B. Elsaesser, S. Scholl and S. Bischoff, "Field measurements of a full scale tidal turbine," International Journal of Marine Energy, vol. 12, pp. 3-20, 2015.

[144] BBC News, "Blade fault on giant tide turbine AK1000 in Orkney," 2010. [Online]. Available: http://www.bbc.co.uk/news/uk-scotland-highlands-islands-11492829. [Accessed August 2016].

[145] F. D. Bianchi, H. de Battista and R. J. Mantz, Wind turbine control systems - Principles, modelling and gain scheduling design, London: Springer, 2007.

[146] T. Burton, N. Jenkins, D. Sharpe and E. Bossanyi, Wind energy handbook - Scond edition, Chichester, U.K.: John Wiley and Sons Ltd., 2011.

[147] D. A. Spera, Wind turbine technology: Fundametnal concepts in wind turbine engineering - Second edition, U.S.A.: The American Society of Mechanical Engineers (ASME), 2009.

[148] A. D. Hansen, F. Iov, F. Blaabjerg and L. H. Hansen, "Review of contemporary wind turbine concepts and their market penetration," Wind Engineering, vol. 28, no. 3, pp. 247-263, 2004.

[149] P. W. Carlin, A. S. Laxson and E. B. Muljadi, "The history and state of the art of variable-speed wind turbine technology," National Renewable Energy Laboratory (NREL), 2001.

[150] J. L. Tangler, "Insight into wind turbine stall and post-stall aerodynamics," Wind Energy, vol. 7, pp. 247-260, 2004.

[151] J. L. Tangler and J. D. Kocurek, "Wind turbine post-stall airfoil performance characteristics guidelines for blade-element momentum methods," in 43rd American Institute of Aeronautics and Astronautics (AIAA) Aerospace Sciences Meeting, Reno, NV, U.S.A., 2005.

[152] A. Winter, "Speed regulated operation for tidal turbines with fixed pitch rotors," in OCEANS '11 MTS/IEEE Kona Conference, Kona, Hawai‘i, U.S.A., 2011.

[153] A. Winter and T. Tryfonas, "A constrained optimization process for the design of tidal turbine blades with experimental validation," in OCEANS '11 MTS/IEEE Kona Conference, Kona, Hawai‘i, U.S.A., 2011.

[154] K. Gracie-Orr, T. M. Nevalainen, C. M. Johnstone, R. E. Murray, D. A. Doman and M. J. Pegg, "Development and initial application of a blade design methodology for overspeed power-regulated tidal turbines," International Journal of Marine Energy [In press], 2016.

[155] F. Biskup, M. Arnold, P. Daus, R. Arlitt and M. Hohberg, "Effects of rotor blade tip modifications on a tidal in-stream energy converter - Voith HyTide®," in 10th European Wave and Tidal Energy Conference (EWTEC), Aalborg, Denmark, 2013.

[156] B. Whitby and C. E. Ugalde-Loo, "Performance of pitch and stall regulated tidal stream turbines," IEEE Transactions on Sustainable Energy, vol. 5, pp. 64-72, 2014.

[157] J. L. Godwin and P. Matthews, "Classification and detection of wind turbine pitch faults through SCADA data analysis," International Journal of Prognostics and Health Management, vol. 4, no. 16, pp. 1-11, 2013.

[158] P. J. Tavner, J. Xiang and F. Spinato, “Reliability analysis for wind turbines,” Wind Energy, vol. 10, pp. 1-18, 2007.

[159] M. Wilkinson, K. Harman, B. Hendriks, F. Spinato and T. van Delft, “Measuring wind turbine reliability - Results of the Reliawind project,” in European Wind Energy Conference (EWEA), Brussels, Belgium, 2011.

[160] F. Spinato, P. J. Tavner, G. J. W. van Bussel and E. Koutoulakos, “Reliability of wind turbine subassemblies,” IET Renewable Power Generation, vol. 3, no. 4, pp. 1-15, 2009.

[161] Scotrenewables, “SR250,” 2016. [Online]. [Accessed August 2016].

[162] Tidal Generation Limited (TGL), “Deep-GEN III turbine test report,” TGL, 2011.

[163] Tocardo, “T2,” 2016. [Online]. Available: http://www.tocardo.com/products_and_services/t200.html. [Accessed August 2016].

[164] M. Arnold, F. Biskup and P. W. Cheng, “Load reduction potential of variable speed control approaches for fixed pitch tidal current turbines,” in 11th European Wave and Tidal Energy Conference (EWTEC), Nantes, France, 2015.

[165] ANDRITZ HYDRO Hammerfest, “Renewable energy from tidal currents,” 2012. [Online]. Available: https://www.andritz.com/hy-hammerfest.pdf. [Accessed August 2016].

[166] Scotrenewables, “SR2000,” 2016. [Online]. Available: http://www.scotrenewables.com/technology-development/sr2000. [Accessed August 2016].

[167] GE Renewable Energy, “Oceade* Tidal Turbine Platform,” 2016. [Online]. Available: https://www.gerenewableenergy.com/innovative-solutions/tidal-energy/oceade-tidal-turbine-platform.html. [Accessed August 2016].

[168] Atlantis Resources Ltd., “AR1000,” 2016. [Online]. Available: http://atlantisresourcesltd.com/turbines/ar-series/ar1000.html. [Accessed August 2016].

[169] Atlantis Resources Ltd., “AR1500,” 2016. [Online]. Available: http://atlantisresourcesltd.com/turbines/ar-series/ar1500series.html. [Accessed August 2016].

[170] R. Arlitt and K. Argyriadis, “Development and certification of the Voith Hydro HyTide® 110 tidal turbine,” in 3rd International Conference on Ocean Energy (ICOE), Bilbao, Spain, 2010.

[171] M. Lewis, S. P. Neill, P. E. Robins and M. R. Hashemi, “Resource assessment for future generations of tidal-stream energy arrays,” Energy, vol. 83, pp. 403-415, 2015.

[172] C. Frost, P. S. Evans, C. E. Morris, A. Mason-Jones, D. O'Doherty and T. O'Doherty, “Flow misalignment and tidal stream turbines,” in 1st International Conference on Renewable Energies Offshore, Lisbon, Portugal, 2014.

[173] D. A. Smith, M. Harris, A. S. Coffey, T. Mikkelsen, H. E. Jørgensen, J. Mann and R. Danielian, “Wind lidar evaluation at the Danish wind test site in Høvsøre,” Wind Energy, vol. 9, pp. 87-93, 2006.

[174] M. Harris, D. Bryce, A. S. Coddev, D. A. Smith, J. Birkemeyer and U. Knopf, “Advance measurements of gusts by laser anemometry,” Journal of Wind Engineering and Industrial Aerodynamics, vol. 95, pp. 1637-1647, 2007.

[175] T. Mikkelsen, N. Angelou, K. Hansen, M. Sjöholm, M. Harris, C. Slinger, P. Hadley, R. Scullion, G. Ellis and G. Vives, “A spinner-integrated wind LIDAR for enhanced wind turbine control,” Wind Energy, vol. 16, no. 4, pp. 625-643, 2013.

[176] A. K. Scholbrock, P. A. Fleming, L. J. Fingersh, A. D. Wright, D. Schlipf, F. Haizman and F. Belen, “Field testing LIDAR based feed-forward controls on the NREL controls advanced research turbine,” in 51st AIAA Aerospace Sciences Meeting, Grapevine, TX, U.S.A., 2013.

[177] S. Harper, G. Pittam and J. Harrison, “Tidal turbine and foundation load limiting controller,” in 11th European Wave and Tidal Energy Conference (EWTEC), Nantes, France, 2015.

[178] R. Nicholls-Lee, “Adaptive composite blades for horizontal axis turbines,” PhD Thesis, University of Southampton, 2011.

[179] R. E. Murray, T. Nevalainen, K. Gracie-Orr, D. A. Doman, M. J. Pegg and C. M. Johnstone, “Passively adaptive tidal turbine blades: Design tool development and initial verification,” International Journal of Marine Energy [In press], 2016.

[180] C. Freeman, J. A. Teixeira, F. Trarieux and R. Ayre, “Design of a gravity stabilised fixed pitch tidal turbine of 400kW,” in 8th European Wave and Tidal Energy Conference (EWTEC), Uppsala, Sweden, 2009.

[181] Tidal Energy Ltd., “Tidal turbine system”. U.K. Patent 2467653-A, 2010.

[182] J. M. Jonkman and M. L. Buhl, “FAST user's guide, NREL/EL-500-29798,” National Renewable Energy Laboratory (NREL), 2005.

[183] D. J. Laino and A. C. Hansen, “User's guide to the wind turbine aerodynamics computer software AeroDyn,” Windward Engineering, 2002.

[184] Germanischer Lloyd (GL) WindEnergie GmbH, "Design codes FAST and ADAMS® for load calculations of onshore wind turbines," GL, 2005.

[185] M. L. Buhl and A. Manjock, "A comparison of wind turbine aeroelastic codes used for certification," in 44th American Institute of Aeronautics and Astronautics (AIAA) Aerospace Sciences Meeting, Reno, NV, U.S.A., 2006.

[186] P. Passon, M. Kühn, S. Butterfield, J. Jonkman, T. Camp and T. J. Larsen, "OC3 - Benchmark exercise of aero-elastic offshore wind turbine codes," in 2nd European Academy of Wind Energy (EAWE) International Conference on the Science of Making Torque from Wind, Lyngby, Denmark, 2007.

[187] M. Singh, E. Muljadi, J. Jonkman, V. Gevorgian, I. Girsang and J. Dhupia, "Simulation for wind turbine generators - with FAST and MATLAB-Simulink modules, NREL/TP-5D00-59195," National Renewable Energy Laboratory (NREL), 2014.

[188] B. J. Jonkman and L. Kilcher, "TurbSim user's guide," National Renewable Energy Laboratory (NREL), 2012.

[189] International Electrotechnical Commission (IEC), "IEC/TS 61400-1. Wind turbines - Part 1: Design requirements," IEC, 2005.

[190] L. A. Viterna and D. C. Janetzke, "Theoretical and experimental power from large horizontal-axis wind turbines," in 5th Binnial Wind Energy Conference and Workshop, Washington, DC, U.S.A., 1981.

[191] Germanischer Lloyd (GL), "Guideline for the certification of ocean energy converters," GL, 2005.

[192] D. Schlipf, L. Y. Pao and P. W. Cheng, "Comparison of feedforward model predictive control of wind turbines using LIDAR," in 51st IEEE Conference on Decision and Control, Maui, Hawai'i, U.S.A., 2012.

[193] S. Tatum, C. H. Frost, M. Allmark, D. M. O'Doherty, A. Mason-Jones, P. W. Prickett, R. I. Grosvenor, C. B. Byrne and T. O'Doherty, "Wave-current interaction effects on tidal stream turbine performance and loading characteristics," International Journal of Marine Energy [In press], 2015.

[194] V. Petrovic, M. Jelavic and N. Peric, "Identification of wind turbine model for individual pitch controller design," in International Universities Power Energy Conference, Padova, Italy, 2008.

[195] Baldor, "MicroFlex Servo Control - Installation Manual," Baldor, 2003.

[196] A. Mason-Jones, "Performance assessment of a horizontal axis tidal turbine in a high velocity shear environment," PhD Thesis, Cardiff University, 2010.

[197] Nortek USA, "Post Processing," 2016. [Online]. Available: http://www.nortekusa.com/usa/knowledge-center/table-of-contents/vectrino-ii/post-processing. [Accessed August 2016].

[198] Baldor, "Mint Help, Version HF0004A03," Baldor, 2015.

[199] D. Marten and J. Wendler, "QBlade Guidelines v0.6," TU Berlin, 2013.

[200] ITTC, "Subject 1 - Reynolds number for model propeller experiments," ITTC, 1948.

[201] Nortek AS, "Vectrino: 3D water velocity sensor Lab Probe," 2013. [Online]. Available: http://www.nortek-as.com/lib/data-sheets/datasheet-vectrino-lab. [Accessed August 2016].

[202] Baldor, "PC programming guide," Baldor, 2001.

[203] Nortek AS, "Active X module for system integrators - Paradopp family of products," Nortek AS, 2008.

[204] Teledyne RD Instruments, "Workhorse Sentinel. Datasheet," 2009. [Online]. Available: http://rdinstruments.com/__documents/Brochures/sentinel_datasheet_lr.pdf. [Accessed August 2016].

[205] Nortek AS, "Aquadopp® Profiler. Datasheet," 2013. [Online]. Available: http://www.nortek-as.com/lib/brochures/aquadopp-profiler. [Accessed August 2016].

[206] University of Strathclyde, "Kelvin Hydrodynamics Laboratory," Date unknown. [Online]. Available: https://www.strath.ac.uk/engineering/navalarchitectureoceanmarineengineering/ourfacilities/kelvinhydrodynamicslaboratory/. [Accessed August 2016].

[207] K. Oberg, "In search of easy-to-use methods for calibrating ADCP's for velocity and discharge measurements," in ASCE-IAHR Hydraulic Measurements and Experimental Methods Conference, Estes Park, CO, U.S.A., 2002.

[208] H. Madsen, N. N. Sørensen and S. Schreck, "Yaw aerodynamics analysed with three codes in comparison with experiment," in 41st Aerospace Sciences Meeting and Exhibit, American Institute of Aeronautics and Astronautics, Reno, NV, U.S.A., 2003.

[209] W. M. J. Batten, A. S. Bahaj, A. F. Molland and J. R. Chaplin, "Hydrodynamics of marine current turbines," Renewable Energy, vol. 31, pp. 249-256, 2006.

[210] T. M. Nevalainen, C. M. Johnstone and A. D. Grant, “A sensitivity analysis on tidal stream turbine loads caused by operational, geometric design and inflow parameters,” International Journal of Marine Energy, vol. 16, pp. 51-64, 2016.

Appendix A: List of Publications

The work in this thesis led to the publication of the following:

M. Harrold, P. Bromley, M. Broudic, D. Clelland, A. Kiprakis and M. Abusara, “Assessment of an ADCP’s capabilities in laboratory conditions,” in *IEEE/OES 11th Currents, Waves and Turbulence Measurement (CWTM) Workshop*, St. Petersburg, FL, U.S.A., 2015.

M. J. Harrold, P. Bromley, D. Clelland, A. Kiprakis and M. Abusara, “Evaluating the thrust control capabilities of the DeltaStream^{TM} turbine,” in *11th European Wave and Tidal Energy Conference (EWTEC)*, Nantes, France, 2015.

M. Harrold, P. Bromley, M. Broudic and D. Clelland, “Demonstrating a tidal turbine control strategy at laboratory scale,” in *35th ASME International Conference on Ocean, Offshore and Arctic Engineering*, Busan, South Korea, 2016.

These publications are reproduced in the subsequent pages of this appendix.

Assessment of an ADCP's Capabilities in Laboratory Conditions

Magnus Harrold, Peter Bromley and Merin Broudic
Tidal Energy Ltd. (TEL)
Cardiff, UK
magnus.harrold@tidalenergyltd.com

David Clelland
University of Strathclyde
Glasgow, UK

Aristides Kiprakis
The University of Edinburgh
Edinburgh, UK

Mohammad Abusara
University of Exeter
Exeter, UK

Abstract— **A Nortek Aquadopp current profiler was tested at the University of Strathclyde's Kelvin Hydrodynamics Laboratory. To evaluate both the accuracy and precision of the instrument, it was towed on a carriage at a range of speeds up to 3.5ms^{-1}. The effect of the spatial resolution and range parameter settings on these uncertainties has also been studied. Subsequent tests were performed to assess the disturbance characterisation and tracking capabilities of the instrument. These tests took place under regular wave conditions with the carriage held stationary. The precision of the instrument was found to be unaffected by tow speed, while accuracy decreased. Disturbance profiles similar to those predicted from theory were observed and tracked over consecutive time steps, despite the induced currents from the waves being low in magnitude. The instrument underestimated the peak values of these horizontal velocities, however, but this should be expected considering the instrument's principles of operation. Measurements of wavelength and phase velocity, both constant with respect to time, were found to be more accurate.**

Keywords—ADCP, tank testing, accuracy, precision, disturbance identification, tidal energy

I. INTRODUCTION

Acoustic Doppler Current Profilers (ADCP) are used extensively in the tidal stream energy industry, from energy resource assessment [1, 2] at the project planning and feasibility study stage, to evaluation of device performance [3, 4] at the testing and operation phase. It is the instrument's ability to profile the entirety of the water column that makes it particularly useful, considering that some of the larger turbine structures are taller than 20m. This vertical profile of flow information allows engineers to develop an understanding of the environmental conditions they must design to. Parameters of interest include shear profile, wave loading and turbulence metrics [5, 6, 7].

Due to the intrinsic averaging, both spatial and temporal, that is inherent to an ADCP's principles of operation, point-based instruments tend to perform better at capturing turbulence. Usually these instruments also operate at higher sampling rates. However, it would require an array of point-based devices to obtain the spatial coverage of an ADCP, which is both difficult to arrange in an energetic, tidal environment and has cost implications on the survey. The other key limitation that ADCPs present to the tidal stream energy industry is the lack of geographic, spatial flow information they can cover from seabed surveys, an important consideration during turbine siting. This can, in some part, be resolved by undertaking a vessel mounted ADCP survey [8, 9], although this leads to temporal variations in measurements. An alternative is to use shore based Radar systems [10, 11], but these only provide information on surface currents.

Tidal Energy Ltd. (TEL) will soon install its first commercial scale tidal turbine, known as DeltaStream™ (Fig. 1) [12], off the Pembrokeshire coast in Wales, UK. During operation, both seabed and turbine mounted ADCPs will be used. The latter is a horizontally oriented single-beam device that is to be used for detailed flow characterisation and advanced control system purposes [13]. To better understand

Fig. 1. DeltaStream™

The work presented here is supported by the Industrial Doctoral Centre for Offshore Renewable Energy (IDCORE) programme, a partnership between the Universities of Edinburgh, Exeter and Strathclyde, the Scottish Association for Marine Science (SAMS) and HR Wallingford.

the capabilities of this instrument, it has been tested in the regulated conditions of a laboratory. While this environment differs significantly from that of its real application, it does provide the opportunity to repeat experiments, leading to confidence in the results. This is something that cannot be guaranteed at sea.

II. METHODOLOGY

A. The Kelvin Hydrodynamics Laboratory

The towing tank at the University of Strathclyde is 76m L x 4.6m W x 2.5m D, with a water depth of 2.1m during testing. At the upstream end of the tank, an absorbing wavemaker can produce regular and irregular waves of heights up to 0.6m. A beach at the other end of the tank is used to minimise wave reflections, while lane markers can be raised between runs to reduce the settling time of the tank. A resistance based wave probe was positioned 10m in front of the wavemaker. This position also marks the extent at which the tow carriage can travel along the tank. Additionally, the carriage's default starting position was greater than 10m away from the beach end, meaning that typically it would travel about 50m during each run. The carriage itself can reach speeds up to 4ms^{-1}, although 3.5ms^{-1} was never exceeded during these tests. Positional measurements were determined from a laser on the carriage that evaluates signal return time from a fixed target above the wavemaker. For each run, measurements of carriage speed, position and wave height were obtained using the facility's data acquisition system, at a sampling rate of 74Hz. Carriage speeds can be controlled to in excess of International Towing Tank Conference (ITTC) standards [14].

B. Single-Beam ADCP Configuration

The 1MHz single-beam ADCP was mounted off the front of the tow carriage and lowered 1m below the water surface. Most of the tests were performed with the instrument configured to profile a 20.4m range at a sampling rate of 1Hz, and the cell resolution set to 1m. The effect of this resolution parameter on performance was assessed by doing a number of tests with 0.5, 1.5 and 2m cell sizes. Some tests also took place with the profiling range set to 25.4m, the recommended measurement extent of the instrument. Care was taken to ensure that a sufficient amplitude signal was measured by the instrument. This parameter indicates the signal strength and is inversely proportional to the gain applied. Similar experiments with ADCPs have struggled to attain high enough signal responses due to a lack of scattering material in laboratory tanks [15]. This did not prove to be a problem at this facility, with signal strengths considerably higher than the noise floor stated in Nortek's guidelines [16], and marginally lower than real sea tests with the instrument.

As part of a separate study, two additional acoustic instruments were present in the tank during testing. Both of these instruments operated at lower frequencies. To confirm that they did not acoustically interference with the single-beam and affect its performance, a number of tests were repeated both with and without these other instruments operating. The only slight, albeit consistent, difference observed from these tests was an increase in the single-beam's amplitude signal. Measurements of tow speed were unaffected, however. The results of this study have not been presented here.

C. Data Handling

Due to the finite length of the tank and the fixed sampling rate of the instrument, tests performed at higher speeds yielded fewer measurements. Typically, over 60 measurements were made during the 0.5ms^{-1} tests, while less than 10 were recorded at speeds 3ms^{-1} and above. To make reasonable, statistical comparisons of results at different tow speeds, it was necessary to perform more tests at higher speeds. Table I lists the number of tests and the resulting measurements for each tow speed.

Data recorded from each tow run have been cut during the start and end of each test. This removed measurements made while the carriage was accelerating to the desired speed, as well as the subsequent deceleration to stop. Additionally, measurements were removed once the end of the tank was in the instrument's profiling range. This was achieved by identifying a clear peak in the amplitude signal once the wall was in range. Fig. 2 illustrates this data removal process for a 2ms^{-1} run. Note that the instrument's convention is to record a negative flow speed for water approaching the device.

TABLE II. MEASUREMENTS RECORDED AT EACH TOW SPEED

Tow Speed (ms^{-1})	Tests	Measurements
0.5	4	254
1	5	142
1.5	4	70
2.0	8	102
2.5	8	83
3.0	9	74
3.5	12	78

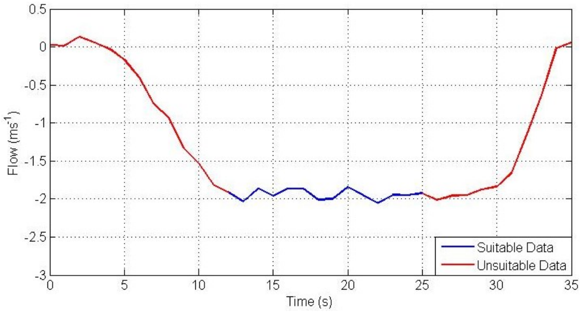

Fig. 2. Data removal process

III. ACCURACY AND PRECISION

A. *Constant Speed Tests*

Fig. 3 summarises the results from the measurements listed in Table 1. Note that there are clear discrepancies between measured and true values up to range 10.4m. Generally the difference is greater the nearer the measurements are made to the instrument's transducer head. Additionally, the higher standard deviations, as represented by the error bars in Fig. 3, of these measurements suggest that there are greater uncertainties at these ranges. It is unclear what has caused these results. The remainder of this section refers only to measurements made at ranges greater than 10.4m.

In terms of absolute error, i.e. the difference between measured and reference values, this tends to increase with tow speed but is unaffected by range. This is visibly apparent in Fig. 3, where measurements of the target tow speed of 0.5ms^{-1} are within ± 0.02ms^{-1}, whereas measurements of 3.5ms^{-1} are lower by as much as 0.08ms^{-1}. The relative absolute errors are never greater than 3.1% at ranges 12.4m and above. It cannot be conclusively stated that these relative errors vary with tow speed. The results here imply that the accuracy of the instrument decreases with speed, but it is unclear whether or not the relative accuracy changes. Note that, instead of using the targeted tow speeds for these error calculations, the mean values were determined from all of the runs. These were always slightly lower than the target values.

The standard deviations do not appear to be affected by measurement range or tow speed. All standard deviations were within the range of 0.05 – 0.09ms^{-1}. The higher values tended to be recorded at lower tow speeds, but there is not enough evidence to suggest that there is more variation at these speeds. This result also implies that the standard error should not vary with range or tow speed, given that the standard error is the ratio of the standard deviation to the square root of the sample size. This quantity cannot be fairly compared between tow speeds due its dependence on the number of measurements. However, since the tests at 1.5, 2.5, 3 and 3.5ms^{-1} produced a similar number of measurements, these results have been used to confirm that standard error is unaffected with speed. This suggests that the relative standard error should decrease with tow speed. All relative standard errors were found to be less than 0.6%. These results suggest that the instrument's precision is unaffected by range or speed, while the relative precision improves with speed.

B. *Profiling Range and Resolution Tests*

Further constant speed tests were performed with the instrument configured to profile at its recommended maximum range of 25.4m with 0.5, 1, 1.5 and 2m cell sizes. Each cell size was tested once only at 1 and 1.5ms^{-1}, and yielded an almost identical number of measurements at each speed. As expected, the size of the standard errors decreased with cell size due to the greater spatial averaging. The Aquapro software used to configure the instrument indicates how much the precision should vary with cell size, but not enough measurements have been made here to evaluate if an agreement exists.

Accuracy was again determined by calculating the difference in mean tow and measured speeds. This quantity also tended to improve with cell size. A maximum absolute error of 0.08ms^{-1} was recorded during the 0.5m cell size tests, while the 2m cell tests had an equivalent value of 0.03ms^{-1}. Again, the lack of data recorded from these tests would make any comparison on the relative sizes of these errors unfair.

Both accuracy and precision appeared to be unaffected at the increased range extent, with both of these parameters agreeing well with the results from the previous 20.4m range.

IV. DISTURBANCE IDENTIFICATION

A. *Characterising the Wave Properties*

The tow carriage was then held stationary at the midpoint of the tank's length, where the waves generated are usually of a better quality. This location is also sufficiently far enough away from the beach end to minimise the effects of any reflections. Regular waves of 0.3Hz were sent down the tank with the ADCP profiling. To determine the amplitude of the waves, a first order Fourier fit has been applied to the wave

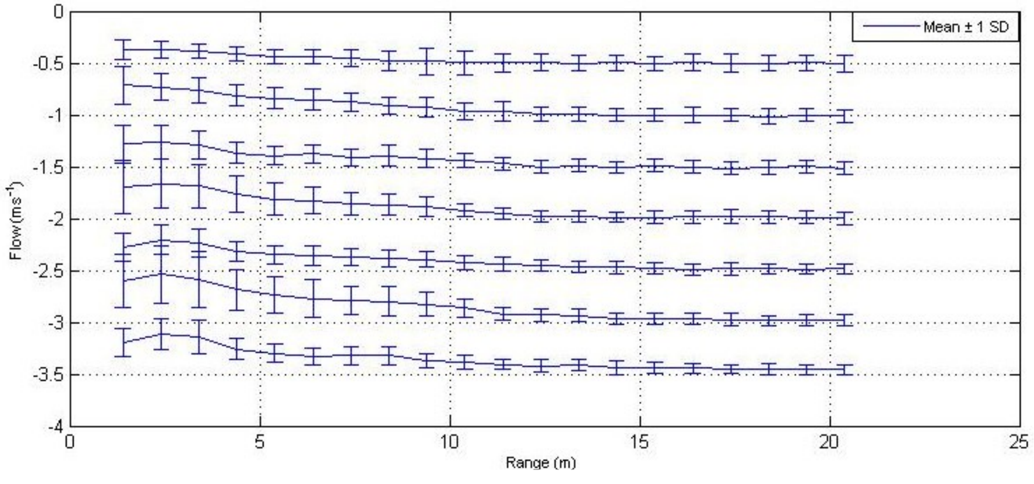

Fig. 3. ADCP measurements of constant tow speed

probe measurements. This fit and its equations are shown in Fig. 4. The amplitude of the waves can be estimated by taking the square root of the sum of the cosine and sine multipliers squared, resulting in an amplitude of 128mm. The intermediate water depth equations of linear wave theory were then applied to determine the wavelength, horizontal wave induced currents at the instrument's depth, and the phase velocity. The calculated wave properties are listed in Table II.

B. *ADCP Disturbance Capabilities*

As shown in Table II, the sinusoidal wave induced current profile has a maximum speed of 0.234ms^{-1}. This is not significantly greater than the amount of expected random noise inherent to the ADCP, implying that it might be difficult to determine these currents. Despite this, the instrument did appear, at times, to reproduce a representative profile. Fig. 5 shows the measurements made by the ADCP at four consecutive time steps during this test. Again, a first order Fourier fit has been applied to these measurements. A clear, progressing sinusoidal curve is moving towards the ADCP over these time steps.

The fitted curves have amplitudes within the range 0.13 – 0.16ms^{-1}. This is lower than the predicted maximum wave induced current at this depth. However, this result should not be unexpected considering the instrument's principles of operation. Firstly, the instrument performs a spatial, weighted average of measurements around the measurement location, and this averaging space is twice as large as the cell size (1m resolution in this case). This implies that the ADCP will never truly be able to capture the peak induced currents because it is averaging around the peak values. Secondly, the instrument pings multiple times during each sample (1Hz in this case), and the recorded measurement is an average of the returning pings. This temporal averaging also makes it difficult to characterise a progressing disturbance because it will have moved between each ping. Decreasing the cell size and increasing the sample rate might lead to a better characterisation, although this would have detrimental effects on the precision of measurements.

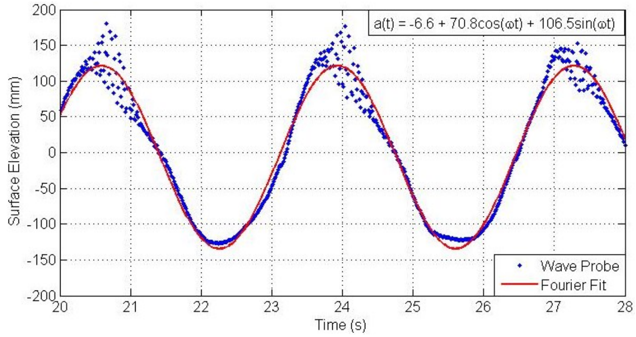

Fig. 4. Fourier fit of the wave probe measurements

TABLE II. 0.3Hz WAVE PROPERTIES

Property	Value
Frequency (Hz)	0.300
Tank Depth (m)	2.100
Instrument Depth Below Surface (m)	1.000
Amplitude (m)	0.128
Wavelength (m)	13.206
Max. Wave Induced Current (ms^{-1})	0.234
Wave Phase Velocity (ms^{-1})	3.961

The fitted curves in Fig. 5 suggest that the phase velocity of the wave is in the range 3 – 3.8ms^{-1}. This is also an underestimate of the theoretical prediction, although relatively it is more accurate than the measurements of induced current. Similarly, the fitted curves have wavelengths between 10.9 – 11.8m, which again is more accurate than the induced current estimate. These improved measurements should be expected considering that both the phase velocity and wavelength do not vary spatially or with respect to time. A subsequent test where 0.6Hz waves of a higher amplitude were sent down the tank produced similar results.

V. CONCLUSIONS

A single-beam ADCP was tested in a laboratory tank to assess its capabilities. The towing tests revealed that the instrument is more accurate at lower speeds. However, it is unclear whether the relative accuracy is affected. Precision did not appear to be influenced by speed, and instead measures of variation (standard deviation and standard error) were unchanged. This implies that the instrument is relatively more precise at greater speeds.

As expected, both accuracy and precision were adversely affected by decreasing the cell resolution of the instrument. Not enough experiments were performed to determine if the amount by which this uncertainty increased agreed with that stated by the manufacturer. The instrument did not appear to be affected by increasing its profiling range to its recommended maximum.

With the ADCP held stationary, regular waves were sent down the tank to evaluate if an induced current profile could be identified. Although these currents were low in magnitude, the instrument did reproduce representative profiles that could be tracked over consecutive time steps. The magnitudes of the currents were underestimated, but this result was anticipated given the spatial and temporal averaging that is inherent to the instrument's principles of operation. The instrument made better measurements of the phase velocity and wavelength, both of which do not vary with time.

The results of these tests should be considered promising for the tidal stream application. In general, flows have been measured along the line of sight of the instrument with considerable certainty, while disturbances have been identified

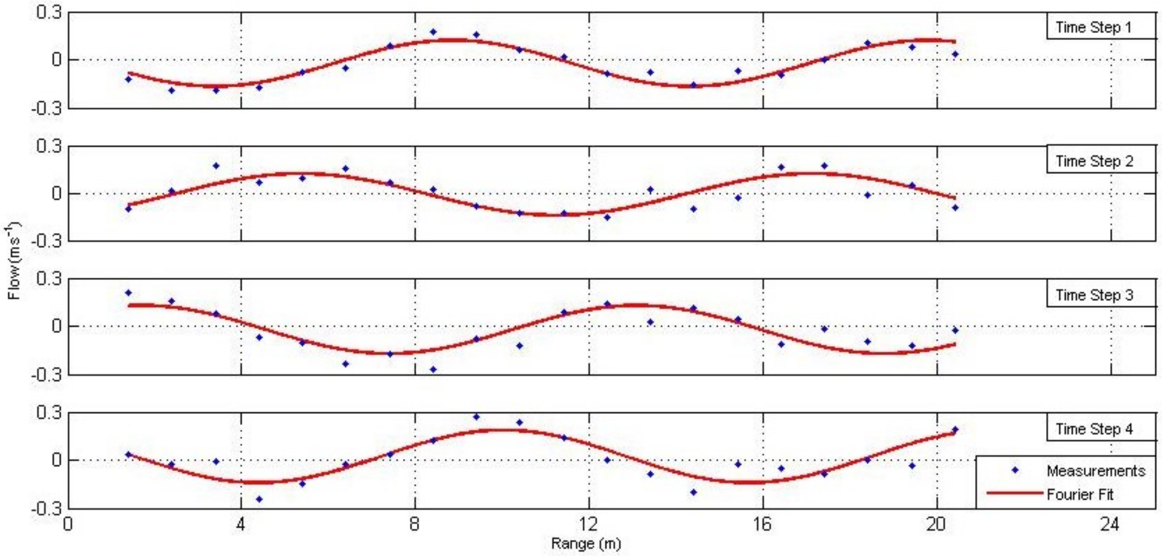

Fig. 5. ADCP measurements of induced current from 0.3Hz regular waves

and tracked. The tidal environment is much more complex than the laboratory, however, and this is where the limitations of the ADCP become apparent. The tests performed here revealed the difficulty in fully characterising a 1-dimensional disturbance, while the reality is that the turbulent events that affect tidal turbine performance will have 3-components.

ACKNOWLEDGMENT

The primary author wishes to thank the staff at the Kelvin Hydrodynamics Laboratory for their assistance throughout the test period, as well as their preparatory work involved in manufacturing support frames for the instruments.

REFERENCES

[1] The European Marine Energy Centre (EMEC), Assessment of Tidal Energy Resource, BSI, 2009.

[2] International Electrotechnical Commission (IEC), Tidal Energy Resource Assessment and Characterization, IEC/TS 62600-201, 2014.

[3] The European Marine Energy Centre (EMEC), Assessment of Performance of Tidal Energy Conversion Systems, BSI, 2009.

[4] International Electrotechnical Commission (IEC), Electricity Producing Tidal Energy Converters – Power Performance Assessment, IEC/TS 62600-200, 2013.

[5] J. Thomson, B. Polagye, M. Richmond, and V. Durgesh, “Quantifying turbulence for tidal power applications,” in: Proc: MTS/IEEE OCEANS Conf., Seattle, WA, 2010.

[6] J. Thomson, B. Polagye, V. Durgesh, and M. C. Richmond, “Measurements of turbulence at two tidal energy sites in Puget Sound, WA,” IEEE Journal of Oceanic Engineering, vol. 37, pp. 363-374, 2012.

[7] D. R. J. Sutherland, B. G. Sellar, and I. Bryden, “The use of Doppler sensor arrays to characterise turbulence at tidal energy sites,” in: Proc. 4th International Conference on Ocean Energy (ICOE), Dublin, Ireland, 2012.

[8] P. Evans, S. Armstrong, C. Wilson, I. Fairley, C. Wooldridge, I. Masters, “Characterisation of a highly energetic tidal energy site with specific reference to hydrodynamics and bathymetry,” in: Proc. 10th European Wave and Tidal Conf. (EWTEC), Aalborg, Denmark, 2nd-5th September 2013.

[9] I. Fairley, P. Evans, C. Woodbridge, M. Willis, and I. Masters, “Evaluation of tidal stream resource in a potential array via direct measurements,” Renewable Energy, vol. 57, pp. 70-78, 2013.

[10] P. S. Bell, J. Lawrence, and J. Norris, “Determining currents from marine radar data in an extreme current environment at a tidal energy test site,” in: Proc. Of the IEEE International Geoscience and Remote Sensing Symposium (IGARSS), Piscataway, NJ, USA, IEEE, pp. 7647-7650, 2012.

[11] M. L. Heron, “Mapping currents at tidal turbine sites using VHF resolution ocean radar,” in Proc: MTS/IEEE OCEANS Conf., Bergen, 2013.

[12] Tidal Energy Ltd. (TEL), DeltaStream: The Core Design Principles and Intellectual Property, 2013, [Online] Available: http://www.tidalenergyltd.com/?page_id=17

[13] Tidal Energy Ltd. (TEL), Predictive Control Patent, Grant pending, 2010.

[14] International Towing Tank Conference (ITTC), Recommended Procedures and Guidelines, ITTC, 2011.

[15] K. Oberg, “In search of easy-to-use methods for calibrating ADCP’s for velocity and discharge measurements,” in Proc: Hydraulic Measurements and Experimental Methods, Estes Park, CO, USA, pp. 908-918, 2002.

[16] Nortek AS, Comprehensive Manual, 2013, [Online] Available: http://www.nortek-as.com/lib/manuals/the-comprehensive-manual

Evaluating the Thrust Control Capabilities of the DeltaStream^{TM} Turbine

M. J. Harrold[α1], P. Bromley[α], D. Clelland[β], A. Kiprakis[γ], M. Abusara[δ]

[α]*Tidal Energy Ltd.*
Vision House, Oak Tree Court, Mulberry Drive, Cardiff Gate Business Park, Cardiff, UK, CF23 8RS
[1]magnus.harrold@tidalenergyltd.com

[β]*University of Strathclyde*
Henry Dyer Building, 100 Montrose Street, Glasgow, UK, G4 0LZ

[γ]*The University of Edinburgh*
Faraday Building, King's Buildings, Edinburgh, UK, EH9 3JL

[δ]*University of Exeter*
College of Engineering, Mathematics and Physical Sciences, Penryn Campus, Penryn, Cornwall, UK, TR10 9FE

***Abstract*— Tidal Energy Ltd. (TEL) will soon install its first commercial scale tidal turbine, known as DeltaStream^{TM}, at its own fully consented test site in South West Wales, Ramsey Sound. This will initiate a series of tests that will allow TEL to assess the performance of DeltaStream^{TM} and determine the value of a number of key patents incorporated into the turbine's design. One of these patents is referred to as 'Thrust Control', a methodology for limiting the thrust loads acting on the rotor in above rated flow conditions, while, crucially, maintaining the turbine's rated power output. This is achieved by allowing the rotor to enter a controlled overspeed, where the blades have thrust shedding characteristics.**

This paper evaluates the capabilities of the thrust control strategy through mathematical modelling performed internally by TEL, and externally using commercially available tools. The results from these unsteady simulations demonstrate that this simple controller is an effective means of managing thrust loads without consequences on power output. This system offers benefits in cost and reliability over turbines that pitch, while there are performance and thrust management gains over fixed-pitch designs that use stall methods.

***Keywords*— Tidal Energy, DeltaStream^{TM}, Thrust Control, Mathematical Modelling, Control Strategy**

INTRODUCTION

Towards the end of 2014, Tidal Energy Ltd. (TEL) unveiled the first commercial scale iteration of its DeltaStream^{TM} technology (Fig. 1) at its build location in Pembroke Dock, Wales. This device features a 12 m diameter, fixed-pitch rotor and is rated at 400 kW in steady flows above 2.6 $m.s^{-1}$, after accounting for losses in the drivetrain. A bespoke, hydraulic yaw system allows ± 100^{o} rotation about its default parked position, a safe orientation that the turbine will revert back to after operating, or in the event of a communications or grid loss during power production. This yaw capability is sufficient for testing at Ramsey Sound (Fig. 2), where approximately bidirectional currents travel north (flood) and south (ebb) through the site [1]. These currents are significantly influenced by the complex bathymetry at the site, which can create considerable turbulence [2]. This is particularly evident in the vicinity of Horse Rock, a surface piercing pinnacle in the sound that disturbs the flow, creating a substantial wake that extends beyond 400 m downstream [3, 4]. These challenges do, however, create a suitable proving ground for tidal stream technology at this site.

Testing of this single-rotor unit will also enable TEL to evaluate the core design principles of DeltaStream^{TM} technology, before scaling to its multiple turbines on a single foundation concept [5]. Emphasis on the design has been placed on cost minimisation, reliability and simplicity. This is perhaps most apparent in the foundation and rotor. The turbine sits atop an open tower on one apex of a triangular base, or delta-shaped, gravity frame, which spans 16 m along each length. The key driver here is to avoid the costs and environmental impacts associated with installing piled structures. For any gravity based turbine, however, it is paramount to manage the thrust loads acting on the device, otherwise it may become unstable on the seabed. Pitch systems can be used to handle these thrust loads, but introduce cost, complexity and additional failure modes. These systems have also been shown to be less effective on tidal turbines than their wind counterparts, due to the delay in pitch actions compared with the faster variation in flow [6].

Fig. 1 DeltaStream^{TM}

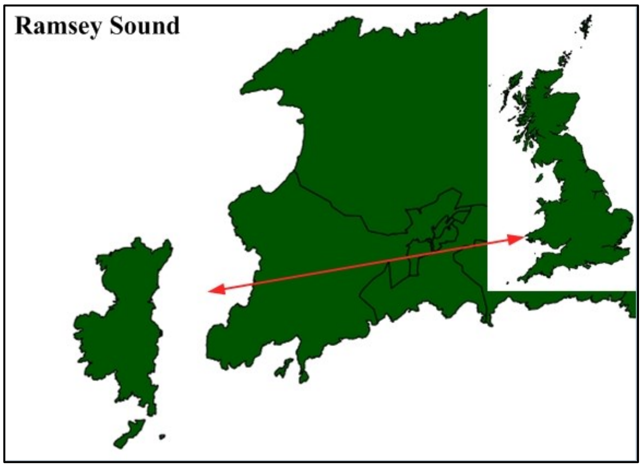

Fig. 2 Ramsey Sound

The frequently used stall regulation methods in fixed-pitch turbines, on the other hand, usually offer inferior rotor thrust management in above rated conditions than devices that pitch. Furthermore, the power capture efficiencies of stall regulated turbines tend to be lower. This is particularly true in the case of passive stall regulation [7].

TEL has patented a control strategy that differs from both pitch and stall methods [8]. Instead of limiting the rotational speed of the turbine, as is the case in stall methods, the rotor is allowed to enter a controlled overspeed once the generator reaches its rated power output. The blades, which utilise an unconventional geometry, have thrust shedding characteristics in this operational region. This allows the turbine to produce constant, rated power without taking more rotor thrust as flow speed increases further.

In this paper, the steady-state performance characteristics of the DeltaStream™ rotor are outlined, before detailing the objectives of the thrust control strategy. The results from unsteady simulations of the turbine operating in conditions similar to that expected at Ramsey Sound are then presented, demonstrating this control system's capabilities.

THRUST CONTROL

Rotor Performance Curves

The steady-state performance of a horizontal axis turbine can be determined from blade element momentum (BEM) theory. The power coefficient, C_p, is a dimensionless measure of the efficiency of the rotor and is defined by:

$$C_p = \frac{P_{rot}}{\frac{1}{2}.\rho.\pi.R^2.v^3} \tag{1}$$

Where P_{rot} is the power output of the rotor, ρ is the density of the fluid in which the turbine operates, R is the rotor radius, and v is the undisturbed current velocity. Similarly, the thrust coefficient, C_t, is a normalised measure of the axial force, T, acting on the rotor:

$$C_t = \frac{T}{\frac{1}{2}.\rho.\pi.R^2.v^2} \tag{2}$$

Both C_p and C_t are a function of pitch angle and tip speed ratio, λ. The former is of no interest for the fixed-pitch case, while the latter is a dimensionless quantity that relates the rotational speed of the rotor, ω, to the current velocity:

$$\lambda = \frac{\omega.R}{v} \tag{3}$$

The C_p-λ and C_t-λ relationships are shown by the blue and orange lines respectively in Fig. 3 for DeltaStream™. The C_p curve is fairly generic in shape, with a peak in efficiency at the optimum tip speed ratio, λ_{opt}. Notice, however, that C_t decreases rapidly above λ_{opt}. This behaviour is uncharacteristic in typical horizontal axis turbines. In general, C_t will not decrease at the same rate with increasing λ, if at all [9, 10]. Operating the turbine at λ greater than λ_{opt}, therefore, reduces the thrust loads on the rotor. The consequence of this is that the rotor operates off its point of maximum power efficiency, but this is desirable once the turbine's rated output is achieved.

Controller Objectives

DeltaStream™ is equipped with a variable speed induction generator. This allows the rotor speed to be controlled through the reactive torque demanded by the generator. Below rated power, the controller's objective is to keep the rotor at λ_{opt}, maximising power production. Similar to other variable speed drive control strategies, the torque demand during this region is proportional to the square of generator shaft speed, ω_{gen}:

$$Generator\ torque\ demand = k_\lambda . \omega_{gen}^2 \tag{4}$$

Where the gain term, k_λ, depends on the physical dimensions of the turbine and is a function of λ.

Once rated power is achieved at speed ω_{rated}, the torque demand is decreased. This allows the rotor to accelerate, moving it above λ_{opt} and into the thrust control region. The increase in rotational speed and the decrease in generator torque

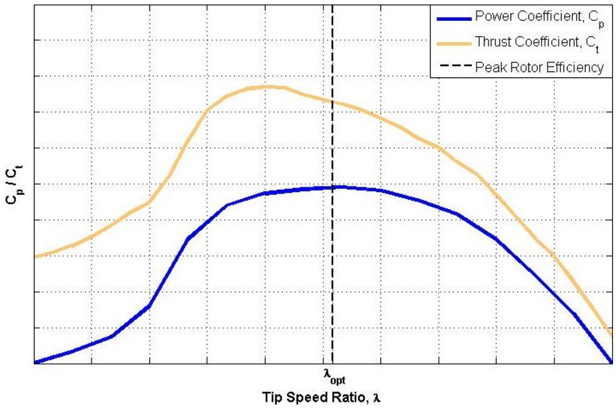

Fig. 3 Steady-state rotor power (blue) and thrust (orange) characteristics

are controlled such that the output power remains constant. The relationship between generator torque and speed is shown in Fig. 4 for the thrust control strategy. This curve illustrates that the only input required by the controller is shaft speed, while generator torque is the only quantity it must control. This is very simple to implement, adds no further complexities or costs to the turbine, and ensures that good power performance is achieved in all operating regions.

The development of blade geometries that could utilise this control strategy has recently attracted considerable academic interest, where thrust limiting characteristics have been demonstrated through the use of mathematical models [11] and at laboratory scale [12, 13, 14]. Other developers, meanwhile, have tested fixed-pitch devices which have similar concepts of operation [15, 16]. This suggests that, unlike the wind industry, it is still unclear whether a pitch mechanism is necessary at commercial scale.

MATHEMATICAL MODELLING

A. Tidal Bladed

TEL requested that DNV GL perform a set of load calculations for DeltaStream™ using its Tidal Bladed software. The development history of this software is well documented [17, 18], and it is currently the only validated, industry-standard tool for simulating tidal turbines at the design stage.

DNV GL added a number of environmental conditions specific to Ramsey Sound in their simulations, determined from field measurements at the turbine's location. This included establishing typical current shear profiles and turbulence characteristics at the site. Of the turbulence options available within Tidal Bladed, a von Kármán model was identified as the most appropriate for the site's conditions. Additionally, the influence of waves has been included in these simulations.

B. In-House Model

TEL has also developed its own in-house mathematical model of DeltaStream™. This is a hybrid of two separate models that continuously interface with each other during simulations. The electrical aspects of the turbine, including the generator and its controller, were built in the Simulink® environment due to its renowned excellence in modelling these components. The other aspects of the turbine, including the environment, hydrodynamics and drivetrain, are handled by a tool that links several, individual, dynamic models together. Many of the calculations performed in these codes are similar to those used in Tidal Bladed.

Where possible, this hybrid model has been configured to match the setup parameters used in the work by DNV GL. This includes the blade geometry (Fig. 5), aerofoil properties (drag and lift tables), masses, inertias, and environmental conditions. For the latter, a von Kármán turbulence model and current shear profiles similar to those used by DNV GL were incorporated. Currently the TEL model does not include the effects from waves, although these were of little influence during the Tidal Bladed simulations due to the sheltered wave climate seen in Ramsey Sound.

C. Simulations

In both models, the simulations were performed at five mean hub flow speeds, $\bar{v}_1$ - $\bar{v}_5$. These flows were chosen to cover the expected operational currents in Ramsey Sound, and do not represent long-term extremes. The DNV GL simulations were repeated a number of times at each mean hub flow speed, but the turbulence seeding was changed to guarantee that no two simulations were the same. This process was also adopted for the TEL simulations, such that the number and duration of simulations were the same for both models. The data output time step was also configured to be the same. This allows for fair, statistical comparisons to be made between results.

RESULTS

A. Time Series Evaluation

Fig. 6 shows a time series output from the in-house mathematical model during a period where rated power is achieved, and hence the turbine starts operating in the thrust control region. From top to bottom, the plots are of hub flow speed magnitude, tip speed ratio, rotor thrust load, F_x, and generator power output. The period of thrust control is highlighted in orange.

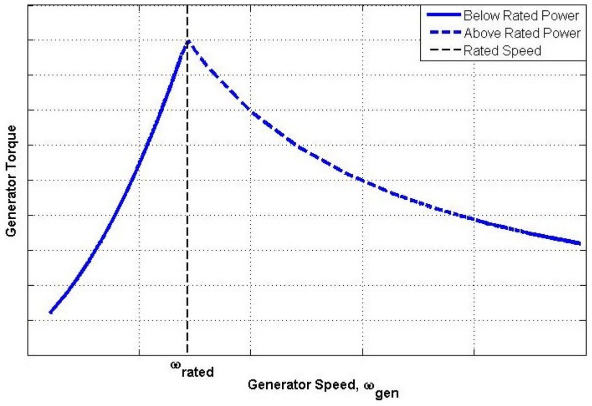

Fig. 4 Thrust control strategy

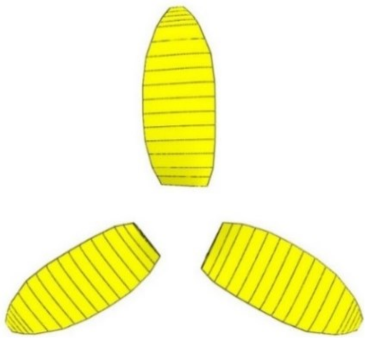

Fig. 5 Modelled DeltaStream™ blades

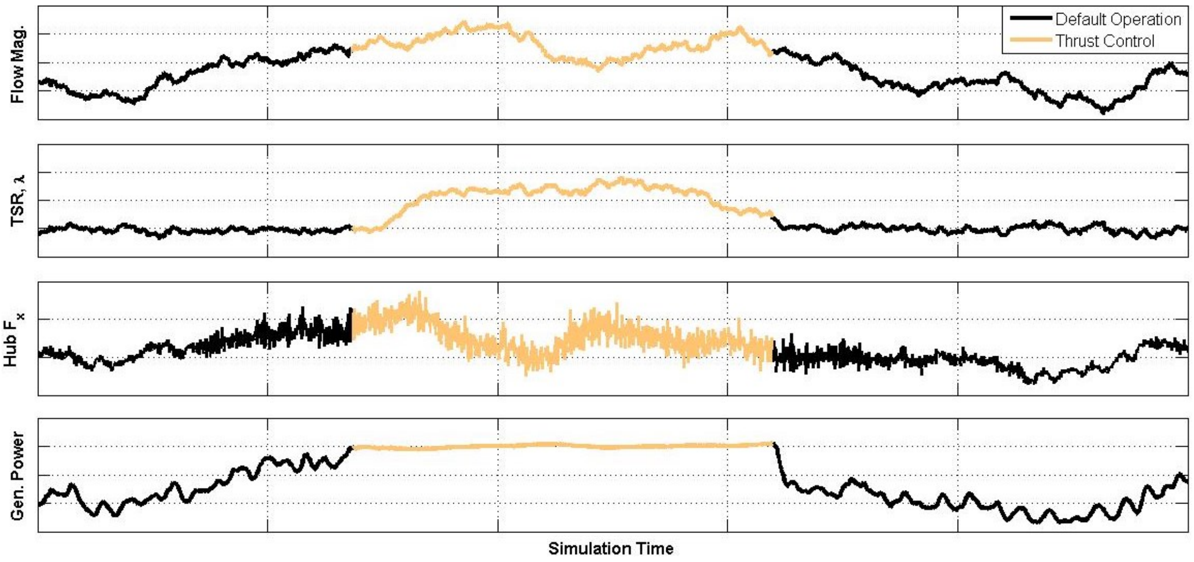

Fig. 6 Time series output from the TEL model during a period of thrust control

Notice that prior to the turbine reaching rated power, it is well controlled at a near constant λ corresponding to peak rotor efficiency, i.e. λ_{opt}. Once rated power is achieved, the turbine can be seen increasing its λ to operate in the thrust control region. It then returns to λ_{opt} after the rated power period ends.

In the plot of rotor thrust, the loads, as expected, tend to decrease and increase with flow during below rated operation. Entering the thrust control region, these loads are generally prevented from increasing further. There is a manageable increase at the very beginning of this period due to the time it takes for the rotor to reach a considerably higher λ than λ_{opt}. Once this is achieved the loads are effectively reduced.

Limiting the thrust loads in this manner does not affect the generated power output. Instead, it can be seen that a near steady and constant power is generated while operating in the thrust control region.

B. Thrust Profile

In Fig. 7, the rotor thrust profiles are plotted from both models. Data in blue and red are from the Tidal Bladed and TEL simulations respectively. The scatter represents one second moving average values, while the solid lines are the mean values from each simulated flow speed. The error bars represent ± 1 standard deviation from the simulation at this flow speed where this measure of variation was greatest. Note that thrust control usually occurs in currents above $\bar{v}_4$. Due to the inclusion of turbulence, however, simulations at $\bar{v}_4$ do regularly take the turbine into the thrust control region. For the same reason, the turbine does not always operate in this region during simulations at $\bar{v}_5$, although generally it does.

Below the thrust control region, results from the two models agree well, both in terms of mean value and variation. There is an evident difference in thrust loading in higher flows, however. This is a result of differing generator efficiencies between the models. The TEL model currently does not account for this, and as a result it reaches the rated point earlier. This leads to the turbine prematurely entering the thrust control region in the TEL model, due to a lower peak torque demanded by the generator. Only simulations at $\bar{v}_4$ and $\bar{v}_5$ are affected by this inconsistency, since the turbine does not reach rated power in the other cases.

Despite this configuration difference, both models show similar thrust limiting capabilities as a result of the controlled overspeeds. Mean thrust is shown to decrease between $\bar{v}_4$ and $\bar{v}_5$. The trend of the scatter suggests that this decrease continues in higher flows. Variation in thrust loading increases with respect to flow speed before and after rated power is achieved, although the relative increase reduces in the thrust control region. The peak loads are comfortably below the maximum value the turbine has been designed to, which was derived from separate simulations with the turbine encountering extreme conditions that are rarely seen in Ramsey Sound.

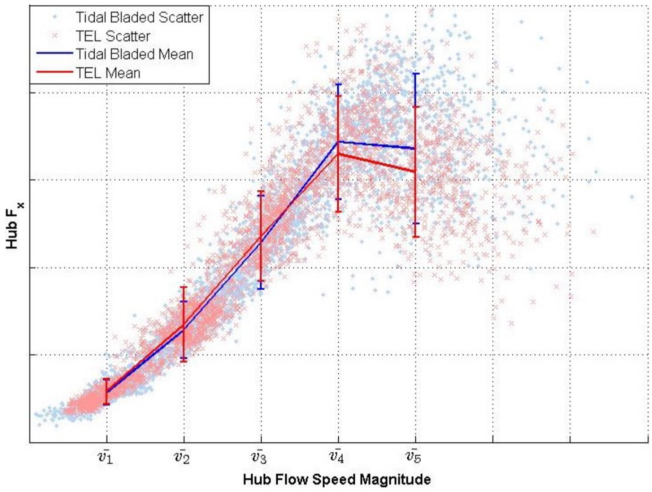

Fig. 7 Rotor thrust profiles

C. Power Profile

The corresponding profile of generator output power is shown in Fig. 8. Again, the scatter represents one second moving average values. The power profiles are in good agreement between models. The effect of the aforementioned difference in generator efficiency between the models is more apparent in this plot, however, with the TEL model generally producing more power and reaching the rated point earlier. In addition to this, it should be noted that, on average, the rotor efficiencies were marginally higher in the TEL simulations due to the turbine operating closer to λ_{opt}. Steady state simulations confirmed that the torque demanded by the generator during below rated conditions in the Tidal Bladed simulations is slightly higher than it is in those performed by TEL, causing the turbine to rotate slower.

Both models show the turbine maintaining its rated power output during thrust control. This can be seen up to flow speeds considerably greater than the rated point, confirming that there are no consequences on power output from this control strategy. The TEL simulations do, however, appear to show some scatter in the above rated region. This often occurs when the flow speed is declining. During such instances, the rotor must also slow down to ensure that it starts returning towards λ_{opt}. If this is not achieved, the rotor will be running too fast for the flow conditions, consequently producing less power than the rated capacity. The scatter is a result of small delays in the reduction of rotor speed. Without further knowledge of the Tidal Bladed model, it is unclear why a similar amount of scatter is not seen in these simulations.

CONCLUSIONS

The capabilities of TEL's thrust control system have been evaluated in unsteady, mathematical simulations of the turbine operating in environmental conditions comparable to Ramsey Sound. An in-house model developed at TEL and DNV GL's Tidal Bladed software were both used for this assessment. Where possible, care was taken to ensure that setup parameters in each model were consistent, while the processes for handling and presenting simulation output data were equivalent.

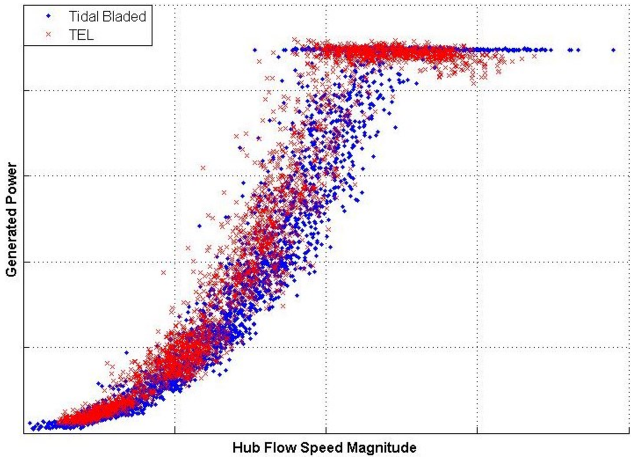

Fig. 8 Generated power profiles

A time series extract from a simulation where rated power output is achieved showed the rotor coming off its default operation point and entering the thrust control region. Rotor thrust loads during this controlled overspeed were limited without affecting power output. The generator achieves near constant power during thrust control.

Thrust and power profiles have been produced from a number of simulations at five mean hub flow speeds, chosen such that the expected operating range of the turbine is covered. The results from both models show good agreement. Minor discrepancies have been attributed to differences in the modelling of the generator efficiency and controller performance. The profiles produced from both models confirm that the control strategy achieves its objective of limiting rotor thrust loads while producing constant power.

These results suggest that good power performance and thrust regulation can be achieved from this control strategy without the drawbacks of traditional methods. No additional components must be added or controlled as part of this system, ensuring that complexity, cost and potential failure modes are kept to a minimum. In the case of DeltaStream^{TM}, this effective thrust management allows the turbine to utilise a gravity foundation, where further cost savings are made. TEL will soon verify the turbine's key design principles, including thrust control, during the upcoming sea trials at Ramsey Sound.

ACKNOWLEDGMENT

The primary author wishes to acknowledge the support from the Industrial Doctoral Centre for Offshore Renewable Energy (IDCORE) programme, a partnership between the Universities of Edinburgh, Exeter and Strathclyde, the Scottish Association for Marine Science (SAMS), and HR Wallingford. IDCORE is funded by the Energy Technologies Institute (ETI) and the EPSRC RCUK Energy programme.

REFERENCES

[1] C. H. Frost, P. S. Evans, C. E. Morris, A. Mason-Jones, T. O'Doherty, and D. M. O'Doherty, "The effect of axial flow misalignment on tidal turbine performance," in: *Proc. 1st International Conference on Renewable Energies Offshore (Renew)*. 24th-26th November 2014, Lisbon, Portugal.

[2] I. Masters, and M. Togneri, "The influence of micrositing on marine turbulence," in: *Proc. ASRANet Offshore Renewable Energy International Conference*. 15th-17th September 2014, Glasgow, UK.

[3] P. S. Evans, S. Armstrong, C. A. M. E. Wilson, I. Fairley, C. F. Wooldridge, and I. Masters, "Characterisation of a highly energetic tidal energy site with specific reference to hydrodynamics and bathymetry," in: *Proc. 10th European Wave and Tidal Conf. (EWTEC)*. 2nd-5th September 2013, Aalborg, Denmark.

[4] I. Fairley, P. Evans, C. Woodbridge, M. Willis, and I. Masters, *Evaluation of tidal stream resource in a potential array via direct measurements,* Renewable Energy, Vol. 57, pp. 70-78, 2013.

[5] Tidal Energy Ltd., *DeltaStream: The Core Design Principles and Intellectual Property*, Technical Report, [Online]. Available: http://www.tidalenergyltd.com/?page_id=17, 2013.

[6] A. I. Winter, "Differences in fundamental design drivers for wind and tidal turbines," in: *Proc. OCEANS '11 IEEE Santander Conference.* 6th-9th June 2011, Santander, Spain.

[7] B. Whitby, and C. E. Ugalde-Loo, *Performance of pitch and stall regulated tidal stream turbines*, IEEE Transactions on Sustainable Energy, Vol. 5, No. 1, January 2014.

[8] Tidal Energy Ltd., *Tidal Turbine System*, UK Patent 2467653-A, 2011.

[9] S. Way, M. Thomson, and J. Goldsmith, "Modeling a floating, multiple rotor tidal energy converter using tidal bladed," in: *Proc. 1st Marine Energy Technology Symposium (METS13).* 10th-11th April 2013, Washington, D.C., USA.

[10] A. Mason-Jones, D. M. O'Doherty, C. E. Morris, T. O'Doherty, C. B. Byrne, P. W. Prickett, R. I. Grosvenor, I. Owen, S. Tedds, and R. J. Poole, *Non-dimensional scaling of tidal stream turbines*, Energy, Vol. 44, pp. 820-829, 2012.

[11] A. Winter, "Speed regulated operation for tidal turbines with fixed pitch rotors," in: *Proc. OCEANS '11 MTS/IEEE Kona Conference. 19*th-22nd September 2011, Kona, Hawai'i.

[12] K. Gracie, R. E. Murray, C. M. Johnstone, D. A. Doman, and M. J. Pegg, "Fixed-pitch blades for passive-feather power regulation of second-tier site tidal turbines," in: *Proc. 10th European Wave and Tidal Conf. (EWTEC)*. 2nd-5th September 2013, Aalborg, Denmark.

[13] K. Gracie, T. Nevalainen, C. Johnstone, "Impact analysis of blade shape on performance of tidal turbine for passive feather power regulation," in: *Proc. 5th International Conference on Ocean Energy (ICOE),* 4th-6th November 2014, Halifax, Canada.

[14] A. Winter, and T. Tryfonas, "A constrained optimization process for the design of tidal turbine blades with experimental validation," in: *Proc. OCEANS '11 MTS/IEEE Kona Conference. 19*th-22nd September 2011, Kona, Hawai'i.

[15] R. Starzmann, M. Baldus, E. Groh, N. Hirsch, N. A. Lange, and S. Scholl, "Full-scale testing of a tidal energy converter using a tug boat," in: *Proc. 10th European Wave and Tidal Conf. (EWTEC)*. 2nd-5th September 2013, Aalborg, Denmark.

[16] F. Biskup, M. Arnold, P. Daus, R. Arlitt, and M. Hohberg, "Effects of rotor blade tip modifications on a tidal in-stream converter – Voith HyTide®," in: *Proc. 10th European Wave and Tidal Conf. (EWTEC)*. 2nd-5th September 2013, Aalborg, Denmark.

[17] G. McCann, and R. Rawlinson-Smith, "Development of a design tool for tidal current turbines," in: *Proc. 6th European Wave and Tidal Conf. (EWTEC).* 2005, Glasgow, UK.

[18] G. McCann, R. I. Rawlinson-Smith, and K. Argyriadis, "Load simulation for tidal turbines using wind turbine experience," in: *Proc. 1st International Conference on Ocean Energy (ICOE).* 23rd-24th October 2006, Bremerhaven, Germany.

Proceedings of the ASME 2016 35th International Conference on Ocean, Offshore and Arctic Engineering
OMAE16
June 19-24, 2016, Busan, South Korea

OMAE2016-54364

DEMONSTRATING A TIDAL TURBINE CONTROL STRATEGY AT LABORATORY SCALE

Magnus Harrold
Peter Bromley
Merin Broudic
Tidal Energy Ltd. (TEL)
Cardiff, UK
Email: magnus.harrold@tidalenergyltd.com

David Clelland
Department of Naval Architecture, Ocean
& Marine Engineering
University of Strathclyde
Glasgow, UK

ABSTRACT

Ahead of the installation of a commercial tidal stream turbine, a 1:30 scale model of the device was tested in a recirculating flume tank. This proved to be the first physical demonstration of the turbine's unconventional control strategy, which limits the thrust forces on the device by allowing the rotor to enter an overspeed. The tests showed that this simple to implement concept of operation is a cost-effective and reliable means of managing the rotor thrust loads in energetic flows. Subsequent tests highlighted the importance of correctly calculating the controller gain parameter, otherwise detrimental turbine performance characteristics can be expected. When relating these results to that of the commercial device, there are a number of important differences associated with both the environment and scale of the model tests. Despite this, the results are considered encouraging, and provided confidence for the full-scale deployment.

NOMENCLATURE

A	Rotor swept area
c_p	Power coefficient
c_t	Thrust coefficient
F	Measured strain gauge force
F_d	Structural drag force
F_t	Rotor thrust force
G	Gearbox ratio
k_λ	Controller gain
λ	Tip speed ratio
P_{rotor}	Rotor power
R	Rotor radius
ρ	Water density
τ_{dem}	Torque demand
v	Flow velocity
ω	Turbine rotational velocity

INTRODUCTION

The tidal stream energy industry has matured to the point where a number of individual, commercial-scale turbines have been installed and tested in energetic seas, with some developers reporting on the results from these deployments [1-3]. The next, logical step will involve these devices operating over longer deployment periods to prove that they can reliably generate power, as well as the installation of multiple turbines at a given site, forming tidal farms that aim to make a significant contribution to local energy demands.

Many of the early developments, however, were undertaken at a much smaller scale in laboratories. Compared with full-scale testing, these facilities offer an inexpensive, controlled and repeatable environment where experiments can quickly establish some of the basic turbine properties. Rotor performance, for example, is usually one of the first studies of interest for a particular design [4], which is often then coupled with the development and validation of numerical models of the turbine [5-7]. While in general the laboratory is a much calmer environment than that of an energetic tidal stream, some model experiments have sought to investigate the unsteady performance of turbines in more realistic conditions, including the effects of turbulence [8] and waves [9]. The latter is of particular interest because it introduces unique environmental forces that are not experienced on wind turbines, which share many of the loading mechanisms with their tidal counterparts.

Figure 1. DeltaStream™

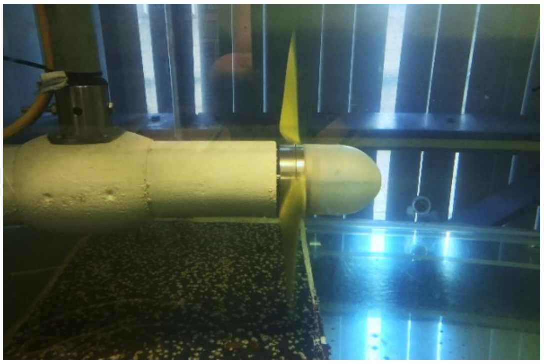

Figure 2. THE 1:30 SCALE MODEL TURBINE

Some of the larger laboratory facilities have even been used to host multiple turbines, leading to an understanding of device to device interactions and wake effects [10].

In this paper, a laboratory was used to test a 1:30 scale model of Tidal Energy Ltd.'s (TEL) turbine (Figure 1), referred to as DeltaStream™, which was recently installed for sea trials in Ramsey Sound, Wales, UK. This commercial-scale turbine has a 12 m diameter rotor and is capable of generating 400 kW. The geometry of the rotor was chosen for its thrust shedding characteristics at high rotational velocities, and led to the development of a control strategy that could utilize these properties in high flows. Essentially the turbine is allowed to enter a controlled overspeed once it reaches its rated power output, which results in effective management of structural loading while maintaining a steady output of 400 kW. This control strategy differs from turbines equipped with pitch mechanisms, which instead limit the rotational velocity and decrease loading by mechanically pitching the blades. Pitch systems have proven to be the control strategy of choice on commercial wind turbines, but the level of academic [11-14] and industrial interest [15], [16] in this overspeed system suggests that the tidal application might be different. Despite the similarities in appearance, there are a number of key and subtle differences between wind and tidal technologies [17], with the most noteworthy being the greater amount of loading that the latter experiences for a given power rating.

To date, this overspeed control strategy has only been evaluated numerically, using both commercially available and in-house models [18]. Thus the tests presented in this paper formed the first physical demonstration of this concept of operation. The paper outlines the methodology for selecting the optimal gain for the turbine controller, while results from tests where a sub-optimal gain parameter was used highlight the importance of this procedure. The authors wish to stress that both the laboratory and scale in which these experiments were conducted in differs significantly from the real sea environment. Some of these key differences are discussed at the end of the paper before forming any conclusions.

METHODOLOGY

Model Turbine Description

A turbine test rig that housed a programmable servomotor was obtained from Cardiff University. This rig has been extensively used for the testing of a 0.5 m diameter turbine [19], [20]. The basic test procedure involved applying an opposing load from a dynamic brake to the hydrodynamic torque developed by the turbine rotor. Torque, angular velocity and hence power could all be controlled via software from the drive manufacturer, or using the ActiveX framework in LabVIEW. Full details of this test rig arrangement can be found in [21].

Since the laboratory tank had a shallow water depth (see next section), this placed a constraint on the rotor size due to concerns relating to blockage effects. A rotor size of 0.4 m diameter was selected as a compromise to minimize these effects, but maintain a geometry that is large enough to produce meaningful results. However, the hub diameter on the rig was fixed at 0.1 m, and scaling of the commercial device to fit this hub would result in a rotor size larger than 0.4 m. To compensate for this, the bottom sections of the model scale blades were removed in the region where the larger hub instead occupied, since these portions of the blades produce the least amount of hydrodynamic torque. As a result, the ratio of hub to rotor size was greater than that of the commercial turbine, i.e. the model had an oversized hub. Even though this did not represent true geometric scaling, the model was expected to maintain similar performance characteristics of the larger device, albeit with reduced hydrodynamic loading and rotor efficiency.

The remaining region of the turbine blades were geometrically scaled from the commercial turbine, measuring 0.15 m in length. These were 3-D printed and fitted with circular pins to position into holes on the circumference of the turbine hub. The correct pitch angles were set by resting the blades on 3-D printed molds that aligned with the back of the hub. Once the pitch angle was set, screws inside the hub were tightened to prevent the pins from moving. The 1:30 scale model turbine is shown in Figure 2.

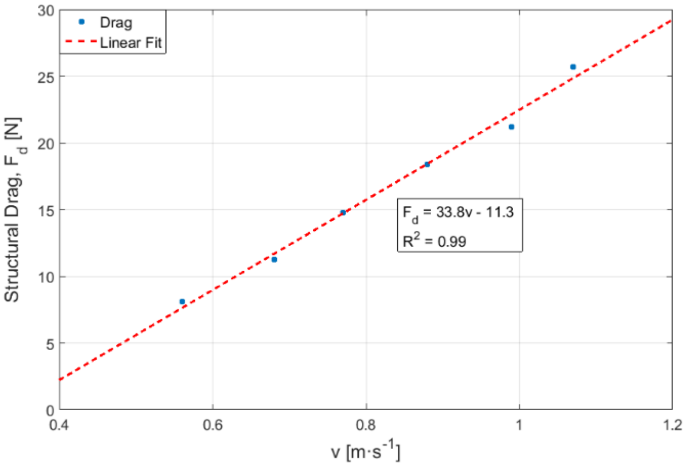

Figure 3. SUPPORT STRUCTURE DRAG CALIBRATION

Test Facility and Arrangement

The model was tested at Cardiff University's Hydro-environmental Research Centre, in a 1.20 m W x 0.66 m D recirculating flume. The turbine was supported by a Y-shaped frame that was fixed to a platform over the flume, with the rotor positioned approximately in the center of the tank cross-section. The support frame was allowed to pivot under loading exerted on it by the flow. This load was measured using a strain gauge positioned on the main supporting pole above the turbine.

A Nortek acoustic Doppler velocimeter (ADV) was positioned upstream and in line with the rotor, capable of measuring flow up to a sampling rate of 200 Hz. Maximum flow speeds of approximately 1.2 m·s^{-1} were reached during testing.

Strain Gauge Calibration

To determine the thrust forces acting on the turbine, two conversions were required to relate the strain gauge measurements to the rotor. The first accounts for drag associated with the turbine support structure. This was determined by removing the blades from the turbine hub and measuring the drag with respect to flow. Figure 3 shows the relationship. The measurements correspond to mean values obtained over two minute periods while the pump power was held constant, producing near steady flume speeds. The ADV flow measurements were quality controlled for low correlation and signal to noise ratios (SNR), as recommended by the manufacturer. Plus, any measurements found to be outside ± 3 standard deviations from the mean value were removed.

At these flow velocities, the structural drag was found to be approximately linear, as demonstrated by the high coefficient of determination (R^2) on the fit in Figure 3. This fitted line was used in all subsequent analysis to evaluate the drag force, F_d, as a function of flow velocity, v, as shown in Eqn. (1):

$$F_d = 33.8v - 11.3 \tag{1}$$

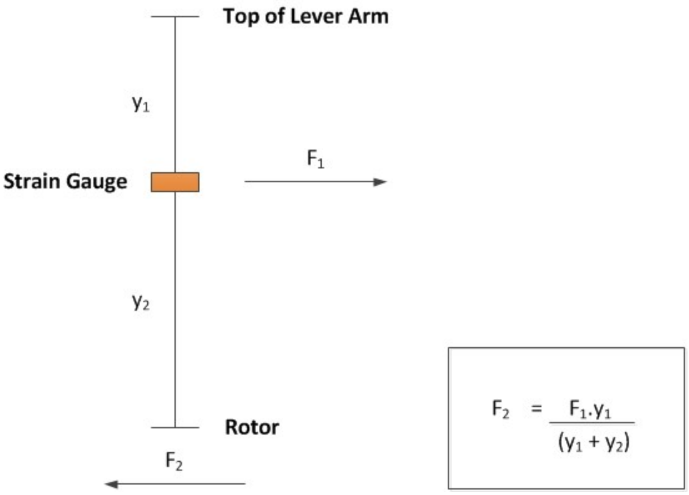

Figure 4. THE LEVER ARM MADE BY THE TURBINE SUPPORT POLE

The second conversion relates the load measured at the strain gauge, F_1, to that at the rotor, F_2. The turbine support pole forms a lever arm, meaning that careful measurements of both its length and the position of the strain gauge allow the relevant moments to be evaluated. This is illustrated in Figure 4. The strain gauge was measured to be at 0.345 m from the top of the lever arm (y_1), which itself was 0.865 m long (y_1 + y_2). Using these measurements and the expression in Figure 4, the thrust on the rotor is approximately 40% of the force measured by the strain gauge. Thus, the final expression used to relate the strain gauge load, F, to rotor thrust, F_t, is shown in Eqn. (2):

$$F_t = 0.4 * (F - F_d) \tag{2}$$

Steady-State Performance Curves

Before implementing the control strategy to the model turbine, it was necessary to determine the steady-state rotor characteristics. These are often expressed using normalized variables. Firstly, the power coefficient, c_p, is expressed as the ratio of the power produced by the rotor, P_{rotor}, to that of a body of water passing through a disk of equivalent swept area, A, with density, ρ, as in Eqn. (3):

$$c_p = \frac{P_{rotor}}{\frac{1}{2}\cdot\rho\cdot A\cdot v^3} \tag{3}$$

Similarly, a thrust coefficient, c_t, is used to normalize the axial loading on the rotor via Eqn. (4):

$$c_t = \frac{F_t}{\frac{1}{2}\cdot\rho\cdot A\cdot v^2} \tag{4}$$

These quantities are then related to the rotor tip speed ratio, λ, a non-dimensional parameter used to compare the tangential

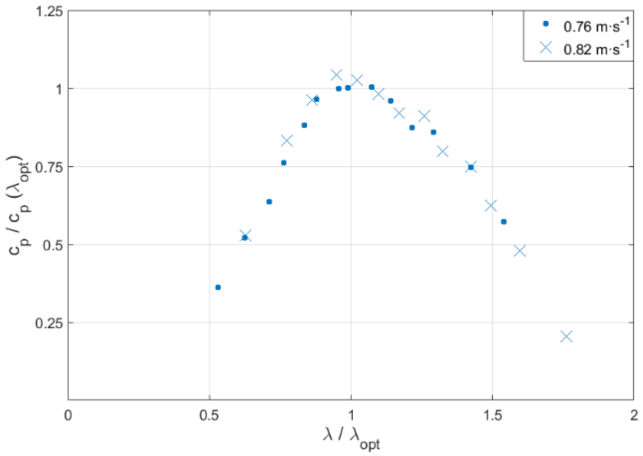

Figure 5. ROTOR $c_p - \lambda$ CURVES

speed of the tip of the rotor blade to the flow velocity, as in Eqn. (5):

$$\lambda = \frac{\omega \cdot R}{v} \tag{5}$$

Where ω is the rotational velocity of the turbine and R is the rotor radius.

To experimentally measure these power and thrust characteristics of the rotor, the turbine was controlled to step through various targeted rotational speeds in a near, constant flow. This started with the turbine free-wheeling in the flow, before speed commands were executed to slow the rotor to a new desired speed by applying an opposing torque. Once the lowest desired speed was achieved, the turbine was allowed to speed up again. Each speed step lasted for 1 minute, with measurements of flow, rotational velocity, thrust and torque all averaged over this period. Note that rotor power is the product of rotational velocity and torque. Measurements obtained within ± 5 seconds of each step change were discarded to allow the rotor some settling time for each operational point. Additionally, the aforementioned quality control techniques for the ADV measurements were also applied here.

Due to the rotor occupying approximately 16% of the flume cross-sectional area, its power performance was artificially enhanced due to blockage effects. Thrust loads were also increased. These effects are a result of flow being forced through the rotor at a greater rate than it would in a less constrained environment, such as that which the commercial device will experience. A prevalent blockage correction method [4] was applied to the measurements of c_p, c_t and λ to estimate the unconstrained performance.

Figure 5 shows the rotor $c_p - \lambda$ curves, obtained in flows of 0.76 m·s^{-1} and 0.82 m·s^{-1}. The results have been scaled to show the power performance relative to the peak of the curve at the optimum tip speed ratio, λ_{opt}. The curves derived from both flows agree well and feature only small deviations. The general shape is skewed to the right of λ_{opt}. This implies that a greater power performance can be expected if the rotor operates above λ_{opt} than it would at the same relative position below λ_{opt}.

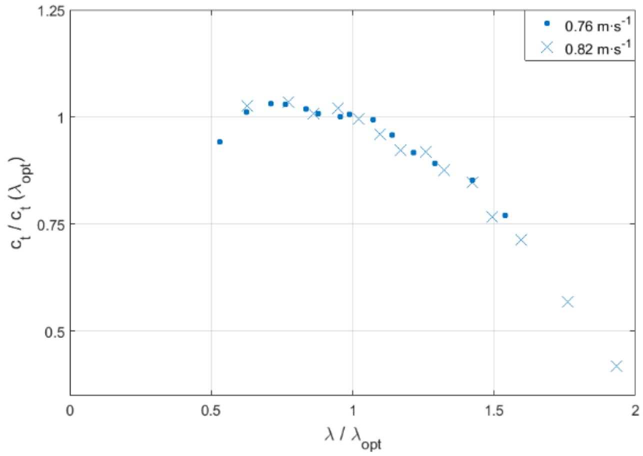

Figure 6. ROTOR $c_t - \lambda$ CURVES

The corresponding $c_t - \lambda$ curves are shown in Figure 6. Again, the measurements have been scaled to the values found at λ_{opt}. Similar to the c_p results, the curves are consistent at both flow velocities. These results also highlight that the rotor has a decreasing c_t above λ_{opt}. This behavior is atypical from many other turbine rotors, which generally show an increasing c_t above λ_{opt} [4], [19]. This combination of decreased c_p and c_t at high λ is desirable for any turbine once it reaches its rated power output, since the generator cannot produce more power and the thrust loads must be managed in high flows. Often pitch mechanisms are used to achieve this, but these results suggest that simply overspeeding the rotor could have the same result.

Control Strategy Theory and Implementation

It is clear from Figure 5 that in order to generate the maximum amount of power from the turbine, it must track λ_{opt} as the flow varies. This can be achieved by measuring the turbine rotational velocity and applying the correct amount of resistive, generator torque, or servomotor torque in the case of the model. Thus no knowledge of the flow velocity is required. Instead, the torque demand, τ_{dem}, follows a quadratic relationship with turbine rotational velocity, as in Eqn. (6):

$$\tau_{dem} = k_{\lambda} \cdot \omega^2 \tag{6}$$

Where k_λ is a gain term that depends on the properties of the turbine and its power characteristics, i.e. the $c_p - \lambda$ curve. The expression for k_λ is shown in Eqn. (7):

$$k_{\lambda} = \frac{\pi \cdot \rho \cdot R^5 \cdot c_p}{2 \cdot \lambda^3 \cdot G^3} \tag{7}$$

Therefore, to generate the maximum amount of power, the values of λ_{opt} and $c_p(\lambda_{opt})$ must be inserted into Eqn. (7). Note that G is the gearbox ratio. This was not applicable to the model turbine, and was set to unity.

After reaching the generator rated power output, P_{rated}, in sufficiently high flows, the controller objective should change

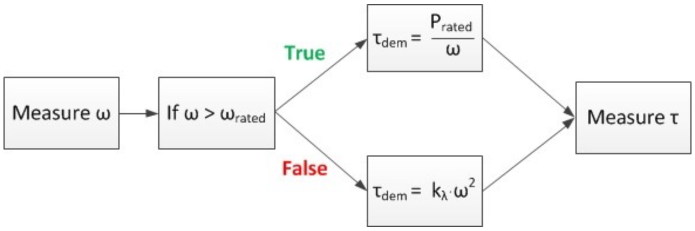

Figure 7. CONTROL STRATEGY BLOCK DIAGRAM

to avoid overloading the drivetrain. For the overspeed control strategy, this can be achieved by decreasing the generator torque once the turbine reaches P_{rated}. In this region the demanded torque varies according to Eqn. (8):

$$\tau_{dem} = \frac{P_{rated}}{\omega} \tag{8}$$

This ensures that turbine torque and rotational velocity are balanced such that P_{rated} continues to be generated. For the model turbine, a P_{rated} value was chosen to occur in flows of approximately 0.8 $\mathrm{m{\cdot}s^{-1}}$. This prediction was made from the rearrangement of Eqn. (3) and using the measured $c_p(\lambda_{opt})$. Since the flume would comfortably run up to flows of 1.2 $\mathrm{m{\cdot}s^{-1}}$, this would allow for sufficient measurements to be obtained both above and below P_{rated} to assess the controller in a wide range of conditions.

The servomotor could be controlled within a LabVIEW program by using the ActiveX framework. Based on the current turbine rotational velocity, the controller logic simply instructed the turbine to either track λ_{opt} or overspeed, using Eqns. (6) and (8) respectively. The turbine would overspeed if it exceeded the rated rotational velocity, ω_{rated}. Figure 7 illustrates the controller logic.

Test Procedure and Data Processing

The basic test procedure involved steadily ramping the flow velocity up to 1.2 $\mathrm{m{\cdot}s^{-1}}$, before returning to a still tank. This would take the turbine through a cycle that is broadly similar to the generating patterns experienced at a tidal energy site.

Measurements from both the ADV and servomotor were recorded in the LabVIEW program at 10 Hz, enabling synchronisation to the PC time. The strain gauge measurements were acquired on an independent PC, and hence had a different time-series. Synchronisation with the other measurements was achieved via the identification of a trigger event on a separate channel on the strain gauge DAQ. This trigger event corresponded to a known PC time on the LabVIEW program. Therefore, it was possible to align each time-series in post-processing through careful identification of the trigger events.

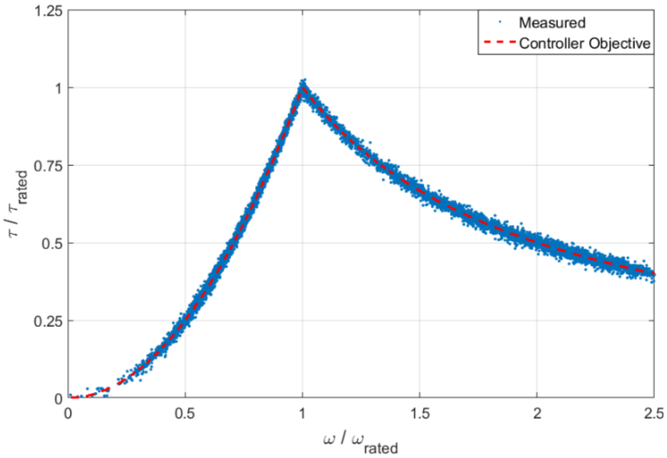

Figure 8. CONTROLLER PERFORMANCE COMPARED WITH THE IDEALIZED OBJECTIVES

RESULTS

Controller Performance

In Figure 8 the measured turbine torque is scattered with respect to rotational velocity, and compared with the idealized controller objective curve. The variables are normalized by their values at the rated point. There is only a small amount of deviation in the measured data about the idealized curve, implying that the turbine controller performed well both above and below the rated point. The scatter broadens marginally in the overspeed region, but this should be expected given that the turbine torque is decreasing while its rotational velocity is allowed to increase in high flows.

Time-Series Evaluation

The time-series results from one of the tests are shown in Figure 9. From top to bottom, the plots are of flow velocity, tip speed ratio, torque and power. A 10 second moving mean line is superimposed on the instantaneous values. Note that the turbine did not start rotating until the flow reached near 0.5 $\mathrm{m{\cdot}s^{-1}}$, and as a result the first 300 seconds of this test are not shown while the flow built up from a still tank. It should also be noted that the thrust measurements are not presented in this section due to the difficulty in using instantaneous flow measurements for the support structure drag calibration, which was previously shown in Eqn. (1). The instantaneous flow features considerable variation and would lead to the prediction of erratic support structure drag. The moving mean values are a better representation of the flow at any point in the time-series, and are used in the next section to present the thrust measurements.

The time-series shows the flow steadily increasing from 0.5 to 0.8 $\mathrm{m{\cdot}s^{-1}}$ between 300 and 480 seconds. During this time the turbine succeeds in tracking λ_{opt}, while both torque and power increase with flow speed. The rated torque is reached at the end of this period and the turbine can be seen to come off λ_{opt}, entering overspeed. λ continues to increase until it is about

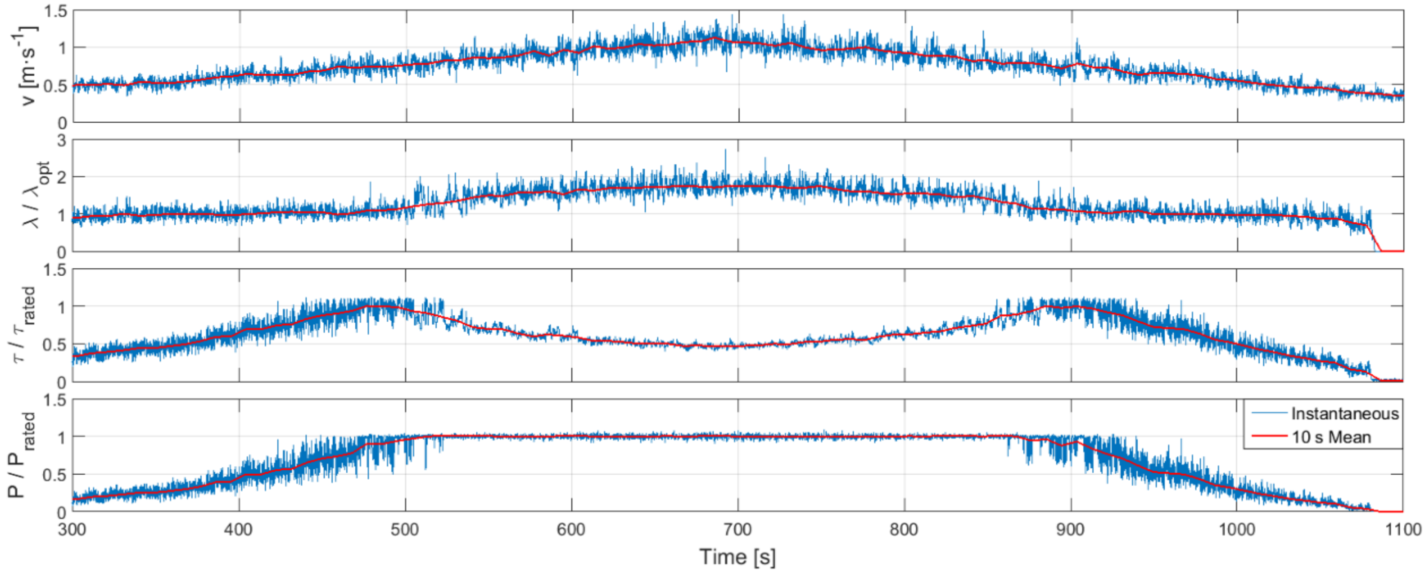

Figure 9. TIME-SERIES OF TURBINE PERFORMANCE

twice λ_{opt} at 700 seconds, by which point the flow exceeds 1.1 m·s^{-1}. During overspeed, the decrease in torque is handled such that power is capped at P_{rated}. The instantaneous results show very little scatter about P_{rated}, suggesting that the turbine performs well at providing a steady power output in high flows.

The flow then starts to decrease after 700 seconds, with the increasing torque causing the rotor to slow down. Peak torque is reached for the second time at 900 seconds, by which point the flow has returned to 0.8 m·s^{-1}. This is accompanied by the rotor leaving the overspeed region to resume tracking λ_{opt}, marking the point at which the turbine stops producing P_{rated}.

The last 200 seconds of this test sees the turbine continue tracking λ_{opt} as the flow continues to decrease, along with both torque and power. Once the flow drops to 0.4 m·s^{-1}, not enough hydrodynamic torque is produced by the rotor to overcome the resistive load provided by the servomotor, and hence the turbine stops rotating.

Dynamic Performance

The moving mean values have been used to form dynamic power and rotational velocity plots, using data obtained from the results presented in Figure 9 and other, similar tests. The plots are shown in Figure 10.

On the power plot a steady-state curve is included, derived from rearranging Eqn. (3) and using the value of $c_p(\lambda_{opt})$ for flows up to 0.8 m·s^{-1}. After which, the curve is capped at P_{rated}. The measured scatter shows good agreement with the steady-state curve, suggesting that the turbine performed well at tracking λ_{opt}. This is confirmed by studying the corresponding plot of rotational velocity, which shows the turbine linearly increasing its speed with flow and following the λ_{opt} line. The turbine successfully moves above this line in the overspeed region, resulting in the generation of P_{rated}.

There are, however, two areas where the measurements show some variation from the steady-state curve. The first is at flows below 0.5 m·s^{-1}, where the measured power is noticeably lower than the prediction. This is in the start-up region where the turbine begins rotating. By looking at this same region on the turbine speed curve, it is clear that the turbine rotated slower than optimum during these periods. It is speculated that the turbine just had enough energy to rotate in this region, but not enough to consistently track λ_{opt}. The other area of interest is just below the rated point of 0.8 m·s^{-1}, which has scatter to the left of the steady-state curve that suggests the turbine outperformed the prediction in this region. This could be a result of stored rotational energy in the rotor as it slows down from a period of overspeed. The turbine speed plot also hints at this, where the rotor can be seen moving above the λ_{opt} line before 0.8 m·s^{-1}. Care should be taken when reading the speed plot in this region, however, since the averaging that has been used to produce the scatter will have shifted the results above the λ_{opt} line, due to the non-linearity of the overspeed.

Figure 11 shows the corresponding plot of the dynamic rotor thrust. The measurements have been normalized by the thrust prediction at the rated point of 0.8 m·s^{-1}, $F_{t_{rated}}$, found by rearranging Eqn. (4) and using the experimentally derived $c_t(\lambda_{opt})$ from Figure 6. This steady-state rotor thrust prediction is also plotted in Figure 11 for all flows.

The measurements closely scatter about the steady-state curve up until the rated point, as expected from the successful λ_{opt} tracking shown in Figures 9 and 10. Above the rated point, the measurements are prevented from following the steady-state curve due to the overspeed. Instead, the rate at which thrust increases with flow reduces significantly. For example, since the steady thrust varies with the square of flow velocity, a 56% increase in thrust would be expected between flows of 0.8 m·s^{-1} and 1.0 m·s^{-1}. However, in this same region the measured thrust increases by approximately just 5% from the steady equivalent

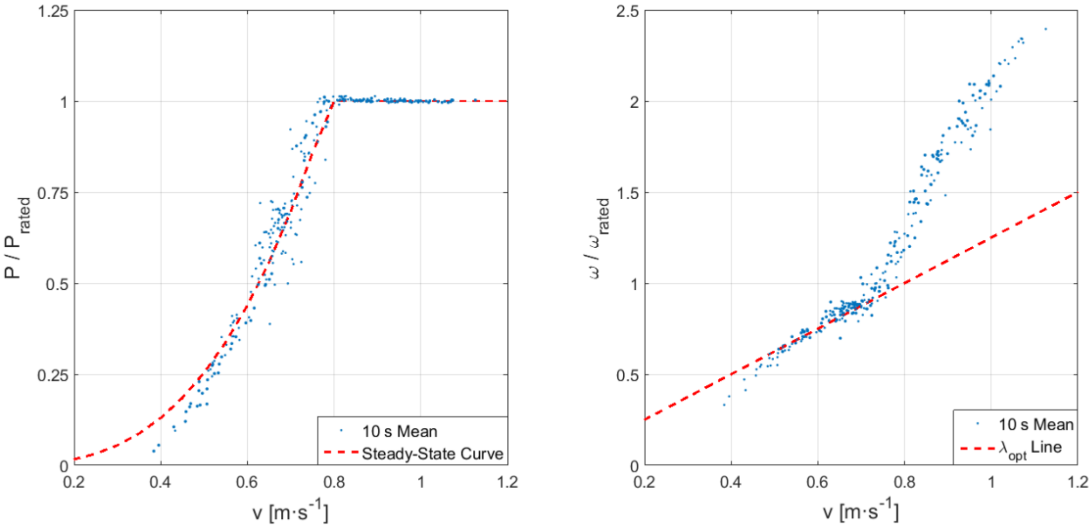

Figure 10. DYNAMIC TURBINE POWER (LEFT) AND SPEED (RIGHT)

at 0.8 m·s^{-1}. This overspeed control strategy, therefore, not only offers good power production, but effectively prevents the structural loading from becoming excessive in high flows, both of which are desirable characteristics for any turbine.

The control strategy did not prevent the mean thrust loads from increasing entirely in the overspeed region, however, with values observed to exceed $F_{t_{rated}}$. Possible explanations for this are given in the discussion section of this paper.

Alternative Control Strategies

Two variations were made to k_λ to assess its influence on turbine performance. k_λ was both decreased and increased from the optimal value, resulting in the turbine rotating faster and slower respectively below the rated point. To compare these variations with the optimal control strategy, the same P_{rated} value was maintained. This meant that each control strategy had identical overspeeds. The torque-speed curves for these alternative control strategies are shown in Figure 12, compared relative to the optimal strategy. Peak torque has decreased by approximately 25% on the reduced gain strategy, while it has increased by 20% on the other variation.

The dynamic turbine power and speed curves for each k_λ variation are displayed in Figure 13, again compared relative to the default control strategy. Both of these controller variations have unsurprisingly reduced the power performance of the turbine, with the majority of the scatter falling below that of the optimal control strategy and its steady-state curve. The increased gain strategy, in particular, notably underperforms at lower flows. This result is not unexpected given the asymmetric $c_p - \lambda$ curve of the rotor displayed in Figure 5. The turbine speed curves clearly show that the controller variations have moved the λ away from the the λ_{opt} line. Interestingly, the results suggest that the reduced gain strategy begins rotating, and hence producing power, in flows lower than the optimal strategy, despite obtaining fewer measurements in these tests. In contrast to this, the turbine did not start rotating until higher flows in the increased gain strategy. Thus there are small benefits from reducing the torque gain during turbine start-up.

In Figure 14, the dynamic rotor thrust curves are compared for each control strategy. Reducing the controller gain has, in general, decreased the axial loading on the rotor, with most of the measurements found to be lower than optimal strategy's steady-state curve. The effect that increasing the controller gain has on thrust is less clear, due to the low number of measurements obtained. The results do, however, appear to be similar to the optimal strategy. Both of these findings agree with the measured $c_t - \lambda$ curve in Figure 6, where considerable reductions in c_t were found only at λ higher than λ_{opt}.

DISCUSSION

The results from dynamically testing the overspeed control strategy have proven that it achieves the power and thrust characteristics that are necessary for reliable turbine operation at a range of flow velocities. This system, therefore, is expected to offer a number of benefits to alternative control strategies, which tend to be based on either pitch or stall regulated methods. The former usually requires the introduction of motors to change the pitch angles of the blades, often with the aim of limiting the turbine rotational speed and torque it develops once the rated values are reached. While this does not add an unmanageable amount of complexity to the control system, the extra components do increase the cost of the turbine and its number of failure modes. This might not be a large concern for onshore wind turbines, but for the tidal application any unplanned maintenance can lead to comparatively long periods of operational downtime, due to the offshore distance and weather dependent nature of accessing the subsea turbine. Additionally, it has been suggested that pitch systems are less effective on tidal turbines due to the expectation that the achievable pitch rates are lower in water than in air [17].

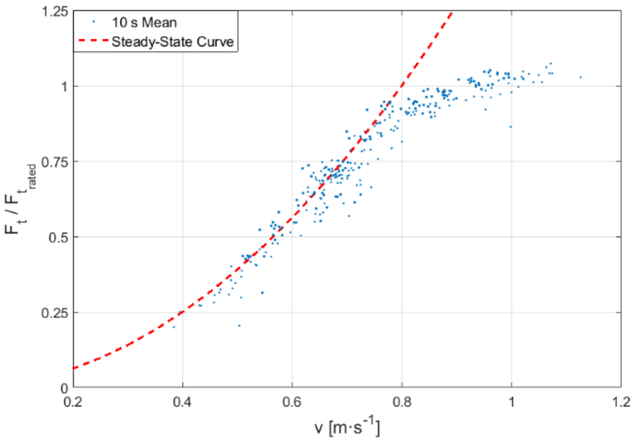

Figure 11. DYNAMIC ROTOR THRUST

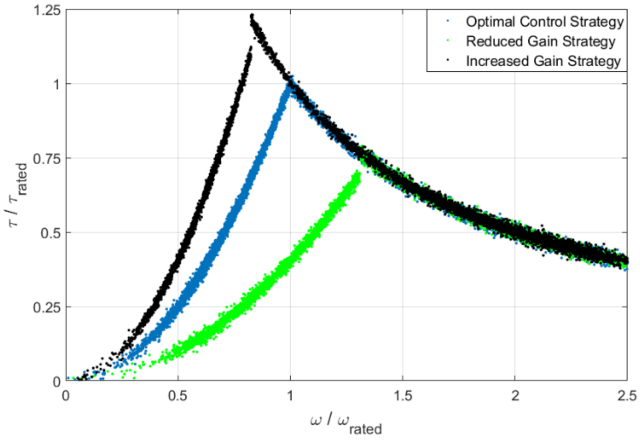

Figure 12. TURBINE TORQUE-SPEED CURVES FOR THE ALTERNATIVE CONTROL STRATEGIES

Stall regulation can be achieved on fixed-pitch rotors without the addition of further complexity to the turbine system, similar to the overspeed control strategy. The basic principle involves capping or reducing the turbine speed once it reaches its rated output, meaning that the rotor operates at large angles of attack and is subject to increased drag. From a power production perspective, stall based systems do not perform as well as pitch systems at sites where a wide range of operating conditions are experienced [22]. Thrust loading is also difficult to manage in high flows. These concerns are often not an issue for small devices, such as domestic scale wind turbines, and as a result the stall regulated system is suitable for this market.

The overspeed strategy, then, would appear to maintain the simplicity of the stall based system, but achieve the greater power and thrust performance of the pitchable rotor. It does, however, introduce its own potential concerns that need to be assessed further during the design process, including cavitation, blade-tower interactions, and out-of-plane forces.

From the results of this laboratory test campaign, it was noted that the mean thrust on the rotor kept increasing above the rated power point. Overspeeding the rotor only decreased the rate of the thrust increase. The numerical analyses performed on the full-scale turbine did not show this behaviour, and instead mean thrust loading decreased above the rated point [18]. Upon comparing the measured $c_t - \lambda$ curve (Figure 6) with the numerically derived equivalent, the latter predicted lower c_t values at high λ. The magnitude of the difference is sufficient to account for the unobserved full thrust limitation. While the numerical prediction was based on a Reynolds number that is appropriate for the full-scale device, it is unclear whether scaling is the main cause of this difference. The numerical predictions rely on drag and lift data for the airfoil sections of the turbine blades, and it is notoriously difficult to obtain these empirical measurements at low Reynolds numbers, i.e. at scales suitable for the model turbine. In addition, the simulation tools that are available to predict the drag and lift on an airfoil are unreliable at this scale. Thus, it has not been possible to form a numerical prediction for the model turbine.

In addition, it should be stated that there are a number of geometrical uncertainties with the model turbine that could account for observed differences in rotor thrust. The printed accuracy of the blades at model scale is unknown, and any discrepancies associated with this would dramatically change the performance characteristics of the rotor. Similarly, any blade flexing or incorrectly set pitch angles would have a comparable effect on performance, despite the best efforts made to prevent the latter.

CONCLUSIONS

This paper has outlined the objectives of an overspeed control strategy, based on that of a recently installed commercial scale tidal turbine. This device was sized to 1:30 scale and tested in a recirculating flume tank. After completing a number of calibrations and corrections on experimental measurements, the rotor characteristics were derived in near steady flows, showing good agreement at differing flume velocities. This allowed the determination of the optimal controller torque gain for maximum power extraction.

Subsequently, the laboratory turbine was tested under varying flow conditions and programmed to follow the overspeed control strategy logic. The turbine demonstrated that in these dynamic conditions it performed well against the idealized controller objectives at all operational ranges. This was further confirmed from a time-series analysis, where the turbine was observed to track its point of maximum power extraction up to a pre-defined rated point, before entering a controlled overspeed that regulated the power output.

The resulting turbine dynamic power, speed and thrust curves from these experiments were found to be in good agreement with steady predictions, formed from the measured rotor characteristics. A minor deviation from the steady prediction at low flows was attributed to the rotor attempting to start-up, while near the rated point the turbine showed signs of exceeding expectations. It has been speculated that this is due to stored rotational energy in the rotor after it slows down from

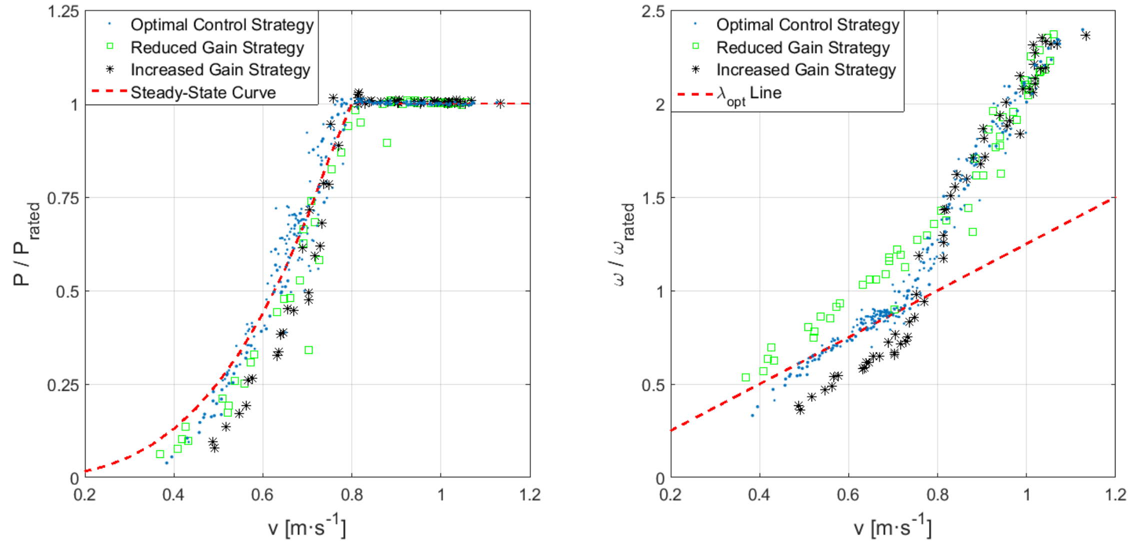

Figure 13. DYNAMIC TURBINE POWER (LEFT) AND SPEED (RIGHT) CURVES FOR EACH CONTROL STRATEGY

a period of overspeed. The dynamic thrust curve clearly showed that the rate at which the axial loads increase with flow is significantly reduced from overspeed. The significance of this is that good power regulation and thrust management were both achieved from this control strategy, the combination of which is desirable for any turbine operating across a wide range of conditions.

Further testing was performed to evaluate the effect on turbine performance if a less than optimal controller torque gain was applied. These variations saw the turbine rotate both faster and slower than the optimal speed. Unsurprisingly, in each case the power performance was adversely affected by the controller variations, emphasizing the importance of careful deduction of the gain parameter. However, when the gain was reduced, allowing the turbine to rotate faster, the rotor was observed to start-up in lower flows. Thus there are small benefits from reducing the torque gain during the initial phases of power production.

Although the results from these tests have shown that this unconventional control strategy maintains many of the benefits of alternative options, it now requires supplementary data from full-scale testing to provide a complete appraisal. This is an ongoing area of research after the installation of the commercial DeltaStream^{TM} turbine in December, 2015.

ACKNOWLEDGMENTS

The primary author wishes to acknowledge the support from the Industrial Doctoral Centre for Offshore Renewable Energy (IDCORE) programme, a partnership between the Universities of Edinburgh, Exeter and Strathclyde, the Scottish Association for Marine Science (SAMS), and HR Wallingford. IDCORE is funded by the Energy Technologies Institute (ETI) and the EPSRC RCUK Energy programme.

REFERENCES

[1] McNaughton, J., Harper, S., Sinclair, R., and Sellar, B., 2015. “Measuring and modelling the power curve of a commercial-scale tidal turbine”. In proceedings of the 11th European Wave and Tidal Energy Conference (EWTEC), Nantes, France.

[2] Jeffcoate, P., Starzmann, R., Elsaesser, B., Scholl, S., and Bischoff, S., 2015. “Field measurements of a full scale tidal turbine”. *International Journal of Marine Energy, Volume 12*, pp. 3-20.

[3] Starzmann, R., Jeffcoate, P., Scholl, S., Bischoff, S., and Elsaesser, B., 2015. “Field testing a full-scale tidal turbine part 1: power performance assessment”. In proceedings of the 11th European Wave and Tidal Energy Conference (EWTEC), Nantes, France.

[4] Bahaj, A.S., Molland, A.F., Chaplin, J.R., Batten, W.M.J., 2007. “Power and thrust measurements of marine current turbines under various hydrodynamic flow conditions in a cavitation tunnel and a towing tank”. *Renewable Energy, Volume 32(3),* pp. 407-426.

[5] Batten, W.M.J., Bahaj, A.S., Molland, A.F., and Chaplin, J.R., 2007. “Experimentally validated numerical method for the hydrodynamic design of horizontal axis turbines”. *Ocean Engineering, Volume 34(7),* pp. 1013-1020.

[6] Bahaj, A.S., Batten, W.M.J., and McCann, G., 2007. “Experimental verifications of numerical predictions for the hydrodynamic performance of horizontal axis marine current turbines”. *Renewable Energy, Volume 32(15),* pp. 2479-2490.

[7] Batten, W.M.J., Bahaj, A.S., Molland, A.F., and Chaplin, J.R., 2008. “The prediction of the hydrodynamic performance of marine current turbines”. *Renewable Energy, Volume 33(5),* pp. 1085-1096.

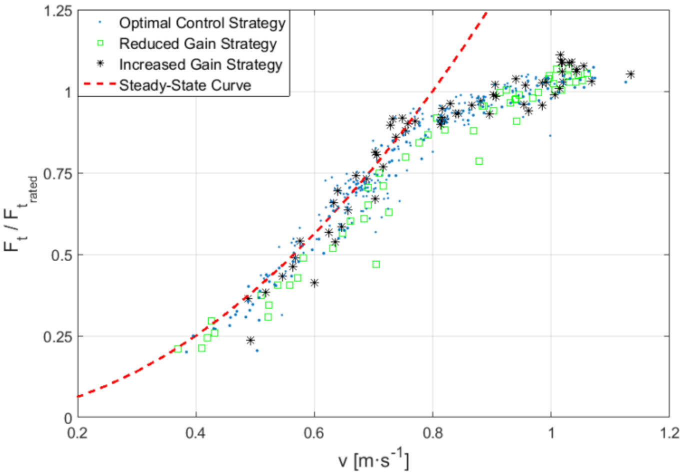

Figure 14. DYNAMIC ROTOR THRUST CURVES FOR EACH CONTROL STRATEGY

[8] Mycek, P., Gaurier, B., Germain, G., Pinon, G., and Rivoalen, E., 2014. "Experimental study of the turbulence intensity effects on marine current turbines behavior. Part I: One single turbine". *Renewable Energy, Volume 66,* pp. 729-746.

[9] Barltrop, N., Varyani, K.S., Grant, A., Clelland, D., and Pham, X.P., 2007. "Investigation into wave-current interactions in marine current turbines". *In proceedings of the Institution of Mechanical Engineers (IMechE), Part A: Journal of Power and Energy, Volume 221(2),* pp. 233-242.

[10] Mycek, P., Gaurier, B., Germain, G., Pinon, G., and Rivoalen, E., 2014. "Experimental study of the turbulence intensity effects on marine current turbines behavior. Part II: Two interacting turbines". *Renewable Energy, Volume 68,* pp. 876-892.

[11] Winter, A., 2011. "Speed regulated operation for tidal turbines with fixed pitch rotors". In proceedings of the MTS/IEEE OCEANS Conference, Kona, Hawai'i, USA.

[12] Winter, A., and Tryfonas, T., 2011. "A constrained optimization process for the design of tidal turbine blades with experimental validation". In proceedings of the MTS/IEEE OCEANS Conference, Kona, Hawai'i, USA.

[13] Gracie, K., Murray, R.E., Johnstone, C.M., Doman, D.A., and Pegg, M.J, 2013. "Fixed-pitch blades for passive-feather power regulation of second-tier site tidal turbines". In proceedings of the 10th European Wave and Tidal Energy Conference (EWTEC), Aalborg, Denmark.

[14] Gracie, K., Nevalainen, T., and Johnstone, C., 2014. "Impact analysis of blade shape on performance of tidal turbine for passive feather power regulation". In proceedings of the 5th International Conference on Ocean Energy (ICOE), Halifax, Canada.

[15] Starzmann, R., Baldus, M., Groh, E., Hirsch, N., Lange, N.A., and Scholl, S., 2013. "Full-scale testing of a tidal energy converter using a tug boat". In proceedings of the 10th European Wave and Tidal Energy Conference (EWTEC), Aalborg, Denmark.

[16] Biskup, F., Arnold, M., Daus, P., Arlitt, R., and Hohberg, M., 2013. "Effects of rotor blade tip modifications on a tidal in-stream converter – Voith HyTide®". In proceedings of the 10th European Wave and Tidal Energy Conference (EWTEC), Aalborg, Denmark.

[17] Winter, A.I., 2011. "Differences in fundamental design drivers for wind and tidal turbines", 2011. In proceedings of the IEEE OCEANS Conference, Santander, Spain.

[18] Harrold, M.J., Bromley, P., Clelland, D., Kiprakis, A., and Abusara, M., 2015. "Evaluating the thrust control capabilities of the DeltaStream™ turbine". In proceedings of the 11th European Wave and Tidal Energy Conference (EWTEC), Nantes, France.

[19] Tedds, S.C., Poole, R.J., Owen, I., Najafian, G., Bode, S.P., Mason-Jones, A., Morris, C., O'Doherty, T., and O'Doherty D.M., 2011. "Experimental investigation of horizontal axis tidal stream turbines". In proceedings of the 9th European Wave and Tidal Energy Conference (EWTEC), Southampton, UK.

[20] Mason-Jones, A., O'Doherty, D.M., Morris, C.E., O'Doherty, T., Byrne, C.B., Prickett, P.W., Grosvenor, R.I., Owen, I., Tedds, S., and Poole, R.J., 2012. "Non-dimensional scaling of tidal stream turbines". *Energy, Volume 44,* pp. 820-839.

[21] Mason-Jones, A., 2010. "Performance assessment of a horizontal axis tidal turbine in a high velocity shear environment". PhD thesis, Cardiff University.

[22] Whitby, B., and Ugalde-Loo, C.E., 2014. "Performance of pitch and stall regulated tidal stream turbines". *IEEE Transactions on Sustainable Energy, Volume 5, No. 1,* pp. 64-72.